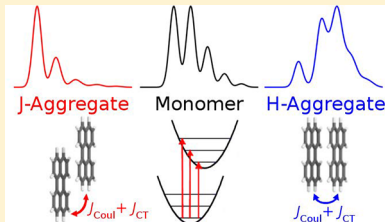


## Expanded Theory of H- and J-Molecular Aggregates: The Effects of Vibronic Coupling and Intermolecular Charge Transfer

Nicholas J. Hestand<sup>ID</sup> and Frank C. Spano<sup>\*ID</sup>

Department of Chemistry, Temple University, Philadelphia, Pennsylvania 19122, United States

**ABSTRACT:** The electronic excited states of molecular aggregates and their photophysical signatures have long fascinated spectroscopists and theoreticians alike since the advent of Frenkel exciton theory almost 90 years ago. The influence of molecular packing on basic optical probes like absorption and photoluminescence was originally worked out by Kasha for aggregates dominated by Coulombic intermolecular interactions, eventually leading to the classification of J- and H-aggregates. This review outlines advances made in understanding the relationship between aggregate structure and photophysics when vibronic coupling and intermolecular charge transfer are incorporated. An assortment of packing geometries is considered from the humble molecular dimer to more exotic structures including linear and bent aggregates, two-dimensional herringbone and “HJ” aggregates, and chiral aggregates. The interplay between long-range Coulomb coupling and short-range charge-transfer-mediated coupling strongly depends on the aggregate architecture leading to a wide array of photophysical behaviors.



### CONTENTS

1. Introduction	7070	4.3. Energetically Disordered J- and H-Aggregates	7097
2. A Brief Description of Kasha Theory	7072	4.3.1. Knapp's Model	7097
3. Vibronic Frenkel Excitons	7076	4.3.2. The Spectral Impact of Disorder and Vibronic Coupling	7099
3.1. 1D Frenkel–Holstein Hamiltonian with Extended Interactions	7076	4.4. The Effect of Thermal Excitations	7102
3.2. The Multiparticle Basis Set	7076	4.5. Monitoring Exciton Coherence using PL	7105
3.3. Exciton–Phonon Representation	7077	4.5.1. Steady-State Coherence	7105
3.4. Vibronic Exciton Bands	7078	4.5.2. Time Evolutions of Coherence	7107
3.5. The Exciton Coherence Function	7079	4.5.3. Utility of $R_{PL}$	7108
3.6. Vibrational Distortion Field	7081	4.6. Linear Aggregates with Two Molecules Per Unit Cell	7108
4. Absorption and Photoluminescence in Vibronically Coupled H- and J-Aggregates	7082	4.6.1. Polarized Absorption and the Ratio Formula	7109
4.1. The Spectral Observables: Steady-State Absorption and PL	7083	4.6.2. Polarized PL and the Ratio Rule	7110
4.1.1. The Absorption Spectrum	7083	4.7. Herringbone Aggregates	7111
4.1.2. The Photoluminescence (PL) Spectrum	7084	4.7.1. Exciton Band Structure in HB Lattices	7112
4.1.3. Single Molecule Spectra	7084	4.7.2. Polarized Photoluminescence	7113
4.1.4. Summary of the Vibronic Signatures of J- and H-Aggregates	7085	4.8. Segregated HJ-Aggregates and “Null” Aggregates	7116
4.2. Absorption and PL in Ideal H- and J-Aggregates	7086	4.9. Multiple Mode Vibronic Coupling	7119
4.2.1. Impact of Increasing Exciton Bandwidth	7086	4.10. Curved Aggregates	7121
4.2.2. J- vs H-Vibronic Signatures: Selected Examples	7089	4.11. Chiral H-Aggregates	7122
4.2.3. Weak Excitonic Coupling: Ratio Formula for Absorption	7090	4.11.1. Unpolarized Absorption and PL	7122
4.2.4. Ratio Rule for PL in J-Aggregates	7092	4.11.2. Optical Activity	7124
4.2.5. Strong Excitonic Coupling and Mirror Image Symmetry	7093	5. The Impact of Intermolecular Charge Transfer on J- and H-Aggregate Behavior	7126
4.2.6. Strong Exciton Coupling in a One-Dimensional Crystal	7095	5.1. Frenkel–Holstein Hamiltonian with Charge transfer	7126
4.2.7. Herzberg–Teller Coupling in H-Aggregates	7096		

**Special Issue:** Theoretical Modeling of Excited State Processes

**Received:** September 22, 2017

**Published:** April 17, 2018

5.2. The Multiparticle Basis Set for Charge-Transfer States	7127
5.3. Charge-Transfer Excitons	7128
5.4. Charge-Transfer Induced J- and H-Aggregate Behavior in the Perturbative Regime	7128
5.5. Charge-Transfer Induced J- and H-Aggregate Behavior in the Resonance Regime	7130
5.6. Interference between Coulombic and CT-Mediated Coupling	7133
5.7. Interference Effects in Energy and Charge Transport	7134
5.8. Dependence of Coulomb and Charge-Transfer Interactions on Molecular Packing	7135
5.8.1. Geometric Dependence of Charge-Transfer Integrals	7136
5.8.2. Conjugated Polymers as J-Aggregates	7137
5.8.3. The Assignment of Phase	7138
5.8.4. Comparing the Geometric Dependencies of $J_{CT}$ and $J_C$	7139
5.9. Generalized J- and H-Aggregates: Selected Examples	7141
5.9.1. H- to J-Aggregate Transformations	7141
5.9.2. TAT Nanopillars	7142
5.9.3. Giant Davydov Splitting in Isopentyl Perylenebisimide	7143
5.10. The Oligoacenes	7144
6. Summary and Future Directions	7147
Author Information	7149
Corresponding Author	7149
ORCID	7149
Notes	7149
Biographies	7149
Acknowledgments	7149
References	7149

## 1. INTRODUCTION

The  $\pi$ -conjugated organic molecules continue to generate interest for applications in display technology,<sup>1–4</sup> photovoltaics,<sup>3–5</sup> and wearable technology,<sup>6,7</sup> motivating many investigations into the nature of the fundamental electronic excitations in organic aggregates, films, and crystals.<sup>4,8–19</sup> Intermolecular interactions, which depend strongly on the packing arrangement, drive the collective behavior in which neutral excitations (excitons) and charges (polarons) are transported, either coherently or incoherently depending on the competing influences of the exciton bandwidth, which promotes delocalization, and disorder and thermal fluctuations, which promote localization. Unlike their inorganic counterparts, organic molecular assemblies are “soft” in the sense that transport is accompanied by significant nuclear rearrangements within the constituent chromophores. Optical excitations or excitons are therefore comprised of both electronic and vibrational degrees of freedom, which play an essential role in determining photophysical and transport properties.

One of the earliest models with which to understand the photophysical properties of molecular aggregates was introduced by Michael Kasha nearly six decades ago.<sup>20–24</sup> Interestingly, Kasha initially sought to understand why aggregation in certain chromophores led to an enhancement in phosphorescence with a simultaneous loss in singlet fluorescence. In a seminal work from 1958, McCrae and Kasha<sup>23</sup> introduced the “card-pack” model for linear molecular

aggregates predicated entirely on the Coulomb coupling between neighboring chromophores, which derives from the interaction between molecular transition dipole moments. Employing the exciton theory of Davydov,<sup>25</sup> McCrae and Kasha surmised that in certain aggregates, which would later come to be known as H-aggregates, the Coulomb coupling is positive, resulting in a band of singlet states (excitons) in which the highest energy state consumes all of the oscillator strength. Because in many cases fluorescence proceeds from the lowest excited state (Kasha’s rule<sup>26</sup>), fluorescence is suppressed, thereby favoring intersystem crossing and phosphorescence. In contrast, when the Coulomb coupling is negative, as in what has come to be known as J-aggregates or Scheibe aggregates, the oscillator strength is focused in the lowest energy exciton, and no suppression of fluorescence (or enhancement in phosphorescence) is expected. McCrae and Kasha further related the sign of the Coulomb coupling to the relative orientation between neighboring chromophores, leading to the often utilized association of “side-by-side” transition dipoles with H-aggregates and “head-to-tail” transition dipoles with J-aggregates. Finally, McCrae and Kasha showed that in “J-aggregates” the emitting state (the exciton with lowest energy) has a transition dipole moment that scales as  $N^{1/2}$ , where N is the number of chromophores in the aggregate. Curiously, they did not emphasize the association with “superradiance”, the coherent enhancement of the radiative decay rate,  $\gamma_R$ , discovered several years earlier by Dicke.<sup>27</sup> The classical manifestation of superradiance follows by recognizing that  $\gamma_R$  scales as the square of the transition dipole moment. Hence,  $\gamma_R$  in J-aggregates is N-times larger than a single chromophore. Isolating the radiative contribution to the overall fluorescence decay rate is often challenging due to the presence of competing temperature-dependent nonradiative relaxation (internal conversion, intersystem crossing, defect traps) requiring accurate measures of the quantum yield. There are also complications due to singlet exciton annihilation<sup>28,29</sup> and the formation of excimers,<sup>30</sup> which are quite common in  $\pi$ -stacks with close contacts (<0.4 nm) between nearest neighbors.<sup>31–37</sup> Not surprisingly, it would take several more decades to confirm superradiance in J-aggregates<sup>38–47</sup> due largely to the efforts of Wiersma and co-workers.<sup>38–42</sup>

The Kasha model provided a means to qualitatively account for the curious photophysics of a class of molecular aggregates based on cyanine dyes. Independently discovered by Jelley<sup>48</sup> and Scheibe,<sup>49–51</sup> aggregation of pseudoisocyanine (PIC) chloride is accompanied by the appearance of an intense, red-shifted narrow band in the absorption spectrum,<sup>48–60</sup> which has come to be known as the J-band (J after Jelley). Hence, according to the Kasha model, neighboring dye chromophores in PIC aggregates are arranged in a head-to-tail fashion giving a negative value for the Coulomb coupling. In the ensuing years, many examples of J-aggregation have been discovered based primarily on the occurrence of an aggregation-induced red-shift. In addition to cyanine-based dyes (pseudoisocyanine,<sup>48–60</sup> merocyanine,<sup>52,61–65</sup> and thiacyarbocyanine<sup>29,43,66–68</sup>), some of which assemble into exotic nanotubular structures,<sup>69–73</sup> perylene diimides<sup>34,37,74–81</sup> and porphyrins<sup>82–84</sup> also form J-aggregates, as detailed in recent reviews.<sup>85,86</sup> Conversely, in H-aggregates, which are typical of side-by-side “sandwich” orientations, the main absorption peak is generally blue-shifted (“H” for hypsochromic), and aggregation suppresses the radiative decay rate. PIC dyes also form H-aggregate dimers as a first step toward extended J-aggregation, as discovered early

on by Cooper<sup>55</sup> and Kopainsky et al.<sup>56</sup> A more recent and very convincing example of a cyanine H-aggregate is the dimer complex formed by two indocarbocyanine chromophores covalently bound in a side-by-side orientation with butyl linkers.<sup>87,88</sup> Other H-aggregating chromophores include certain carotenoids,<sup>89–91</sup> oligothiophenes,<sup>92–120</sup> oligophenylenevinylenes,<sup>92,93,121–138</sup> and also perylene diimides,<sup>31,33,35,139–142</sup> some of which can assume both H- and J-configurations.<sup>76,81</sup> H-aggregates also characterize polymer  $\pi$ -stacks of poly(3-hexylthiophene) formed in thin films spin-cast from solution.<sup>143–149</sup>

Although the Kasha model is highly successful in accounting for the basic photophysical properties of many molecular aggregates, it has two main shortcomings that were already recognized early on by Kasha; the model does not account for the vibronic fine structure pervasive in a great many aggregating chromophores, and the model is limited to Coulomb coupling (i.e., “through space”) between chromophores. In this review, we highlight the latest developments in theories that address the aforementioned shortcomings. These include (1) a more detailed treatment of vibronic coupling focusing primarily on local electron-vibrational coupling and (2) the incorporation of wave function overlap and intermolecular charge transfer in otherwise Coulomb-coupled aggregates. With regard to (1), a primary goal is to understand how vibronic coupling manifests differently in J- vs H-aggregates with the aim of uncovering additional vibronic signatures with which to distinguish the two aggregate types. For many  $\pi$ -conjugated chromophores, the dipole-allowed  $S_0 \rightarrow S_1$  electronic transition is strongly coupled to the nuclear coordinate corresponding to a symmetric vinyl stretching mode with energy of  $\sim 0.15\text{--}0.18$  eV. The coupling leads to pronounced vibronic progression in the absorption and photoluminescence spectra of single (unaggregated) chromophores in solution or gas phase. Kasha and co-workers recognized that increasing the strength of the excitonic coupling in a molecular aggregate should eventually lead to vibronic decoupling, as noted in a qualitative discussion in ref 20. However, it was Fulton and Gouterman’s numerical treatment of molecular dimers,<sup>150,151</sup> which showed in much greater detail how the vibronic fine structure responds to the magnitude and especially the *sign* of the Coulomb coupling that laid the groundwork for an enduring fascination for the impact of vibronic coupling on molecular aggregate photophysics,<sup>3,10,14,79,140,150–188</sup> that has culminated in some recent, rather sophisticated non-Markovian treatments of aggregate–bath interactions.<sup>185,186</sup>

Despite the complexity arising from the inclusion of vibronic coupling, a set of simple vibronic signatures in the absorption and photoluminescence spectra that distinguish J- and H-aggregates have been identified.<sup>14,176</sup> Generally, the ratio  $A_1/A_2$  of the oscillator strengths of the first two vibronic peaks in the absorption spectrum ( $R_{\text{abs}}$ ) reports directly on the exciton bandwidth ( $W$ );  $R_{\text{abs}}$  increases with  $W$  in J-aggregates and decreases with  $W$  in H-aggregates. Conversely, the PL counterpart,  $R_{\text{PL}}$  (ratio of the 0–0 and 0–1 vibronic peaks), provides complementary information about the nature of the exciton coherence<sup>176</sup> as quantified by the number of chromophores,  $N_{\text{coh}}$ , over which the exciton is delocalized and wavelike;  $R_{\text{PL}}$  increases with  $N_{\text{coh}}$  in J-aggregates and decreases with  $N_{\text{coh}}$  in H-aggregates. The role of coherence in energy transport is currently a topic of great interest in chemistry and biology.<sup>18,189–194</sup> As a tantalizing example relevant to the theme of this review, consider an ideal defect-

free J-aggregate at low temperature. An exact solution based on the Holstein Hamiltonian shows that, as the number of chromophores,  $N$ , increases,  $R_{\text{abs}}$  eventually becomes  $N$ -independent, reflecting a convergent exciton bandwidth  $W$ , whereas  $R_{\text{PL}}$  continues to increase linearly with  $N$ , faithfully tracking the exciton coherence number,  $N_{\text{coh}} = N$ . Importantly,  $R_{\text{PL}}$  remains an accurate probe of exciton coherence in the presence of disorder<sup>176</sup> and thermal fluctuations,<sup>195</sup> where  $N_{\text{coh}} < N$  and can even be used to map the temporal evolution of coherence.<sup>36,195</sup>

Another pressing motivation for extending Kasha theory beyond Coulomb-coupled aggregates is the ubiquity of  $\pi$ -stacked aggregates where close nearest-neighbor contacts ( $<4$  Å) enable substantial wave function overlap and intermolecular charge transfer. Although Frenkel excitations are no longer a valid description of the excited states (because of the mixing between Frenkel and charge-transfer excitons), such  $\pi$ -stacked aggregates are nevertheless often classified as H- and J-aggregates based solely on spectral shifts. Indeed, Kasha recognized the limitations of his approach by stating that “to satisfy the application of the [Frenkel] exciton model, electron overlap between the light absorbing units must be small”.<sup>20</sup> The effort to understand intermolecular charge transfer and its impact on photophysical and transport properties followed soon thereafter, beginning with the pioneering work of Merrifield<sup>196</sup> and carried through with seminal works by Choi and co-workers,<sup>197,198</sup> Petelenz and co-workers,<sup>199–209</sup> Kazmaier and Hoffman,<sup>210</sup> Soos and co-workers,<sup>211–213</sup> Gisslen and Scholz,<sup>214,215</sup> and Hoffman et al.<sup>216</sup> Such approaches are based on coupled Frenkel/CT excitations, best justified when the molecular ( $S_0 \rightarrow S_1$ ) transition is dominated by the HOMO–LUMO configuration. More general quantum chemical calculations on supramolecular complexes have been conducted by Bredas and co-workers.<sup>9,217–219</sup> A general framework with which to describe collective electronic excitations in molecular ensembles, termed the collective electronic oscillator approach, was introduced by Mukamel and co-workers.<sup>220–222</sup>

From the onset, the relative phase between the electron ( $t_e$ ) and hole ( $t_h$ ) charge transfer integrals was recognized to play a prominent role in determining photophysical properties; for instance, Hennessy and Soos<sup>213</sup> noted that the optically bright (Frenkel) exciton couples to charge-transfer (CT) excitons according to the sum of the electron and hole transfer integrals, whereas the dark exciton at the edge of the Brillouin zone couples according to the difference. The sensitivity of  $t_e$  and  $t_h$  to long- and short-axis “slips” between neighboring chromophores was explored by Kazmaier and Hoffman,<sup>210</sup> who showed that even in cases where the intermolecular orbital overlap is large quantum interference effects can drive  $t_e$  or  $t_h$  to zero; in effect,  $t_e$  or  $t_h$  are highly sensitive to the shapes and especially the nodal patterns of the LUMOs and HOMOs, respectively, leading to complex dependences of  $t_e$  or  $t_h$  on the intermolecular orientation. The effect is responsible for the wide array of pigment colors displayed by perylene derivatives due to slightly different crystal packing arrangements, an effect known as crystallochromy. Gisslen and Scholz<sup>214,215</sup> further explored crystallochromy, analyzing in detail how the  $t_e/t_h$  interference impacts the absorption spectrum of several perylene derivatives in the crystalline state. In the most recent development, Kasha theory was generalized to include  $\pi$ -stacked aggregates<sup>223–230</sup> by incorporating the effective short-range excitonic coupling, which is derived from a second-order mixing between Frenkel and (virtual) CT states. The so-called

“superexchange” coupling was analyzed theoretically by Scholes and co-workers and shown to be a dominant mechanism for energy transfer in bridged naphthalene dimers.<sup>231–237</sup> As shown in refs 223–230, the short-range coupling induces vibronic spectral signatures identical to those of conventional (Coulomb-coupled) H- and J-aggregates; i.e., H- and J-aggregates can be formed in the absence of Coulomb coupling due to intermolecular CT-mediated interactions. Furthermore, because of the hypersensitivity of  $t_e$  and  $t_h$  to small, sub-angstrom slips, such aggregates possess different geometries from the conventional Kasha H- and J-geometries. Hence, the knee-jerk association of side-by-side stacking for H-aggregates and head-to-tail stacking for J-aggregates is not generally justified for aggregates with significant wave function overlap between neighboring chromophores. The theory further shows how both short-range interactions and long-range (Coulombic) interactions can interfere with each other, leading to a rich array of photophysical behaviors. For example, one can speak of “hJ”-aggregates where the first and second letters respectively refer to the signs of the long- and short-range couplings while the lower/upper case indicate relative magnitudes. An excellent example of HJ-aggregates with destructively interfering long- and short-range couplings of comparable magnitudes are the nanopillars of 7,8,15,16 tetraazaterrylene or TAT.<sup>225,238</sup> Such aggregates are referred to as “integrated” HJ-aggregates because the interfering interactions occur between the same set of chromophores (i.e., between nearest neighbors within a  $\pi$ -stack). In “segregated” HJ-aggregates, the dominant H- and J-interactions arise between *different* sets of chromophores (see section 4.9).

The generalized theory for J- and H-aggregates outlined in this review encompasses a wide array of aggregate/crystal architectures based on chromophores coupled via varying degrees of short- and long-range intermolecular interactions, leading to a rich array of photophysical behaviors. Even within the subset of herringbone-packed molecular crystals, the photophysical behaviors range from Kasha-like, arising from molecules with large  $S_0 \rightarrow S_1$  transition dipole moments inducing dominant Coulombic coupling (like the popular oligo-phenylenevinylenes<sup>92,93,121–138</sup>) to the more unconventional behaviors displayed by the oligoacenes such as tetracene and pentacene, which possess small  $S_0 \rightarrow S_1$  transition dipoles but significant Frenkel-CT mixing.<sup>224,226,239</sup> Helical  $\pi$ -stacks, such as those formed from the carotenoid lutein,<sup>89,90</sup> are noteworthy because they behave like conventional Coulomb-coupled H-aggregates despite close nearest-neighbor contacts. This stems from the rapid decrease in intermolecular wave function overlap with increasing twist angle; in perylene dimers, for example, both  $t_e$  and  $t_h$  are driven to zero at a twist angle close to 30 degrees,<sup>227,240</sup> whereas the Coulomb coupling hardly changes. Indeed, Sarbu et al.<sup>81</sup> measured a conventional H-aggregate absorption spectrum for helical aggregates of a perylene bisimide derivative with a twist angle of approximately 20 degrees as determined from electron diffraction analysis. Interestingly, by disrupting the hydrogen bonding via alcohol vapor exposure, such aggregates can be made to undergo an unusual H- to J-aggregate transformation<sup>76,81,241</sup> in which a slight change in the relative orientation of neighboring chromophores is enough to restore dominant CT-mediated (J-like) coupling as reflected by an enormous red-shift ( $\sim 3000 \text{ cm}^{-1}$ ) in the absorption spectrum.

In the expanded theory, even a single conjugated polymer chain can be understood as a linear J-aggregate with repeat-unit

chromophores coupled primarily via short-range interactions.<sup>15,242–248</sup> A  $\pi$ -stack of polymer chains with dominant H-like interchain (Coulomb) interactions is then a segregated HJ-aggregate, where “segregated” indicates dominant interactions occurring between different sets of chromophores: the J-like interactions are entirely intrachain, whereas the H-like interactions are interchain.<sup>249</sup> As polymer aggregates have been recently reviewed,<sup>15,242,244</sup> we will only briefly mention them in the current review, which is dedicated primarily to the more conventional molecular aggregates with the exception of light-harvesting assemblies, which was the subject of a recent thematic issue of Chemical Reviews (2017). We further restrict our focus to mainly photophysical properties; excellent reviews covering transport properties have recently appeared, notably those of Scholes,<sup>18</sup> Bardeen,<sup>8</sup> Schroter et al.,<sup>10</sup> Brixner et al.,<sup>17</sup> Kohler and Bassler,<sup>250</sup> Agranovich,<sup>251</sup> Tretiak and co-workers,<sup>252,253</sup> Huang and co-workers,<sup>254</sup> Ginsberg and co-workers,<sup>255</sup> and Mukamel and co-workers.<sup>256–258</sup>

In what follows, we begin with a brief review of Kasha theory, describing the photophysical response of Frenkel excitons in aggregates dominated by Coulombic intermolecular coupling but without any vibronic coupling. Section 3 introduces the effects of local exciton-vibrational coupling via the celebrated Frenkel-Holstein Hamiltonian. Here, the Frenkel excitons become dressed with vibrations and are sometimes referred to as “excitonic polarons” with the extent of the vibrational field surrounding the central vibronic excitation characterized by a “polaron” radius. The photophysical response of vibrational excitons under a variety of coupling regimes defined by comparing the exciton bandwidth to the local nuclear relaxation energy follows in section 4, where the effects of disorder, finite temperature, and coupling to multiple vibrational modes is addressed. The vibronic signatures of J- and H-aggregates are introduced with applications to a variety of packing arrangements including linear aggregates with one or more molecules in a unit cell, “bent” or curved aggregates, two-dimensional herringbone and “HJ” aggregates, and helical aggregates. In all cases under consideration, the emphasis is on the impact of vibronic coupling. The coupling of Frenkel excitons to charge-transfer excitons is taken up in section 5, which begins with an analysis of the Frenkel/CT Holstein Hamiltonian and a detailed discussion of novel forms of J- and H-aggregates formed via CT-mediated short-range coupling. Applications to a variety of systems are discussed, including the H-to J-aggregate transformation, TAT nanopillars, and finally the very popular oligoacenes. Future directions are discussed in section 6.

## 2. A BRIEF DESCRIPTION OF KASHA THEORY

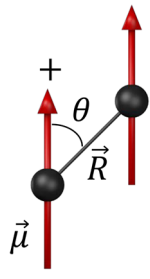
Before discussing the impact of vibronic coupling and charge transfer on aggregate photophysics, we first briefly review the Kasha classification of H- and J-aggregates.<sup>20–24</sup> The classification is predicated entirely on Coulombic intermolecular coupling within the framework of Frenkel exciton theory.<sup>25,251,259</sup> In its most elementary form, the theory neglects vibronic coupling and nearest-neighbor wave function overlap. As stated in section 1, the exciton approach has been enormously successful in qualitatively accounting not only for the basic photophysics of the cyanine dye aggregates, and especially the celebrated PIC “Scheibe” aggregates, but also for numerous other dye chromophore assemblies.

Most applications of Frenkel exciton theory<sup>25,251,259</sup> in molecular aggregate photophysics employ the point-dipole

approximation for the Coulomb coupling between molecules “1” and “2”,

$$J_C^{pd} = \frac{\mu_1 \cdot \mu_2 - 3(\mu_1 \cdot \hat{R})(\mu_2 \cdot \hat{R})}{4\pi\epsilon R^3} \quad (1)$$

where  $\mu_1$  and  $\mu_2$  are the dipole moments corresponding to the  $S_0 \rightarrow S_1$  transition of molecules “1” and “2”, respectively,  $\hat{R} = R\hat{R}$  is the displacement vector connecting the molecular mass centers, and  $\epsilon$  is the dielectric constant of the medium. The case for parallel transition dipole moments, which characterizes packing geometries with one molecule per unit cell, is depicted in Figure 1. Kasha initially identified two aggregation species



$$J_C^{pd} = \frac{\mu^2(1-3\cos^2\theta)}{4\pi\epsilon R^3}$$

**Figure 1.** Relative orientation of transition dipole moments defining a J-aggregate ( $\theta < \theta_M$ ) and H-aggregate ( $\theta_M < \theta < \pi/2$ ) under the point dipole approximation. The magic angle  $\theta_M$  is 54.7 degrees.

based on the relative orientation of  $\vec{\mu}_1$  and  $\vec{\mu}_2$ , which is quantified by the angle  $\theta$  in Figure 1. In what have come to be known as J-aggregates, the dipoles maintain a “head-to-tail” orientation where  $\theta$  is less than the so-called “magic angle”  $\theta_M = 54.7$  degrees, the angle for which  $J_C^{pd}$  is zero. In this case, the Coulomb coupling is negative ( $J_C^{pd} < 0$ ). Conversely, H-aggregates maintain a “side-by-side” orientation ( $\theta_M < \theta \leq \pi/2$ ) leading to a positive Coulomb coupling ( $J_C^{pd} > 0$ ).

As shown by Kasha and co-workers,<sup>20–24</sup> the sign of the Coulomb coupling has a direct bearing on the photophysical response. This is depicted in Figure 2 for the simplest case of a molecular dimer, where the Coulomb coupling  $J_C$  leads to the formation of two delocalized excited states split by  $2|J_C|$ . The two states consist of in- and out-of-phase linear combinations of the two local excited states,  $|e_1g_2\rangle$  and  $|g_1e_2\rangle$ . The in-phase or symmetric state, shifted by  $J_C$ , is characterized by an enhanced transition dipole moment relative to the monomer (by  $\sqrt{2}$ ), whereas the out-of-phase state, shifted by  $-J_C$ , is optically dark due to a cancellation of the transition dipole moments. Hence, in J-aggregates, the negative coupling ( $J_C < 0$ ) results in the (absorbing) symmetric state having lower energy than the antisymmetric state, whereas in H-aggregates with  $J_C > 0$ , the ordering is reversed. The Coulomb-induced energetic shifts lead to predictable changes in the absorption spectrum: in J-aggregates, the main absorption peak is red-shifted compared to the monomer, whereas in H-aggregates, the absorption peak is blue-shifted.

In addition to opposing absorption spectral shifts, Kasha also showed that the radiative decay rate is very different for J- and H-aggregates. In H-aggregates, there is likely rapid intraband relaxation subsequent to absorption, leading to efficient population of the lowest energy state. Because the state is

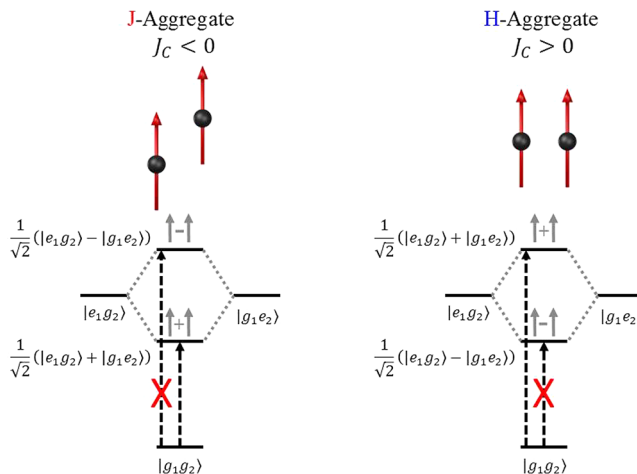


**Figure 2.** Energy level diagrams for J- and H-aggregate dimers. Transitions from the ground state are allowed only to the state with in-phase transition dipole moments, which lie at the bottom and top of the band in J- and H-aggregates, respectively. The symmetric splitting observed in either case is  $2|J_C|$ .

characterized by the out-of-phase alignment of transition dipoles, it has no direct radiative coupling to the ground state  $|g_1g_2\rangle$ . The transition is strictly forbidden by symmetry. Conversely, in J-aggregates, the lowest energy (in-phase symmetric) state is radiatively coupled to the ground state with a transition dipole enhanced relative to the monomer by a factor of  $\sqrt{2}$ . Because the radiative decay rate scales as the transition dipole moment squared, the dimer decay rate is twice that of the monomer; for an aggregate containing  $N$ -coupled molecules, the rate is enhanced by a factor of  $N$ , a phenomenon known as superradiance.<sup>27</sup> At this point, it is worth mentioning that the difference in the PL between H- and J-aggregates is entirely confined to the radiative decay rates and not the total emission (quantum) yield. The latter depends on how large the radiative rate is relative to the nonradiative rate. Hence, one can have strongly emissive H-aggregates if the weak radiative decay rate dominates an even weaker nonradiative decay rate, as convincingly shown by Gierschner and co-workers.<sup>126,127</sup>

For linear aggregates with  $N$ -coupled chromophores and one molecule per unit cell ( $\mu_n = \mu$ ), the delocalized excited states are generally described as molecular excitons,<sup>25,259</sup> which abide by the Frenkel exciton Hamiltonian

$$H_{ex} = E_M + D + \sum_{m,n} J_{m,n} |m\rangle\langle n| \quad (2)$$

where  $\hbar = 1$  is taken so that energy and frequency have equivalent units.  $E_M$  is the (gas-phase) monomer  $S_0 \rightarrow S_1$  transition energy and  $D$  is the gas-to-crystal frequency shift, which is typically a negative quantity reflecting the ability of neighboring molecules to better stabilize an excited state via nonresonant interactions.  $J_{n,m}$  is the resonant Coulomb coupling between molecules  $m$  and  $n$ . The ket  $|n\rangle \equiv |g_1, g_2, \dots, e_n, \dots, g_N\rangle$  represents a local excited state where the  $n$ th chromophore is electronically excited to the state  $S_1$  while all other molecules remain in their electronic ground states  $S_0$ . When periodic boundary conditions are imposed, the eigenstates of  $H_{ex}$  are the wavelike excitations or excitons, each characterized by a (dimensionless) wave vector  $k$

$$|k\rangle = \frac{1}{\sqrt{N}} \sum_n e^{ikn} |n\rangle \quad k = 0, \pm 2\pi/N, \pm 4\pi/N, \dots, \pi \quad (3)$$

In eq 3, the wave vector is dimensionless because the  $n$  in the exponential phase factor is the dimensionless position. If instead the position  $nd$  was used (where  $d$  is the nearest neighbor spacing), the appropriate wave vector would be  $k/d$  having conventional units of reciprocal length. Moreover, the allowed values of  $k$  written alongside eq 3 assume an even value for  $N$ ; for odd values, the  $k = \pi$  value is omitted. The energy  $E_k$  of the  $k$ th exciton is given by

$$E_k = E_M + D + J_k \quad (4)$$

where  $J_k$  is the  $k$ -dependent (Fourier) component of the Coulombic coupling

$$J_k \equiv \sum_n J_{m,n} \cos(k(n-m)) \quad (5)$$

Here, periodic boundary conditions ensure the sum is independent of  $m$ . When only the nearest neighbor (n.n.) coupling  $J_C$  is retained, eq 5 reduces to

$$J_k = 2J_C \cos(k) \quad (6)$$

which is a good approximation for linear aggregates. Based on the dispersion relations in eq 4 the free exciton bandwidth for linear aggregates is defined as,

$$W \equiv |J_{k=0} - J_{k=\pi}| \quad (7)$$

which reduces to  $W = 4|J_C|$  in the limit of n.n. coupling only. Before continuing, it is worth pointing out that finite size aggregates are better described using open boundary conditions, where the dispersion  $J_p = 2J_C \cos(\pi p/(N+1))$  with  $p = 1, 2, \dots, N$  describes how the exciton energies evolve with  $N$ .

The energy dispersion curves for H- and J-aggregates as well as representative absorption and emission spectra are shown in Figure 3. The Kasha spectral shifts follow by recognizing that the  $k = 0$  exciton is the bright exciton, which resides at the band-bottom and band-top in J- and H-aggregates, respectively. The  $k = 0$  exciton possesses the entirety of the oscillator strength, which is proportional to  $|\langle g|\hat{M}|k\rangle|^2$  for state  $|k\rangle$ . Here  $\hat{M}$  is the transition dipole moment operator, given by

$$\hat{M} \equiv \mu \sum_n \{ |g\rangle \langle nl + ln\rangle \langle gl| \} \quad (8)$$

where  $|g\rangle \equiv |g_1, g_2, \dots, g_N\rangle$  is the aggregate ground state in which all molecules are in their electronic ground states. It readily follows that the transition dipole moment in the bright state ( $k = 0$ ) is enhanced by  $\sqrt{N}$  relative to the monomer, i.e.,<sup>23</sup>

$$\langle g|\hat{M}|k\rangle = \sqrt{N}\mu \delta_{k,0} \quad (9)$$

The enhanced transition dipole moment directly leads to the aforementioned  $N$ -fold increase in the radiative decay rate realized in J-aggregates at sufficiently low temperatures.

In most cases, J- and H-aggregate assignments are based on whether the aggregate absorption peak is red- or blue-shifted relative to the monomer peak in solution,  $E_M + D'$ , where  $D'$  is the gas-to-solution frequency shift. The Kasha-based J/H-assignment therefore depends on the condition

$$|D - D'| < 2|J_C| \quad (10)$$

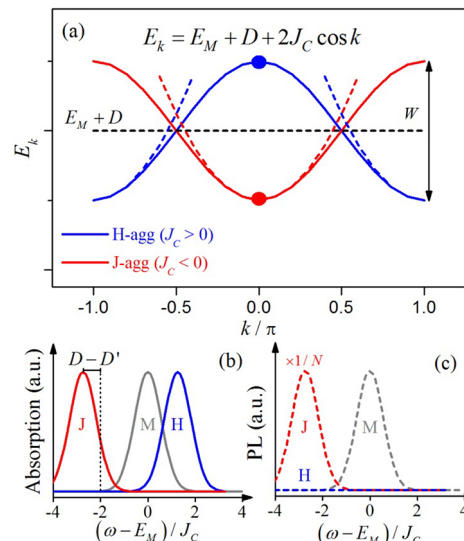


**Figure 3.** (a) Energy dispersion curves for J- and H-aggregates. The parabolic approximations around the band minima are shown as dashed curves. The idealized (b) absorption and (c) photoluminescence (PL) spectrum of J- and H-aggregates are compared to the monomer spectrum. Note that the peak maxima of the aggregates are not symmetric about the monomer peak maximum due to the solution-to-crystal red-shift  $D'$ .

where  $D - D'$  is the solution-to-aggregate spectral shift. Because  $D - D'$  is likely negative, the situation may be problematic in weakly coupled H-aggregates, where the solution-to-crystal shift can overwhelm the exciton blue-shift leading to an overall red-shifted spectrum and an incorrect assignment. This is apparently the case in certain carotenoid aggregates as detailed in ref 91.

As in the dimer, the emissive properties of J- and H-aggregates follow from Kasha's rule<sup>26</sup> in which, to an excellent approximation, emission occurs from the lowest energy excited state. For J-aggregates, emission occurs from the  $k = 0$  exciton; on the basis of eq 9, the radiative decay rate, which scales as the square of the transition dipole moment, is enhanced by  $N$  (superradiance), and ideally, there is no Stokes shift as indicated in Figure 3. By contrast, in H-aggregates, rapid intraband relaxation from the highest energy ( $k = 0$ ) exciton populates the  $k = \pi$  exciton. Emission is then only possible in the presence of symmetry-breaking disorder or vibronic coupling.

Another way to distinguish J- and H-aggregates is through the band curvature, the second derivative of  $E_k$  with respect to  $k$  (evaluated at the point  $k = 0$ ). In J-aggregates, the curvature is positive at  $k = 0$ , because the  $k = 0$  exciton defines the band bottom, whereas in H-aggregates, the curvature is negative because the  $k = 0$  state resides at the top of the band. However, for both J- and H-aggregates, emission occurs from the band minimum, where the band necessarily has positive curvature for J- and H-aggregates, as indicated by the fitted parabolas in Figure 3a. Here, the band curvature has a significant impact on the absorption origin and the PL spectrum.<sup>176,183,260–262</sup> The free-exciton band curvature at the band minimum,  $k_{\min}$ , is defined as

$$\omega_c \equiv \left. \frac{1}{2} \frac{d^2 E_k}{dk^2} \right|_{k=k_{\min}} \quad (11)$$

where  $k_{\min} = 0$  for J-aggregates and  $k_{\min} = \pi$  for H-aggregates. Hence, the exciton dispersion immediately surrounding the point  $k_{\min}$  is parabolic

$$E_k \approx E_M + D + J_{k_{\min}} + \omega_c(k - k_{\min})^2 \quad (12)$$

as indicated by the dashed curves in Figure 3a. Under the n.n. approximation, the positive curvature at the band minimum simplifies to  $\omega_c = -J_C$  for J-aggregates and  $\omega_c = J_C$  for H-aggregates. In the more general treatment in refs 176, 260, and 261 the curvature was also defined in the presence of vibronic coupling, which, in order to avoid confusion, we denote as  $\tilde{\omega}_c$  with a tilde overstrike. Finally, we note that in some works  $2\omega_c$  is referred to as the “band curvature” to eliminate the factor of 1/2 on the rhs of eq 11.<sup>262</sup> As was shown in ref 183, the band curvature at  $k_{\min}$ , and not the exciton bandwidth, is far more useful in defining exciton–phonon coupling regimes especially in two-dimensional aggregates where the nearest neighbor approximation is not well justified.

A significant improvement in the Kasha/Frenkel model for J- and H-aggregates can be made by going beyond the point dipole approximation in eq 1, which breaks down when the intermolecular separation becomes smaller than approximately the length over which charges separate to produce  $\mu$ . The extended dipole model of Czikkely et al.<sup>263</sup> was one of the earliest attempts to go beyond the point-dipole approximation in defining J- and H-aggregates. Subsequent treatments based on quantum chemical approaches,<sup>127,218,264–270</sup> which account for the distributed nature of the transition dipole, have proved very successful in evaluating the Coulomb coupling for general intermolecular orientations. For rod-shaped,  $\pi$ -conjugated chromophores with transition dipole moments directed along the long-axis, a good rule of thumb is that the sign of the coupling changes from positive (H) to negative (J) when the longitudinal slip distance is roughly half the molecular length.<sup>127,271</sup> Hence, one cannot readily obtain Coulomb-based polymer J-aggregates as conjugation lengths are typically much greater than nearest-neighbor separations. (This does not preclude polymer J-aggregates based on intermolecular charge-transfer, see the discussion in section 4.9.) For this reason, polymer  $\pi$ -stacks such as those based on P3HT are generally well described as H-aggregates.<sup>144</sup>

The Coulomb coupling in  $\pi$ -conjugated macromolecular/polymer aggregates also displays unusual behavior with respect to the molecular length, which cannot be accounted for using the point dipole approximation. In a side-by-side dimer, the Coulombic coupling actually decreases with oligomer length once the latter surpasses approximately the separation between the two chains ( $d$ ). This phenomenon has been confirmed theoretically using a variety of approaches by several groups<sup>125,127,219,272–274</sup> but is most easily appreciated by considering a distributed dipole approach where a point dipole resides in each repeat unit, consistent with a Frenkel-like description for each oligomer. A schematic is shown in the inset of Figure 4. Summing over all interchain repeat-unit interactions to obtain the total Coulomb coupling gives

$$J_C = \frac{1}{N} \frac{\mu^2}{4\pi\epsilon} \sum_{m,n} \frac{(1 - 3\cos^2 \theta_{mn})}{R_{mn}^3}$$

where periodic boundary conditions were also taken. Figure 4 shows how the  $J_C$  varies with the number of repeat units  $N$  in each oligomer for several interchain distances  $d$ .  $J_C$  initially increases with  $N$ , peaking when the oligomer length is slightly

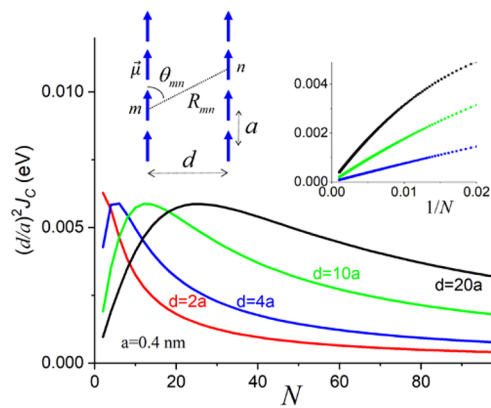


**Figure 4.** Coulomb coupling between two oligomer chains as a function of the number of repeat units  $N$  assuming a transition point dipole within each repeat unit of 1 D and a distance between adjacent repeat units of  $a = 0.4$  nm. Curves for several values of the interchain separation  $d$  are shown. The right inset shows the coupling approaches zero approximately as  $1/N$ .<sup>274</sup> In all calculations,  $\epsilon = \epsilon_0$ .

larger than the separation between chains ( $((N - 1)a > d$  in Figure 4) but then decreases to practically zero in the large  $N$  limit (see right inset). The compromised coupling in the polymer limit is due to a cancellation between H-like (side-by-side) repeat-unit dipole–dipole interactions with the more numerous but weaker J-like interactions in the obliquely oriented pairs. The decrease in Coulomb coupling with oligomer length has been demonstrated experimentally by Westenhoff et al. in chiral oligothiophene complexes.<sup>116</sup> In thin films of larger oligomers and polymers, the diminished interchain coupling figures prominently in the photophysical response.<sup>15,144,275</sup>

Another straightforward way to improve upon the Kasha/Frenkel model is to incorporate higher-energy excited states ( $S_2, S_3, \dots$ ) beyond the state  $S_1$ , which can also form exciton bands. Higher-energy bands can be treated independently with one-band Hamiltonians like eq 2 unless the bands begin to overlap, allowing for significant interband mixing. An excellent example is crystalline tetracene. To model the absorption spectrum, Schlosser and Philpott<sup>276</sup> used nine molecular excited states and showed that inclusion of the higher transitions generally increased the exciton splittings of the lower bands. Higher-energy transitions are also necessary to account for the phenomenon of hypochromism in which an aggregate or polymer comprised of  $N$  chromophoric units exhibits a reduction in the oscillator strength of a particular band below what is expected for  $N$  independent chromophores. Hypochromism is well documented in DNA<sup>277–279</sup> and is consistent with the Thomas–Reiche–Kuhn sum rule,<sup>280</sup> which states that the sum of the oscillator strengths of all bands is conserved. In DNA, the loss of oscillator strength in the low-energy region of the spectrum (hypochromism) is compensated by an increase in the high-energy region (hyperchromism).

To summarize this section, within the Kasha/Frenkel model there are two main signatures identifying J-aggregates (H-aggregates): (1) a spectral red-shift (blue-shift) of the main peak in the UV–vis spectrum induced by Coulombic coupling and (2) an enhancement (attenuation) of the radiative component of the fluorescence decay rate. There are, however, several difficulties in a reliable application of the above signatures. Spectral shifts can arise from other effects such as the aforementioned “solution-to-crystal” shift sourced by

nonresonant dispersion interactions as well as other effects such as the red-shift accompanying aggregation-induced planarization in polymer aggregates. Moreover, reliable measures of the radiative component of the fluorescence decay rate often require low-temperature environments where competing nonradiative decay processes are minimal. Extracting the radiative component requires accurate measures of the quantum yield, which can be experimentally challenging, especially for solid-phase samples. To assist in the identification of J- and H-aggregates, additional signatures have been developed based on vibronic coupling, as described in greater detail in the following sections.

### 3. VIBRONIC FRENKEL EXCITONS

In this section, we review what is known about the nature of vibronic Frenkel excitons, which are Frenkel excitons “dressed” with intramolecular vibrations. Here, we focus on the profound impact symmetric intramolecular vibrations, such as the vinyl stretching mode (or aromatic-quinoidal stretching mode in ring systems), make on the structure of the excited states. Such vibrations are sometimes referred to as progression-building modes due to their impact on the monomer absorption and emission spectrum and are responsible for substantial nuclear relaxation subsequent to ( $S_0 \rightarrow S_1$ ) electronic excitation. The local nuclear relaxation energy of several hundred meV’s is comparable to the exciton bandwidth in organic aggregates and crystallites and can strongly influence photophysical and transport properties. In what follows, we explore the nature of Frenkel “polaronic” excitons and, in particular, how they differ in H- and J-aggregates.

#### 3.1. 1D Frenkel–Holstein Hamiltonian with Extended Interactions

Local exciton-vibrational coupling arises from nuclear relaxation along one (or more) intramolecular vibrational coordinates subsequent to electronic excitation. The process is easiest to understand by considering just a single mode, like the symmetric vinyl stretching mode common to  $\pi$ -conjugated molecules, and taking the ground ( $S_0$ ) and excited ( $S_1$ ) nuclear potentials to be shifted harmonic wells of identical curvature, as portrayed in Figure 5. The vibrational frequency is denoted as  $\omega_{\text{vib}}$ , and the shift is quantified by the displacement  $\Delta Q_0$ . As shown in Figure 5, the Franck–Condon (vertical) transition energy is the sum of the 0–0 transition energy,  $\omega_{0-0}$  (identified with  $E_M$  in eq 2) plus the quantity  $\lambda^2 \omega_{\text{vib}}$ , which is the nuclear relaxation energy, the quantity of energy released when the molecule subsequently relaxes to the minimum of the excited

state potential. Here, the dimensionless Huang–Rhys (HR) factor,  $\lambda^2$ , is given by  $k_f \Delta Q_0^2 / 2 \omega_{\text{vib}}$ , where  $(1/2)k_f Q^2$  describes the shape of the nuclear potentials and  $k_f$  is the force constant of the oscillator. The HR parameter is proportional to  $\Delta Q_0^2$  and hence quantifies the relative shift of the excited state potential; for example, when  $\lambda^2$  is zero, the two potentials are unshifted relative to each other, and the nuclear relaxation energy is zero.

The Hamiltonian describing the delocalizing influence of electronic coupling in the presence of local electron-vibrational coupling was derived by Fulton and Gouterman,<sup>150</sup> Witkowski and Moffitt,<sup>156</sup> and Merrifield<sup>158</sup> for molecular dimers and by Merrifield for aggregates containing an arbitrary number of chromophores.<sup>157</sup> The form of the Hamiltonian adheres to the molecular crystal form of the celebrated Holstein polaron Hamiltonian.<sup>281</sup> Written in the local basis set of excited chromophores and restricted to include only a single excited chromophore out of the entirety of  $N$  chromophores comprising the system (i.e., excluding two-excitons<sup>282</sup> and higher) the Frenkel–Holstein (or just “Holstein”) Hamiltonian takes the form

$$\begin{aligned} H_{\text{FH}} = & \omega_{0-0} + D + \sum_{m,n} J_{m,n} |m\rangle\langle nl + \omega_{\text{vib}} \sum_n b_n^\dagger b_n \\ & + \omega_{\text{vib}} \sum_n \{\lambda(b_n^\dagger + b_n) + \lambda^2\} |n\rangle\langle nl \end{aligned} \quad (13)$$

where recall  $\hbar = 1$ . The first three terms comprise the Frenkel exciton Hamiltonian from eq 2. The energy of an intramolecular vibration with energy  $\omega_{\text{vib}}$  is accounted for in the fourth term in eq 13. Here, the operator  $b_n^\dagger(b_n)$  creates (annihilates) a vibrational quantum within the  $S_0$  nuclear potential of the  $n$ th chromophore assumed to be harmonic. The shift of the excited state ( $S_1$ ) nuclear potential (with identical curvature to  $S_0$ ) is represented by the remaining terms in eq 13 and quantified by the HR parameter,  $\lambda^2$ , see Figure 5.

#### 3.2. The Multiparticle Basis Set

An accurate basis set for describing excitonic eigenstates in the weak to intermediate exciton coupling regimes is the multiparticle basis set introduced some time ago by Philpott<sup>160</sup> and employed by several groups<sup>13,165,171,211,283–287</sup> in analyzing the photophysics of molecular aggregates. Here, the term “particle” indicates a chromophore hosting either a vibronic (electronic/vibrational) excitation or a purely vibrational excitation. For linear spectroscopy, which is the focus of the current review, one only need be concerned with excitations consisting of a single electronically excited molecule. Hence, an  $r$ -particle state consists of a single electronically excited molecule and  $r - 1$  purely vibrationally excited molecules. In general, an  $r$ -particle state is represented as

$$|n, \tilde{v}; n_1, v_1; n_2, v_2; \dots; n_{r-1}, v_{r-1}\rangle, \quad \tilde{v} \geq 0, v_1 \geq 1, \dots, v_{r-1} \geq 1$$

where the first entry indicates that the chromophore at site  $n$  is electronically excited with  $\tilde{v} \geq 0$  vibrational quanta in its  $S_1$  nuclear potential. Here, the overstrike indicates that the vibrational quanta are referenced to the electronically excited  $S_1$  potential (see Figure 5); when the overstrike is absent, the number of quanta are referenced to the ground (unshifted) nuclear potential  $S_0$ . The remaining entries in the ket refer to pure vibrational excitations where  $n_s$  ( $s = 1, 2, \dots, r - 1$ ) labels the chromophore hosting  $v_s$  ( $\geq 1$ ) vibrational quanta in its  $S_0$  potential.

In practical applications, the multiparticle basis set is truncated by enforcing a cap,  $\nu_{\max}$  on the total number of

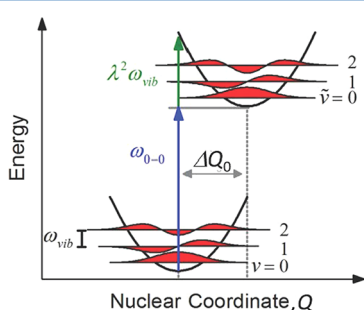


**Figure 5.** Harmonic nuclear potential wells for ground and excited states. The excited state potential is shifted relative to the ground state potential by  $\Delta Q_0$ . The vibrational energy is denoted by  $\omega_{\text{vib}}$ , the 0–0 transition energy by  $\omega_{0-0}$ , and the relaxation energy by  $\lambda^2 \omega_{\text{vib}}$ .

vibrational quanta,  $\tilde{v} + \sum_j \nu_j \leq \nu_{\max}$ . Normally,  $\nu_{\max}$  is determined from the vibronic bandwidth of the solution phase UV-vis spectrum of the unaggregated species. For the 0.18 eV vinyl stretching mode characteristic of many  $\pi$ -conjugated organic molecules  $\nu_{\max}$  needs to be at least four to obtain converged absorption and PL spectra.<sup>283</sup> Even so, the multiparticle basis set diverges exponentially with the number of chromophores in the aggregate. Fortunately, for the aforementioned vinyl stretching mode, accurate calculations are obtainable by making the two-particle approximation (TPA) in which the basis set is truncated to contain only one- and two-particle states,<sup>13,14,283</sup> see Figure 6. In one-particle

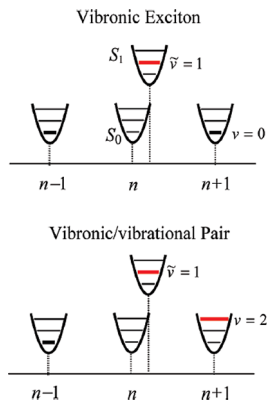


**Figure 6.** Examples of vibronic excitons (one-particle states) and vibronic/vibrational pair excitons (two-particle states). Excitations indicated in red. Reprinted with permission from ref 14. Copyright (2010), American Chemical Society.

states, denoted as  $|n, \tilde{v}\rangle$ , the  $n$ th chromophore hosts an electronic excitation in state  $S_1$  with  $\tilde{v}$  vibrational quanta, whereas all other molecules are in their electronic ( $S_0$ ) and vibrational ( $v = 0$ ) ground states. In two-particle states, denoted as  $|n, \tilde{v}; n', \nu'\rangle$ , an additional purely vibrational excitation resides at chromophore  $n'$  with  $\nu' \geq 1$  quanta in the  $S_0$  potential. One- and two-particle states are also referred to as vibronic excitons and vibronic/vibrational pair excitons, respectively. In this truncated basis set, the  $\alpha$ th eigenstate of the Frenkel–Holstein Hamiltonian in eq 13 can be expanded as

$$|\psi_\alpha\rangle = \sum_n \sum_{\tilde{v}=0,1,\dots} c_{n,\tilde{v}}^\alpha |n, \tilde{v}\rangle + \sum_{n,\tilde{v}=0,1,\dots} \sum_{n',\nu'=1,2,\dots} c_{n,\tilde{v};n',\nu'}^\alpha |n, \tilde{v}; n', \nu'\rangle \quad (14)$$

In cases where periodic boundary conditions apply, the exciton's wave vector  $k$  is a good quantum number. The  $\alpha$ th eigenstate having wave vector  $k$  is written as

$$|\psi_k^\alpha\rangle = \sum_{\tilde{v}=0,1,\dots} c_{k,\tilde{v}}^\alpha |k, \tilde{v}\rangle + \sum_{\tilde{v}=0,1,\dots} \sum_{\substack{s=\pm 1,\pm 2,\dots \\ \nu'=1,2,\dots}} c_{k,\tilde{v};s,\nu'}^\alpha |k, \tilde{v}; s, \nu'\rangle \quad (15)$$

where the appropriately symmetrized one- and two-particle wave functions are

$$|k, \tilde{v}\rangle = \frac{1}{\sqrt{N}} \sum_n e^{ikn} |n, \tilde{v}\rangle \quad (16)$$

and

$$|k, \tilde{v}; s, \nu'\rangle \equiv \frac{1}{\sqrt{N}} \sum_n e^{ikn} |n, \tilde{v}; n+s, \nu'\rangle \quad (17)$$

In eq 17, the wave vector satisfies  $k = 0, \pm 2\pi/N, \pm 4\pi/N, \dots, \pi$  and  $s (= \pm 1, \pm 2, \dots, N/2)$  represents the separation between the vibronic and vibrational excitations. (Here, we have taken  $N$  to be even; limits for odd  $N$  are straightforward.) Generally, the two-particle approximation is excellent within the weak-to-intermediate exciton coupling regimes. Stronger exciton coupling requires the inclusion of higher multiparticle states. The three-particle approximation has been studied in detail by Stradomska and Petelenz,<sup>286</sup> who showed its importance in accurately describing high-energy states in aggregates of conjugated molecules.

### 3.3. Exciton–Phonon Representation

The multiparticle basis set is not a convenient starting point in the strong exciton coupling regime as it requires the inclusion of three and higher particle states. For treating the strong coupling regime, it is beneficial to work instead with the exciton–phonon basis set utilized early on by McRae and co-workers<sup>152–155</sup> and Merrifield<sup>157</sup> and later on by Scherer and Fisher<sup>165</sup> and Meskers et al.<sup>288</sup> to describe aggregate absorption and photoluminescence. In the exciton–phonon basis set, the nuclear degrees of freedom are described as delocalized wavelike phonons much like their excitonic counterparts. This can most easily be appreciated by first rewriting the Frenkel–Holstein Hamiltonian for a (disorder-free) linear chain with periodic boundary conditions in the product basis of excitons and phonons. Within a subspace containing a single electronic excitation, the Frenkel–Holstein Hamiltonian is

$$H_{\text{FH}} = \omega_{0-0} + D + \left(1 - \frac{1}{N}\right)\lambda^2 \omega_{\text{vib}} + \sum_k J_k |k\rangle\langle k| + \omega_{\text{vib}} \tilde{b}_{q=0}^\dagger \tilde{b}_{q=0} + \omega_{\text{vib}} \sum_{q \neq 0} b_q^\dagger b_q + \frac{\omega_{\text{vib}} \lambda}{\sqrt{N}} \sum_{k,q \neq 0} \{|k+q\rangle\langle klb_q + \text{h.c.}\} \quad (18)$$

where the  $k$ th exciton  $|k\rangle$  was given in eq 3, and the operators creating phonons with wave vector  $q$  are given by

$$b_q^\dagger \equiv \frac{1}{\sqrt{N}} \sum_{n=1}^N e^{iqn} b_n^\dagger, \quad q = 0, \pm 2\pi/N, \pm 4\pi/N, \dots, \pi \quad (19)$$

with  $b_q$  being the Hermitian conjugate of  $b_q^\dagger$ . The allowed values of  $q$  in eq 19 assume an even value of  $N$ . (As in the case for the  $k$  values when  $N$  is odd, the value of  $\pi$  is omitted, see eq 3).

The form of the Hamiltonian in eq 18 recognizes the unique quality of the totally symmetric phonon with  $q = 0$ . By defining the  $q = 0$  phonon relative to a slightly shifted nuclear potential

$$\tilde{b}_{q=0}^\dagger \equiv b_{q=0}^\dagger + \frac{\lambda}{\sqrt{N}} \quad (20)$$

it no longer is involved in exciton–phonon coupling; note the  $q = 0$  term is omitted in the summation in the last term in eq 18.

Hence, the term  $\omega_{\text{vib}} \tilde{b}_{q=0}^\dagger \tilde{b}_{q=0}$  is separable, and its eigenvalues are good quantum numbers.

A convenient basis set for representing the Hamiltonian in eq 18 is given by the exciton–phonon product states

$$|\tilde{n}_{q=0}\rangle \otimes |k; n_{q_1}, n_{q_2}, \dots, n_{q_{N-1}}\rangle \equiv |k\rangle \otimes |\tilde{n}_{q=0}\rangle \otimes |n_{q_1}\rangle \dots \otimes |n_{q_{N-1}}\rangle \quad (21)$$

where  $|k\rangle$  is a pure exciton state and the phonon parts are expressed in the number basis. The state of a nontotally symmetric phonon, so defined because its wave vector is nonzero, is given by  $|n_{q_i}\rangle$ , where  $n_{q_i}$  is the number of phonons

(quanta) with wave vector  $q_l$ . The latter is expressed as  $q_l = (2\pi/N)l$  where the index  $l$  ranges from 1 to  $N - 1$ . (Note the equivalence of  $q_{N-s}$  and  $q_{-s}$ .) Because  $b_{q_l}^\dagger b_{q_l}$  is the associated “number” operator, we have

$$b_{q_l}^\dagger b_{q_l} |n_{q_l}\rangle = n_{q_l} |n_{q_l}\rangle \quad n_{q_l} = 0, 1, 2, \dots \quad (22)$$

The wave functions for the totally symmetric phonon are defined similarly except with respect to the potential shifted by  $\lambda/\sqrt{N}$  as denoted by the double tilde overstrike. Hence,  $|\tilde{n}_{q=0}\rangle$  denotes the number state with  $\tilde{n}_{q=0}$  quanta. In the exciton–phonon basis set of eq 21, an eigenstate of  $H_{FH}$  in eq 18 can be expanded as

$$|\psi_{\kappa,\alpha,n_0}\rangle = |\tilde{n}_0\rangle \otimes \sum_k \sum'_{n_{q_1}, n_{q_2}, \dots} c_{k; n_{q_1}, n_{q_2}, \dots}^{(\kappa,\alpha)} |k; n_{q_1}, n_{q_2}, \dots, n_{q_{N-1}}\rangle \quad (23)$$

Here, the wave vector  $\kappa$  represents the total (quasi) momentum

$$\kappa = k + \sum_{l=1}^{N-1} n_{q_l} q_l \quad (24)$$

which is a good quantum number as long as translational symmetry is upheld. The prime on the summation in eq 23 restricts the exciton and phonon wave vectors to those satisfying eq 24. Note that  $k$  in the exciton–phonon basis set denotes the exciton wave-vector alone and not the total “center-of-mass” wave vector  $\kappa$ . This differs from the multiparticle basis set in section 3.2 where  $k$  also represents the “center-of-mass” wave vector.

### 3.4. Vibronic Exciton Bands

Vibronic coupling can lead to profound deviations from the “free” exciton bands for H- and J-aggregates shown in Figure 3. In this section, we briefly review the band structures in the weak-to-intermediate ( $W \lesssim \lambda^2 \omega_{\text{vib}}$ ) and strong ( $W \gg \lambda^2 \omega_{\text{vib}}$ ) exciton coupling regimes, which will be useful for understanding the associated spectral properties in section 4. We consider linear, ideal aggregates, where “ideal” refers to aggregates with no disorder and with one molecule per unit cell. For such aggregates, the eigenfunctions and energies corresponding to the Holstein-style Frenkel exciton Hamiltonian in eqs 13 and 18 are readily obtained numerically<sup>14,147,242</sup> using either the multiparticle or exciton–phonon representation of the Hamiltonian.

Figure 7 shows the vibronic band structure for J- and H-aggregates in the intermediate coupling regime,  $W = \omega_{\text{vib}}$ , assuming the ubiquitous vinyl-stretching mode ( $\omega_{\text{vib}} = 0.17$  eV,  $\lambda^2 = 1$ ). The J-aggregate band structure is essentially the same as that appearing in ref 242. Several features in Figure 7 are worthy of note. The most obvious is the appearance of vibronic bands, labeled  $\nu_t (= 0, 1, 2, \dots)$ , with neighboring bands separated by approximately a vibrational quantum.<sup>147</sup> The lowest energy band ( $\nu_t = 0$ ), from which emission originates, consists of a cosine-like dispersion curve with a single energy (and eigenstate) for each value of center-of-mass momentum  $k$ , as is the case for the free-excitons in Figure 3a. In contrast, the higher vibronic bands with  $\nu_t \geq 1$  consist of a dense collection of sub-bands but with a discernible interior cosine dispersion pattern most obvious in the  $\nu_t = 1$  band. The unusual eigenstructure, and in particular the multiplicity of excitons for each value of  $k$ , arises from the extra degree of freedom inherent in two-particle states; two coordinates are required to

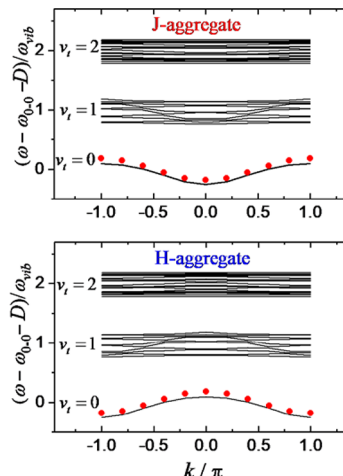


**Figure 7.** Energy dispersion bands for J- and H-aggregates in the intermediate coupling regime with  $W = \omega_{\text{vib}}$  and  $\lambda^2 = 1$ . Aggregates consist of  $N = 10$  chromophores, and the Coulomb coupling is restricted to nearest neighbors. Bands are evaluated using the Holstein Hamiltonian in eq 13 under the two-particle approximation and using periodic boundary conditions. Discrete points are connected by smooth lines for better viewing. Red dots are from eq 25.

locate the vibronic and vibrational excitations. The two-particle states contribute only to the bands with  $\nu_t \geq 1$  because by definition they must have at least one quantum of vibrational energy. In order to index the energies from all of the vibronic bands, we denote the energy of the  $\alpha$ th state with wave vector  $k$  as  $\omega_{k,\alpha}$ , where  $\alpha (= 1, 2, 3)$  increases in order of increasing energy. Hence, the lowest energy band in Figure 7 has energies given by  $\omega_{k,\alpha=1}$ .

The overall vibronic band structure in Figure 7 can most easily be appreciated by treating the Coulomb coupling perturbatively, i.e., by dividing the Hamiltonian in eq 13 into an unperturbed part,  $H_{FH} - H'$ , and perturbed part

$$H' = \sum_{m,n} J_{m,n} |m\rangle\langle n|$$

The zero-order wave functions in the band  $\nu_t$  obtained using degenerate perturbation theory, are dominated by single-particle states in eq 16 having  $\tilde{\nu} (= \nu_t)$  vibrational quanta admixed with two-particle states in eq 17 having a total  $\tilde{\nu} + \nu' = \nu_t$  vibrational quanta as described in greater detail in ref 147. To zero-order, the states comprising the lowest energy band ( $\nu_t = 0$ ) are single-particle excitons,  $|k, \nu_t = 0\rangle^{(0)} = |k, \tilde{\nu} = 0\rangle$ . Two-particle states do not contribute to the zero-order wave functions in the  $\nu_t = 0$  band as they are higher in energy by at least one vibrational quantum. The energies of the excitons in the lowest vibronic band, correct to first-order, are denoted as  $\omega_{k,\alpha=1}^{(1)}$  with

$$\begin{aligned} \omega_{k,\alpha=1}^{(1)} &= \omega_{0-0} + D + \langle k, \tilde{0} | H' | k, \tilde{0} \rangle \\ &= \omega_{0-0} + D + 2J_C e^{-\lambda^2} \cos k \end{aligned} \quad (25)$$

where the Franck–Condon factor  $\langle \tilde{\nu} = 0 | \nu = 0 \rangle^2 = \exp(-\lambda^2)$  appears in the final expression.

Eq 25 represents a renormalized exciton band with a bandwidth of  $W \exp(-\lambda^2)$ . The red dots in Figure 7a and b represent the energies calculated using eq 25. The deviations from the numerically calculated band comes from higher-order corrections involving interband interactions. Similar to the case of free-excitons, the band curvature at  $k = 0$  is positive in J-

aggregates and negative in H-aggregates; in J-aggregates, the band-bottom exciton has  $k = 0$ , whereas in H-aggregates, the band-bottom exciton has  $k = \pi$  in agreement with the free-exciton dispersion curves in Figure 3.

The unusual band structure in the higher vibronic bands with  $\nu_t \geq 1$  is due to the admixture of one-particle and two-particle ("vibronic/vibrational pair") states. For example, to zero-order, the  $\nu_t = 1$  band is comprised of the states<sup>147</sup>

$$\begin{aligned} |k, p\rangle^{(0)} &= a^{k,p}|k, \tilde{1}\rangle + \sum_{s=1,2\dots} c_s^{k,p} \{ e^{iks}|k, \tilde{0}; s, 1\rangle \\ &+ e^{-iks}|k, \tilde{0}; -s, 1\rangle \} \end{aligned} \quad (26)$$

where  $k$  is the center-of-mass wave vector of the  $p$ th (zero-order) eigenstate, and the one- and two-particle excitons are defined in section 3.2. The states dominated by the single-particle states are dispersed in a manner similar to those in the  $\nu_t = 0$  band and can be faintly discerned in the  $\nu_t = 1$  band in Figure 7 for both aggregate types.

Overall, when the coupling is relatively weak,  $W < \lambda^2 \omega_{\text{vib}}$ , the bandwidth for band  $\nu_t$  is

$$W(\nu = 0|\tilde{v} = \nu_t)^2 = W\lambda^{2\nu_t}e^{-\lambda^2}/\nu_t!$$

Summing over all  $\nu_t$  gives the free-exciton bandwidth  $W$ . Within each band, the exciton ordering is reflective of the sign of the Coulomb coupling; in J- (H-) aggregates, the  $k = 0$  ( $k = \pi$ ) exciton defines the band bottom as is most clearly observed in the  $\nu_t = 0$  band. First-order corrections to the wave functions arise from the coupling between excitons with the same  $k$  but from different bands. Such interband coupling is discussed in detail in ref 147 and has a major impact on the shape of the optical spectra as captured by the absorption ratio rule (see section 4.2.3).

As the exciton coupling increases, the vibronic bands widen and eventually merge into a single broad band of width  $W$ . In the strong coupling limit  $W \gg \lambda^2 \omega_{\text{vib}}$ , the Frenkel–Holstein Hamiltonian expressed in the exciton–phonon basis, as in eq 18, becomes the starting point for perturbation theory, where the perturbation is now the exciton–phonon coupling term, the last term in eq 18. In this picture, the states

$$|\tilde{n}_{q=0}\rangle \otimes |k; n_{q_1}, n_{q_2} \dots n_{q_{N-1}}\rangle$$

in eq 21 serve as the zero-order wave functions. Figure 8 shows the calculated exciton band structure for J-aggregates with  $W = 40\omega_{\text{vib}}$  with all other parameters the same as in Figure 7. (To make this value of  $W$  physically relevant, one would need to restrict the vibrational frequencies to values  $\lesssim 300 \text{ cm}^{-1}$ ). In this limit, the total momentum,  $\kappa$ , equivalent to the center-of-mass momentum of Figure 7 is readily resolved into contributions from the exciton ( $k$ ) and phonon momenta ( $q_l$ ), see eq 24. Figure 8 shows that bands are now more evenly distributed within the entire exciton bandwidth  $W$ . The zero-order wave functions,  $|\tilde{n}_{q=0} = 0\rangle \otimes |k; 0, 0 \dots 0\rangle$ , consisting of an exciton with wave vector  $k$  but with no phonons (i.e.,  $\kappa = k$ ), are responsible for the highly dispersive band outlined in red (top). The band energies corrected to first order are given by

$$\omega_k^{(1)} = \omega_{0-0} + D + \left(1 - \frac{1}{N}\right)\lambda^2 \omega_{\text{vib}} + 2J_C \cos k \quad (27)$$

The lowest energy (zero-order) exciton in the strongly coupled J-aggregate in Figure 8 is given by  $|\tilde{n}_{q=0} = 0\rangle \otimes |k =$

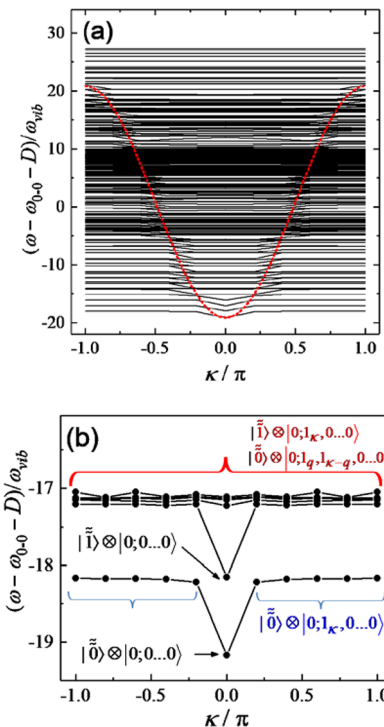


**Figure 8.** (a) Energy dispersion bands for J-aggregates with  $N = 10$ ,  $\lambda^2 = 1$ , and  $W = 40\omega_{\text{vib}}$ . (Discrete values are connected by smooth lines for better viewing.) The band in red is evaluated from eq 27. (b) Enlarged view of the lowest energy bands. Calculations are based on the Holstein Hamiltonian under the three-particle approximation.

$0, 0, 0 \dots 0\rangle$ ; the remaining states in the flat lowest-energy band, better observed in the expanded view at the bottom of Figure 8, are roughly one vibrational quanta higher in energy, and to zero-order are given by  $|\tilde{n}_{q=0} = 0\rangle \otimes |k = 0; 0, 1_{q=k} \dots 0\rangle$ . Hence, the dispersion of the lowest band is entirely derived from the phonons, and because such phonons are Einstein phonons, the band is flat. In the next higher energy band, the state with  $\kappa = 0$  now has a single vibrational quantum in the totally symmetric phonon  $|\tilde{n}_{q=0} = 1\rangle \otimes |k = 0; 0, 0 \dots 0\rangle$ , whereas the rest of the band is derived from states with two vibrational quanta. Such states can be either  $|\tilde{n}_{q=0} = 1\rangle \otimes |k = 0; 0, 1_{q=k} \dots 0\rangle$  or the degenerate set of nontotally symmetric phonons  $|\tilde{n}_{q=0} = 0\rangle \otimes |k = 0; 0, 1_{q'} \dots 1_{q'=k-q} \dots 0\rangle$ . The latter mix together to form the complex band structure shown in the figure.

### 3.5. The Exciton Coherence Function

Spatial exciton coherence relates to the distance over which the exciton retains wavelike properties and is of considerable interest for its possible impact on exciton transport.<sup>18,189–194</sup> Spatial coherence is identified with the off-diagonal terms of the electronic density matrix,  $\rho_{mn}$ , when written in the site basis. Several authors<sup>190,289–291</sup> have defined a coherence function dependent upon the site separation,  $s = m - n$ , for pure as well as mixed states. Kuhn and Sundstrom,<sup>289</sup> for example, define the coherence function,  $C_{\text{KS}}(s)$  to be

$$C_{\text{KS}}(s) \equiv \sum_n |\langle \rho_{n,n+s} \rangle_C| \quad (28)$$

where the average indicated by  $\langle \dots \rangle_C$  is taken over configurations of disorder. In the most general case, the density matrix  $\rho$  in eq 28 represents a mixed state because it

includes an average over a Boltzmann distribution of populations at a given temperature  $T$

$$\rho \equiv \sum_i |\psi_i\rangle\langle\psi_i| \frac{e^{-(\omega_i - \omega_{\text{em}})/k_B T}}{Z} \quad (29)$$

where  $|\psi_i\rangle$  is the  $i$ th eigenstate of the system with energy  $\omega_i$ ,  $\omega_{\text{em}}$  is the lowest exciton energy representative of the emissive state at  $T = 0$  K, and  $Z$  is the partition function. After introducing the local exciton creation and annihilation operators  $B_n^\dagger \equiv |n\rangle\langle g|$  and  $B_n = |g\rangle\langle n|$ , respectively, the density matrix elements in eq 28 become  $\rho_{n,n+s} = \langle\langle\psi_i|B_n^\dagger B_{n+s}|\psi_i\rangle\rangle_T$ , where  $\langle\cdots\rangle_T$  represents the thermal average with the sum over the index  $i$  implied and conducted as in eq 29.

In cases where vibronic coupling was included, it proved convenient in several studies<sup>145,176,182</sup> to base the coherence function on the *vibronic* creation operator

$$\tilde{B}_n^\dagger \equiv |n; \text{vac}\rangle\langle g; \text{vac}| \quad (30)$$

which, unlike  $B_n^\dagger$  defined after eq 29, depends on both electronic and nuclear degrees of freedom (note the tilde overstrike in eq 30). Here,  $|n; \text{vac}\rangle \equiv |g_1 0_1; g_2 0_2, \dots, g_n 0_n, \dots, g_N 0_N\rangle$  represents the state with an electronic excitation ( $S_1$ ) at site  $n$  but with a global vacuum phonon state in which all chromophores are devoid of vibrations ( $v = 0$ ) relative to the ground state nuclear potential  $S_0$  (see Figure 5).  $|g; \text{vac}\rangle$  is defined similarly except without any electronic excitations. Hence,  $\tilde{B}_n^\dagger$  creates an electronic excitation ( $S_1$ ) at site  $n$  but leaves the nuclear wave function undisturbed and equal to the ground ( $v = 0$ ) vibrational wave function. With  $\tilde{B}_n^\dagger$  and its Hermitian conjugate  $\tilde{B}_n$  so defined, the coherence function associated with the  $i$ th eigenstate becomes<sup>145,176,182</sup>

$$C_i(s) \equiv \sum_n \langle\psi_i|\tilde{B}_n^\dagger \tilde{B}_{n+s}|\psi_i\rangle \quad (31)$$

Note that  $C_i(s)$  lacks the absolute value, which appears in the summand of eq 28. As described below, the absolute value is inserted later when determining the exciton coherence number. The thermal coherence function follows directly from eq 31 by averaging over a Boltzmann distribution of populations

$$\langle C(s)\rangle_T \equiv \sum_n \sum_i \langle\psi_i|\tilde{B}_n^\dagger \tilde{B}_{n+s}|\psi_i\rangle \frac{e^{-(\omega_i - \omega_{\text{em}})/kT}}{Z} \quad (32)$$

One can further average over various configurations of site disorder to obtain  $\langle C(s)\rangle_{C,T}$ .

As discussed in refs 145, 176, and 182, the main difference between  $\langle C(s)\rangle_{C,T}$  and coherence functions like  $C_{KS}(s)$ , which are based solely on electronic degrees of freedom,<sup>190,289–291</sup> can be appreciated when the separation  $s$  is zero. In this case,  $C_{KS}(s = 0)$  is exactly unity because the right-hand side of eq 28 reduces to the average number of excitons, which is one.<sup>289</sup> This is consistent with the form of the Hamiltonian in eq 13, which neglects two and higher excitons. By comparison,  $C_i(s = 0)$  as well as  $\langle C(s = 0)\rangle_{C,T}$  are generally less than unity due to vibrational relaxation at the site of the electronic excitation.<sup>145,176,182</sup> For example, inserting the wave function expansion in eq 14 into eq 31 gives

$$C_i(0) = \sum_n \left| \sum_{\tilde{v}} c_{n,\tilde{v}}^{(i)} \langle \tilde{v} | 0 \rangle \right|^2$$

Hence,  $C_i(s = 0)$  is a measure of nuclear relaxation experienced by the electronically excited molecule in the eigenfunction  $|\psi_i\rangle$ .

As described in refs 145, 176, and 182 for the important band-bottom (“emitting”) exciton in ideal H- or J-aggregates,  $C_{\text{em}}(0)$  ranges from  $\exp(-\lambda^2)$  in the limit of weak excitonic coupling ( $W \ll \lambda^2 \omega_{\text{vib}}$ ), indicative of full relaxation within the  $S_1$  potential, to  $\exp(-\lambda^2/N)$  in the strong coupling limit ( $W \gg \lambda^2 \omega_{\text{vib}}$ ), where there is little to no relaxation, i.e., a “free” exciton uncoupled from vibrations.<sup>176</sup>  $C_{\text{em}}(0)$  can also be referred to as a generalized Franck–Condon factor  $F$ .

Figure 9 shows  $C_{\text{em}}(s)$  for ideal J- and H-aggregates containing  $N = 60$  chromophores in the intermediate coupling

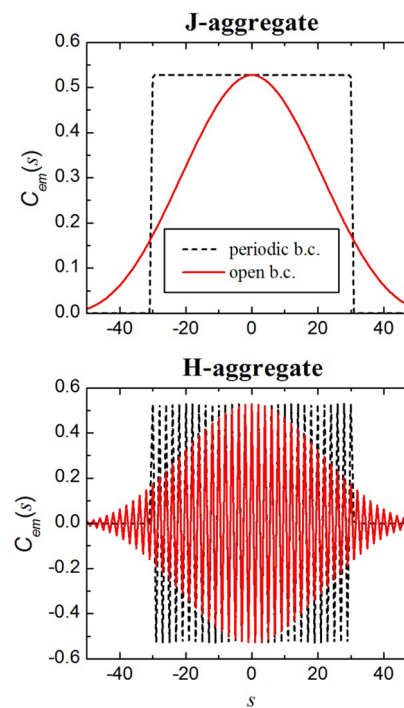


**Figure 9.** Coherence function for perfectly ordered linear J-aggregates ( $J_C = -0.25\omega_{\text{vib}}$ ) and H-aggregates ( $J_C = 0.25\omega_{\text{vib}}$ ) containing  $N = 60$  chromophores. The solid (dashed) curve corresponds to aggregates with open (periodic) boundary conditions. In both cases,  $\omega_{\text{vib}} = 0.17$  eV and  $\lambda^2 = 1$ .

regime using the same parameters that define the band structure in Figure 7. The lowest energy exciton,  $|\psi_{\text{em}}\rangle$ , in J-aggregates (H-aggregates) corresponds to the state with  $k = 0$  ( $k = \pi$ ) and  $\alpha = 1$ . The uniform phase of the band-bottom exciton in J-aggregates results in a nodeless coherence function shown in Figure 9 (top). Under periodic boundary conditions, the coherence function is flat,  $C_{\text{em}}(s) = C_{\text{em}}(0)$ , independent of  $s$  over the entire range,  $-N/2 + 1 \leq s \leq N/2$ . The value  $C_{\text{em}}(0) = 0.52$  lies between  $\exp(-1)$  and unity, indicating incomplete nuclear relaxation within the  $S_1$  nuclear potential. For the H-aggregates in the lower panel of Figure 9, there exists a rapid phase oscillation  $(-1)^s$  due to the wave vector,  $k = \pi$ , of the band-bottom exciton. In the case of open boundary conditions, where  $s$  now ranges from  $-(N - 1)$  to  $N - 1$ , the envelope of  $C_{\text{em}}(s)$  diminishes with increasing  $|s|$  due to end effects in both aggregate types, similar to what happens to particle-in-a-box wave functions.

Localized excitations manifest as narrow coherence functions can occur when traps are present, chromophores with unusually low transition energies due to various disorder mechanisms. In the simplest example, a deep trap at chromophore  $n$  is

characterized by a negative deviation (red-shift)  $\Delta_T$  in its transition energy. If  $|\Delta_T|$  is much greater than the exciton bandwidth  $W$ , the lowest energy eigenstate is completely localized on chromophore  $n$ , and the coherence function of the lowest energy state reduces to a kronecker delta function

$$C_{\text{em}}(s) = C_{\text{em}}(0)\delta_{s,0} \quad (33)$$

From the coherence function, one can readily determine the coherence number,  $N_{\text{coh}}$ , the number of chromophores over which the exciton is wavelike. In refs 145, 176, and 182, the coherence number corresponding to the lowest-energy state was defined as

$$N_{\text{coh}} \equiv \frac{1}{C_{\text{em}}(0)} \sum_s |C_{\text{em}}(s)| \quad (34)$$

which can be viewed as the “area” of the peak-normalized envelope of the coherence function (see Figure 9). The expression is valid for both J- and H-aggregates with the latter demanding the absolute value in the summand of eq 34 to eliminate the phase changes, see Figure 9b. Note, in  $C_{\text{KS}}$  defined in eq 28, the absolute value was introduced at the level of the coherence function.

The coherence number defined in eq 34 has the correct limiting behaviors. When the coherence function is completely localized as in eq 33,  $N_{\text{coh}}$  reduces to unity. Conversely, for a completely delocalized excitation,  $N_{\text{coh}}$  becomes equal to the total number of chromophores,  $N$ , independent of the wave vector of the exciton. This last result is strictly valid under periodic boundary conditions and is readily appreciated by inserting the coherence functions for the H- and J-aggregates in Figure 9 into eq 34. For open boundary conditions, the additional localization due to end effects leads to  $N_{\text{coh}} < N$ . Indeed, in Figure 9,  $N_{\text{coh}}$  is  $\sim 0.82N$  for either J- or H-aggregates when open boundary conditions are adapted. For an ensemble of disordered aggregates at temperature  $T$ , the coherence function is readily generalized by replacing  $C_{\text{em}}(s)$  in eq 34 with  $\langle C(s) \rangle_{C,T}$ . Further examples of the coherence function as a function of temperature and site disorder are given in section 4.5, where the intimate connection between the coherence function and the PL spectrum is made. Finally, in linear aggregates, the exciton coherence length is identified with  $N_{\text{coh}}$  through

$$L_{\text{coh}} \equiv (N_{\text{coh}} - 1)d \quad (35)$$

where  $d$  is the nearest neighbor separation. To summarize, the coherence function  $\langle C(s) \rangle_{C,T}$  contains information about both the extent of the exciton’s spatial coherence as well as the level of nuclear relaxation, specifically at the site of the central electronic excitation comprising the “Frenkel polaron”.<sup>14,292</sup>

Other metrics for exciton coherence, delocalization, and entanglement in molecular aggregates have been compared and contrasted in an insightful review by Smyth et al.<sup>293</sup> Perhaps the most popular metric for exciton delocalization is the inverse participation ratio (IPR).<sup>294</sup> In excitonic systems (no vibrational degrees of freedom), the IPR for state  $|\psi_i\rangle$  is

$$\text{IPR}_i = \sum_n |c_n^{(i)}|^4 \quad (36)$$

Unlike  $N_{\text{coh}}$ , the IPR is not strictly a measure of exciton coherence because it does not depend on the off-diagonal elements of the density matrix in the site basis but nevertheless remains a measure of the delocalization as determined by site

populations. (The difference can be important for mixed states.) The IPR is unity for localized excitations and reduces to  $O[1/N]$  for delocalized excitations. For molecular aggregates, Schreiber and Toyozawa<sup>295,296</sup> and Fidder et al.<sup>40</sup> have studied the IPR as a function of the exciton’s energy in an ensemble of site-disordered aggregates, showing how it correlates to other measures of exciton delocalization such as the radiative enhancement factor. More recently, Barford and co-workers have utilized the participation ratio to interpret the photoluminescence spectrum in Frenkel chains,<sup>245,248</sup> see section 4.

### 3.6. Vibrational Distortion Field

As shown in the prior section, the coherence function at  $s = 0$  reports on the nuclear relaxation at the site of the electronically excited molecule within the vibronic exciton. However, molecules surrounding the central vibronic excitation are also excited vibrationally, but not electronically, creating a vibrational “cloud” or vibrational distortion field (VDF). Within the multiparticle basis set, it is the two-particle states (i.e., vibronic/vibrational pair states) and beyond that are necessary for establishing the VDF.

A quantitative description of the VDF in molecular aggregates already appeared in the seminal work of Scherer and Fischer<sup>165</sup> and later by Hoffmann and Soos<sup>211</sup> and Spano and co-workers.<sup>181,284,292</sup> For an exciton with wave function  $|\psi_i\rangle$ , the vibrational distortion field is defined as

$$D_i(r) \equiv \langle \psi_i | \sum_n |n\rangle \langle n| \frac{b_{n+r}^\dagger + b_{n+r}}{2} | \psi_i \rangle \quad (37)$$

where  $D_i(r)$  measures the average displacement (from the  $S_0$  minimum) in the vibrational coordinate for a molecule  $r$  units away from the central electronically excited molecule. For example,  $D_i(r)$  can represent the expansion in the aromatic-quinoidal coordinate in poly(3-hexylthiophene) (P3HT). In the absence of any intermolecular coupling, all excited molecules are relaxed in the  $S_1$  potential well (see Figure 5), and the VDF reduces to  $D_i(r) = -\lambda\delta_{r,0}$ . Hence, expansion along the nuclear coordinate occurs when  $\lambda$  is negative, consistent with how  $\lambda$  appears in the exciton–phonon coupling term in the Hamiltonian of eq 13. For example, the exciton-vibrational coupling term can be rewritten as

$$H_{FH} - H_{\text{ex}} = \omega_{\text{vib}} \sum_n \left\{ \sum_{m \neq n} b_m^\dagger b_m + (b_n^\dagger + \lambda)(b_n + \lambda) \right\} |n\rangle \langle n|$$

showing that the minimum in the nuclear well of the excited molecules ( $S_1$ ) appears at  $-\lambda$  relative to the minimum of  $S_0$ . In all that follows,  $\lambda$  is taken as negative to indicate a realistic expansion, as was assumed in ref 292. (Of course,  $\lambda$  could have been negated in the Hamiltonian, but that would have been inconsistent with many prior works, in particular, the pioneering work of Scherer and Fischer<sup>165</sup>).

The limiting form  $D_i(r) = -\lambda\delta_{r,0}$  also corresponds to a completely localized or trapped excitation where the trap depth,  $|\Delta_T|$ , is much greater than the exciton bandwidth  $W$ . In this case, the wave function is limited to single-particle components with the electronic exciton located at the trap site; coupling to two-particle states scales as  $W/|\Delta_T|$ . In the opposite limit of very strong exciton coupling ( $W \gg \lambda^2 \omega_{\text{vib}}, |\Delta_T|$ ), the exciton is delocalized over all sites and  $D_i(r) = -\lambda/N$  for all  $r$ , i.e., a large radius polaron where the nuclear distortion is distributed evenly over all sites. Interestingly, in both limiting cases, the sum of the

distortions over all sites is  $-\lambda$ . In fact, if one maintains periodic boundary conditions, the sum rule

$$\sum_r D_i(r) = -\lambda$$

is rigorously obtained.<sup>212</sup> This can be seen by rewriting the rhs of eq 37 in the  $k, q$  basis set and inserting the multiphonon form of the wave function in eq 23.

As demonstrated in ref 292, the form of the VDF is quite different in J- vs H-aggregates. Figure 10 shows  $\Delta D_{\text{em}}(r)$  as a

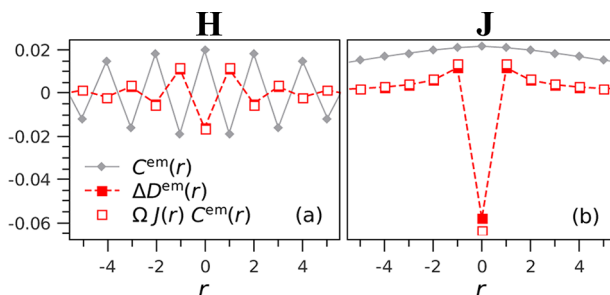


**Figure 10.** Calculated coherence function (gray diamonds) and vibrational distortion field (red squares) for H-aggregates in (a) and J-aggregates in (b) consisting of  $N = 15$  chromophores. Open red squares in each panel represent the product in eq 38. In both cases, the HR factor is unity, and the Coulomb coupling is  $1/r$  with a nearest neighbor value of  $0.031\omega_{\text{vib}}$  ( $-0.031\omega_{\text{vib}}$ ) for H-aggregates (J-aggregates). Reprinted with permission from ref 292. Copyright (2013), American Chemical Society.

function of  $r$  (red squares) for the emitting exciton (lowest energy exciton) in disorder-free J- and H-aggregates with extended ( $1/r$ ) Coulomb coupling. In both cases,  $\lambda = -1$ . Here,  $\Delta D_{\text{em}}(r)$  is defined as

$$\Delta D_{\text{em}}(r) \equiv D_{\text{em}}(r) + \lambda \delta_{r,0}$$

differing from  $D_{\text{em}}(r)$  only at  $r = 0$ , at which point it measures the deviation from the  $S_1$  minimum and not the  $S_0$  minimum as in  $D_{\text{em}}(r)$ .

As observed in Figure 10,  $\Delta D_{\text{em}}(r = 0)$  is negative for both H- and J-aggregates, indicating that the central electronic excitation is not completely relaxed in the  $S_1$  potential; the expansion  $D_{\text{em}}(r = 0)$  along the vibrational coordinate does not quite reach  $-\lambda$ . In H-aggregates,  $\Delta D_{\text{em}}(r = 0)$  changes phase-like ( $-1$ ), indicating an interesting expansion/contraction along the vibrational coordinate within the vibrational cloud. A similar behavior was found for the chiral (H-like) MOPV4 aggregates in ref 181. By contrast, in J-aggregates, the phase is uniform and positive for all values of  $r$  (except  $r = 0$ ). Here, the positive values represent small coordinate expansions for all molecules in the surrounding vibrational cloud. Overall, the phase behavior within the vibrational cloud in both aggregate types traces back to the form of the lowest-energy excitons;  $k = \pi$  in H-aggregates and  $k = 0$  in J-aggregates.

As discovered in ref 292 for linear aggregates, an interesting relationship exists between the  $r$ -dependent form of the Coulomb coupling,  $J_{n,n+r}(r)$ , the coherence function,  $C_{\text{em}}(r)$ , and the vibrational distortion field,  $D_{\text{em}}(r)$ , for the band-bottom emitting exciton. In the weak-to-intermediate exciton coupling regime ( $W \gtrsim \lambda^2 \hbar \omega_{\text{vib}}$ ), the simple relationship<sup>292</sup>

$$D_{\text{em}}(r) = \Omega C_{\text{em}}(r) J_{n,n+r}(r) \quad r \neq 0 \quad (38)$$

holds for both aggregate types, where  $\Omega$  is an  $r$ -independent proportionality constant that depends on the HR factor,  $\lambda^2$ , and the level of disorder. (In disorder-free aggregates,  $\Omega = -1$  when  $\lambda = -1$ .) The relationship is demonstrated in Figure 10 for H- and J-aggregates and shows that the phase oscillations present in H-aggregates are due to the oscillations in the coherence function. The expression also provides important limitations on the spatial extent or radius of the vibrational cloud for realistic organic materials for which  $W \gtrsim \lambda^2 \hbar \omega_{\text{vib}}$  is valid. A far more detailed discussion of the limitations of eq 38 can be found in ref 292.

#### 4. ABSORPTION AND PHOTOLUMINESCENCE IN VIBRONICALLY COUPLED H- AND J-AGGREGATES

Many groups have considered the impact of vibronic coupling on the UV-vis absorption and PL spectral line shapes in molecular aggregates,<sup>3,10,14,79,140,150–188</sup> beginning with the seminal works of McRae<sup>152–155</sup> and Fulton and Gouterman.<sup>150,151</sup> In this section, we review the progress made on interpreting the steady-state optical spectra of J- and H-aggregates using the Holstein-style Hamiltonians based on eq 13. For most of this section, vibronic coupling is limited to a single symmetric intramolecular mode, which in the case of  $\pi$ -conjugated oligomers and polymers is the ubiquitous progression-building vinyl-stretching (or aromatic-quinoidal) mode with energy  $\omega_{\text{vib}}$  in the range of 150–180 meV. The vibronic progression associated with this mode is clearly evident in the UV-vis spectrum of water-solvated pseudoisocyanine (PIC) molecules shown in Figure 11 (curve 1) taken

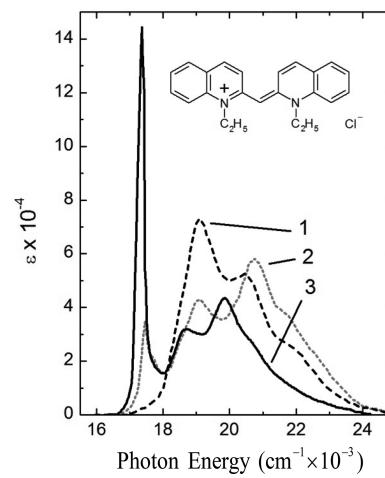


**Figure 11.** Absorption spectrum of PIC in water as a function of increasing PIC concentration (1–3). Redrawn as a function of wavenumber from the data presented in ref 51.

from one of the classic Scheibe-aggregate papers.<sup>51</sup> The line shape can be accurately modeled using an HR factor of  $\sim 0.6$ .<sup>165</sup> The figure also shows the significant changes to the spectral line shape that occur with increasing concentration, most notably the formation of the narrow red-shifted J-band signifying aggregation (curve 3) along with higher-energy vibronic peaks that are not simply attributed to unaggregated molecules. Indeed, it was shown that the J-band is mainly polarized along the aggregate axis, whereas the higher energy vibronic peaks are mainly polarized orthogonal to the aggregate axis.<sup>50</sup> The J-band is also a strong source for radiative emission with a PL spectrum dominated by 0–0 emission with virtually no Stokes

shift. An excellent example of this behavior is provided by the merocyanine aggregates in Figure 12.<sup>61</sup>

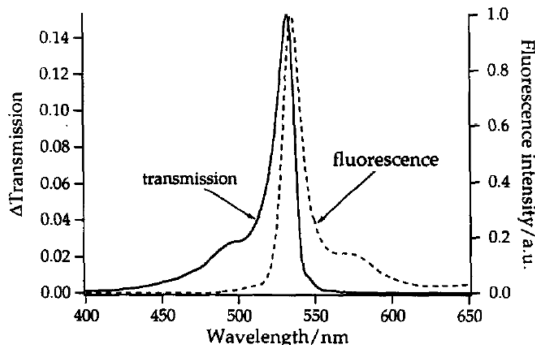


**Figure 12.** Absorption and PL spectra of a merocyanine J-aggregate from ref 61. Reprinted with permission from ref 61. Copyright 1994, Elsevier.

In accordance with the Kasha model, the negative (J-promoting) excitonic coupling responsible for the large, observed spectral red-shift in cyanine aggregates arises entirely from Coulombic interactions,<sup>20–24</sup> providing the basis for several proposed structures for the cyanine J-aggregates,<sup>51–54,61</sup> the most popular of which is the “brick-stone” packing in which neighboring dyes are slipped about a half molecular length along the long-molecular axis. The Kasha model, however, cannot account for the vibronic fine structure. To properly understand the vibronic sidebands, including their polarization properties, one must include local exciton-vibrational coupling. Kopainsky et al.<sup>56</sup> were the first to successfully describe the aggregation-induced changes in the vibronic progression incurred upon PIC dimerization using the vibronic theory developed by Fulton and Gouterman.<sup>150,151</sup> However, Scherer and Fischer<sup>165</sup> provided the first detailed account of the polarization-dependent vibronic structure of the PIC J-aggregate absorption spectrum observed in Figure 11 by using the Holstein Hamiltonian in eq 13 represented in a multiparticle basis set of Philpott.<sup>160</sup> Many other works have appeared subsequent to ref 165 employing a variety of methods to unravel the impact of vibronic coupling on the absorption and PL spectra of J- and H-aggregates, including multiparticle diagonalizations,<sup>13,14,260,283–287,297</sup> the coherent scattering approximation of Briggs and Eisfeld,<sup>167,168,170,171</sup> variational techniques pioneered by Merrifield,<sup>157,180</sup> wave packet propagation techniques of Engel and co-workers,<sup>140,172–174</sup> and the (time domain) hierarchy of coupled differential equations approach of Eisfeld and co-workers.<sup>185,186</sup> In this section, we review what is known about the impact of vibronic coupling on the photophysics of linear aggregates as well as more complex geometries including herringbone (two-dimensional) aggregates, curved aggregates, and helical aggregates.

On the basis of the Holstein Hamiltonian in eq 13, the minimal phase space defining a vibronically coupled linear J- or H-aggregate consists of at least four degrees of freedom: the free-exciton bandwidth,  $W$ , the vibrational energy,  $\omega_{\text{vib}}$ , the nuclear relaxation energy,  $\lambda^2 \omega_{\text{vib}}$  (where  $\lambda^2$  is the HR factor), and the number of chromophores in the aggregate,  $N$ . (One can simplify the problem by scaling all of the energies by a vibrational quantum.) The presence of diagonal and off-diagonal disorder, different topologies like curved or bent aggregates, and coupling to two (or more) vibrational modes

leads to additional degrees of freedom requiring more terms in the Hamiltonian. Moreover, the aggregate temperature, even when excluding its influence on packing structure (i.e., phase changes), leads to an additional degree of freedom for properties like photoluminescence, which depend on the thermal exciton populations. The general problem is therefore quite complex,<sup>155</sup> leading to a rich array of photophysical behaviors, some of which are described below.

#### 4.1. The Spectral Observables: Steady-State Absorption and PL

The steady-state absorption and photoluminescence (PL) spectral line shapes contain a treasure trove of information concerning the nature of the fundamental electronic excitations, including the magnitude of the exciton bandwidth, the curvature of the band at  $k = 0$  (i.e., J- vs H-aggregation), the spatial coherence properties of the band-bottom excitons, details regarding the way molecules pack together, and the nature of the (disordered) energy landscape. Much of this information derives from the vibronic fine structure and in particular how the aggregate spectrum deviates from the nonaggregated (“single-molecule”) spectrum; for example, in the way the mirror-image relationship between absorption and PL present in the monomeric spectrum becomes distorted upon aggregation (see section 4.2). To fully appreciate the information stored in spectral line shapes, the present subsection briefly reviews the forms of the steady-state absorption and PL spectra in molecular aggregates.

**4.1.1. The Absorption Spectrum.** The homogeneous absorption spectrum  $A(\omega)$  derives from the sum over all electronic transitions beginning from the vibrationless ground state  $|G\rangle$  to all eigenstates,  $|\psi_i\rangle$ , of the aggregate Hamiltonian

$$A(\omega) = \frac{1}{N\mu^2} \sum_i f_i W_{\text{LS}}(\omega - \omega_i) \quad (39)$$

where  $f_i$  is the oscillator strength for the  $|G\rangle \rightarrow |\psi_i\rangle$  transition

$$f_i = \omega_i |\langle \psi_i | \hat{M} | G \rangle|^2 \quad (40)$$

and  $W_{\text{LS}}(\omega)$  is the line shape function. Note that we have omitted the constant prefactors present in the more conventional expression for the oscillator strength and have divided by  $\mu^2$  in  $A(\omega)$  to make the “reduced” spectrum (see section 4.1.3) dimensionless. Furthermore, the division by  $N$  renders the spectrum normalized to the number of chromophores,  $N$ . (A similar division is not made in the PL spectrum because the  $N$ -dependence in PL is not uniform for all transitions; the  $N$ -scaling of just the 0–0 peak, for example, is responsible for superradiance, see the following section.) In eq 39, the vibrationless electronic ground state is denoted as  $|G\rangle \equiv |g; 0_1, 0_2, \dots, 0_N\rangle$ , where  $|g\rangle$  is the collective electronic ground state where all  $N$  chromophores are in the ground ( $S_0$ ) electronic state and  $0_n$  indicates that the  $n$ th chromophore has zero vibrational quanta in its ground (unshifted) nuclear potential  $S_0$ , see Figure 5.  $\hat{M}$  is the purely electronic aggregate transition dipole moment operator defined in eq 8.

The homogeneous line shape function,  $W_{\text{LS}}(\omega)$ , has a shape reflective of the details of the system-bath interactions and is generally derived via Fourier transformation of the dipole-dipole correlation function.<sup>10,174,282</sup> When the latter decays exponentially,  $W_{\text{LS}}(\omega)$  has a (dimensionless) Lorentzian form

$$W_{\text{LS}}(\omega) = \frac{\Gamma_h^2}{\omega^2 + \Gamma_h^2} \quad (41)$$

where the homogeneous line width,  $\Gamma_h$ , is the half-width at half-maximum, taken here to be the same for all  $|G\rangle \rightarrow |\psi_i\rangle$  transitions. The details of the homogeneous broadening are not that important in cases where the spectral width is dominated by static inhomogeneous broadening. In such cases, the spectrum must be further averaged over a distribution of transition energies chosen randomly from a distribution function usually taken to be Gaussian (see section 4.3). Finally, the form of the absorption spectrum in eq 39 neglects hot-band transitions arising from thermally populated vibrations in the electronic ground state. This is an excellent approximation given that the vibrational energy  $\omega_{\text{vib}}$  is typically much greater than  $k_B T$  at room temperature ( $\sim 26$  meV). (For example, the aforementioned vinyl stretching mode has energy of 0.17 eV.)

**4.1.2. The Photoluminescence (PL) Spectrum.** In evaluating the photoluminescence (PL) spectrum, it is assumed that emission originates from the lowest energy exciton  $|\psi_{\text{em}}\rangle$  in accordance with Kasha's rule.<sup>26</sup> For example, in disorder-free J-aggregates,  $|\psi_{\text{em}}\rangle$  corresponds to the lowest energy exciton with  $k = 0$ , the state with  $k = 0$  in the  $\nu_t = 0$  band of Figure 7. When the temperature is low enough to neglect emission from thermally excited excitons, the PL spectrum consists of a well-defined vibronic progression

$$S(\omega) \approx \sum_{\nu_t=0,1,2,\dots} (\omega_{\text{em}} - \nu_t \omega_{\text{vib}})^3 I^{0-\nu_t} W_{\text{LS}}^{\text{PL}}(\omega - \omega_{\text{em}} + \nu_t \omega_{\text{vib}}) \quad (42)$$

where the (dimensionless)  $0-\nu_t$  PL line strengths corresponding to emission from  $|\psi_{\text{em}}\rangle$  to ground electronic states containing a total of  $\nu_t$  vibrational quanta (with  $\nu_t = 0, 1, 2, \dots$ ) are defined as<sup>260,283,284</sup>

$$I^{0-0} \equiv \frac{1}{\mu^2} |\langle \psi_{\text{em}} | \hat{M} | G \rangle|^2 \quad (43)$$

$$I^{0-1} \equiv \frac{1}{\mu^2} \sum_{n=1}^N |\langle \psi_{\text{em}} | \hat{M} | g; 0_1, 0_2, \dots, 1_n, \dots, 0_N \rangle|^2 \quad (44)$$

$$\begin{aligned} I^{0-2} \equiv & \frac{1}{\mu^2} \left\{ \sum_{n=1}^N |\langle \psi_{\text{em}} | \hat{M} | g; 0_1, 0_2, \dots, 2_n, \dots, 0_N \rangle|^2 \right. \\ & \left. + \sum_{m,n=1}^N |\langle \psi_{\text{em}} | \hat{M} | g; 0_1, 1_m, 0_{m+1}, \dots, 1_n, \dots, 0_N \rangle|^2 \right\} \end{aligned} \quad (45)$$

with straightforward extensions for  $I^{0-3}$  and higher terms. In all cases, the  $0-\nu_t$  line strengths involve summations over all possible terminal states having a total of  $\nu_t$  vibrational quanta distributed over  $N$  chromophores. In the simplest case, the line shape function in eq 42 can be taken to be Lorentzian, independent of the transition, an excellent approximation when static inhomogeneous broadening is dominant. In such cases, the spectrum needs to be averaged over a distribution of molecular transition frequencies. Further averaging over a thermal (Boltzmann) distribution of emitting excitons is required to obtain the PL spectrum at higher temperatures.

Before continuing, it is worth mentioning some additional properties of the PL line strengths. Most importantly, the  $0-0$  line strength is directly sensitive to exciton coherence (see

section 3.5), whereas the sidebands are largely incoherent. This essential distinction is readily appreciated by inserting the emitting exciton's wave function expressed in the multiparticle basis set (see eq 14) into eq 43 giving<sup>260,283,284</sup>

$$I^{0-0} = \frac{1}{\mu^2} \left| \sum_{n,\tilde{v}} c_{n,\tilde{v}}^{\text{em}} \langle \tilde{v} | 0 \rangle \boldsymbol{\mu}_n \right|^2 \quad (46)$$

The coherence is manifest as the square of the sum over the emitting dipole moments with site-dependent phase factors. In H-aggregates, the sum represents a destructive interference with  $c_{n,\tilde{v}}^{\text{em}} \approx (-1)^n / \sqrt{N}$ , whereas in J-aggregates, the sum represents a constructive interference with  $c_{n,\tilde{v}}^{\text{em}} \approx 1 / \sqrt{N}$ . Here, we have assumed ideal J-/H-aggregates with  $\boldsymbol{\mu}_n = \boldsymbol{\mu}$  and with no disorder. Hence, for ideal H-aggregates, the  $0-0$  emission is forbidden by symmetry, whereas in J-aggregates, the  $0-0$  emission is coherently enhanced or superradiant, scaling as  $N$ . The connection between the  $0-0$  emission and exciton coherence can be further developed through the realization that, when  $\boldsymbol{\mu}_n = \boldsymbol{\mu}$ , the sum in eq 46 is exactly equal to the sum over the coherence function defined in eq 31 for  $i = \text{em}$ <sup>145,176</sup>

$$I^{0-0} = \sum_s C_{\text{em}}(s) \quad (47)$$

In marked contrast, the PL side-band line strengths have the form of an incoherent "sum over the squares" of the transition dipole moments. For example, inserting the wave function in eq 14 into eq 44 gives<sup>283</sup>

$$I^{0-1} = \sum_n \left| \sum_{\tilde{v}} c_{n,\tilde{v}}^{\text{em}} \langle \tilde{v} | 0 \rangle \boldsymbol{\mu}_n + \sum_{n',\tilde{v}'} c_{n',\tilde{v}';n,1}^{\text{em}} \langle 0 | \tilde{v}' \rangle \boldsymbol{\mu}_{n'} \right|^2 \quad (48)$$

which is devoid of the complete destructive or constructive interferences present in  $I^{0-0}$ . Hence, in ideal H-aggregates, the PL line shape takes the form of a vibronic progression sans the  $0-0$  peak, whereas in marked contrast, the PL line shape in J-aggregates is entirely dominated by the superradiant  $0-0$  peak. Interestingly, eq 48 portrays a higher order interference arising between the one- and two-particle terms in the emitting wave function, which has been shown to be destructive for H-type lattices, such as the herringbone lattices of oligophenyleneninylenes and oligothiophenes.<sup>13,283,284,298,299</sup> The resulting interference leads to a  $0-1$  line strength, which is not generally zero but does vanish with increasing exciton coupling. By contrast, the one-/two-particle interference is constructive in J-aggregates,<sup>14</sup> leading to a  $0-1$  line strength that increases and eventually converges to the value of  $\lambda^2$  (see section 4.2.4) as the exciton bandwidth increases.

**4.1.3. Single Molecule Spectra.** In this section, we consider the absorption and emission spectra from an ensemble of noninteracting molecules governed by the Frenkel–Holstein Hamiltonian in eq 13 after neglecting the Coulombic intermolecular coupling. In what follows, it proves convenient to introduce the reduced absorption and PL spectra adopted by many early works, for example, the pioneering work of Fulton and Gouterman.<sup>151</sup> Reduced spectra are obtained by suppressing the  $\omega_i$  dependence in the oscillator strength in eq 40, making it depend solely on the transition dipole moment squared (which we refer to as simply the "line strength") and by suppressing the cubic frequency term in eq 42 derived from the photon density of states. Only under such conditions will the spectra display the often-quoted mirror-image symmetry in the limit of a single, vibrationally coupled molecule.<sup>300</sup>

When intermolecular coupling is neglected, the eigenstates of the Frenkel–Holstein Hamiltonian are the localized multiparticle states defined in section 3.2. Only the single-particle states,  $|n, \tilde{\nu}\rangle$ , where molecule  $n$  is electronically excited with  $\tilde{\nu}$  vibrational quanta in the  $S_1$  potential, carry oscillator strength. As indicated in Figure 13, absorption arises from the molecular

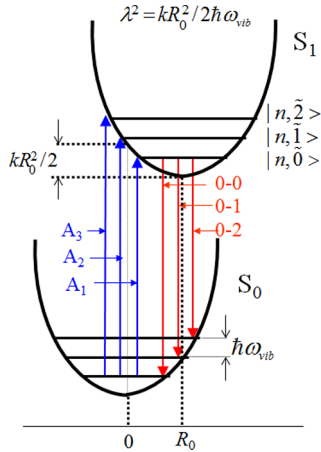


**Figure 13.** Absorption (blue) and emission (red) transitions in a single molecule.

transitions  $|G\rangle \rightarrow |n, \tilde{\nu}\rangle$  with energies  $\omega_{0-0} + \tilde{\nu}\omega_{\text{vib}}$  and line strengths  $|\langle n, \tilde{\nu} | \hat{M} | G \rangle|^2 = \mu^2 |\langle \tilde{\nu} | 0 \rangle|^2$ . Consequently, the spectrum consists of the vibronic progression

$$A_M(\omega) = \sum_{\tilde{\nu}=0,1,2,\dots} \frac{e^{-\lambda^2} \lambda^{2\tilde{\nu}}}{\tilde{\nu}!} W_{\text{LS}}(\omega - \omega_{0-0} - \tilde{\nu}\omega_{\text{vib}}) \quad (49)$$

where the Franck–Condon factors have been resolved using  $\langle \tilde{\nu} | 0 \rangle^2 = \exp(-\lambda^2) \lambda^2 \tilde{\nu} / \tilde{\nu}!$ . Conversely, the PL spectrum (see Figure 13) consists of all transitions from the vibrationally relaxed, electronically excited molecules,  $|n, \tilde{\nu}\rangle$ , to the electronic ground state with  $\nu$  vibrational quanta.

$$S_M(\omega) \approx \sum_{\nu=0,1,2,\dots} \frac{e^{-\lambda^2} \lambda^{2\nu}}{\nu!} W_{\text{LS}}(\omega - \omega_{0-0} + \nu\omega_{\text{vib}}) \quad (50)$$

The reduced absorption and PL spectra for noninteracting molecules abiding by eqs 49 and 50 are shown in Figure 14 for two values of the HR parameter:  $\lambda^2 = 1$  and  $\lambda^2 = 0.5$ . In both cases, the vibronic progressions in the absorption and PL spectra are mirror-images. Note that the line strength ratios,  $I_{A_1}/I_{A_2}$ , in the absorption spectrum, as well as  $I^{0-0}/I^{0-1}$  in the PL spectrum are equal to  $1/\lambda^2$ , which is unity when the HR factor is unity. In what follows, these spectral ratios will play prominent roles in revealing exciton coupling and coherence, as intermolecular interactions generally lead to a redistribution of intensities among the various vibronic bands.

Often, there is a cluster of closely spaced (unresolvable) modes with energies near  $\omega_{\text{vib}}$  responsible for the vibronic progression observed in the absorption and emission spectra. In such cases, all modes within the cluster can be treated as a single effective mode with energy  $\omega_{\text{vib}}$  and with an effective HR factor equal to the sum of all the constituent HR factors. A cluster of modes, however, will also lead to effective vibronic peak broadening in the absorption spectrum, which increases with energy: for example, if there are two modes with energies 1350 and 1450 cm<sup>-1</sup>, then there is a single 0–0 peak at  $\omega_{0-0}$ , a

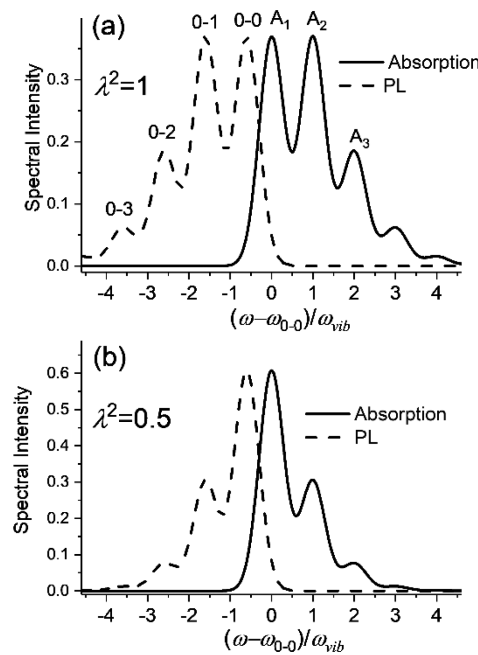


**Figure 14.** (a) The single molecule reduced absorption spectrum (solid) and PL spectrum (dashed) for  $\lambda^2 = 1$  and (b)  $\lambda^2 = 0.5$ . In both cases, the PL spectrum is artificially red-shifted by  $0.6\omega_{\text{vib}}$  for clarity; otherwise, the 0–0 PL peak and the  $A_1$  absorption peak spectrally overlap.

doublet in the “0–1” region ( $\omega_{0-0} + 1350, \omega_{0-0} + 1450 \text{ cm}^{-1}$ ), a triplet in the “0–2” region ( $\omega_{0-0} + 2700, \omega_{0-0} + 2800, \omega_{0-0} + 2900 \text{ cm}^{-1}$ ) and so on. The increasing number of modes leads to increased (unresolved) line broadening, which can roughly be captured by introducing the progressive line widths,<sup>225</sup>  $\Gamma_{0-\nu} = \Gamma + \Delta\Gamma\nu$ , where  $\Gamma$  and  $\Delta\Gamma$  are fitting parameters. The progressive line width can also be extended to the case of a molecular aggregate, where the transition from the vibrationless ground state to the  $i$ th eigenstate is assigned the homogeneous line width  $\Gamma_i = \Gamma + \Delta\Gamma \langle \nu \rangle_i$ , where  $\langle \nu \rangle_i$  is the average number of vibrational quanta in state  $i$ . The vibrational quanta refer not just to the excited ( $S_1$ ) potential but also the ground state ( $S_0$ ) potential (as is important in two-particle excitations), giving

$$\langle \nu \rangle_i = \langle \psi_i | \sum_n |n\rangle \langle n| \left\{ \tilde{b}_n^\dagger \tilde{b}_n + \sum_{m \neq n} b_m^\dagger b_m \right\} | \psi_i \rangle$$

In cases where charge transfer is allowed, the expression  $\langle \nu \rangle_i$  is readily amended to also include vibrational quanta within the cationic and anionic potentials.

**4.1.4. Summary of the Vibronic Signatures of J- and H-Aggregates.** In addition to the Kasha signatures discussed in section 2, J- and H-aggregates can be further differentiated by the manner in which the Poissonian vibronic progression characterizing the monomer absorption and PL spectra changes upon aggregation. Before proceeding to the details of how vibronic coupling impacts the spectral response of molecular H- and J-aggregates, we first summarize the vibronic signatures of Coulomb-coupled H- and J-aggregates, which originally appeared in ref 14. They are as follows:

- (1) In J-aggregates (H-aggregates), the ratio of the line strengths of the first two vibronic peaks  $A_1$  and  $A_2$  in the absorption spectrum,  $I_{A_1}/I_{A_2}$ , increases (decreases) with increasing exciton bandwidth.

(2) In J-aggregates with no disorder and at temperatures low enough to ensure emission from only the lowest energy exciton, the PL ratio,  $I^{0-0}/I^{0-1}$ , is exactly  $N/\lambda^2$ , where  $N$  is the number of chromophores; in H-aggregates, the ratio is exactly zero.

Generally, in J-aggregates (H-aggregates), the PL ratio increases (decreases) as the exciton coherence number  $N_{coh}$  increases. This manifests in the following manner:

(3) In J-aggregates (H-aggregates), the ratio  $I^{0-0}/I^{0-1}$  decreases (increases) with increasing energetic disorder.

(4) In J-aggregates (H-aggregates),  $I^{0-0}/I^{0-1}$  decreases (increases) with increasing temperature.

The PL properties (2–4) properly apply to the aggregates of the current section, which assume dominant Coulomb coupling, i.e., negligible wave function overlap between neighboring chromophores. When the latter is no longer justified, as is common in molecular  $\pi$ -stacks, the emission may also derive from excimers<sup>31–36</sup> for which the PL spectrum is much further red-shifted and entirely lacks vibronic structure. In section 5, the impact of wave function overlap on the photophysical properties of H- and J-aggregates is studied in greater detail.

As an important practical matter, the line strengths appearing in the absorption and PL ratios discussed above should be evaluated from the experimental spectra via spectral integration. For example,

$$I_{A_n} \approx \int \omega^{-1} A_{n,\exp}(\omega) d\omega$$

and

$$I^{0-v} \approx \int \omega^{-3} S_{v,\exp}(\omega) d\omega$$

where  $A_{n,\exp}(\omega)$  describes the measured absorption line shape for the  $A_n$  band, and  $S_{v,\exp}(\omega)$  describes the measured PL line shape for the  $0-v$  band.

#### 4.2. Absorption and PL in Ideal H- and J-Aggregates

To understand the impact intermolecular (Coulombic) coupling makes on the absorption and emission spectrum, we begin with the simplest manifestation of H- and J-aggregates; ideal aggregates defined as linear aggregates with one molecule per unit cell and with no disorder or defects of any kind. In this section, it also proves convenient to restrict the Coulomb coupling to nearest neighbors and assume the low-temperature limit such that PL is limited to emission from just the lowest energy exciton.

**4.2.1. Impact of Increasing Exciton Bandwidth.** Fulton and Gouterman were the first to demonstrate the disparate behaviors exhibited by vibronically coupled J- and H-aggregates with increasing exciton bandwidth in their seminal study of molecular dimers ( $N = 2$ ).<sup>151</sup> Their numerical analysis revealed a blue-shift (red-shift) of the absorption spectral centroid for dimers with positive (negative) values of the excitonic coupling in accordance with Kasha's model. With respect to the overall line shapes, they concluded that "throughout the range of weak to strong coupling the negative system [i.e. J-aggregate] appears as a normal vibrational progression. However, the positive system [i.e. H-aggregate] has an erratic appearance in the intermediate coupling regime". In what follows, progress made toward placing the qualitative observations of Fulton and Gouterman on more firm theoretical grounds will be reviewed.

The impact of increasing exciton bandwidth on the absorption and PL spectra of linear J- and H-aggregates containing a sufficient number of molecules to achieve spectral

convergence was reported in ref 14. The results for aggregates containing  $N = 20$  chromophores are displayed in Figure 15. As

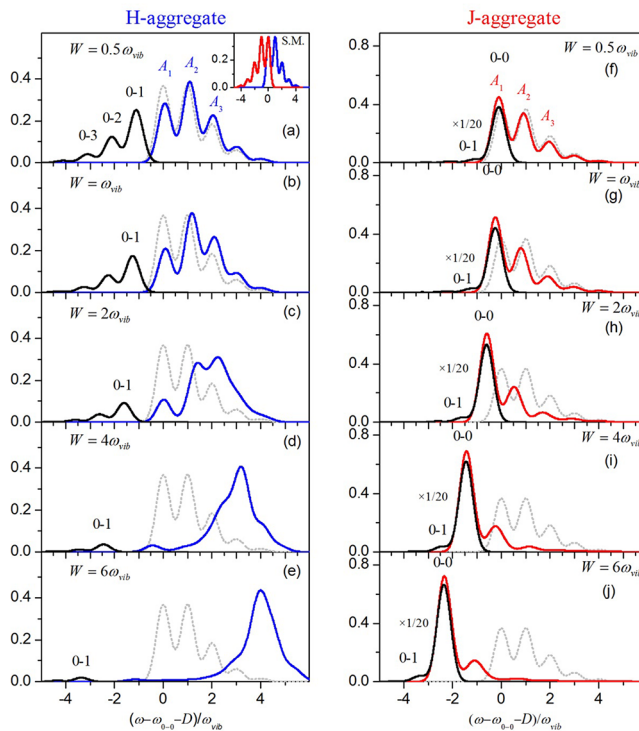


**Figure 15.** Calculated absorption (blue and red lines) and PL (black lines) spectra for linear H- and J-aggregates containing  $N = 20$  molecules as a function of increasing exciton bandwidth  $W$  (from top to bottom). For comparison, monomer absorption spectra (gray lines) are also shown in each panel. Spectra were evaluated using the Holstein Hamiltonian with open boundary conditions, nearest-neighbor coupling only, and the two-particle approximation. Aggregates contain no disorder, and PL is assumed to originate only from the lowest energy exciton ( $T = 0$  K). As in the dimer calculations of Fulton and Gouterman reported in ref 151, the HR factor was set to  $\lambda^2 = 1$ ; the reported spectra are "reduced" (see section 4.1.3), and the homogeneous line shape function was taken to be Gaussian (with standard deviation,  $\Gamma_h = 0.28\omega_{vib}$ ). Note that the PL spectra for the J-aggregates have been scaled by 1/20. Adapted with permission from ref 14. Copyright (2010), American Chemical Society.

with the dimer spectra of Fulton and Gouterman, the calculated spectra are based on a Holstein-style Hamiltonian with an HR factor of unity ( $\lambda^2 = 1$ ). Hence, in the monomer limit ( $N = 1$ ), the first two vibronic peaks in either the absorption or PL spectrum have identical peak intensities (see Figure 14a and the inset of Figure 15a), making it easier to discern the impact of intermolecular coupling. Finally, the calculated spectra in Figure 15 assume aggregates with n.n. coupling only ( $J_C$ ) and with open boundary conditions. Although the exciton bandwidth under open boundary conditions is size dependent,  $W = 4|J_C|\cos[\pi/(N + 1)]$ , it is sufficiently converged to  $W \approx 4|J_C|$  when  $N = 20$ . In the figure,  $W$  increases from the weak exciton coupling regime ( $W \ll \lambda^2\omega_{vib}$ ) to the strong coupling regime ( $W \gg \lambda^2\omega_{vib}$ ), where the coupling regimes are consistent with McRae's interpretation<sup>152</sup> of the Simpson and Peterson condition,<sup>301</sup> which compares the exciton bandwidth  $W$  to the vibronic bandwidth of the monomer. Jablonski-style energy level diagrams showing the various optical transitions which contribute to absorption and emission are shown in

Figure 16 for the weak coupling regime, where vibronic bands are still resolvable, and the strong coupling regime, where vibronic structure is largely lost (see section 3.4).

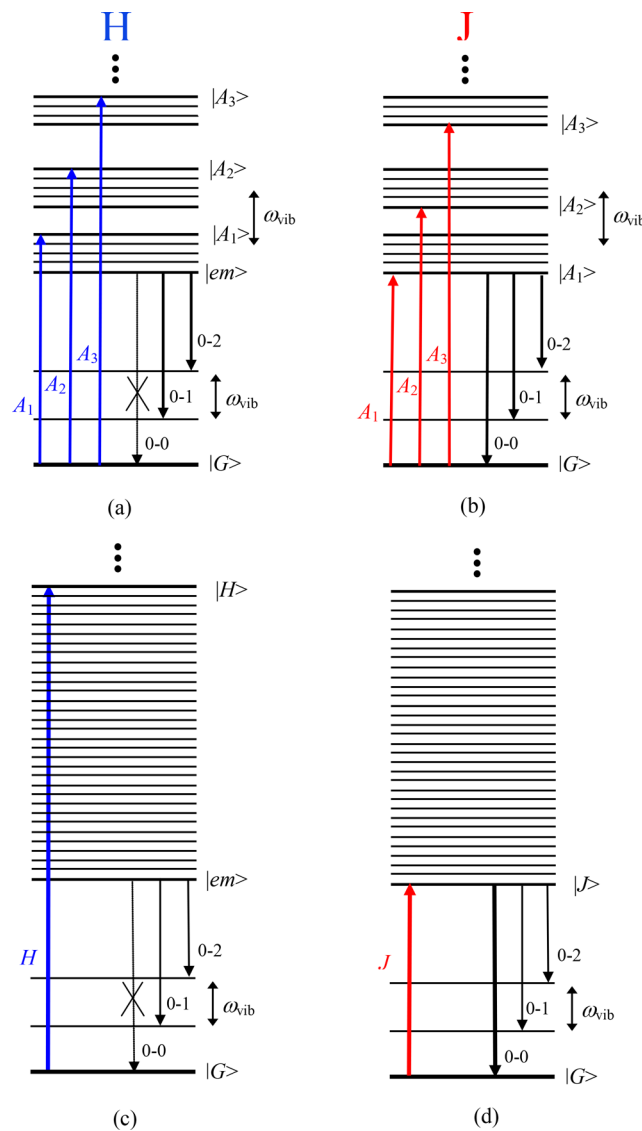


**Figure 16.** Energy level diagrams depicting absorption (blue arrows for H, red arrows for J) and emission (back arrows) in ideal H- and J-aggregates in the weak exciton coupling regime (a,b) and the strong exciton coupling regime (c,d). Adapted with permission from ref 14. Copyright (2010), American Chemical Society.

**Kasha Signatures.** Before discussing vibronic signatures, we pause to consider the Kasha signatures for H- and J-aggregates based on spectral shifts and radiative decay rates. As the bandwidth  $W$  increases in Figure 15, the main absorption peak increasingly red-shifts for J-aggregates and blue-shifts for H-aggregates (relative to  $\omega_{0-0} + D$ ) in agreement with the predictions of Kasha.<sup>20–24</sup> One can also consider the shift of the spectral centroid or “center of gravity”. As shown for dimers by Fulton and Gouterman<sup>151</sup> and Wikowski and Moffit,<sup>156</sup> and generalized for aggregates containing an arbitrary number of chromophores by Briggs and Herzenberg<sup>162</sup> and Gisslen and Sholz,<sup>214</sup> the spectral centroid is given by,

$$\langle E \rangle = \frac{\sum_i |\langle G | \hat{M} | \psi_i \rangle|^2 \omega_i}{\sum_i |\langle G | \hat{M} | \psi_i \rangle|^2} = \omega_{0-0} + D + J_{k=0} + \lambda^2 \omega_{\text{vib}} \quad (51)$$

which is strictly valid for aggregates with periodic boundary conditions (or large aggregates with open boundary conditions). When only n.n. coupling is included, as in the aggregates in Figure 15, then  $J_{k=0} = 2J_C$  in eq 51. (For dimers,  $J_{k=0} = J_C$ .) Further analysis shows that, in the strong exciton coupling limit (see section 4.2.5), the peak of the absorption spectrum approaches the spectral centroid, as can be appreciated from Figure 15e,j (see also Figure 17e,j). In this

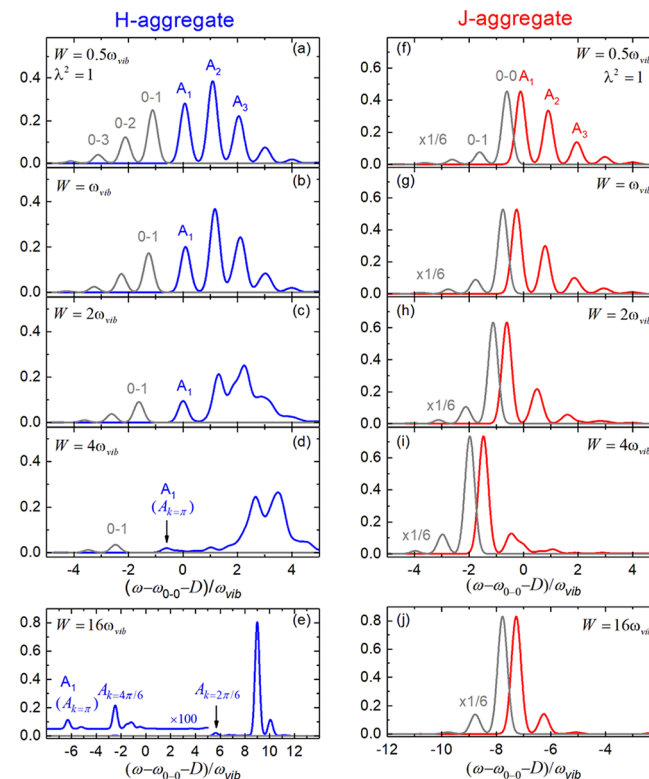


**Figure 17.** Calculated absorption and PL spectra for H- and J-aggregates containing  $N = 6$  molecules as a function of increasing exciton bandwidth (from top to bottom). Spectra were evaluated using the Holstein Hamiltonian with periodic boundary conditions, nearest-neighbor coupling only, and the three-particle approximation. As in Figure 15, the HR factor is set to  $\lambda^2 = 1$ , but the homogeneous line width,  $\Gamma_h = 0.18\omega_{\text{vib}}$ , is slightly smaller. Note that the J-aggregate PL spectrum is scaled by 1/6 and artificially red-shifted from the absorption spectrum for enhanced clarity (without the shift, the 0–0 PL peak exactly overlaps the  $A_1$  absorption peak). The HT peaks appearing in the strongly coupled H-aggregate are labeled in panels (d) and (e).

limit, the spectral shift consists of the free-exciton shift,  $J_{k=0}$ , introduced in section 2, plus an extra blue-shift given by  $\lambda^2 \omega_{\text{vib}}$ , which derives from the vertical nature of the transition and the fact that when the exciton coupling is strong the excitation cannot relax in the excited state potential before being transferred to a neighbor.

The Kasha signatures regarding radiative emission are also evident in aggregates with vibronic coupling. For the steady-state PL spectra in Figure 15, emission is assumed to originate solely from the lowest energy exciton in accordance with Kasha’s rule,<sup>26</sup> strictly valid when the temperature is sufficiently

low. The PL transitions are indicated by the black arrows in Figure 16. As is apparent from Figure 15, the PL spectral line shapes for J- and H-aggregates differ dramatically, reflective of the natures of the emitting  $k = 0$  and  $k = \pi$  excitons that define the band-bottom states in J- and H-aggregates, respectively, independent of vibronic coupling (see section 3.4). In J-aggregates, the band-bottom exciton provides the origin for both absorption and emission, as demonstrated in Figure 16b and d. As a result, the  $A_1$  absorption peak and 0–0 emission peak lie on top of each other in Figure 15f–j, so that ideally there is no Stokes shift. Because of the in-phase nature of the emitting dipoles in the  $k = 0$  state, the 0–0 peak is maximized in J-aggregates and enhanced by a factor of  $N$ , ultimately due to the  $\sqrt{N}$  enhancement of the transition dipole moment,<sup>23</sup> which is then squared to give  $I^{0-0}$ , see eq 43. (Note that the J-aggregate PL spectra are scaled by  $1/N$  in Figure 15.) As discussed at greater length below, a more detailed treatment gives  $I^{0-0} = FN$ , where the generalized Franck–Condon factor  $F$  ranges from  $\exp(-\lambda^2)$  to  $\exp(-\lambda^2/N)$  in going from the weak to strong exciton coupling regimes, thereby accounting for the increase in  $I^{0-0}$  with  $W$  in Figure 15f–j. Interestingly, the radiative decay rate  $\gamma$  depends (approximately) on the sum,  $\sum_\nu I^{0-\nu}$ , and therefore only receives an  $N$ -fold coherent enhancement from the 0–0 component, as the sidebands are largely incoherent, as discussed in section 4.1. Thus, whenever the 0–0 intensity dominates, as in the J-aggregates of Figure 15f–j,  $\gamma$  will also scale with  $N$ , leading to the characteristic superradiance observed from J-aggregates at low temperatures.<sup>38–47</sup>

In marked contrast, the 0–0 transition in ideal H-aggregates is strictly forbidden due to the cancellation of dipole moments in the band-bottom state with  $k = \pi$ . Hence, the 0–0 peak is entirely suppressed in Figure 15a–e, preventing any coherent emission (superradiance). In ideal H-aggregates, the highest energy component of the PL spectrum is therefore the 0–1 sideband. The substantial Stokes shift arises not only from the lack of any 0–0 peak but also because the origins for emission and absorption now involve different excitons as seen in the energy level diagrams of Figure 16a and c.

**Vibronic Signatures.** Figure 15 also reveals additional vibronic signatures of J- and H-aggregation as manifested primarily by deviations of the relative vibronic peak intensities from the Poissonian distribution characteristic of unaggregated molecules shown in the figure inset (see also Figure 14). As the exciton bandwidth ( $W$ ) increases, the ratio of the line strengths of the first two vibronic peaks in the absorption spectrum<sup>14,91,144,146,147</sup>

$$R_{\text{abs}} \equiv I_{A_1}/I_{A_2} \quad (52)$$

increasingly deviates from the monomer value of  $1/\lambda^2$  ( $= 1$  in Figure 15). As demonstrated in Figure 15, in J-aggregates  $R_{\text{abs}}$  increases monotonically relative to the monomer value with increasing bandwidth  $W$ , whereas in H-aggregates, the ratio decreases with  $W$ . In H-aggregates, clear vibronic progressions become obscured in the intermediate exciton coupling regime, whereas in J-aggregates, the vibronic peaks remain discernible throughout, as originally noted by Fulton and Gouterman in their work on molecular dimers.<sup>151</sup> In the strong coupling regime, the vibronic structure is suppressed as the aggregate spectrum becomes dominated by a single peak (see Figure 15e,j), which is strongly red-shifted (blue-shifted) in J- (H-) aggregates. The evolution of the aggregate spectrum with  $W$

just described is consistent with the analyses of Roden et al.<sup>171</sup> and Seibt et al.<sup>174</sup>

Panels f–j in Figure 15 further reveal a peculiar effect regarding the PL spectral line shape in J-aggregates. The PL ratio,  $R_{\text{PL}}$ , defined by

$$R_{\text{PL}} \equiv I^{0-0}/I^{0-1} \quad (53)$$

is remarkably constant and approximately equal to 20 ( $= N$ ) throughout the entire range of exciton couplings. For J-aggregates, the constancy of  $R_{\text{PL}}$  was proven analytically in ref 176, where it was shown that  $R_{\text{PL}}$  was exactly equal to  $N/\lambda^2$ , independent of exciton bandwidth in ideal J-aggregates with periodic boundary conditions. In addition, the temperature must be sufficiently low to ensure emission from only the lowest energy exciton (as is assumed in Figure 15f–j). The slight deviation in  $R_{\text{PL}}$  from  $N/\lambda^2$  in the figure (independent of  $W$ ) is due to open boundary conditions. The unusual behavior of  $R_{\text{PL}}$  in J-aggregates is discussed in greater detail in section 4.2.4 and forms the basis for obtaining the steady-state exciton coherence length directly from the PL spectrum (see section 4.5).

In sharp contrast, the PL spectra for the ideal H-aggregates of Figure 15a–e lack a 0–0 component entirely ( $R_{\text{PL}} = 0$ ) due to the symmetry of the  $k = \pi$  emitting exciton.<sup>288,298</sup> Moreover, although the remaining bands in the vibronic progression (0–1, 0–2, ...) are symmetry-allowed, they vanish with increasing excitonic coupling. In the strong coupling limit, the emitting exciton behaves like a “free” exciton in the simple Kasha model of section 2, and the emission vanishes.

An interesting observation revealed in the J-dimer ( $N = 2$ ) spectra of Fulton and Gouterman<sup>151</sup> is the recovery of mirror-image symmetry between the absorption and PL spectra in the strong coupling limit but with an “apparent” HR factor reduced by 1/2. Despite setting  $\lambda^2 = 1$  (which predicts equal intensities for the first two vibronic peaks in the monomer absorption spectrum, see Figure 14a), the strongly coupled J-dimer spectrum in ref 151 shows the  $A_2$  peak to be exactly one-half as large as the  $A_1$  peak, and the  $A_3$  peak to be one-eighth as large as if the HR factor itself was reduced to 1/2. A similar transformation happens in the PL spectrum, thereby maintaining mirror-image symmetry as well as a Poissonian distribution of peak intensities. The behavior revealed in Fulton and Gouterman’s calculations apparently contradicts what is observed in Figure 15f–j for  $N = 20$  J-aggregates; mirror-image symmetry is clearly not recovered, at least within the range of exciton couplings considered. To test whether the recovery of mirror-image symmetry is a finite size and/or boundary condition effect, the spectra were recalculated for much smaller aggregates containing just  $N = 6$  molecules and with periodic boundary conditions. The results are shown in Figure 17. (Here, the absorption and PL spectra for J-aggregates were artificially separated by a small frequency shift to better distinguish them.) Note the recovery of mirror-image symmetry for the J-aggregate having the largest Coulomb coupling, but with absorption and PL Poissonian progressions described by an “effective” HR factor of 1/6, i.e., reduced by  $N$  from the actual HR factor ( $\lambda^2 = 1$ ). The  $N$ -fold reduction in the HR factor is entirely consistent with the dimer ( $N = 2$ ) results of Fulton and Gouterman. A more subtle observation of Figure 17f–j concerns the form of the PL vibronic progression. Although as noted earlier, the PL ratio,  $R_{\text{PL}}$ , is always  $N/\lambda^2$  independent of  $W$ , it is only in the very strong exciton coupling limit that the entire progression becomes Poissonian with an

effective HR factor of  $\lambda^2/N$ , i.e., with the relative line intensities obeying

$$I^{0-v} \approx Ne^{-\lambda^2/N} \frac{(\lambda^2/N)^v}{v!}$$

The absorption spectrum similarly abides by a Poissonian with an effective HR factor reduced  $N$ -fold. Interestingly, the absorption spectrum for H-aggregates in Figure 17 is also well described with an effective HR factor of  $\lambda^2/N$  when the excitonic coupling is very strong but with a vanishing PL spectrum. We will revisit the ultrastrong coupling regime in section 4.2.5, where a full account of mirror-image recovery is given. At this point, we simply point out that the reason why mirror-image symmetry is not recovered for the J-aggregates in Figure 15 is that the maximum coupling reported is not large enough.

#### 4.2.2. J- vs H-Vibronic Signatures: Selected Examples.

The PIC absorption spectrum measured by Scheibe in Figure 11 is perhaps the earliest example demonstrating the profound impact of intermolecular interactions on the Poissonian vibronic progression characterizing the monomer spectrum. The J- and H-like vibronic features are described in greater detail in section 4.6, where the effects of having two molecules per unit cell are included for a proper account. Although many other examples of vibronic J- and H-aggregates abound in the literature, in this section we highlight just a few that demonstrate some of the vibronic signatures discussed so far.

The UV-vis spectra of a series of linear perylene-3,4:9,10-bis(dicarboximide) complexes (monomer, dimer, and trimer) measured by Langhals et al.<sup>302,303</sup> are shown in Figure 18. As is readily discerned, the spectra red-shift and  $R_{abs}$  increases significantly as the number of PDI units increases from  $N = 1$  to  $N = 3$  as expected for J-aggregates. A similar trend was observed by Wilson et al.<sup>80</sup> In such complexes, torsional rotations of near

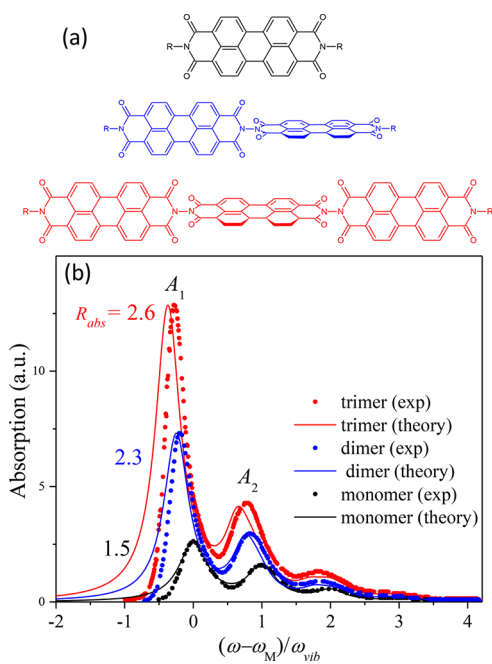


**Figure 18.** (a) A series of PDI complexes along with (b) their measured absorption spectra from ref 302. Also shown are the calculated spectra from ref 79. Adapted with permission from ref 79. Copyright (2012), American Chemical Society.

90° between neighboring perylene chromophores break the  $\pi$ -conjugation, restricting the interchromophoric interactions to be mainly Coulombic. As the  $S_0 \rightarrow S_1$  transition dipole moment in a single PDI chromophore is oriented along the long-molecular axis, the linear complexes can be described as head-to-tail-oriented J-aggregates. Indeed, the calculated nearest neighbor Coulombic coupling based on atomic transition charge densities is negative,  $J_C \approx -0.06$  eV.<sup>79</sup> The red-shift and increase in  $R_{abs}$  with increasing  $N$  are therefore signatures of increasing exciton bandwidth in J-aggregates; the free-exciton bandwidth is zero in the monomer,  $2J_C$  in the dimer, and  $2\sqrt{2}J_C$  in the trimer. To demonstrate this quantitatively, Figure 18 also shows the calculated spectra of Pochas et al.<sup>79</sup> using the Frenkel–Holstein Hamiltonian in eq 13 under the two-particle approximation with Coulombic couplings evaluated using atomic transition charge densities. The theory accurately captures the increasing spectral red-shift and ratio,  $R_{abs}$ , in going from the monomer to trimer.

As shown by Yoo et al.,<sup>78</sup> the steady-state PL spectrum of a linear trimer PDI complex similar to that investigated by Langhals in Figure 18 also conforms to what is expected for J-aggregates:  $R_{PL}$  is several times larger in the trimer complex compared to monomeric PDI. Yoo et al. also obtained effective monomer, dimer, and trimer emission spectra via sequential photobleaching of linear trimers and found that the ratio of the 0–0 and 0–1 spectral intensities,  $S_{exp}^{0-0}/S_{exp}^{0-1}$ , approximately triples in going from the monomer to the trimer, as observed in Figure 19, and in good agreement with theory. Note also the increasing red-shift in going from the monomer to trimer, as expected for J-aggregates. The PL ratio,  $R_{PL}$ , is obtained from the measured intensity ratio,  $S_{exp}^{0-0}/S_{exp}^{0-1}$  using

$$R_{PL} \approx (S_{exp}^{0-0}/S_{exp}^{0-1})(\omega_{0-1}/\omega_{0-0})^3$$

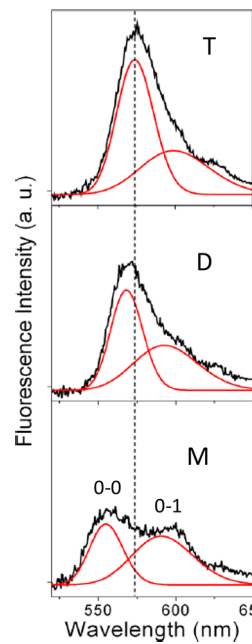


**Figure 19.** Single-molecule PL spectra obtained via sequential photobleaching of a linear PDI trimer complex. From top to bottom: emission from the entire trimer (T), a dimer portion (D), and a monomer portion (M). Adapted with permission from ref 78. Copyright (2012), American Chemical Society.

Recall that  $R_{PL}$  is a ratio of the line strength alone, requiring the cubic frequency dependence to be removed from the measured intensity ratio. On the basis of Yoo et al.'s data,  $R_{PL} \approx 2.6$  for the trimer, smaller than the ideal theoretical value of  $N/\lambda^2 = 5$  (using  $\lambda^2=0.6$  obtained from the monomer spectrum). Much of the discrepancy arises from the open boundary conditions inherent to the trimer as well as thermal effects;  $R_{PL}$  is  $N/\lambda^2$  only for aggregates with periodic boundary conditions and at temperatures low enough to neglect emission from thermally excited excitons (see section 4.4 for a discussion of thermal effects). End effects can be considered as a type of disorder that reduces  $R_{PL}$  relative to  $N/\lambda^2$  by roughly 20%. In addition, Yoo's measurements were made at room temperature. From the calculated exciton bandwidth, the separation between the lowest two excitons in the trimer is on the order of  $k_B T$  at room temperature, so that the emitting exciton population is reduced by a factor of  $\sim 0.7$ , which together with the reduction factor of  $\sim 0.8$  arising from the boundary condition brings the measured value of  $R_{PL}$  in line with theoretical predictions.

One might further expect that the same PDI chromophores bound covalently in a cofacial "side-by-side" orientation should result in H-aggregates with opposing spectral signatures to the J-aggregates in Figure 18. There are many examples in the literature showing that this is indeed the case.<sup>31,35,77,141,304–306</sup> A particularly striking demonstration was provided by Margulies et al.<sup>35</sup> who synthesized PDI dimer complexes with the two chromophores linked covalently by a triptycene bridge. Figure 20 shows two such complexes, one that is cofacial (panel

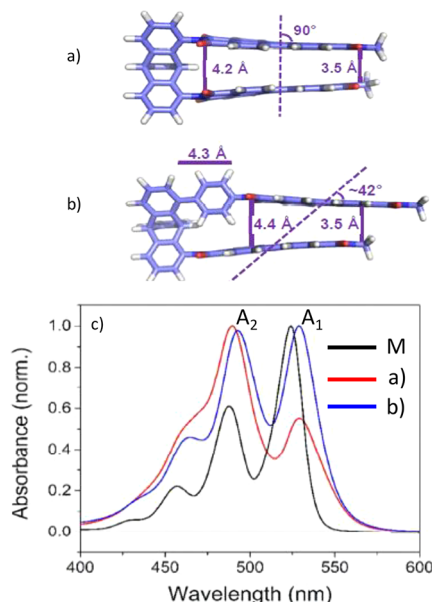


**Figure 20.** Cofacial (a) and slipped (b) triptycene-linked PDI complexes from ref 35. (c) The corresponding absorption spectra along with the monomer (M) spectrum. Reproduced with permission from ref 35. Copyright 2014, PCCP Owner Societies.

a) and another that is slipped along the long PDI axis (panel b). Panel c shows the associated absorption spectra along with the PDI monomer spectrum. In contrast to the head-to-tail PDIs of Figure 18, the ratio  $R_{abs}$  for the cofacial dimer is substantially reduced compared to the monomer value as expected for H-aggregates. The "inversion" of the 0–0 and 0–1 peak intensities relative to the monomer has been noted for some time and has been effectively used by A.D.Q. Li and co-workers to probe

DNA folding.<sup>305,306</sup> Using DFT and including several vibrational modes, Clark et al. linked the ratio inversion to exciton coupling in H-aggregates.<sup>307</sup>

Interestingly, although the slipped dimer in Figure 20 shows an increase in  $R_{abs}$  compared to that of the cofacial dimer consistent with a decrease in the Coulombic coupling, the ratio remains smaller than the monomer value. Hence, the slipped dimer is also H-like. However, for the closely spaced dimers in Figure 20, one cannot discount the possible contribution of short-range, charge-transfer-mediated couplings due to wave function overlap, consistent with the observation of excimer emission from the dimers in Figure 20.<sup>35</sup> As discussed at length in section 5, the decrease in  $R_{abs}$  upon dimerization remains a steadfast signature for H-aggregation independent of the nature of the electronic coupling; vibronic signatures are more reliable indicators of H- (or J-)aggregation than are spectral shifts.

We conclude this section with one of the most celebrated H-aggregates:  $\pi$ -stacks of poly(3-hexylthiophene) chains, which form in films spin-cast from solution.<sup>143–147</sup> Figure 21 shows

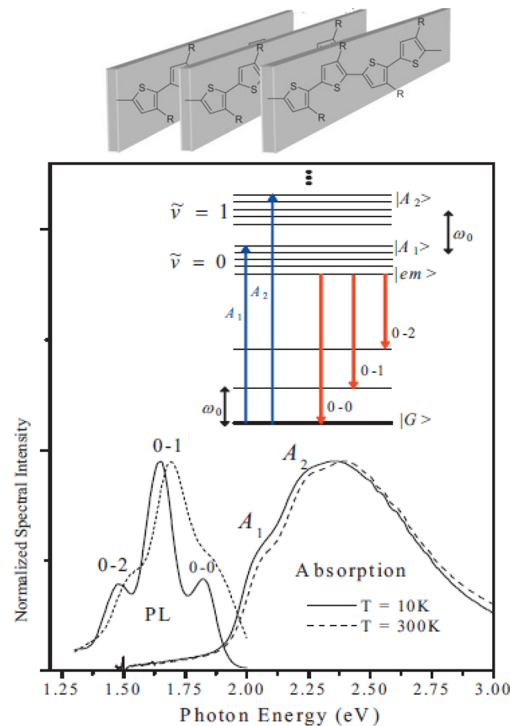


**Figure 21.** Absorption and PL spectra of P3HT aggregates from ref 145 at two temperatures. Inset shows the absorption and emission transitions for an H-aggregate. Reprinted from ref 145 with the permission of AIP Publishing.

the absorption and PL spectra measured at two temperatures: 10 and 300 K. The HR factor is approximately unity as determined from the PL spectrum of unaggregated P3HT molecules in solution (not shown).<sup>144,145</sup> In Figure 21, both  $R_{abs}$  and  $R_{PL}$  are significantly less than  $1/\lambda^2 (=1)$  as expected for H-aggregates. Moreover, the PL ratio increases with temperature, which is also characteristic of H-aggregates as discussed in section 4.4. Detailed analysis of the PL spectrum further shows that exciton coherence is spread over approximately three chains.<sup>145</sup>

**4.2.3. Weak Excitonic Coupling: Ratio Formula for Absorption.** As discussed in section 3.4, in the weak exciton coupling regime ( $W \lesssim \lambda^2 \omega_{vib}$ ) the aggregate excited states are

organized into vibronic bands, where each band contains states with a total of  $\nu_t$  vibrational quanta as depicted in the energy level diagram of Figure 7. Such a band structure is responsible for vibronic progressions in the absorption and emission spectrum, but the relative band intensities do not abide by a Poissonian distribution as they do for unaggregated molecules, and the deviations are markedly different for J- and H-aggregates as detailed in refs 14, 15, 143–147, 176, and 242. Perhaps the most well-studied examples of weak excitonic coupling are  $\pi$ -stacks of conjugated polymers such as P3HT,<sup>143–147</sup> where the exciton coupling is compromised due to the extended nature of the transition dipole moment, the associated intermolecular Coulomb coupling actually diminishes with increasing conjugation length when the polymers are separated by distances comparable to or smaller than the conjugation length (see also Figure 4 and surrounding text).<sup>125,219,272–274</sup>

In what follows, we outline the key steps in the derivation of a ratio formula, an analytical expression for  $R_{\text{abs}}$  in eq 52 valid for weakly coupled J- and H-aggregates following closely the development in ref 147. Treating the exciton coupling term in the Holstein Hamiltonian in eq 13 as a perturbation results in zero-order eigenfunctions in which the total number of vibrational quanta is constant, consistent with the band structure in Figure 7. In the lowest vibronic bandwidth  $\nu_t = 0$ , the zeroth order wave functions are given by the single-particle excitons

$$|k, \nu_t = 0\rangle^{(0)} = |k, \tilde{\nu} = 0\rangle \quad (54)$$

where the states  $|k, \tilde{\nu}\rangle$  are defined in eq 16. In the higher vibronic bands with  $\nu_t \geq 1$ , the zeroth order wave functions can admix with resonant two-particle states containing the same total number of vibrational quanta. For example, in the  $\nu_t = 1$  band the bright, single-particle exciton  $|k = 0, \tilde{1}\rangle$  admixes with two-particle excitons of the form<sup>147</sup>

$$\frac{1}{\sqrt{2}}\{|k = 0, \tilde{0}; s, 1\rangle + |k = 0, \tilde{0}; -s, 1\rangle\}$$

to create  $N/2 + 1$  zero-order states (when  $N$  is even). The intrinsically dark two-particle states can therefore borrow oscillator strength from the optically bright single particle state (when  $k = 0$ ), somewhat akin to the Fermi resonances in infrared spectroscopy.<sup>147</sup> This leads to generally  $(N/2)\nu_t + 1$  closely spaced peaks in the spectral region approximately  $\nu_t$  vibrational quanta above the absorption origin. Such fine structure is not discernible in Figure 15 because the associated splittings are much smaller than the line width used in the homogeneous Gaussian line shape function ( $\Gamma_h = 0.18 \omega_{\text{vib}}$ ). As shown in ref 147, in the weak exciton coupling limit, the single-particle approximation can be used to determine the total line strength for each vibronic band, allowing a quantitative evaluation of how the line strength is redistributed among the vibronic bands with increasing excitonic coupling. Accordingly, the ratio,  $R_{\text{abs}}$ , defined in eq 52 abides by<sup>147</sup>

$$R_{\text{abs}} \approx \frac{[1 - e^{-\lambda^2} G(0; \lambda^2) J_{k=0}/\omega_{\text{vib}}]^2}{\lambda^2 [1 - e^{-\lambda^2} G(1; \lambda^2) J_{k=0}/\omega_{\text{vib}}]^2} \quad (55)$$

where  $J_{k=0} = \sum_n J_{m,n}$  is the  $k = 0$  component of free-excitonic coupling in eq 5, and the vibronic function  $G(\nu_t; \lambda^2)$  is defined as

$$G(\nu_t; \lambda^2) \equiv \sum_{u=0,1,2,\dots} \frac{\lambda^{2u}}{u!(u - \nu_t)} \quad (u \neq \nu_t) \quad (56)$$

Figure 22a shows how  $\exp(-\lambda^2)G(0; \lambda^2)$  and  $\exp(-\lambda^2)G(1; \lambda^2)$  vary with  $\lambda^2$ .

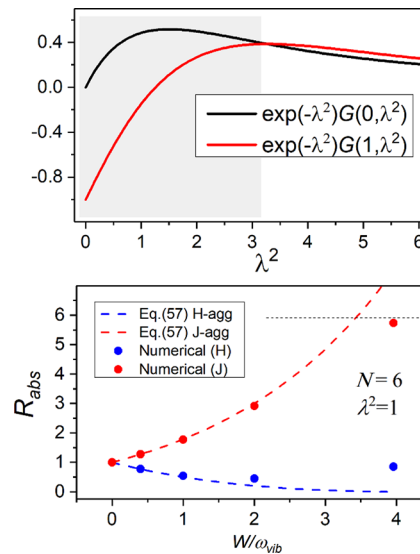


Figure 22. (top) The dependence of the vibronic functions shown in the inset on the HR factor. The gray shaded regions correspond to  $G(1; \lambda^2) < G(0; \lambda^2)$ . (bottom) The absorption ratio  $R_{\text{abs}}$  as a function of exciton bandwidth for the J- and H-aggregates of Figure 17 evaluated numerically (dots) and using eq 57 (or 55).

Eq 55 shows that whenever  $G(1; \lambda^2) < G(0; \lambda^2)$ , the ratio  $R_{\text{abs}}$  decreases with increasing exciton coupling in H-aggregates ( $J_{k=0} > 0$ ) and increases with increasing exciton coupling in J-aggregates ( $J_{k=0} < 0$ ). Figure 22a shows that the “ratio rule” for absorption in H- and J-aggregates holds over a substantial range of HR factors,  $\lambda^2 < 3.26$ , as indicated in the gray-shaded region. This range includes most vibrational modes of interest for organic molecules and in particular the ubiquitous vinyl stretching mode in conjugated molecules where  $\lambda^2$  is of order unity. Interestingly, beyond this range,  $G(1; \lambda^2) \approx G(0; \lambda^2)$  and  $R_{\text{abs}}$  reverts back to the monomer value,  $1/\lambda^2$ . The monomer value also derives from eq 55 when the Coulomb coupling is zero.

When the Coulomb coupling is restricted to nearest neighbors,  $J_{k=0}$  in eq 55 can be replaced by  $W/2$  ( $-W/2$ ) in H-aggregates (J-aggregates) where  $W$  is the free-exciton bandwidth from eq 7. If, in addition,  $\lambda^2$  is taken to be unity, eq 55 reduces to<sup>146,147</sup>

$$R_{\text{abs}} \approx \frac{[1 \pm 0.24W/\omega_{\text{vib}}]^2}{[1 \mp 0.073W/\omega_{\text{vib}}]^2} \quad \lambda^2 = 1 \quad (57)$$

where the lower sign applies to H-aggregates while the upper sign applies to J-aggregates. The H-form of eq 57 first appeared in an analysis of P3HT aggregates in refs 143–147. The validity of eq 57 is demonstrated in Figure 22b for the numerical data corresponding to Figure 17 where  $\lambda^2 = 1$ ; the figure shows that the ratio formula works well for both J- and H-aggregates when  $W \gtrsim \omega_{\text{vib}}$ . Finally, in addition to changes in the vibronic peak intensities, exciton coupling also disrupts the regular spacing of the peaks comprising the vibronic progression. In the

perturbation regime, small corrections to the peak positions have been reported in refs 91 and 147.

The ratio formulas in eqs 55 and 57 are strictly valid for aggregates with periodic boundary conditions and for sufficiently large aggregates that the boundary condition (i.e., open or periodic) is unimportant. Simple molecular dimers also abide eqs 55 and 57 with  $J_{k=0} = J_C$ . For small aggregates beyond the dimer, open boundary conditions lead to slight deviations from the ratio formula in eq 55 as discussed in detail by Pochas et al.<sup>79</sup> Importantly, the ratio formulas are remarkably robust to disorder, for example, the site-energy deviations responsible for inhomogeneous broadening. This arises because the terms in the Hamiltonian which represent site disorder can only mix states within a given vibronic band (see section 4.3.2); hence, disorder leads to line broadening but virtually no oscillator strength “sharing” among the vibronic bands. In principle the ratio formula can be used to obtain the generally size-dependent exciton coupling  $J_{k=0}$  containing extended interactions even when disorder is significant. The impact of off-diagonal disorder affecting the intermolecular couplings on  $R_{\text{abs}}$  has not yet been investigated, although to a first approximation it may require a simple replacement of  $J_{k=0}$  with its mean value in eq 55.

The simplicity of the ratio formulas in eqs 55 and 57 has led to their widespread use for extracting the free-exciton bandwidth in a variety of aggregate systems including P3HT  $\pi$ -stacks,<sup>143–147</sup> MEH-PPV assemblies,<sup>308</sup> polydiacetylene chains,<sup>243,249</sup> carotenoid aggregates,<sup>91</sup> and perylene diimide complexes.<sup>79,309</sup> It should be emphasized, however, that in its most general form, the ratio formula in eq 55 is sensitive to  $J_{k=0}$  and not the exciton bandwidth  $W = |J_{k=0} - J_{k=\pi}|$ . The dependence on  $W$  as it occurs in eq 57 is only valid under the n.n. only approximation.

**4.2.4. Ratio Rule for PL in J-Aggregates.** Perhaps the most intriguing feature present in Figures 15 and 17 is the invariance of  $R_{\text{PL}}$ , the ratio of the 0–0 and 0–1 PL line strengths in eq 53, to the exciton bandwidth in J-aggregates. As shown in ref 176 for ideal J-aggregates with periodic boundary conditions, the PL ratio satisfies

$$R_{\text{PL}} = \frac{N}{\lambda^2} \quad \text{J-aggs} \quad (58)$$

The expression further requires the temperature to be sufficiently low so that only the lowest energy ( $k = 0$ ) exciton is thermally populated during emission. Quite remarkably, eq 58 holds throughout the entire phase space ( $W, \lambda^2, \omega_{\text{vib}}$ ) defining the Holstein Hamiltonian. As a purely practical application, eq 58 serves as a reliable check of approximate treatments of the Holstein Hamiltonian.

The invariant behavior of  $R_{\text{PL}}$  was not yet realized in ref 14, where the association of  $R_{\text{PL}}$  with  $N/\lambda^2$  was assumed to be limited to the strong exciton coupling regime only. This was partly because in Figure 15 (which is Figure 4 of ref 14) open boundary conditions were taken so that  $R_{\text{PL}}$  is then slightly smaller than  $N/\lambda^2$ . (In effect, the open boundary conditions serve as a type of disorder that localizes the exciton.) This is clearly not the case for the  $N = 6$  J-aggregates in Figure 17f–j, where periodic boundary conditions are taken. As is readily discernible from the figure,  $R_{\text{PL}}$  is exactly 6 (=  $N/\lambda^2$ ) independent of exciton bandwidth.

The proof of eq 58 for arbitrary  $W^{176}$  is straightforward in the exciton–phonon basis set defined in eq 21. In this basis set,

the emitting band-bottom exciton in J-aggregates,  $|\psi_{\text{em}}\rangle$ , is generally represented by

$$|\psi_{\text{em}}\rangle = |\tilde{0}\rangle \otimes \sum'_k c_{k; n_{q_1}, n_{q_2}, \dots}^{\text{em}} |k; n_{q_1}, n_{q_2}, \dots, n_{q_{N-1}}\rangle \quad (59)$$

where the prime on the summation restricts the values of the exciton wave vector  $k$  and the phonon occupation numbers,  $n_{q_i}$ , to those satisfying the condition for zero total quasi-momentum  $\kappa$ , i.e.,

$$\kappa = k + \sum_l n_{q_l} q_l = 0$$

On the basis of the wave function in eq 59, the 0–0 and 0–1 emission strengths satisfy the simple exact relationships<sup>176</sup>

$$I^{0-0} = FN \quad (60)$$

$$I^{0-1} = F\lambda^2 \quad (61)$$

where  $F$  is the generalized Franck–Condon factor, which in the exciton–phonon basis set takes on the form

$$F \equiv e^{-\lambda^2/N} |c_{k=0, \dots, 0}^{\text{em}}|^2 \quad (62)$$

$F$  is very sensitive to the exciton bandwidth, varying from  $\exp(-\lambda^2)$  in the weak exciton coupling limit to  $\exp(-\lambda^2/N)$  in the strong exciton coupling limit. Eqs 60 and 61 underscore the unique sensitivity of just the 0–0 emission to exciton coherence; only  $I^{0-0}$  is enhanced by a factor of  $N$  (see also section 4.1), leading to superradiance. In marked contrast, the 0–1 emission has no coherence enhancement. Quite conveniently, the factor  $F$ , which carries the strong dependence on exciton bandwidth, cancels out when eq 60 is divided by eq 61, yielding the ratio rule in eq 58.

The invariance of  $R_{\text{PL}}$  to exciton bandwidth embodied in eq 58 is more dramatically demonstrated in Figure 23, where the

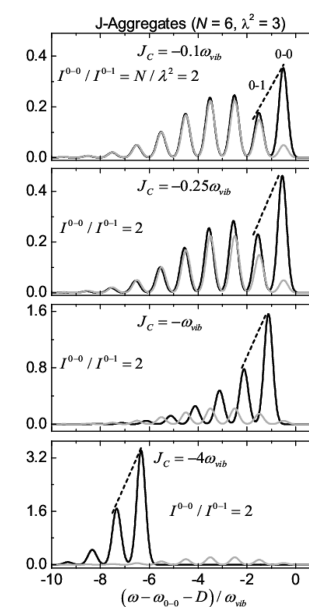


**Figure 23.** Reduced PL spectra for disorder-free J-aggregates at  $T = 0$  K as a function of increasing exciton coupling (top to bottom) evaluated using the Holstein Hamiltonian under the three-particle approximation.  $R_{\text{PL}}$  is completely independent of the coupling and equal to  $N/\lambda^2$ . For reference, the monomer PL spectrum is also shown in gray.

HR factor is increased to  $\lambda^2 = 3$  for the aggregates with  $N = 6$ . In going from the top to bottom panel, the factor of  $F$  increases from  $\sim e^{-3}$  to  $\sim e^{-1/2}$  (because  $\lambda^2/N = 1/2$ ) causing both the 0–0 and 0–1 intensities to increase by over an order of magnitude. However, the ratio  $R_{PL}$  remains steadfast and is exactly equal to  $N/\lambda^2$  ( $= 2$ ) for all values of the exciton coupling.

The ratio formula in eq 58 is further demonstrated in Figure 24a and c for J-aggregates with two different HR factors but the

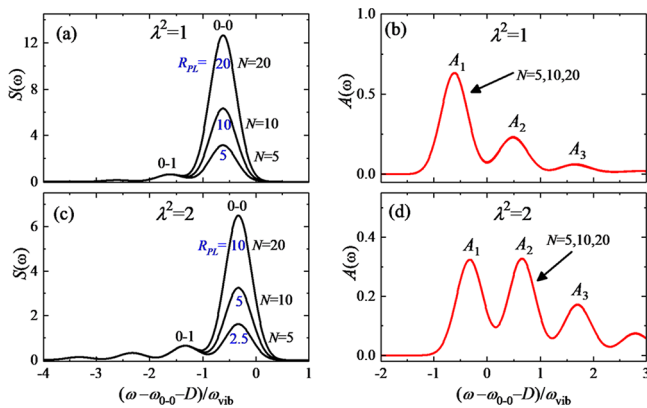


**Figure 24.** Calculated PL spectrum for linear J-aggregates of various sizes ( $N$ ) and with HR factor  $\lambda^2 = 1$  (a) and  $\lambda^2 = 2$  (c). The corresponding absorption spectra are shown in (b) and (d). In all calculations, the nearest-neighbor coupling is  $J_C = -0.5\omega_{vib}$ , the homogenous line width is  $\Gamma_h = 0.25\omega_{vib}$ , and the periodic boundary conditions are assumed.  $R_{PL}$  in (a) and (c) is exactly  $N/\lambda^2$ . Note that the absorption spectra for various  $N$  values are indistinguishable. All calculations are based on the Holstein Hamiltonian within the two-particle approximation.

same value of  $W$ . The figure shows how increasing  $N$  results in a linear increase of the 0–0 peak due to its coherent origin (see eq 60) in sharp contrast to sidebands, which are essentially unchanged in accordance with eq 61. The figure also underscores the important difference between absorption and emission: the corresponding (per molecule) absorption spectra shown in Figure 24b and d are entirely independent of  $N$ , consistent with the expected behavior in the weak-to-intermediate exciton coupling regime where the exciton bandwidth  $W$ , under the n.n. approximation, is already converged to  $4|J_C|$  when  $N > 2$ . This is consistent with the absorption ratio rule in eq 57, which is also  $N$ -independent under the same conditions. Hence, the absorption spectral line shape reports on the exciton bandwidth, whereas the PL spectral line shape reports on the exciton coherence number. As shown in subsequent sections, when disorder and higher temperatures are introduced, the PL ratio remains a reliable measure of the number of coherently connected chromophores within the subset of emitting excitons.

**4.2.5. Strong Excitonic Coupling and Mirror Image Symmetry.** In this section, we consider in greater detail the mirror-image recovery exhibited by J-aggregates for very strong exciton coupling, as observed in Figure 17j, but with an effective HR factor equal to  $\lambda^2/N$ . Approximate mirror-image symmetry can be seen in Figure 12 for the brickwork merocyanine aggregates investigated by Wolthaus et al.<sup>61</sup> The  $N$ -fold reduction in the effective HR factor can be viewed as a form of “exchange” or “motional” narrowing, as shown by Walczak et al.<sup>170</sup> An HR reduction by a factor of 2 was accounted for early

on by Forster in his treatment of molecular dimers.<sup>159</sup> It was also demonstrated by Chang et al.<sup>310</sup> and later by Barford and Marcus<sup>248</sup> for conjugated polymer chains modeled as Frenkel J-chains. Reducing the effective HR factor by  $N$  results in an  $N$ -fold enhancement of the spectral ratios  $R_{abs} = R_{PL} = N/\lambda^2$  compared to the monomer values. The  $N$ -scaling of  $R_{abs}$  in the strong exciton coupling limit can also be observed in the calculated absorption spectra of Eisfeld and Briggs<sup>171</sup> in their Figure 5 and in Figure 2 of Bloemsma et al.<sup>180</sup> It is important to note that, although the PL ratio obeys  $R_{PL} = N/\lambda^2$ , independent of  $W$  in ideal J-aggregates (see the previous section), only in the finite-size strong coupling limit is the entire PL progression describable as Poissonian with an effective HR factor given by  $\lambda^2/N$  (see Figure 23).

The recovery of mirror-image symmetry in J-aggregates is not simply associated with the Simpson–Peterson condition for strong exciton coupling,  $W \gg \lambda^2\omega_{vib}$ , because the number of chromophores is also important, compare Figures 15 and 17. There are in fact two regimes of strong exciton coupling, one that applies to finite size aggregates, as in Figure 17e and j, and considered in the present section, and another that pertains to the limit of a one-dimensional crystal or “polymer”. In the latter case, treated in the following section, mirror image symmetry is no longer obtained.<sup>242,243</sup>

An early investigation of the strong excitonic coupling limit was made by McRae<sup>152–154</sup> using an exciton–phonon product basis set similar to that appearing in eq 21. More refined treatments appeared later by Walczak et al.<sup>170</sup> and others.<sup>176,248</sup> In the strong excitonic coupling limit, also referred to as the adiabatic limit by Barford and Marcus,<sup>248</sup> the exciton and vibrational degrees of freedom become separable, making the exciton–phonon states in eq 21 approximate (zero-order) eigenstates. In this regime, optical excitation from the vibrationless ground state is limited to the exciton states,  $|\tilde{n}\rangle \otimes |k=0; 0, \dots, 0\rangle$ , where  $\tilde{n}$  is the number of quanta in the totally symmetric phonon mode with wave vector  $q = 0$ . Importantly,  $\tilde{n}$  ( $= 0, 1, 2, \dots$ ) is a good quantum number for any level of coupling.<sup>176</sup> As noted early on by McRae,<sup>152,153</sup> exciton–phonon coupling, as represented by the last term in the Hamiltonian in eq 18, can induce mixing only between the optically bright states,  $|\tilde{n}\rangle \otimes |k=0; 0, \dots, 0\rangle$  and dark states hosting a single nontotally symmetric phonon,  $|\tilde{n}\rangle \otimes |k; 0, \dots, 1_{q=-k} \dots, 0\rangle$  ( $k \neq 0$ ), but with a total of zero quasi-momentum  $\kappa$  ( $= k + q$ ). McRae showed that the mixing is small and the perturbative approach justified when<sup>152,153</sup>

$$\sum_{k \neq 0} \frac{\lambda^2 \omega_{vib}^2}{N(\omega_{vib} + J_k - J_{k=0})^2} \ll 1 \quad (63)$$

where the free-exciton dispersion  $J_k$  is given in eq 5. The inequality can also be applied to higher dimensional aggregates, such as the two-dimensional herringbone aggregates,<sup>183</sup> which are important packing motifs for many unsubstituted thiophenes and phenylenevinylene.<sup>13</sup>

As depicted schematically in Figure 25a, condition 63 can be satisfied for sufficiently small  $N$  when the energy separation between neighboring free excitons is much larger than a vibrational quantum, i.e., when

$$|J_{k=0} - J_{k=2\pi/N}| \approx 4\pi^2|J_C|/N^2 \gg \omega_{vib} \quad (64)$$

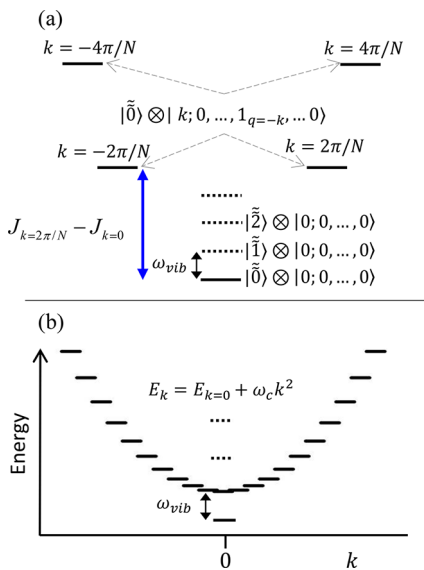


**Figure 25.** (a) First-order energy level structure for a J-aggregate near the band bottom. In the strong coupling limit defined by condition 65, the blue double arrow is much larger than the black arrow. Also shown are the vibronic levels (dashed), which contribute to the Poissonian absorption spectrum. Increasing  $N$  into the polymer limit results in the level scheme shown in (b). Note that only states that have oscillator strength are shown. Strong coupling now depends on a sufficiently large band curvature through condition 71.

where the n.n. approximation was made in the middle expression. Under condition 64, the first term in the sum of 63 is small when

$$4\pi^2|J_C|/N^{3/2} \gg \omega_{\text{vib}}|\lambda| \quad (65)$$

The remaining terms (with  $k = \pm 4\pi/N, \pm 6\pi/N, \dots$ ) scale initially as  $|k|^{-4}$  and can therefore be neglected. Hence, condition 65 serves to describe the finite-size strong coupling regime.

When condition 65 is satisfied, the absorption spectrum is dominated by transitions from the vibrationless ground state to the excited states  $|\tilde{n}\rangle \otimes |k = 0; 0, \dots, 0\rangle$  with  $\tilde{n} = 0, 1, 2, \dots$  as indicated in Figure 25a, where the states with  $\tilde{n} \geq 1$  are indicated by the dashed levels. The oscillator strengths, which are proportional to the FC factors,  $|\langle 0 | \tilde{n} \rangle|^2$ , form a Poissonian distribution with an effective HR factor given by  $\lambda^2/N$ .<sup>176</sup> As follows directly from eqs 39 and 40, the (reduced) absorption spectrum for both J- and H-aggregates evaluated under condition 65 is

$$A(\omega) \approx e^{-\lambda^2/N} \sum_{v=0,1,2,\dots} \frac{(\lambda^2/N)^v}{v!} W_{\text{LS}}(\omega - \omega_{A_{\max}} - v\omega_{\text{vib}}) \quad \text{J-, H-agg} \quad (66)$$

where the peak absorption frequency is given by

$$\omega_{A_{\max}} \equiv \omega_{0-0} + D + (1 - 1/N)\lambda^2\omega_{\text{vib}} + J_{k=0} \quad (67)$$

Eq 66 accurately describes the main absorption peaks in the H- and J-aggregate spectra in Figure 17e and j, respectively. Interestingly, one may wonder why the H-aggregate apparently has a value of  $R_{\text{abs}}$  greater than the monomer value ( $= 1/\lambda^2$ ), which is the one in Figure 17), contradicting the H-aggregate signature  $R_{\text{abs}} < 1/\lambda^2$ . This is reconciled by the fact that the main absorption peak for the H-aggregate in Figure 17e is not

the  $A_1$  peak involved in the ratio  $R_{\text{abs}}$ . Because of the very strong coupling, the actual  $A_1$  peak, which represents the origin of absorption, is extremely weak and is indicated by  $A_{k=\pi}$  in Figure 17e. Hence, the actual value of  $R_{\text{abs}}$  is close to zero in line with what one expects for a strongly coupled H-aggregate. The form of the J-aggregate absorption spectrum in eq 66 is similar to an expression derived by Walczak et al.<sup>170</sup> and supported by the analyses of Eisfeld and Briggs,<sup>171</sup> Bloemsma et al.,<sup>180</sup> and Barford and Marcus.<sup>248</sup>

For J-aggregates, the state  $|\tilde{0}\rangle \otimes |k = 0; 0, \dots, 0\rangle$  serves as the origin for both absorption and emission, see Figure 16. The (reduced) PL spectrum is therefore given by the mirror image of the absorption spectrum, i.e.,

$$S(\omega) \approx N e^{-\lambda^2/N} \sum_{v=0,1,2,\dots} \frac{(\lambda^2/N)^v}{v!} W_{\text{LS}}(\omega - \omega_{A_{\max}} + v\omega_{\text{vib}}) \quad \text{J-agg} \quad (68)$$

The approximate mirror-image symmetry with an effective HR factor reduced from the actual value  $\lambda^2$  is likely responsible for the measured line shapes of the merocyanine aggregates<sup>61</sup> shown in Figure 12. However, in actual cases, the reduction factor is not  $N$  but  $N_{\text{coh}}$ , the exciton coherence number likely defined by the presence of significant inhomogeneous disorder (see section 4.5).

The recovery of the mirror-image spectra in Figure 17, but not in Figure 15, can now be understood within the framework of finite-size strong excitonic coupling. For the  $N = 6$  J-aggregates of Figure 17j, the value of the n.n. Coulombic coupling,  $|J_C| = 4\omega_{\text{vib}}$ , is large enough to satisfy condition 65. The resulting mirror-image spectra correspond to an effective HR factor given by  $\lambda^2/N = 1/6$ . However, for the  $N = 20$  aggregates of Figure 15, the equivalent value of  $|J_C|$  required to achieve strong coupling is roughly six ( $= (20/6)^{3/2}$ ) times greater, i.e.,  $|J_C| = 24\omega_{\text{vib}}$ , far beyond the maximum coupling portrayed in Figure 15.

In contrast to the behavior of J-aggregates, H-aggregates exhibit no mirror image symmetry. Although the absorption spectrum abides by eq 66, PL is practically nonexistent as observed in Figure 17e. In H-aggregates, PL originates from the band-bottom exciton, which takes the form  $|\tilde{0}\rangle \otimes |k = \pi; 0, \dots, 0\rangle$  in the strong coupling limit. Because the exciton has  $\kappa = \pi$ , 0–0 emission is strictly forbidden. Although the sideband peaks (0–1, 0–2, ...) are weakly allowed, they vanish with increasing exciton bandwidth, scaling as the inverse square of  $W$ ,<sup>260–262,288</sup> consistent with what was observed in Figure 17a–e. For example, the weak 0–1 line strength arises from the symmetry-allowed mixing between the lowest energy (emitting) exciton with  $\kappa = \pi$  and the much higher energy state,  $|\tilde{0}\rangle \otimes |k = 0; 0, \dots, 1_{q=\pi}, \dots, 0\rangle$  (also with  $\kappa = \pi$ ) near the top of the band. The mixing, driven by the last term in the Hamiltonian in eq 18, is the emission form of Herzberg–Teller coupling as further discussed in section 4.2.7 (see Figure 28b).<sup>311</sup> First order perturbation theory gives<sup>260</sup>

$$I^{0-1} = \frac{\omega_{\text{vib}}^2 \lambda^2}{(W + \omega_{\text{vib}})^2} e^{-\lambda^2/W} \quad W \gg \lambda^2 \omega_{\text{vib}} \quad (69)$$

where the free-exciton bandwidth is  $W = J_{k=\pi} - J_{k=0}$  in H-aggregates.

Figure 26 shows how  $I^{0-1}$  and  $I^{0-2}$  diminish with increasing exciton bandwidth in the H-aggregates of Figure 17a–e. The figure shows that the 0–1 intensity is accurately described by

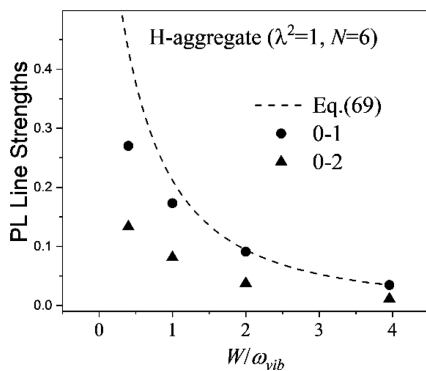


**Figure 26.** Line strengths 0–0 and 0–1 as a function of exciton bandwidth for the H-aggregates of Figure 17. The intensities approach zero at large exciton bandwidths.

eq 69 for bandwidths exceeding approximately one vibrational quantum.

**4.2.6. Strong Exciton Coupling in a One-Dimensional Crystal.** Strong exciton coupling in the one-dimensional crystal, or “polymer”, limit has been considered by McRae<sup>152–154</sup> as well as Briggs and Herzenberg,<sup>161</sup> Hemmerger,<sup>164</sup> and most recently by Eisfeld and Briggs<sup>167,168</sup> to account for the absorption line shape of the Scheibe (PIC) aggregates. In the polymer limit, McRae’s condition (63) can also be satisfied after first converting the sum to an integral when  $N$  is sufficiently large ( $2\pi/N \ll 1$ ), giving

$$\pi^{-1} \int_0^\pi dk \frac{\lambda^2 \omega_{\text{vib}}^2}{(\omega_{\text{vib}} + J_k - J_{k=0})^2} \ll 1 \quad (70)$$

The energy level diagram appropriate for a J-type polymer is shown in Figure 25b. Note that in contrast to the finite-size strong coupling depicted in Figure 25a, there are now many exciton levels within an energy interval defined by a vibrational quantum, the number of which is determined primarily by the band curvature at  $k = 0$ .

In refs 176, 260, and 261, integrals like that appearing in eq 70 were evaluated using the parabolic band approximation introduced in eq 12. For a one-dimensional J-aggregate with n.n. coupling only ( $J_C < 0$ ), the exciton dispersion is approximately given by  $J_k = J_{k=0} + \omega_c k^2$  with the (positive) band curvature  $\omega_c = -J_C$ . For positive curvature values, the integral in eq 70 can be determined analytically, leading to the strong excitonic coupling condition

$$\omega_c \gg \lambda^2 \omega_{\text{vib}} / 16 \quad (71)$$

for a one-dimensional J-aggregate or J-polymer. It is readily satisfied for the  $1400 \text{ cm}^{-1}$  vinyl stretching mode with HR factor of order unity when the curvature  $\omega_c$  is much greater than  $\sim 100 \text{ cm}^{-1}$ . For comparison, the analogous expression for a two-dimensional crystal with isotropic coupling yields the more intuitive expression<sup>262</sup>

$$\omega_c \gg \lambda^2 \omega_{\text{vib}} / 4\pi \quad (72)$$

showing that in this case  $4\pi$  times the curvature must greatly exceed the nuclear relaxation energy.

McRae obtained a more approximate expression for the strong coupling condition by taking the density of states for the one-dimensional crystal to be constant within the bandwidth  $W$ , resulting in<sup>152</sup>

$$\omega_{\text{vib}} + W \gg \lambda^2 \omega_{\text{vib}}$$

which gives rather inadequate results for the important case of  $\lambda^2 = 1$ . McRae also re-expressed the condition of Simpson and Peterson,<sup>301</sup> which states that strong excitonic coupling requires the exciton bandwidth to be greater than the width of the vibronic monomer band<sup>152,153</sup> to obtain the strong coupling condition

$$W \gg \lambda^2 \omega_{\text{vib}} \quad (73)$$

which is far more intuitive, showing that strong exciton coupling results when the free exciton bandwidth is much greater than the nuclear relaxation energy. However, as shown in ref 262, an expression like eq 73 is strictly valid for isotropic two-dimensional lattices (see eq 72).

Similar to the case of finite-size strong coupling in the previous section, the absorption spectrum for a strongly coupled J-polymer is dominated by the transition to the state  $\tilde{|0\rangle} \otimes |k = 0; 0, \dots, 0\rangle$ . However, instead of a pronounced vibronic progression at higher energies found in the previous section, in the present case there exists a broad sideband peaking at approximately one vibrational quantum higher in energy. The side band is due to the contribution of the  $N$  states  $\tilde{|0\rangle} \otimes |k; 0, \dots, 1_{q=-k}, \dots, 0\rangle$ , which borrow intensity from  $\tilde{|0\rangle} \otimes |k = 0; 0, \dots, 0\rangle$  to first order in the exciton–phonon coupling, see Figure 25b. As originally established by McRae,<sup>153</sup> the absorption spectrum for J-polymers has the form of a narrow “0–0” peak followed by a broader, lower intensity shoulder. Under condition 71, the absorption spectrum is

$$A(\omega) \approx W_{\text{LS}}(\omega - \omega_{A_{\text{max}}}) + \frac{\lambda^2 \omega_{\text{vib}}^2}{\pi} \int_0^\pi \frac{W_{\text{LS}}(\omega - \omega_{A_{\text{max}}} - \omega_{\text{vib}} - \omega_c k^2)}{(\omega_{\text{vib}} + \omega_c k^2)^2} dk \quad (74)$$

where the peak absorption is given by  $\omega_{A_{\text{max}}} \equiv \omega_{0-0} + D + \lambda^2 \omega_{\text{vib}} + J_{k=0}$ . Interestingly, the characteristic J-aggregate red-shift,  $J_{k=0} = 2J_C$ , is diminished somewhat by a blue-shifting contribution,  $\lambda^2 \omega_{\text{vib}}$ . The strong-coupling absorption spectrum for H-polymers is more complex due to possible resonances between  $\tilde{|0\rangle} \otimes |k = 0; 0, \dots, 0\rangle$  and a subset of the states  $\tilde{|0\rangle} \otimes |k; 0, \dots, 1_{q=-k}, \dots, 0\rangle$  enabled by a negative band curvature in H-aggregates at the point  $k = 0$ . McRae<sup>153</sup> provided a qualitative description of the structure of the resulting absorption spectrum, but to our knowledge, no analytical expression similar to eq 74 has appeared in the literature. For herringbone lattices, the absorption spectrum for the J-band (lower Davydov component) in the strong coupling limit was derived in ref 183.

Figure 27 shows the absorption spectrum for a J-polymer evaluated from eq 74. The dominance of the main peak and the existence of a broader and much less intense sideband has also been captured by Eisfeld and Briggs in their work using the coherent exciton scattering approximation.<sup>167,168,171</sup> A further integration of the spectrum in eq 74 over frequency gives the ratio between the spectral areas of the sideband vs the main band, as shown in the figure inset.<sup>153</sup> The ratio must be smaller than unity for the perturbation theory to be valid. Interestingly, the PL spectrum (not shown) for J-aggregates still abides by the expression in eq 68, but because  $N$  is very large, the spectrum is entirely dominated by the 0–0 peak, which for the ideal J-aggregates considered here occurs at the same frequency as the

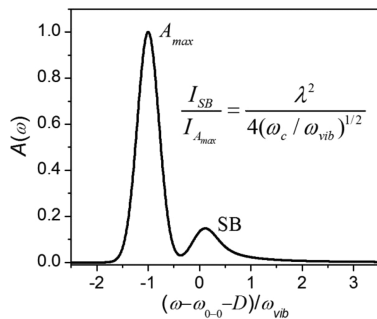


**Figure 27.** Reduced absorption spectrum of a linear J-aggregate in the large  $N$  limit with  $\lambda^2 = 1$ ,  $\omega_c (= -J_C) = \omega_{\text{vib}}$  and using a Gaussian homogeneous line shape function with  $\Gamma_h = 0.21\omega_{\text{vib}}$ . The spectral shape abides by eq 74.

main absorption peak, i.e., there is no Stokes shift. The absorption and PL spectra so described compares quite favorably to the measured spectra of the cyanine dye pseudoisocyanine chloride or PIC in the seminal work of Scheibe on dye aggregates.<sup>49,51</sup>

**4.2.7. Herzberg–Teller Coupling in H-Aggregates.** As originally described by Robinson, intensity borrowing is a general effect in which a “forbidden” electronic transition becomes enhanced through weak interactions with a perturber.<sup>312</sup> Herzberg–Teller (HT) coupling is one such example and is usually invoked to account for vibration-induced intensity borrowing between electronic excited states within a molecule.<sup>313</sup> However, an intermolecular version of the HT effect is operative in molecular aggregates for sufficiently strong exciton coupling, as discussed in the works of Petelenz and co-workers,<sup>314,315</sup> Spano and co-workers,<sup>284,316</sup> and most recently by Wykes et al.<sup>311</sup> Peaks arising from HT coupling can be observed near the origin in the polarized absorption spectra of oligothiophene and oligophenylenevinylene crystals<sup>114,120,183</sup> (see section 4.7). HT coupling can also be operative in the PL spectrum of H-aggregates, as discussed in section 4.2.5. For example, the vibronic fine structure observed in the PL spectrum of crystalline distyrylbenzene (DSB)<sup>128,130,317</sup> was reproduced in detail by Wykes et al.<sup>311</sup> by incorporating multimode HT coupling in atomistic simulations of DSB clusters. In the current section, intermolecular HT coupling is briefly described for the simple case of the ideal H-aggregates considered so far. Because the PL version of intermolecular HT coupling was already introduced in section 4.2.5, the focus here is on how HT coupling impacts the absorption spectrum.

For H-aggregates, the basic mechanisms for HT coupling operative in absorption and emission are depicted in Figure 28. In the absorption spectrum, HT coupling gives rise to a weak peak, sometimes referred to as a false origin, near the band bottom. In Figure 17d, the HT peak is labeled  $A_1$  (or  $A_{k=\pi}$ ). As is characteristic of ideal H-aggregates, the band-bottom state carries no oscillator strength from the vibrationless ground state. In the strong exciton coupling regime, the state is approximated by the  $\kappa = \pi$  wave function  $|\tilde{0}\rangle \otimes |k = \pi; 0, \dots, 0\rangle$ .

The state  $|\tilde{0}\rangle \otimes |k = \pi; 0, \dots, 1_{q=\pi}, \dots, 0\rangle$  ( $\kappa = 0$ , modulo  $2\pi$ ) lying one vibrational quantum higher in energy is also optically dark, but unlike the band-bottom state, it can mix with and borrow oscillator strength from the strongly allowed state,  $|\tilde{0}\rangle \otimes |k = 0; 0, \dots, 0\rangle$  (also with  $\kappa = 0$ ) residing at the top of the band. The mixing is symmetry-allowed by the last term in the Hamiltonian

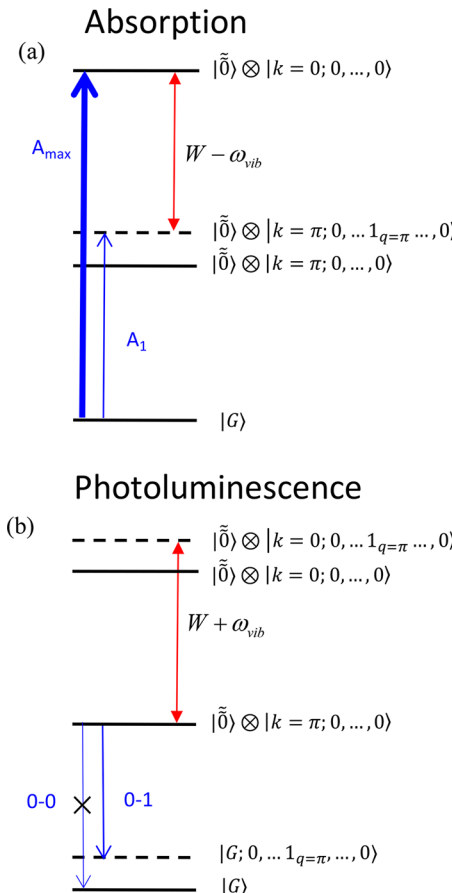


**Figure 28.** Herzberg–Teller coupling is responsible for (a) the weak absorption origin and (b) the weak sideband emission in strongly coupled H-aggregates. States that mix and share oscillator strength have the same value of total quasi-momentum  $\kappa$  and are connected by the red double arrow.

in eq 18. The wave function of the “false origin” correct to first order is given by

$$|A_{k=\pi}\rangle^{(1)} = |A_{k=\pi}\rangle - \frac{\omega_{\text{vib}}\lambda}{\sqrt{N}(W - \omega_{\text{vib}})} |\tilde{0}\rangle \otimes |k = 0; 0, \dots, 0\rangle \quad (75)$$

where  $|A_{k=\pi}\rangle$  is abbreviated notation for the state,  $|\tilde{0}\rangle \otimes |k = \pi; 0, \dots, 1_{q=\pi}, \dots, 0\rangle$ , and the free-exciton bandwidth is  $W = J_{k=0} - J_{k=\pi}$ . The corresponding transition energy, also correct to first-order, is

$$\omega_{A_{k=\pi}} \equiv \omega_{0-0} + D + (1 - 1/N)\lambda^2\omega_{\text{vib}} + \omega_{\text{vib}} + J_{k=\pi} \quad (76)$$

The second term on the rhs of eq 75 makes the transition to state  $|A_{k=\pi}\rangle$  weakly allowed with a line-strength (per chromophore) given by

$$|\langle G | \hat{M} | A_{k=\pi} \rangle^{(1)}|^2 = \frac{\omega_{\text{vib}}^2 \lambda^2}{N(W - \omega_{\text{vib}})^2} e^{-\lambda^2/N} \mu^2 \quad (77)$$

In addition to the HT peak defined by eqs 76 and 77, higher energy HT peaks also appear for other values of  $k$  via absorption to the first-order corrected states,  $|\tilde{0}\rangle \otimes |k; 0, \dots, 1_{q=-k}, \dots, 0\rangle^{(1)}$  also with total quasi-momentum  $\kappa = 0$ . Their energies and intensities are given by eqs 76 and 77 with  $J_{k=\pi}$  replaced by

$J_k$  and  $W$  replaced by  $J_{k=0} - J_k$ . Such peaks are denoted as  $A_k$  in Figure 17d and e.

The inverse  $N$ -dependence in the line strengths in eq 77 is characteristic of the finite-size strong exciton coupling limit assumed so far. However, as  $N$  increases into the one-dimensional crystal limit considered in the last section, the  $N$ -dependence disappears due to the convergence of  $O[N]$  spectral peaks  $A_k$  in the spectral region roughly one vibrational quantum above the band bottom. The effect is very similar to the creation of the sideband in the J-aggregate spectrum of Figure 27 (see also ref 183). In the large  $N$  limit, the absorption spectral line shape near the origin becomes

$$A'(\omega) \approx \frac{\lambda^2 \omega_{\text{vib}}^2}{\pi} \int_0^\pi \frac{W_{\text{LS}}(\omega - \omega_{A_{k=\pi}} - \omega_c(k - \pi)^2)}{(J_{k=0} - J_{k=\pi} - \omega_c(k - \pi)^2 - \omega_{\text{vib}})^2} dk \quad (78)$$

which is similar in structure to the integral in eq 74. Figure 29 shows the small HT peak induced in a linear H-aggregate in the strong coupling limit.

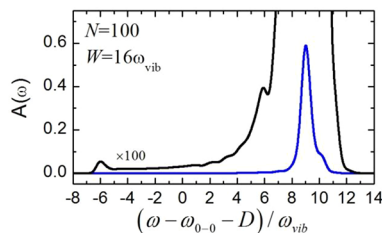


**Figure 29.** Reduced absorption spectrum of a linear H-aggregate in the large  $N$  limit with  $N = 100$  molecules,  $\lambda^2 = 1$ ,  $W = 16\omega_{\text{vib}}$ , and  $\Gamma_h = 0.18\omega_{\text{vib}}$ . HT coupling results in the observed low energy absorption band (shown at 100× magnification).

#### 4.3. Energetically Disordered J- and H-Aggregates

Inhomogeneous broadening is quite ubiquitous in organic materials, especially amorphous solids,<sup>318</sup> and is commonly treated as a Gaussian random distribution of site transition energies with standard deviation  $\sigma_d$ . The site energy dispersion may arise from static defects such as lattice imperfections (stacking faults, dislocations, grain boundaries, etc.) but also from phonons with frequencies much smaller than the exciton bandwidth. Such low-frequency modes lead to an essentially static distribution of nuclear displacements on the time scales of absorption and emission. The associated site energy deviations can be treated as random Gaussian variables with a distribution width  $\sigma_d$  that increases with temperature.<sup>295,319</sup>

The impact of site energetic disorder on the absorption spectral line widths in J-aggregates (without vibronic coupling) has been a subject of keen interest since the discovery of J-aggregates, beginning with the pioneering works of Schreiber and Toyozawa<sup>295,296</sup> and Knapp<sup>319</sup> with subsequent seminal contributions by Knoester and co-workers<sup>40,320</sup> and Walczak et al.<sup>170</sup> Knapp showed that when the Coulomb coupling is sufficiently large, the J-band line width is reduced by  $\sqrt{N}$  due to motional (or “exchange”) narrowing. This occurs when the exciton moves so rapidly as to average out the energetic “potholes”. The narrowing effect can be readily discerned from the PIC spectrum in Figure 11, where the red-shifted J-band is ~5-times narrower than a given monomer vibronic peak, suggesting a coherence length of perhaps 25 chromophores. Hence, Knapp’s model is not only important for its ability to account for the observed spectral narrowing in J-ag-

gates<sup>49–51</sup> but also provides a straightforward spectroscopic method for determining the number of coherently coupled chromophores.<sup>63,64</sup> Knapp further considered the effects of spatial correlation in the site energy distribution, allowing one to distinguish between short- and long-range inhomogeneous broadening via the spatial correlation length  $l_0$ . When the latter is much larger than the aggregate dimensions, the line narrowing effect vanishes entirely. Spatial correlation is readily appreciated in the highway metaphor: if each one-foot segment of highway had a depth determined by a Gaussian distribution with  $\sigma = 0.5$  foot, then a correlation length  $l_0$  of only several feet would make for very unpleasant, bumpy driving. However, if  $l_0$  is expanded to several miles (without changing  $\sigma$ ), one would experience a very smooth ride, likely never encountering a pothole. Recently, Levy distributions, non-Gaussian distributions of site-disorder that increase the occurrence of deep traps, have gained favor in describing molecular aggregate photo-physics.<sup>321–324</sup> In addition, disorder has also been extended to the electronic couplings as well, i.e., off-diagonal disorder.<sup>325</sup>

The impact of site energetic disorder on vibronically coupled J- and H-aggregates was given serious consideration by Walczak et al.,<sup>170</sup> Meskers et al.,<sup>288</sup> and Spano and co-workers.<sup>3,14,145–147,176</sup> In addition to the aforementioned line narrowing effects, site disorder also affects the relative vibronic peak intensities, especially in the PL spectrum. This is most dramatic in H-aggregates, where disorder enables 0–0 emission,<sup>146,288</sup> emission that is otherwise symmetry forbidden in the ideal H-aggregates of section 4.2. In marked contrast, in J-aggregates disorder attenuates 0–0 emission. For such effects to be investigated, the Holstein Hamiltonian enhanced to include spatially correlated site disorder has proven to be quite useful.<sup>14,145–147,176,308</sup> However, even in this “pared down” phenomenological approach, the number of variables defining the phase space,  $\{\omega_{\text{vib}}, \lambda^2, W, \sigma_d, l_0\}$ , is daunting, leaving most of its regions unexplored. In what follows, we illustrate just a sampling of the intriguing properties of vibronically coupled disordered H- and J-aggregates within a limited phase space appropriate for organic chromophores with vibronic coupling derived from the vinyl-stretching mode;  $\omega_{\text{vib}} \approx 0.17$  eV and  $\lambda^2 = 1$ . To most effectively relate to prior sections, we continue to demonstrate the various behaviors using aggregates containing  $N = 6$  chromophores, as in Figure 17.

**4.3.1. Knapp’s Model.** Inhomogeneous broadening derives primarily from a distribution of chromophore transition frequencies represented by  $\{\Delta_1, \Delta_2, \dots, \Delta_N\}$ , where  $\Delta_n$  is the transition frequency offset of the  $n$ th chromophore. Here, we assume linear aggregates comprised of  $N$  molecules. Following the seminal work by Knapp,<sup>319</sup> the various  $\Delta_n$  are chosen from a spatially correlated Gaussian distribution,

$$P(\Delta_1, \Delta_2, \dots, \Delta_N) = \frac{1}{(2\pi)^{N/2} \sqrt{\det \mathbf{A}}} \exp\left(-\frac{1}{2} \sum_{m,n} (\mathbf{A}^{-1})_{m,n} \Delta_m \Delta_n\right) \quad (79)$$

with intersite spatial correlation expressed through the matrix  $\mathbf{A}$  with elements given by  $\mathbf{A}_{mn} \equiv \langle \Delta_m \Delta_n \rangle$ . Knapp further assumed an intersite correlation is exponentially dependent on the distance between chromophores

$$\mathbf{A}_{mn} = \sigma_d^2 e^{-|m-n|/l_0} \quad (80)$$

where  $\sigma_d$  is the standard deviation of the site-energy distribution and  $l_0$  is the (unitless) spatial correlation length. When  $l_0 = 0$ , the transition frequency offsets, which define a

given aggregate configuration  $C \equiv \{\Delta_1, \Delta_2, \dots, \Delta_N\}$ , are spatially uncorrelated and are therefore randomly assigned independently of each other within a given aggregate. In this important case, the distribution in eq 79 reduces to a product of area-normalized Gaussians

$$P(\Delta_1, \Delta_2, \dots, \Delta_N) = \prod_{i=1}^N p(\Delta_i) \quad l_0 = 0 \quad (81)$$

where the Gaussian distribution function for a single site is

$$p(\Delta) = (\sqrt{2\pi}\sigma_d)^{-1} \exp(-\Delta^2/2\sigma_d^2) \quad (82)$$

The distribution in eq 81 is often referred to as short-range broadening. In the opposite limit of long-range broadening, the spatial correlation length is much greater than the aggregate length,  $l_0 \gg N - 1$ . Now all offsets within a given aggregate are identical but are chosen independently from the offsets in other aggregates according to a Gaussian distribution of width  $\sigma_d$ . Hence, the broadening is entirely *inter-aggregate*. In this limit, the distribution of eq 79 reduces to

$$P(\Delta_1, \Delta_2, \dots, \Delta_N) = p(\Delta_1) \prod_{i=2}^N \delta(\Delta_i - \Delta_1) \quad l_0 \gg N - 1 \quad (83)$$

**Figure 30** demonstrates the site-energy distributions for four aggregates displaying short-, intermediate- and long-range broadening.

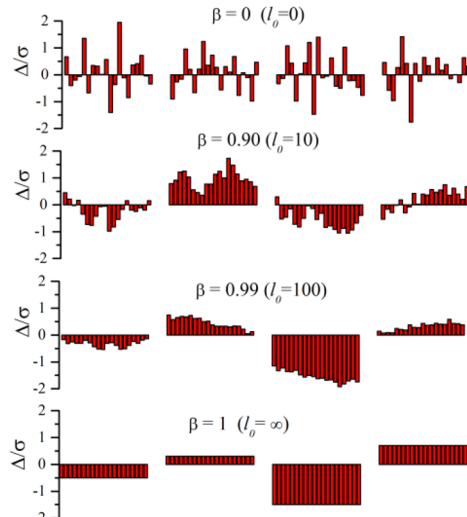


**Figure 30.** Four realizations of site-energy offsets for aggregates containing  $N = 20$  molecules and differing spatial correlation lengths  $l_0$ . The spatial correlation parameter  $\beta$  is defined as  $\exp(-1/l_0)$ . Reprinted from ref 145 with the permission of AIP Publishing.

Before continuing, it should be mentioned that, in refs 14, 146, 147, and 176, the distribution  $p(\Delta)$  was defined by  $(\sqrt{\pi}\sigma)^{-1} \exp(-\Delta^2/\sigma^2)$ , i.e., where the width  $\sigma$  was identified as the half-width at the  $1/e$  point and not the standard deviation  $\sigma_d$ . The two broadening definitions are simply related by  $\sigma = \sqrt{2}\sigma_d$  and care will be taken in what follows to avoid confusion.

Analyses of absorption and emission in disordered linear aggregates with open and periodic boundary conditions are quite numerous.<sup>39,40,46,47,295,319,320,326</sup> When vibronic coupling is neglected, the absorption line shape mainly consists of a single line centered at the frequency,  $\omega_{0-0} + D + 2J_C$ , assuming,

as did Knapp, n.n. coupling only and taking periodic boundary conditions. In this limit, and with disorder described by eqs 79 and 80, Knapp showed that the spectral line shape of the dominant peak is also Gaussian with a half-width half-maximum (HWHM) given by the motionally narrowed line width

$$\sigma_{MN} \equiv \frac{\sigma_d}{\sqrt{N}} \left( \frac{1 + \beta}{1 + \beta^N} \frac{1 - \beta^N}{1 - \beta} \right)^{1/2} (2\ln 2)^{1/2} \quad (84)$$

where  $N$  is the number of chromophores and  $\beta \equiv \exp(-1/l_0)$  is a spatial correlation parameter ranging from  $\beta = 0$  in the limit of short-range broadening ( $l_0 = 0$ ) to  $\beta = 1$  in the limit of long-range broadening ( $l_0 \gg N$ ). Eq 84 shows that, for short-range broadening ( $\beta = 0$ ), the line width is reduced by  $\sqrt{N}$  relative to a monomer ( $N = 1$ ). The effect is demonstrated in Figure 31a.

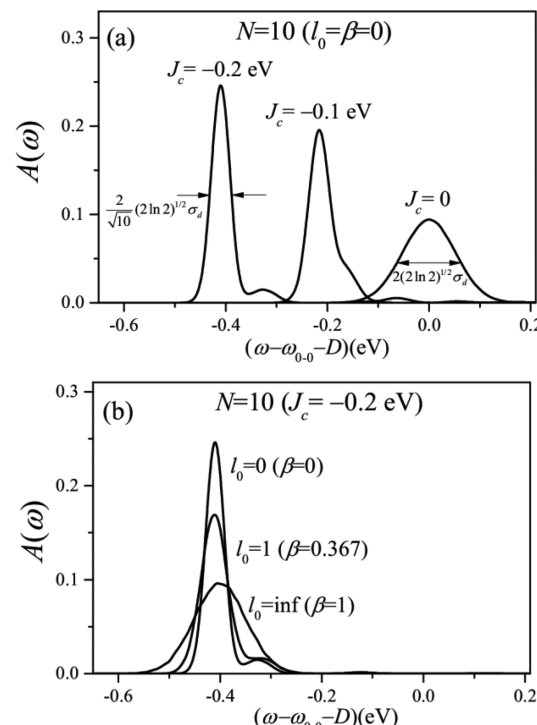


**Figure 31.** Absorption spectrum for disordered J-aggregates containing 10 chromophores with  $\sigma_d = 0.3$  eV. In (a), the n.n. Coulomb coupling is varied in aggregates with short-range broadening, and in (b), the correlation length is varied with  $J_C$  held constant. No vibronic coupling is included, and the homogeneous line width is  $\Gamma_h = 0.1\sigma_d$ . The spectra represent an average over  $10^4$  configurations of disorder.

Such “motional” or “exchange” narrowing results when the FWHM of the narrowed line width is much smaller than the spectral separation between the  $k = 0$  and  $k = 2\pi/N$  excitons, i.e., when<sup>319</sup>

$$2\sigma_d \ll \frac{4\pi^2|J_C|}{N^{3/2}} \quad (85)$$

Eq 84 further shows that the line-width broadens with increasing correlation length until the long-range broadening limit is reached ( $\beta = 1$ ), whereupon the line-width becomes the monomer line width,  $\sigma_{MN} = (2\ln 2)^{1/2} \sigma_d$ , as demonstrated in Figure 31b. Interestingly, this result holds independent of the exciton bandwidth because there is no energetic disorder within individual aggregates when  $l_0 \gg N - 1$ . A more detailed

analysis of the impact of correlated site disorder on the absorption line width, radiative enhancement, and nonlinear absorption in J-aggregates was provided by Knoester and co-workers.<sup>40,320</sup> Of particular relevance to the current discussion is their investigation of the large  $N$  limit, where the inequality in eq 85 is no longer justified and therefore motional narrowing cannot achieve its full effect. In such a scenario, it was shown that for short-range broadening the absorption line width (FWHM) in J-aggregates becomes independent of  $N$  and scales like<sup>40</sup>

$$\text{FWHM} = 0.94|J_C| \left( \frac{\sigma_d}{|J_C|} \right)^{1.34}$$

Hence, the line width continues to narrow with increasing exciton bandwidth.

**4.3.2. The Spectral Impact of Disorder and Vibronic Coupling.** For the impact of inhomogeneous broadening on the optical properties of vibronically coupled molecular aggregates to be evaluated, the Holstein Hamiltonian in eq 13 must be supplemented with the term

$$H_{\text{dis}} = \sum_n \Delta_n |n\rangle \langle n| \quad (86)$$

Representation in an appropriate basis set and subsequent diagonalization for a given configuration of disorder,  $\{\Delta_1, \Delta_2, \dots, \Delta_N\}$ , yields a set of eigenvalues and eigenstates that can be used to construct the component absorption or emission spectrum. Averaging over many such components, each corresponding to a randomly generated configuration with a prescribed  $\sigma_d$  and  $l_0$  then gives the overall spectrum. The reduced absorption and PL spectra (see section 4.1.3) defined in this manner are

$$A(\omega) = \frac{1}{N\mu^2} \left\langle \sum_i |\langle \psi_{i,C} | \hat{M} | G \rangle|^2 W_{\text{LS}}(\omega - \omega_{i,C}) \right\rangle_C \quad (87)$$

$$S_{\text{PL}}(\omega) = \sum_{\nu=0,1,2,\dots} \langle I_C^{0-\nu} W_{\text{LS}}(\omega - \omega_{\text{em},C} + \nu\omega_{\text{vib}}) \rangle_C \quad (88)$$

where  $\langle \dots \rangle_C$  represents the average over site-disorder configurations and  $W_{\text{LS}}$  is the homogeneous line shape function. Following Fulton and Gouterman,<sup>151</sup>  $W_{\text{LS}}$  is taken to be a Gaussian,  $W_{\text{LS}}(\omega) = \exp[-\omega^2/2\Gamma_h^2]$  with a homogeneous line width  $\Gamma_h$ , although when inhomogeneous broadening is dominant ( $\sigma_d \gg \Gamma_h$ ),  $W_{\text{LS}}$  can just as well be replaced by a delta function.

For aggregating organic chromophores with vibronic coupling dominated by the vinyl-stretching mode ( $\omega_{\text{vib}} = 0.17$  eV,  $\lambda^2 = 1$ ), the simultaneous influences of static disorder and vibronic coupling on the absorption and PL spectra still involves a three-dimensional phase space defined by  $W/\omega_{\text{vib}}$ ,  $\sigma_d/\omega_{\text{vib}}$ , and  $l_0$ . (There are also the peripheral variables of  $N$  and  $T$ .) One sensible strategy to appreciate the influence of the relevant phase space variables on the spectral response is to begin with the disorder-free spectra, as in Figure 17, corresponding to the various regimes of exciton coupling ( $W$  vs  $\lambda^2\omega_{\text{vib}}$ ) and analyze the effect of introducing varying levels of disorder, ( $\sigma_d$ ,  $l_0$ ). Because the inhomogeneous broadening typical of most organic solid phases is 100–200 meVs or less, and the dominant vibronic coupling involves symmetric vibrational modes with energies in the same energy interval, the physically important range corresponds to  $\sigma_d/\omega_{\text{vib}} \gtrsim 1$ . Here, the impact of disorder can be felt in several important

ways: line narrowing effects, line shifting effects, and changes in the relative vibronic band intensities, in particular the ratios  $R_{\text{abs}}$  and  $R_{\text{PL}}$ . In what follows, we highlight just some of the relationships worked out so far, beginning with the impact of disorder on the vibronic ratios,  $R_{\text{abs}}$  and  $R_{\text{PL}}$ .

Figure 32 shows how the absorption and PL spectrum for J-aggregates (top) and H-aggregates (bottom) with  $N = 6$

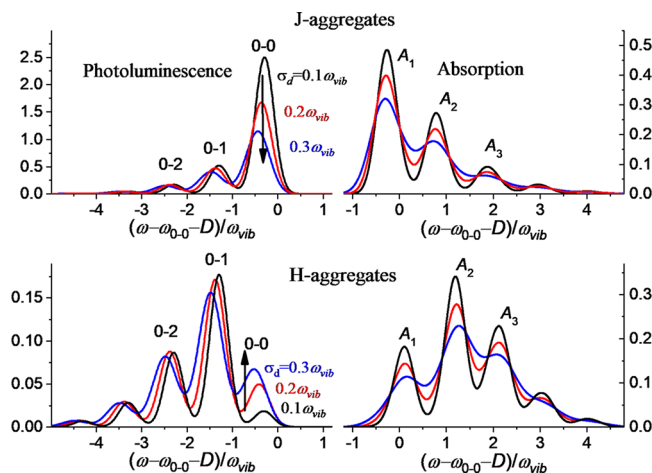


**Figure 32.** J- and H-aggregate spectra as a function of spatially uncorrelated disorder defined by  $\sigma_d$  and  $l_0 = \beta = 0$ . Calculated spectra are based on the site-disordered Holstein Hamiltonian,  $H + H_{\text{dis}}$  from eqs 13 and 86, under the two-particle approximation for  $N = 6$ ,  $\lambda^2 = 1$ , and  $W = \omega_{\text{vib}} = 0.17$  eV (with nearest-neighbor couplings only). The homogeneous line width,  $\Gamma_h = 0.2\omega_{\text{vib}}$ , was kept comparable to  $\sigma_d$  to focus on the changes in band intensities. The spectra represent an average over  $10^4$  configurations of disorder. Note the scale change for absorption and PL.

chromophores are modified as short-range disorder ( $\sigma_d$ ,  $l_0 = 0$ ) is increased while maintaining a constant exciton bandwidth. The homogeneous line width  $\Gamma_h$  was kept comparable to the largest  $\sigma_d$  studied so that the spectral line widths are not adversely affected by the substantial increase in  $\sigma_d$ , thereby allowing one to more clearly resolve changes to the vibronic band intensities. (The impact on line widths will be considered later.) With respect to the relative band intensities, two main conclusions can be drawn: (1) in both J- and H-aggregates, the absorption ratio  $R_{\text{abs}}$  defined in eq 52 is practically independent of  $\sigma_d$ , whereas in marked contrast, (2) the PL ratio  $R_{\text{PL}}$  defined in eq 53 is extremely sensitive to increasing disorder.  $R_{\text{PL}}$  increases in H-aggregates and decreases in J-aggregates as disorder increases, one of the important vibronic signatures with which to differentiate H- vs J-aggregation as introduced in ref 14. The aforementioned disparate behaviors are perfectly consistent with the natures of  $R_{\text{abs}}$  and  $R_{\text{PL}}$ :  $R_{\text{abs}}$  reports on the effective exciton bandwidth, which is not changing in Figure 32, whereas  $R_{\text{PL}}$  reports on the exciton coherence length, which diminishes substantially with increasing disorder in Figure 32.

Before continuing, it should be remarked that the line strengths needed to define the spectral ratios in eqs 52 and 53 should be evaluated using spectrally integrated peak areas and not peak intensities. Because Figure 32 employs a peak-normalized (dimensionless) Gaussian for the homogeneous line shape function,  $W_{\text{LS}}(\omega) = \exp[-\omega^2/2\Gamma_h^2]$ , the line strength of a given vibronic peak is obtained by multiplying the spectrally integrated area by  $1/\sqrt{2\pi}\Gamma_h$ .

Figure 32 shows that the relative  $A_1$  and  $A_2$  peak intensities remain constant as disorder increases, making the ratio formula in eq 55 valid in the presence of disorder. In refs 145–147, the insensitivity of the relative vibronic band intensities to the presence of disorder was demonstrated for H-aggregates. Shortly thereafter, the same conclusion was reached for J-aggregates.<sup>3,14</sup> The insensitivity to disorder can be traced to the form of the matrix elements for the Hamiltonian representing site disorder in eq 86. As  $H_{\text{dis}}$  depends only on electronic degrees of freedom, it can only admix states within a given vibronic band; there is no direct coupling between states in separate bands. Symmetry-breaking matrix elements such as

$$\langle k; \tilde{v} | H_{\text{dis}} | k'; \tilde{v}' \rangle = \frac{1}{N} \sum_n \Delta_n e^{i(k'-k)n} \delta_{\tilde{v}, \tilde{v}'}$$

enable mixing between excitons with different wave vectors,  $k$ , but only when  $\tilde{v} = \tilde{v}'$ . Because the total oscillator strength of a given band  $A_n$ , as obtained via spectral integration, is largely unaffected by such mixing, the absorption ratio rule for both J- and H-aggregates introduced in section 4.2.3 continues to hold in the presence of site disorder,  $\sigma_d \gtrsim \omega_{\text{vib}}$ , and for any level of spatial correlation.

In contrast to the absorption spectrum, the PL spectrum is strongly impacted by disorder because emission originates from primarily the lowest energy exciton, which can dramatically change character (i.e., localization length) via mixing with higher energy excitons with different wave vectors. In particular, the ratio  $R_{\text{PL}}$ , as shown in Figure 32, is especially sensitive to disorder,<sup>145–147</sup> primarily through the unique sensitivity of just the 0–0 emission to the spatial coherence of the emitting exciton (see section 4.2.4). For J-aggregates, the 0–0 emission as well as the ratio  $R_{\text{PL}}$  diminishes with increasing  $\sigma_d$  as the exciton is increasingly localized. As shown in ref 176 and discussed further in section 4.5,  $R_{\text{PL}}$  in disordered J-aggregates directly scales with the exciton coherence number  $N_{\text{coh}}$  introduced in section 3.5

$$R_{\text{PL}} \approx \frac{N_{\text{coh}}}{\lambda^2} \quad (89)$$

Hence, as short-range disorder increases and the exciton localizes ( $N_{\text{coh}} < N$ ),  $R_{\text{PL}}$  diminishes. This is consistent with an associated reduction in the superradiant decay rate  $\gamma_A$  with increasing disorder, as described in refs 40 and 46. Although not shown, in the presence of long-range broadening ( $\beta = 1$ ),  $R_{\text{PL}}$  becomes equal to  $N/\lambda^2$  as it is in the limit of no disorder (see section 4.2.1). This arises because in this limit the J-aggregates comprising the ensemble are individually free of disorder (i.e., there is only *inter*-aggregate disorder) so that  $N_{\text{coh}} = N$ . In section 4.5, the intimate relationship between  $R_{\text{PL}}$  and the exciton coherence length for J-aggregates is explored in greater detail.

Figure 32 shows that the impact of increasing disorder has quite the opposite effect on  $R_{\text{PL}}$  in H-aggregates; unlike in J-aggregates,  $R_{\text{PL}}$  increases with  $\sigma_d$ . In the absence of disorder, the 0–0 emission is exactly zero due to a total destructive interference of transition dipoles in the emitting ( $k = \pi$ ) exciton over the entire length of the aggregate consistent with  $N_{\text{coh}} = N$ . In H-aggregates, the decreasing coherence length with increasing disorder is manifest in a less destructive interference resulting in an increasing 0–0 emission intensity (and  $R_{\text{PL}}$ ) with  $\sigma_d$ . In a slightly alternative view, the 0–0 intensity is made increasingly allowed by disorder-induced symmetry breaking.

As shown in refs 14, 145, 146, and 288, the dark  $k = \pi$  exciton, which resides at the band bottom in H-aggregates (and is therefore responsible for emission), mixes with the higher energy, bright  $k = 0$  exciton that resides at the top of the band via the matrix element

$$\langle k = \pi; \tilde{v} = 0 | H_{\text{dis}} | k = 0; \tilde{v} = 0 \rangle = \frac{1}{N} \sum_n \Delta_n e^{i\pi n} \quad (90)$$

The admixture of the bright exciton in the emitting state leads to 0–0 emission with an intensity that scales to second order in  $\sigma_d/W$ . In the limit of weak exciton coupling and weak disorder ( $\sigma_d \ll W \ll \lambda^2 \omega_{\text{vib}}$ ), the averaged 0–0 line strength and  $R_{\text{PL}}$  were evaluated in refs 145 and 146 to be

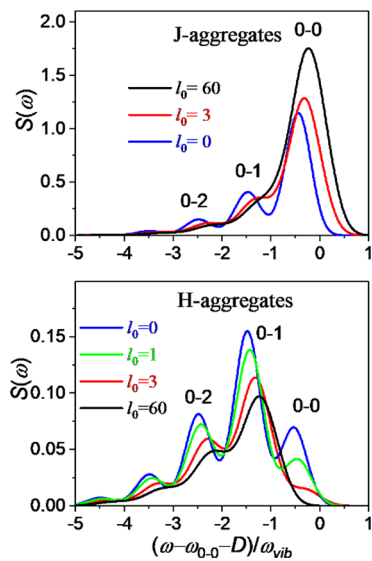
$$\langle I^{0-0} \rangle_C \approx \frac{(1 - \beta)(1 - \beta^N)}{(1 + \beta)(1 + \beta^N)} e^{\lambda^2} (\sigma_d/W)^2 \{1 - O[W/\omega_{\text{vib}}]\} \quad (91)$$

$$R_{\text{PL}} \approx \frac{(1 - \beta)(1 - \beta^N)}{\lambda^2(1 + \beta)(1 + \beta^N)} e^{2\lambda^2} (\sigma_d/W)^2 \{1 - O[W/\omega_{\text{vib}}]\} \quad (92)$$

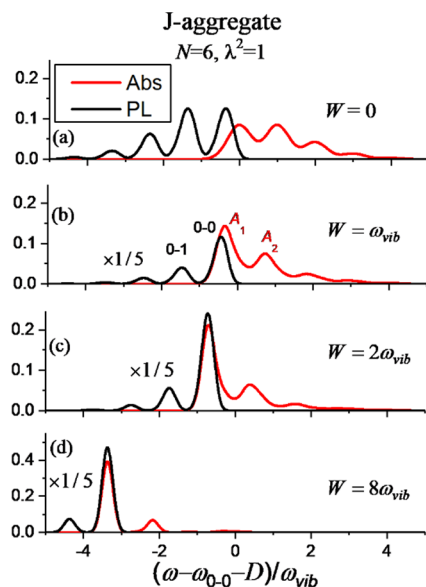
The prefactor in eq 91 contains the influence of spatial correlation: when there is no spatial correlation ( $\beta = 0$ ), the prefactor is unity and disorder is most effective in enhancing the intensity of the 0–0 line strength. On the contrary, when the spatial correlation is very large and  $\beta$  approaches unity, the prefactor and therefore the entire 0–0 line strength approaches zero because in this limit aggregates are individually disorder-free. Increasing the exciton bandwidth further diminishes the 0–0 emission; in the strong exciton coupling limit ( $W \gg \lambda^2 \omega_{\text{vib}}, \sigma_d \ll W$ ), vibronic coupling can be ignored, and the 0–0 line strength is obtained by setting  $\lambda^2 = 0$  in eq 91.<sup>145,146</sup> Unfortunately, there is no simple relation between  $R_{\text{PL}}$  in H-aggregates and the exciton coherence number  $N_{\text{coh}}$  as there is in J-aggregates. However, the coherence number can still be extracted from  $R_{\text{PL}}$  via numerical analysis as was done in refs 145 and 327 for P3HT H-aggregates.

Figure 33 demonstrates the effect of increasing just the spatial correlation length  $l_0$  while holding  $\sigma_d$  constant on the PL spectrum. As the exciton is increasingly delocalized with increasing  $l_0$ ,  $R_{\text{PL}}$  increases in J-aggregates and decreases in H-aggregates. In the limit that  $l_0$  is much greater than  $N - 1$ , the intra-aggregate disorder vanishes entirely, thereby driving the 0–0 intensity to zero in H-aggregates and to the value  $NF$  in J-aggregates, see eq 60. Increasing  $l_0$  also causes significant line broadening and spectral blue-shifting due to increasing intra-aggregate order.

We conclude this section with a review of line narrowing in vibronically coupled H- and J-aggregates. The impact of increasing exciton bandwidth on the absorption and PL spectra of disordered aggregates was analyzed in refs 3, 14, and 176 and is illustrated in Figures 34 and 35 for J- and H-aggregates, respectively. For an easier comparison to the homogeneously broadened aggregates in Figure 17, the aggregate size is maintained at  $N = 6$  chromophores. Calculated spectra for larger disordered aggregates with  $N = 20$  chromophores appear in ref 3. The spectra in Figures 34 and 35 are obtained using eqs 87 and 88 with short-range disorder ( $l_0 = \beta = 0$ ), taking  $\sigma_d = 0.3\omega_{\text{vib}}$ . In contrast to Figure 32, the homogeneous line width,  $\Gamma_h$ , is much smaller than  $\sigma_d$  to ensure dominant inhomogeneous broadening.



**Figure 33.** Calculated PL spectra for disordered J- and H-aggregates ( $\sigma_d = 0.3\omega_{\text{vib}}$ ) as a function of the spatial correlation length  $l_0$ . All other parameters are the same as in Figure 32.



**Figure 34.** Calculated absorption (red) and emission (black) spectra for disordered J-aggregates based on the Holstein Hamiltonian (eqs 13 and 86) under the three-particle approximation. Each aggregate contains  $N = 6$  molecules with nearest-neighbor-only coupling  $J_C$ . The disorder is defined by  $\sigma_d = 0.3\omega_{\text{vib}}$  and  $\beta = 0$  with  $10^4$  configurations included in the spectral average. In addition,  $\lambda^2 = 1$ ,  $\omega_{\text{vib}} = 0.17$  eV, and  $\Gamma_h = 0.07\omega_{\text{vib}}$ .

Comparing Figures 34 and 35 with Figure 17 shows that motional narrowing is clearly operative in both the J- and H-aggregate absorption spectra. For J-aggregates, Walczak et al.<sup>170</sup> described the impact of increasing exciton bandwidth as having a 2-fold narrowing effect on the absorption spectrum; the vibronic progression narrows in response to the reduction in the effective HR factor ( $\lambda^2$  to  $\lambda^2/N$ ) as described in section 4.2, and the individual vibronic peaks are motionally or exchanged narrowed. With respect to the latter, the HWHM of the main peak  $A_1$  in the J-aggregates in Figure 34 significantly narrows from  $(2\ln 2)^{1/2}\sigma_d = 0.35\omega_{\text{vib}}$  in the monomer limit (panel a) to  $\sim 0.14\omega_{\text{vib}}$  in the strong coupling limit in panel d (after the

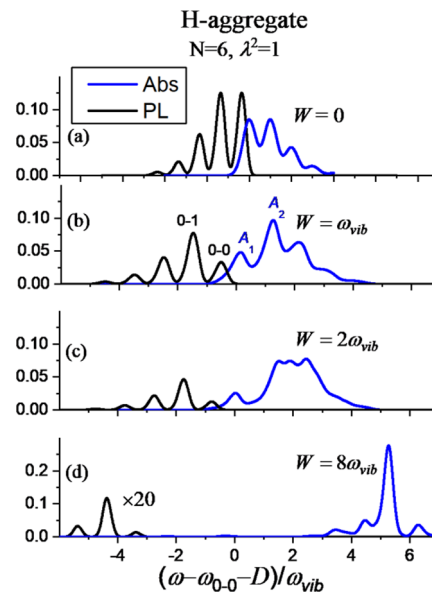


**Figure 35.** Calculated absorption (blue) and emission (black) spectra for disordered H-aggregates based on the Holstein Hamiltonian (eqs 13 and 86) under the three-particle approximation. Each aggregate contains  $N = 6$  molecules with nearest-neighbor-only coupling  $J_C$ . The disorder is defined by  $\sigma_d = 0.3\omega_{\text{vib}}$  and  $\beta = 0$  with  $10^4$  configurations included in the spectral average. In addition,  $\lambda^2 = 1$ ,  $\omega_{\text{vib}} = 0.17$  eV, and  $\Gamma_h = 0.07\omega_{\text{vib}}$ .

small  $0.02\omega_{\text{vib}}$  homogeneous contribution is deconvoluted). The line width reduction factor is very close to  $\sqrt{N} = \sqrt{6}$  in accordance with the generalized Knapp theory in ref 170. Careful inspection shows that the sidebands are less sensitive to narrowing, but when strong coupling is achieved, and inequality (eq 85) holds, all lines are narrowed roughly equally. In the finite-size strong exciton coupling limit of panel d, the mirror-image relationship between absorption and PL is once again recovered as in Figure 17. In this limit, Walczak et al.<sup>170</sup> found that the absorption spectrum reduces to

$$A(\omega) \approx e^{-\lambda^2/N} \sum_{v=0,1,2,\dots} \frac{(\lambda^2/N)^v}{v!} W_{\text{LS}}^{\text{inh}}(\omega - \omega_{A_{\max}} - v\omega_{\text{vib}}) \quad \text{J-, H-agg}$$

with  $\omega_{A_{\max}}$  defined in eq 67 and with the exchange-narrowed inhomogeneous Gaussian line shape given by  $W_{\text{LS}}^{\text{inh}}(\omega) = \exp[-\omega^2/2(\sigma_d^2/N)]$ . Walczak et al.<sup>170</sup> further generalized the spectrum to include coupling to multiple vibrational modes.

For the H-aggregates in Figure 35, the line shapes are more complex, especially for intermediate coupling, but the narrowing is clearly apparent when the coupling becomes strong in panel d. Although not shown, in the opposite limit of infinite spatial correlation ( $\beta = 1$ ), the absorption spectra for both J- and H-aggregates are exactly equivalent to homogeneously broadened spectra with  $\Gamma_h = \sigma_d$ . For the  $N = 6$  aggregates featured here, this corresponds to slightly broader versions of the spectra shown in Figure 17 (where  $\Gamma_h = 0.18\omega_{\text{vib}}$ ).

Line narrowing in the PL spectrum is somewhat more complex than in the absorption spectrum. Line narrowing was investigated in refs 145 and 146 for H-aggregates and in ref 176 for J-aggregates. Interestingly, even when excitonic interactions are absent, as in Figures 34a and 35a, the PL line width (HWHM =  $0.24\omega_{\text{vib}}$ ) is significantly narrower than the absorption line width,  $(2\ln 2)^{1/2}\sigma_d = 0.35\omega_{\text{vib}}$ . In addition,

there is a pronounced Stokes shift due to a red-shift of the PL spectrum by  $\sim 0.35\omega_{\text{vib}}$ . Because such effects occur with no excitonic coupling, they have nothing to do with Knapp's exchange narrowing and arise from the assumption that only the lowest energy state within the aggregate ensemble emits radiation according to Kasha's rule. Under this constraint, the PL narrowing in the absence of excitonic coupling simply reflects the distribution of the lowest energy chromophore in an ensemble of  $N$  chromophores as originally pointed out by Meskers et al.<sup>132</sup> On the basis of the normalized Gaussian distribution,  $p(\Delta)$  in eq 82, the distribution of the lowest energy chromophore in a set of  $N$  chromophores is given by<sup>132,145</sup>

$$L(\Delta) = Np(\Delta) \frac{[\operatorname{erfc}(\Delta/\sqrt{2}\sigma_d)]^{N-1}}{2^{N-1}} \quad l_0 = 0 \quad (93)$$

where  $\operatorname{erfc}(x) \equiv (2/\sqrt{\pi}) \int_x^\infty e^{-t^2} dt$  is the complementary error function. Because of the exponential dependence on  $N - 1$ , the distribution,  $L(\Delta)$ , in eq 93 narrows and red-shifts with increasing  $N$  compared with  $p(\Delta)$ . For  $N = 6$ , the HWHM of  $L(\Delta)$  is  $\sim 0.58$ -times the width of  $p(\Delta)$ , in good agreement with the HWHM of  $0.21\omega_{\text{vib}}$  observed for the PL peaks in Figures 34a and 35a (after deconvoluting out the small homogeneous broadening contribution.) In addition, the distribution  $L(\Delta)$  is red-shifted from  $p(\Delta)$  by  $\sim 0.34\omega_{\text{vib}}$  in very good agreement with the Stokes shift observed in Figures 34a and 35a.

As the bandwidth,  $W$ , increases in the J-aggregates of Figure 34, the 0–0 peak in the PL spectrum increases substantially in response to an increasing exciton coherence length (note the change in the y-axis scale) and continues to narrow well below the width of  $L(\Delta)$  due to the onset of motional narrowing. In the (finite-size) strong coupling regime (panel d), the PL spectrum becomes the mirror image of the absorption spectrum; in this case, the PL line widths for all vibronic peaks are essentially identical to the motional-narrowed value,  $(2\ln 2)^{1/2}\sigma_d/\sqrt{6} \approx 0.14\omega_{\text{vib}}$ . Although the PL spectrum in the H-aggregates of Figure 35 vanishes with increasing bandwidth, the line widths approach the ideal motional narrow value just as for J-aggregates.

#### 4.4. The Effect of Thermal Excitations

Up to this point, it has been assumed that thermal excitations in either the ground or electronic excited states are negligible. Ground state thermal excitations are responsible for hot bands in the absorption spectrum whenever  $k_B T$  approaches the energy of a vibrational quantum,  $\omega_{\text{vib}}$ . Recently, Bloemsma et al.<sup>180</sup> have demonstrated that when  $k_B T$  is on the order of  $\omega_{\text{vib}}$  or larger, the absorption spectrum of J-aggregates undergoes significant spectral broadening with the appearance of a multitude of hot bands reflective of single-molecule absorption (see Figure 4 in ref 180). Such effects can be safely neglected whenever  $k_B T$  is much smaller than a vibrational quantum, which is certainly the case for the progression-building vinyl stretching mode in conjugated organic molecules with an energy of  $\sim 7k_B T$  at room temperature. However, this is not the case for lower-frequency modes such as those derived from torsional motion with energies typically around  $100 \text{ cm}^{-1}$ . Moreover, thermal line broadening, caused mainly by exciton-(lattice) phonon scattering, can be important in the solid phase due to the high density of states for acoustic and optical phonons. Such processes are normally treated perturbatively using a Fermi Golden rule approach.<sup>25</sup> More elaborate models

by Heijs et al. involving acoustic phonon scattering within an energetically disordered landscape have been very successful in accounting for the temperature-dependent line broadening in PIC-Br J-aggregates.<sup>328,329</sup> Arias et al. evaluated the relative impact of the temperature-dependent homogeneous broadening vs the static inhomogeneous broadening in cyanine aggregates using two-dimensional optical spectroscopy.<sup>330</sup>

In what follows, attention is restricted to temperature-dependent spectral signatures distinguishing J- and H-aggregates, assuming  $k_B T \ll \omega_{\text{vib}}$ . Homogeneous dephasing processes such as exciton–phonon scattering mainly cause line broadening but do not affect the vibronic band oscillator strengths (which are derived by spectral integration). Hence, the ratio  $R_{\text{abs}}$  in the absorption spectrum will only be minimally impacted by increasing temperature. Thermal expansion of the lattice constants and the resulting change in the intermolecular couplings can, however, lead to small spectral shifts and changes in  $R_{\text{abs}}$ .<sup>145</sup> By contrast, the PL spectrum, which derives from just the lowest energy (emitting) excitons, is extremely sensitive to temperature. If thermal equilibrium is established before the exciton can decay radiatively or nonradiatively, the PL spectrum will be sensitive to the system temperature through a Boltzmann population of emitting excitons. Interesting cases arise when the exciton radiatively decays before it can thermally equilibrate as can occur in superradiant J-aggregates, see Bednarz et al.<sup>331,332</sup>

The dependence of the steady-state PL spectral line shape on temperature has been investigated theoretically for linear J-aggregates in refs 176 and 242 and also for 2D herringbone (HB) lattices.<sup>176,260,261,333</sup> HB aggregates, or generally any aggregate with two molecules per unit cell, possess PL line shapes resembling ideal J-aggregates as long as the lowest energy exciton has a symmetry allowed 0–0 transition. In such packing arrangements, the 0–0 band in the PL spectrum is particularly sensitive to temperature, which can ultimately be traced back to the uniquely coherent nature of 0–0 (vs sideband) emission, see section 4.1.2.

For an ideal linear J-aggregate with vibronic coupling, the excited state energy levels and transitions to and from the ground electronic states are depicted in Figure 36. In J-aggregates, the lowest energy exciton has  $k = 0$ ; hence, at  $T = 0 \text{ K}$ , emission derives entirely from the  $k = 0$  state and consists of the coherently enhanced 0–0 emission as well as the incoherent sidebands (0–1, 0–2, ...) as indicated by the red arrows in the central part of the figure. Increasing temperature decreases the population of the  $k = 0$  exciton and increases the populations of the higher-energy  $k \neq 0$  states. The  $k \neq 0$  excitons, however, cannot emit to the vibrationless ground state,  $|G\rangle$ , because this does not conserve quasi-momentum. Only sideband emission from  $k \neq 0$  excitons is allowed; for example, 0–1 emission from a  $k \neq 0$  exciton conserves momentum by terminating on the electronic ground state with a single phonon of wave vector  $q = k$  as indicated by the vertical arrows on the left side of Figure 36. Hence, as temperature increases, the 0–0 emission in J-aggregates steadily decreases while the intensity of the sideband emission remains relatively constant because all excitons, independent of  $k$ , contribute sideband emission, and the sideband line-strengths are only weakly dependent on  $k$ .<sup>113,137,156</sup>

The disparate temperature-dependent behavior of the 0–0 vs sideband emission in J-aggregates is illustrated in Figure 37,<sup>176</sup> which shows numerically calculated PL spectra for an aggregate containing  $N = 10$  molecules. Here, the temperature-dependent

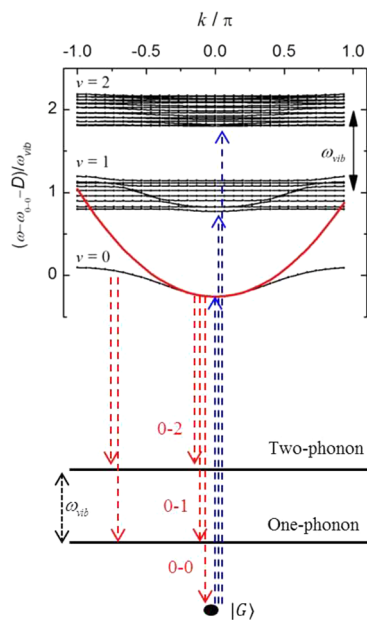


**Figure 36.** Energy level diagram for  $T$ -dependent PL corresponding to a linear J-aggregate with  $N = 30$  chromophores and  $W = \omega_{\text{vib}}$  assuming nearest neighbor coupling. The phonon bands are flat (dispersionless) as defines Einstein phonons. The red curve represents the parabolic approximation defined in eq 12. Reprinted with permission from ref 242. Copyright (2014), American Chemical Society.

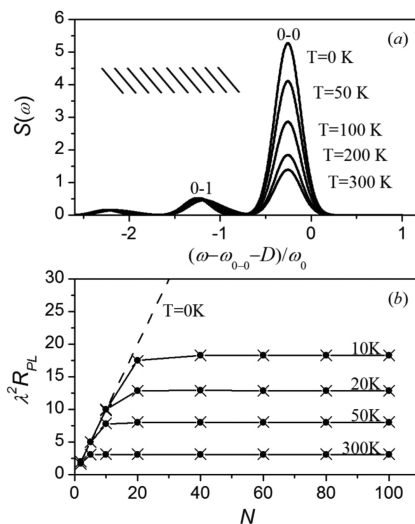


**Figure 37.** (a)  $T$ -dependent PL spectra for a J-aggregate composed of  $N = 10$  molecules with  $\lambda^2 = 1$ , nearest neighbor coupling, and  $W = \omega_{\text{vib}}$ . (b)  $\lambda^2 R_{PL}$  (solid dots) and the thermal coherence number  $N_T$  ( $\times$ ) at various temperatures as a function of the number of chromophores in the aggregate. Adapted with permission from ref 176. Copyright (2011), American Chemical Society.

line broadening is neglected so one can focus on the temperature-induced changes in the line strengths. As anticipated, the 0–0 emission decreases substantially with increasing temperature, whereas the sideband emission remains practically constant except for a small blue-shift reflecting the increasing contributions from the  $k \neq 0$  excitons with higher energies. We emphasize that additional temperature-induced quenching of the 0–0 and 0–1 intensities can arise from nonradiative decay processes. However, such processes serve to

attenuate the entire PL spectrum such that the ratio of 0–0 and sideband intensities (i.e.,  $R_{PL}$ ) remains unaffected.

A quantitative understanding of the temperature-dependent PL spectrum in linear J-aggregates was realized in refs 176, 242, and 243, which strongly paralleled prior work on temperature-dependent emission from the lower Davydov component in herringbone aggregates.<sup>260,261,333</sup> In these works, the vibronic line strengths are obtained by averaging over a Boltzmann distribution of exciton populations. The result for the 0–0 line strength is simply expressed in terms of a thermal coherence number,  $N_T$  ( $\langle N \rangle$ ) which replaces  $N$  in eq 60

$$\langle I_{PL}^{0-0} \rangle_T = N_T F \quad \text{J-aggs} \quad (94)$$

$N_T$  is equal to the total number of chromophores,  $N$ , multiplied by the temperature-dependent fraction of band-bottom ( $k = 0$ ) excitons

$$N_T \equiv \frac{N}{Z(N, T)} \quad (95)$$

Here,  $Z(N, T)$  is the partition function

$$Z(N, T) = \sum_{k,\alpha} \exp[-(\omega_{k,\alpha} - \omega_{k=0,\alpha=1})/k_B T] \quad (96)$$

where  $\omega_{k,\alpha}$  is the energy of the  $\alpha$ th exciton ( $\alpha = 1, 2, \dots$ ) with wave vector  $k$ ; for example, the lowest exciton band in Figure 36 is described by  $\omega_{k,\alpha=1}$  (recall  $\hbar = 1$ ). The thermal coherence number  $N_T$  can also be derived by inserting the thermal coherence function from eq 32 into the expression for  $N_{coh}$  in eq 34.

When the energetic separation between excitons near the band bottom is much larger than  $k_B T$ ,  $Z(N, T)$  reduces to unity and  $N_T$  becomes equal to  $N$ . In this case, eq 94 is physically realizable only for finite size aggregates. For arbitrarily large  $N$ , for example, in the “polymer” limit of section 4.2.6, eq 94 with  $N_T = N$  is untenable as it requires temperatures near absolute zero. Increasing temperature results in an increase in the partition function and a consequential demise in the coherence number via eq 95. Taking the thermodynamic limit and making the parabolic approximation on the exciton band (see eq 12) allows the sum in eq 96 to be replaced by an integral, giving<sup>242</sup>

$$N_T = \sqrt{\frac{4\pi\tilde{\omega}_c}{k_B T}} \quad 4\pi\tilde{\omega}_c > k_B T \gg \frac{4\pi\tilde{\omega}_c}{N^2} \quad (97)$$

where the curvature at  $k = 0$ ,  $\tilde{\omega}_c$  is evaluated under the influence of vibronic coupling (hence the tilde overstrike) and corresponds to the lowest energy band in Figure 36. The left inequality in eq 97, which can be rewritten as  $N_T > 1$ , ensures the validity of the parabolic approximation, whereas the right inequality, which can be rewritten as  $N > N_T$ , expresses the thermodynamic limit. We note that in some works<sup>176,260,261</sup> a “1” was added ad hoc to the right-hand side of eq 97 to obtain the correct high-temperature limit ( $N_T = 1$ ), see the discussion following eq 10 in ref 242.

Eq 97 shows that in linear J-aggregates the thermal coherence number  $N_T$  scales as the inverse square root of temperature ( $T^{-1/2}$ ) and increases with the square root of the band bottom curvature,  $\tilde{\omega}_c^{1/2}$ . An inverse square-root dependence for the coherence number was measured by Arias et al.<sup>330</sup> for thin films of two different cyanine dyes using two-dimensional Fourier transform optical spectroscopy.

Because the superradiant decay rate scales as  $N_T$ , the radiative lifetime,  $\tau_R$ , scales as  $1/N_T$ , and therefore,  $\tau_R \propto T^{1/2}$ . A

square-root dependence of  $\tau_R$  was reported by Schott and co-workers<sup>334–336</sup> for practically defect-free polydiacetylene (PDA)-based chains, which, as emphasized in refs 242 and 243, can be modeled as ideal linear J-aggregates. The inset of Figure 38 shows Schott's results alongside the predicted  $T^{1/2}$  temperature dependence.

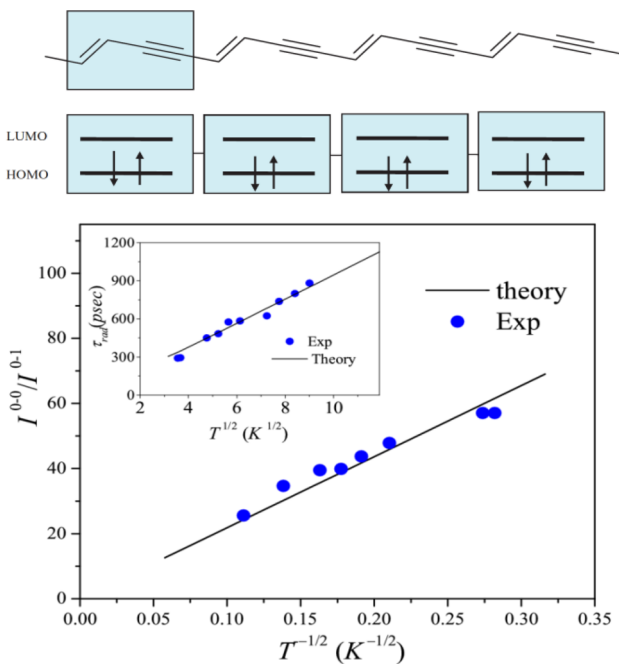


**Figure 38.** PL ratio as a function of the inverse square root of temperature for PDA chains. The blue dots represent the measurements of ref 334. The solid line represents theory based on eqs 97 and 99. Inset shows the radiative lifetimes as a function of the square root of temperature (see ref 243 for details). Reprinted with permission from ref 243. Copyright 2011, AIP Publishing.

By contrast, as shown in ref 176, the 0–1 line strength is essentially independent of temperature

$$\langle I^{0-1} \rangle_T \approx \lambda^2 F \quad k_B T \ll \omega_{\text{vib}} \quad (98)$$

and is not coherently enhanced. The PL ratio defined as the division of eq 94 by eq 98 therefore remains a direct measure of the number of coherently connected molecules in J-aggregates

$$R_{\text{PL}} \approx \frac{N_T}{\lambda^2} \quad (99)$$

Eq 99 is similar to eq 58 but with  $N$  replaced by  $N_T$  ( $\leq N$ ). The numerically evaluated values of  $\lambda^2 R_{\text{PL}}$  and  $N_T$  are plotted together in Figure 37b as a function of  $N$  for the J-aggregates in the top panel, demonstrating the validity of eq 99. The initial linear increase of  $N_T$  (or  $R_{\text{PL}}$ ) with  $N$  is characteristic of the finite size limit, where the energetic separation between neighboring excitons at the band bottom is greater than  $k_B T$ . Once  $N$  is large enough to justify the thermodynamic limit,  $N_T$  levels off to the value given by eq 97, which scales as the inverse square root of temperature. Schott and co-workers also reported an inverse square root temperature dependence for the PL ratio in isolated polydiacetylene chains as shown in Figure 38.<sup>334,336</sup> Finally, note that eq 99 is valid even when temperature-dependent line broadening is active because the latter does not impact the line strengths.

Unlike in J-aggregates, in ideal H-aggregates the 0–0 emission requires thermal activation of the  $k = 0$  exciton because the band-bottom exciton has a wave vector,  $k = \pi$ . For aggregates in the weak exciton coupling regime,  $W \ll \lambda^2 \omega_{\text{vib}}$ , 0–0 emission is activated when  $k_B T$  approaches the  $\tilde{\nu} = 0$  exciton bandwidth,  $\exp(-\lambda^2) W$ , creating a small blue-shift of the 0–0 peak by roughly  $\exp(-\lambda^2) W$ . In contrast to the case of J-aggregates, the 0–0 emission in H-aggregates increases with increasing temperature, although the sideband line-strengths are, as in J-aggregates, largely temperature independent. Figure 39 shows the PL spectrum for several temperatures in an H-

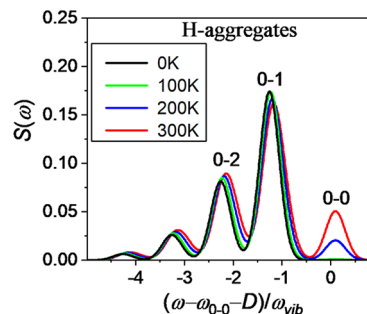


**Figure 39.**  $T$ -dependent PL spectra for H-aggregates composed of  $N = 10$  molecules with  $\lambda^2 = 1$ , nearest neighbor coupling,  $\Gamma_h = 0.2 \omega_{\text{vib}}$ , and  $W = \omega_{\text{vib}}$ .

aggregate for parameters identical to those describing the J-aggregate in Figure 37a (except for the sign change in the Coulomb coupling.) An increase in  $R_{\text{PL}}$  with increasing temperature has been measured in P3HT  $\pi$ -stacks,<sup>337</sup> which behave like weakly coupled H-aggregates,<sup>143–146,327</sup> see Figure 21.

In aggregates of higher dimensionality, the temperature dependence of  $N_T$  and  $R_{\text{PL}}$  strongly depends on the coupling anisotropy. In a two-dimensional (2D) isotropic J-aggregate consisting of a square lattice with all four nearest neighbor couplings equal (and negative), the energy dispersion takes on the shape of a parabolic “bowl” with a minimum at  $k = 0$ . In this case, the two-dimensional partition function can be readily evaluated giving the most general form for the thermal coherence number,  $N_{T,2D}$ , as in eq 95. In the thermodynamic limit, the thermal coherence number becomes

$$N_{T,2D} \approx \frac{4\pi\tilde{\omega}_c}{k_B T} \quad 4\pi\tilde{\omega}_c > k_B T \gg \frac{4\pi\tilde{\omega}_c}{N} \quad (100)$$

which is simply the square of the 1D result in eq 97. The 2D result actually has direct applications in herringbone aggregates<sup>260,261</sup> as discussed later in section 4.7.2. Eq 100 predicts a 0–0 line strength (and  $R_{\text{PL}}$ ) proportional to inverse temperature, which is equivalent to a radiative lifetime proportional to temperature. Such a relationship has been established early on in monolayers of oxacyanine J-aggregates by Möbius and Kuhn.<sup>57,58</sup> They suggested that the thermal coherence size was fixed by the competition between the energy stabilization gained by increasing the coherence size and the thermal fluctuations that disrupt coherence. A  $1/T$  dependence for the radiative decay rate was also measured by De Boer and Wiersma<sup>38</sup> in pseudoisocyanine bromide aggregates in ethylene glycol/water glass. More complex temperature dependences arise in aggregates with anisotropic interactions<sup>338</sup> such as the segregated HJ-aggregates<sup>15,249</sup> of

section 4.9. Such aggregates can display unusual temperature-induced superradiance in addition to other behaviors that are quite different from either H- or J-aggregates.

#### 4.5. Monitoring Exciton Coherence using PL

Determining the number of chromophores over which the exciton is coherently delocalized,  $N_{coh}$ , has been a primary goal of many research efforts in J-aggregates. To this end, several methods have been employed, including techniques based on the inhomogeneous line width of the J-band,<sup>40,319</sup> the enhancement of the radiative decay rate,<sup>38,39,41,43,47,339,340</sup> and the shape of the nonlinear absorption spectrum.<sup>289,320,341</sup> Relatively recently, Arias et al.<sup>330</sup> used two-dimensional optical spectroscopy to probe the exciton coherence length in cyanine dye aggregate films, showing that temperature-dependent dynamical effects, such as exciton–(lattice)-phonon scattering, are mainly responsible for defining the exciton coherence number.

Many of the aforementioned methods used to obtain  $N_{coh}$  downplay the impact of vibronic coupling, which in many cases is not insignificant. For example, if the J-aggregate radiative decay rate is measured to be 10-times larger than the monomer value, then one would estimate  $N_{coh}$  to be ~10 without consideration of vibronic coupling. However, as discussed earlier, the coherent decay rate scales as  $N_{coh}F$  for J-aggregates, where  $F$  is the generalized FC factor, ranging from  $\exp(-\lambda^2)$  in the weak exciton coupling regime to essentially unity in the strong coupling regime. Hence, if the HR factor is one ( $\lambda^2 = 1$ ) and the exciton coupling is relatively weak, the actual value of  $N_{coh}$  is closer to 30 ( $= 10/F$ ) in the example considered. (Note that even under weak coupling,  $N_{coh}$  can substantially exceed the monomer value,  $N_{coh} = 1$ , as long as disorder is minimal and the temperature is sufficiently low, so that only the lowest energy exciton is thermally populated, see section 4.4.)

As demonstrated theoretically in ref 176 in J-aggregates, the steady-state PL ratio  $R_{PL}$  ( $\equiv I^{0-0}/I^{0-1}$ ) scales linearly with the exciton coherence number,  $N_{coh}$ , making  $R_{PL}$  a direct probe of the exciton coherence length. Unlike previous methods, one does not require a priori knowledge of the FC factor,  $F$ , to accurately measure  $N_{coh}$ . The PL ratio rule,  $R_{PL} = N_{coh}/\lambda^2$ , valid over the weak to strong coupling regimes, was introduced in section 4.2.4 for the special case of a defect-free J-aggregate at  $T = 0$  K, where the coherence number is maximal,  $N_{coh}=N$ , and revisited in section 4.4 for ideal J-aggregates at finite temperatures, where  $N_{coh}$  is equal to  $N_T$ , the thermal coherence number. The current section focuses on the generalized ratio rule, applicable for linear, disordered aggregates in thermal equilibrium with their surroundings. As shown in ref 176, the ratio rule also applies to more complex packing architectures with multiple molecules per unit cell such as the ubiquitous herringbone lattice reviewed in section 4.7, as long as the optical transition from lowest energy exciton is symmetry-allowed to the vibrationless ground state (thereby excluding H-aggregates). The ratio rule was also shown to be robust to the presence of charge transfer<sup>342</sup> (see section 5.5) and multiple-mode vibronic coupling<sup>262</sup> (see section 4.9).

On the basis of the ratio rule using integrated 0–0 and 0–1 band intensities to construct  $R_{PL}$ , Sokolowski and co-workers determined the equilibrium number of coherently connected chromophores,  $N_{coh}$ , in monolayers of the perylene derivative PTCDA on a KCl substrate.<sup>338,343</sup> They measured perhaps the largest coherence numbers reported to date with  $N_{coh}$  peaking at ~50 at  $T = 16$  K. The ratio  $R_{PL}$  is also able to monitor

temporal changes in  $N_{coh}$  following impulsive excitation.<sup>195</sup> In this regard, Sung et al. used  $R_{PL}(t)$  obtained from time-resolved photoluminescence measurements to monitor subpicosecond exciton localization in perylene diimide aggregates.<sup>36</sup>  $R_{PL}$  has also been used to justify the ultralarge coherence lengths measured in highly ordered polydiacetylene chains,<sup>243,335</sup> to determine  $N_{coh}$  in oligoacene crystals<sup>176,344,345</sup> and dinaphthothieno-thiophene (DNTT) crystals,<sup>346</sup> and to monitor coherence in a phosphorescent Pt-containing polymer.<sup>347</sup>

Exciton coherence can also be monitored in H-aggregates using  $R_{PL}$ , although there is no simple ratio rule as in J-aggregates. In H-aggregates,  $R_{PL}$  decreases with increasing coherence number, exactly opposite to what happens in J-aggregates. Nevertheless, the PL line shape can still be analyzed numerically to extract  $N_{coh}$  as was successfully accomplished in refs 145 and 327 for P3HT H-aggregates.

In what follows, we will review the basic theory establishing the relationship between  $R_{PL}$  and the exciton coherence number in energetically disordered J- (and H-)aggregates in equilibrium with a bath at temperature  $T$ .<sup>176</sup> We start with steady-state PL, which reports on the steady-state coherence number,  $N_{coh}$ , and conclude with a discussion of time-resolved PL, which can be used to monitor the temporal development of  $N_{coh}(t)$  following impulsive excitation.

**4.5.1. Steady-State Coherence.** A deeper understanding of the PL ratio rule in the steady-state limit is obtained by appreciating the central role the exciton coherence function,  $C(s)$ , introduced in section 3.5, plays in determining the 0–0 line strength,  $I^{0-0}$ , and the coherence number,  $N_{coh}$ .<sup>176</sup> To this end, we begin with an exact relationship between the square of the transition dipole moment,  $|\langle G|\hat{M}|\psi_i\rangle|^2$ , where  $|\psi_i\rangle$  is an eigenstate of the Frenkel–Holstein Hamiltonian in eq 13 generalized to include site disorder (see eq 86) and the corresponding coherence function

$$|\langle G|\hat{M}|\psi_i\rangle|^2 = \mu^2 \sum_s C_i(s) \quad (101)$$

The dipole moment operator,  $\hat{M}$ , was defined in eq 8, and the coherence function  $C_i(s)$  was defined in eq 31. Eq 101 is strictly valid when the transition dipole moment is the same for all chromophores, i.e., when there is no orientational disorder. For aggregates at  $T = 0$  K, (steady-state) 0–0 emission proceeds directly from the lowest-energy excited state,  $|\psi_{em}\rangle$ , which can range from a localized “trapped” excitation to a completely delocalized exciton characteristic of aggregates with no disorder. The 0–0 emission line strength is directly sensitive to the exciton’s coherence function. Using eq 101, the 0–0 line strength defined in eq 43 can be re-expressed as<sup>145,176</sup>

$$I^{0-0} = \sum_s C_{em}(s) \quad (102)$$

where  $C_{em}(s)$  is the coherence function corresponding to  $|\psi_{em}\rangle$ . According to eq 102, the 0–0 line strength is essentially the integral of the coherence function.

The coherence functions for ideal (defect-free) J- and H-aggregates, where  $|\psi_{em}\rangle$  is an exciton delocalized over the entire aggregate, are depicted in Figure 9; recall that, in J-aggregates, the coherence function has uniform phase,  $C_{em}(s) = C_{em}(0)$ , whereas in H-aggregates, the coherence function undergoes rapid phase oscillations,  $C_{em}(s) = C_{em}(0)(-1)^s$ . (Here, we are assuming periodic boundary conditions.) The disparate behaviors reflect the nature of the band-bottom exciton, which has wave vector  $k = 0$  for J-aggregates and  $k = \pi$  for

H-aggregates. Evaluating the rhs of eq 102 gives coherent enhancement,  $I^{0-0} = NC_{\text{em}}(0)$ , in ideal J-aggregates (see eq 60), and coherent suppression,  $I^{0-0} = 0$ , in ideal H-aggregates. However, for both H- and J-aggregates the exciton remains fully delocalized over all  $N$  molecules, i.e.,  $N_{\text{coh}}=N$ . This result follows from the definition of  $N_{\text{coh}}$  in eq 34 after inserting  $C_{\text{em}}(s)$  for the J- and H-aggregates of Figure 9. Hence, whereas the 0–0 line strength derives from the sum over  $C_{\text{em}}(s)$ , the exciton coherence number derives from the sum over  $|C_{\text{em}}(s)|$ . This leads to the following opposing behaviors exhibited by J- and H-aggregates: as the lowest-energy eigenstate,  $|\psi_{\text{em}}\rangle$  localizes and  $C_{\text{em}}(s)$  narrows the 0–0 emission decreases in J-aggregates but increases in H-aggregates. In the limit of complete localization,  $N_{\text{coh}}$  is unity and the 0–0 emission reflects that of an isolated chromophore for both aggregate types. Hence,  $I^{0-0}$  and  $N_{\text{coh}}$  are directly correlated in J-aggregates and anticorrelated in H-aggregates. Furthermore, because the sideband line strength  $I^{0-1}$  is not coherent, the ratio  $R_{\text{PL}}$  obeys the same relationship to  $N_{\text{coh}}$  as does  $I^{0-0}$ .

In ref 176, the relationship among  $I^{0-0}$ ,  $R_{\text{PL}}$ , and the exciton coherence function was investigated for an ensemble of disordered aggregates with exciton populations equilibrated with the environment at temperature  $T$ . The disorder was limited to the site energies (i.e., diagonal disorder) as described in detail in section 4.3. In this more general case, the 0–0 emission is obtained by averaging the left side of eq 101 over a Boltzmann distribution of exciton populations within each configuration of site energy detunings,  $\{\Delta_1, \Delta_2, \dots, \Delta_N\}$  and then averaging the result over all configurations. The result is<sup>145,176,182</sup>

$$\langle I^{0-0} \rangle_{T,C} = \sum_s \langle C(s) \rangle_{T,C} \quad (103)$$

where the ensemble averaged coherence function,  $\langle C(s) \rangle_{T,C}$ , was defined after eq 32. Here,  $\langle I^{0-0} \rangle_{T,C}$  scales as the number of 0–0 photons emitted from all excited states in an interval of approximately  $k_B T$  from the lower exciton band edge. The coherence number can be similarly generalized by averaging over the right-hand-side of eq 34 giving<sup>176</sup>

$$N_{\text{coh}} \equiv \frac{1}{|\langle C(s=0) \rangle_{C,T}|} \sum_s |\langle C(s) \rangle_{C,T}| \quad (104)$$

For disordered J-aggregates at temperature  $T$ , the generalized PL ratio rule

$$R_{\text{PL}} \approx \frac{N_{\text{coh}}}{\lambda^2} \quad (105)$$

with  $N_{\text{coh}}$  taken from eq 104 was found to be highly accurate as long as  $\sigma_d, k_B T \gtrsim 0.3\omega_{\text{vib}}$ , where  $\sigma_d$  is the width of the disorder distribution.<sup>176</sup> For the dominant vinyl stretching mode in  $\pi$ -conjugated oligomers  $\omega_{\text{vib}} \approx 0.18$  eV, eq 105 is therefore valid for physically relevant values of  $\sigma_d$  and for temperatures up to room temperature.

For illustrating the intimate relationships between  $I^{0-0}$ ,  $R_{\text{PL}}$ , and  $N_{\text{coh}}$ , an ensemble of disorder-free H- and J-aggregates in equilibrium with a bath at temperature  $T$  is considered first. In ref 176, the mean coherence function  $\langle C(s) \rangle_T$  was investigated as a function of  $T$  for J-aggregates with  $N = 60$ , the result is shown in Figure 40 (top). The bottom panel shows the results for an H-aggregate obtained by simply changing the sign of  $J_C$ . For both J- and H-aggregates, the envelope of the coherence function narrows with increasing temperature. The temper-

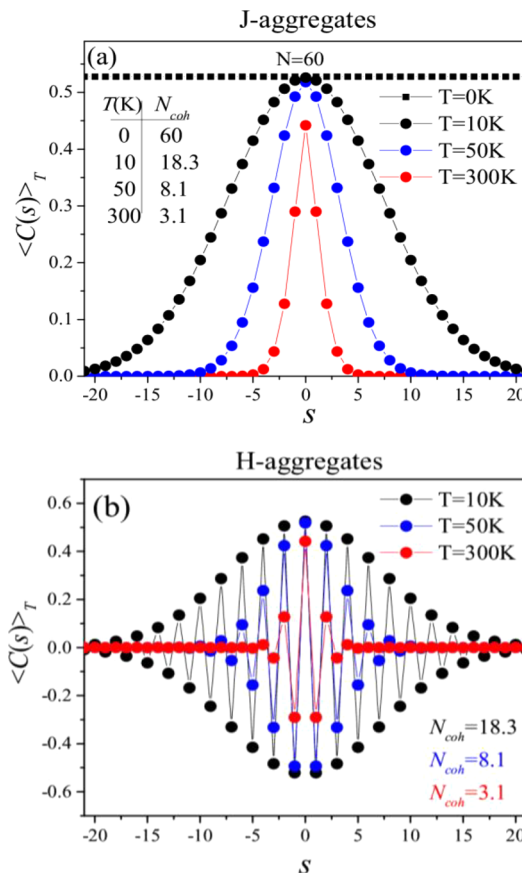


**Figure 40.** Exciton coherence function for disorder-free linear J-aggregates (a) and H-aggregates (b) with  $N = 60$  at several temperatures. In all cases, the bandwidth is  $W = \omega_{\text{vib}} = 0.17$  eV and  $\lambda^2 = 1$ . Adapted with permission from ref 176. Copyright (2011), American Chemical Society.

ature-induced localization is quantified by the diminishing values of  $N_{\text{coh}}$  reported in the figure insets. Note that the  $T$ -dependent coherence number, obtained from eq 104, is identical in both aggregate types in Figure 40. (In ref 176, the equivalence between  $N_{\text{coh}}$  in eq 104 and  $N_T$  in eq 95 was established as long as  $k_B T \ll \omega_{\text{vib}}$ , which is easy to satisfy at room temperature for the vinyl-stretching mode.) In marked contrast, the 0–0 emission line strength differs widely for J- and H-aggregates because  $I^{0-0}$  is also sensitive to the phase of the coherence function. Figure 37a of the previous section demonstrates the demise of  $I^{0-0}$  and  $R_{\text{PL}}$  with increasing temperature for J-aggregates, and Figure 39 shows the opposing behavior exhibited by H-aggregates. (Both figures assume  $N = 10$ ,  $W = \omega_{\text{vib}}$ , and  $\lambda^2 = 1$ .) As shown in Figure 37b, the numerically obtained values of  $R_{\text{PL}}$  are in excellent agreement with  $N_{\text{coh}}/\lambda^2$ , validating eq 105 for J-aggregates.

The central role played by the coherence function in establishing the relationships among  $R_{\text{PL}}$ ,  $I^{0-0}$ , and  $N_{\text{coh}}$  means that such relationships are independent of the details of how the coherence function itself is established. For example, in aggregates with diagonal disorder but held at sufficiently low temperatures (so that the Boltzmann average in eq 104 need not be performed), the coherence function can narrow in response to disorder-induced localization, yet the impact on the PL line shape is very similar to the case of temperature-induced localization. This is demonstrated for J-aggregates (with  $N = 60$ ) in Figure 41, where the coherence function is shown to

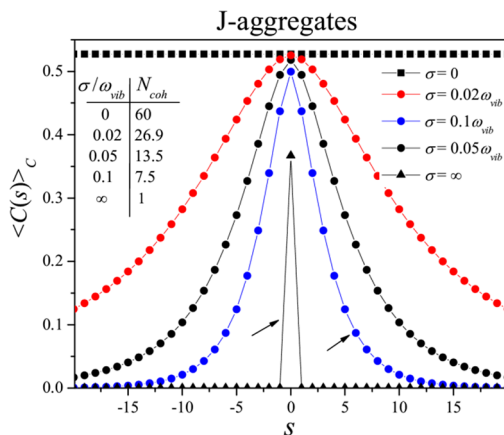


**Figure 41.** Coherence function for a disordered ensemble of J-aggregates with  $N = 60$  for several levels of short-range Gaussian disorder. The disorder distribution has standard deviation  $\sigma_d = \sigma/\sqrt{2}$  (see section 4.3), and  $10^4$  configurations were averaged together to obtain the coherence function. The eigenspectrum for each disordered member of the ensemble was evaluated using the Holstein Hamiltonian with n.n. coupling. In all cases, the bandwidth is  $= \omega_{\text{vib}} = 0.17$  eV,  $\lambda^2 = 1$  and  $T = 0$  K. Adapted with permission from ref 176. Copyright (2011), American Chemical Society.

diminish substantially as short-range disorder increases. Although not shown, in an H-aggregate that differs only by the sign of  $J_C$  from the J-aggregate in Figure 41, the coherence function has the same envelope as that shown in the figure but with an additional phase factor of  $(-1)^s$ .

The impact of disorder on the PL spectrum of the J-aggregate from Figure 41 is shown in Figure 42a. Here, the homogeneous line width was chosen to be at least twice as large as the disorder width ( $\sigma_d$ ) so that the latter has minimal impact on the line widths. This allows one to immediately appreciate the disorder-induced changes in the line strengths from which  $R_{\text{PL}}$  is evaluated directly from the peak intensities (i.e., without

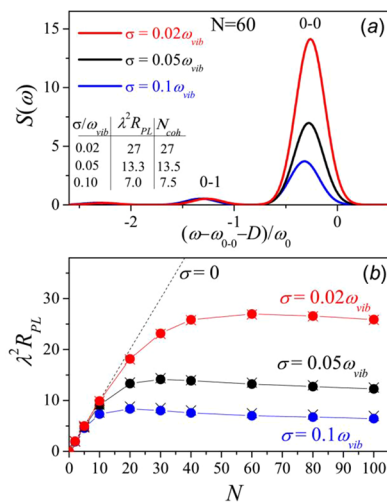


**Figure 42.** (a) The reduced PL spectrum for linear J-aggregates with  $N = 60$  molecules and various amounts of short-range Gaussian disorder with standard deviation  $\sigma_d = \sigma/\sqrt{2}$  (see section 4.3). (b)  $\lambda^2 R_{\text{PL}}$  (solid dots) and  $N_{\text{coh}}$  (x) as a function of  $N$  for several values of  $\sigma$ . All of the parameters needed to define the Holstein Hamiltonian are the same as in Figure 40. Reprinted with permission from ref 176. Copyright (2011), American Chemical Society.

having to perform a spectral integration). As in the case for thermal localization, the ratio  $R_{\text{PL}}$  as well as  $N_{\text{coh}}$  decrease as the coherence function increasingly narrows and the ratio rule is well satisfied. As can be appreciated from Figure 42b, the coherence number initially increases with  $N$  but eventually levels off when  $N$  is much larger than  $N_{\text{coh}}$ . Throughout the evolution, the ratio rule in eq 105 remains accurate, allowing  $N_{\text{coh}}$  to be determined directly from a (steady-state) PL measurement.

**4.5.2. Time Evolutions of Coherence.** Tempelaar et al.<sup>195</sup> extended the steady-state formalism considered so far into the time domain by introducing a time-dependent coherence number,  $N_{\text{coh}}(t)$ , evaluated using the density matrix equations of motion. In this way, dephasing and population relaxation, which occur via interactions between the system and surrounding bath, can be incorporated. In ref 195,  $N_{\text{coh}}(t)$  and  $R_{\text{PL}}(t)$  were evaluated following impulsive excitation into the optically allowed ( $k = 0$ ) exciton residing in the lowest energy vibronic band ( $\tilde{\nu} = 0$ ) in both J- and H-aggregates. The molecular transition frequencies were allowed to undergo temporal fluctuations according to an overdamped Brownian oscillator model, and population relaxation was accomplished through a surface-hopping algorithm constrained so that at long times the populations approach a Boltzmann distribution. The main results appear in Figure 43. For J-aggregates, the

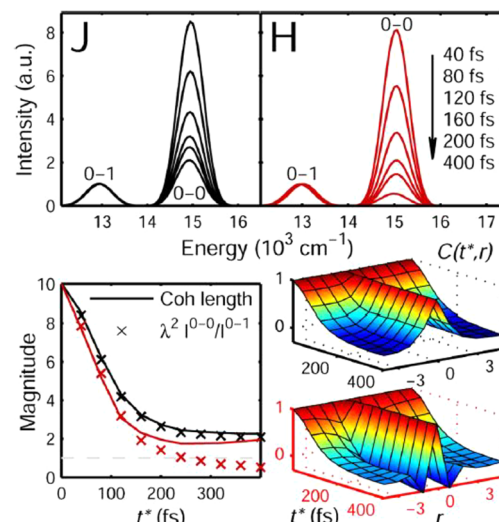


**Figure 43.** (top) Simulated, time-resolved PL spectra for linear J- (black) and H- (red) aggregates with  $N = 10$  molecules. In both cases, nearest neighbor couplings were assumed with  $W = 200$  cm<sup>-1</sup>,  $\lambda^2 = 1$ , and  $\omega_{\text{vib}} = 2000$  cm<sup>-1</sup>. (bottom left) The PL ratio (note  $R_{\text{PL}} = I^{0-0}/I^{0-1}$ ) and the calculated coherence length as a function of time from the initial excitation. (bottom right) Time evolution of the normalized coherence function for J- (upper) and H- (lower) aggregates. Reprinted with permission from ref 195. Copyright (2014), American Chemical Society.

coherence function and PL ratio remain equal throughout the entire evolution, generalizing the ratio rule to read

$$R_{\text{PL}}(t) \approx \frac{N_{\text{coh}}(t)}{\lambda^2} \quad (106)$$

As demonstrated in ref 195, the early time attenuation of  $N_{\text{coh}}$  is due almost entirely to off-diagonal dephasing (relative to the eigenbasis). The H-aggregates in Figure 43 are also quite interesting because at early times the coherence function and

PL ratio track each other quite closely, just as in J-aggregates. This occurs because immediately following impulsive excitation the  $k = 0$  exciton at the top of the vibronic band has not yet relaxed to the band bottom ( $k = \pi$ ); however, as the population eventually relaxes toward the band bottom, the PL ratio drops below the coherence number due to the development of nodes in the coherence function (see the lower right panel of Figure 43). At long times,  $R_{\text{PL}}$  becomes smaller than the molecular value ( $1/\lambda^2$ ) as is characteristic of steady-state (thermal) emission from H-aggregates. Note that  $R_{\text{PL}}$  does not approach zero because the temperature considered in the simulation is 77 K. Interestingly, no spectral evolution is observed in the 0–0 peak position because only the  $k = 0$  exciton at the top of the band can source 0–0 emission. The full spectral relaxation, equal to the  $\tilde{\nu} = 0$  bandwidth, is only  $\sim 60 \text{ cm}^{-1}$ , which is barely discernible as a small red-shift in the sideband emission at long times.

**4.5.3. Utility of  $R_{\text{PL}}$ .** As mentioned at the beginning of this section,  $R_{\text{PL}}$  has advantages over methods based on a direct measurement of the superradiant decay rate in determining the exciton coherence number because application of the ratio rule does not require a priori knowledge of the exciton bandwidth (or the generalized FC factors). In addition, extracting the superradiant decay rate from the overall fluorescence decay rate requires knowledge of the temperature-dependent quantum yield, which is often difficult to measure, especially in crystalline samples. In contrast, the PL ratio is immune to nonradiative processes that compete with the radiative decay because such processes will only serve to dampen the entire PL spectrum, leaving the relative vibronic intensities unaffected. Perhaps the largest concern with using the ratio rule is reabsorption in optically thick samples. Reabsorption of the 0–0 photons will lead to an apparent drop in the PL ratio and hence an underestimation of  $N_{\text{coh}}$ . Reabsorption must therefore be carefully eliminated or accounted for to reliably use the ratio rule.<sup>138</sup>

#### 4.6. Linear Aggregates with Two Molecules Per Unit Cell

A strong dependence of the absorption spectrum of PIC aggregates on the polarization of the excitation source was demonstrated early on by Scheibe.<sup>50</sup> The top panel in Figure 44 shows the PIC absorption spectrum in streaming solution from ref 50. The spectrum contains a narrow, red-shifted J-band that is strongly polarized parallel to the aggregate axis as well as a much broader, blue-shifted band that is polarized orthogonal to the axis. Vibronic coupling is clearly evident in both bands. Note in particular that the dominant J-band at  $\sim 17,500 \text{ cm}^{-1}$  is followed by a weak shoulder at  $\sim 19,000 \text{ cm}^{-1}$ . The difference is roughly one vibrational quantum of the progression forming mode ( $\omega_{\text{vib}} \approx 1400 \text{ cm}^{-1}$ ,  $\lambda^2 \approx 0.6$ ) identified in the monomer spectrum shown in Figure 11. The corresponding large value of  $R_{\text{abs}} \gg 1/\lambda^2$  and the appearance of only one main sideband is indicative of strong exciton coupling in the “polymer” limit; compare the J-band spectrum to that in Figure 27. By contrast, the vibronic structure in the spectrum polarized normal to the aggregate axis resembles an H-aggregate with a blue-shifted main absorption peak and suppressed value of  $R_{\text{abs}}$ . The bottom panel of Figure 44 shows the stick spectra of Scherer and Fischer<sup>165</sup> calculated numerically using the Holstein Hamiltonian for a linear aggregate parametrized with  $J_C \approx -0.5\omega_{\text{vib}}$ ,  $\omega_{\text{vib}} = 1368 \text{ cm}^{-1}$ , and  $\lambda^2 = 0.6$ . The calculated spectra along and normal to the aggregate axis arise from transitions to excitons with  $k = 0$  and  $k = \pi$ , respectively, and reproduce the

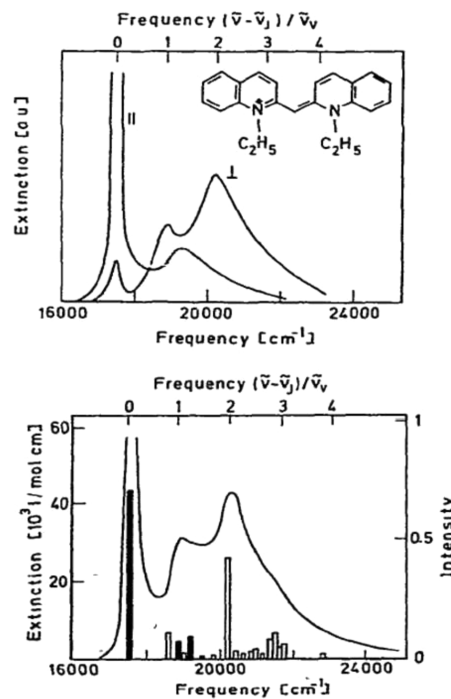


**Figure 44.** (top) Polarized absorption spectra of PIC measured in ref 50. (bottom) Unpolarized spectrum alongside calculated stick spectrum from ref 162. Solid (open) sticks correspond to light polarized along (perpendicular) to the aggregate axis. Reprinted with permission from ref 165. Copyright 1984, Elsevier.

main features of the measured spectrum. Eisfeld and Briggs obtained similarly impressive theoretical reproductions of the PIC absorption spectrum using the coherent exciton scattering approximation.<sup>167,168</sup> Kato et al. also investigated theoretically the polarized absorption spectrum including the effects of vibronic coupling using a coherent potential approximation.<sup>184</sup> Note that although PIC aggregates exhibit polarization-dependent J- and H-aggregate spectra<sup>309</sup> we refrain from calling such aggregates “HJ-aggregates”. The latter classification is reserved for packing geometries that host both H- and J-promoting couplings, see section 4.8.

In addition to PIC aggregates<sup>50,184,348–350</sup> and crystals,<sup>351</sup> strong polarization-dependent absorption and emission spectra have been observed in aggregates of thiacyanine dyes,<sup>66</sup> porphyrins,<sup>82,83</sup> perylenes,<sup>229</sup> and squaraines<sup>352</sup> as well as the many herringbone-packed aggregates and crystals reviewed in section 4.7. The polarization dependence of these systems arises from packing arrangements with two (or more) molecules in a unit cell. The simplest example is the linear aggregate illustrated in Figure 45. Early on, McRae and Kasha<sup>23</sup> considered the band structure of such aggregates using the point-dipole approximation for the Coulomb coupling. The molecular dipole moments  $\mu_1$  and  $\mu_2$  within the unit cell are of equal magnitude ( $\mu$ ) but not aligned with the misalignment defined by the angle  $\alpha$ . Note that we have defined the relative directions (phases) of  $\mu_1$  and  $\mu_2$  differently for H- and J-aggregates, as indicated in the figure. In the J-type aggregate of Figure 45a ( $\alpha < \pi/4$ ),  $\mu_1$  and  $\mu_2$  are mainly head-to-tail, resulting in a negative Coulomb coupling,<sup>23</sup>  $J_C = -\mu^2(1 + \cos^2 \alpha)/4\pi\epsilon d^3$ , where  $d$  is the nearest-neighbor distance assumed to be uniform along the chain. Hence, in J-type aggregates, the  $k = 0$  exciton is positioned at the band bottom, as in the Scheibe (J-) aggregates. By contrast, for the “side-by-

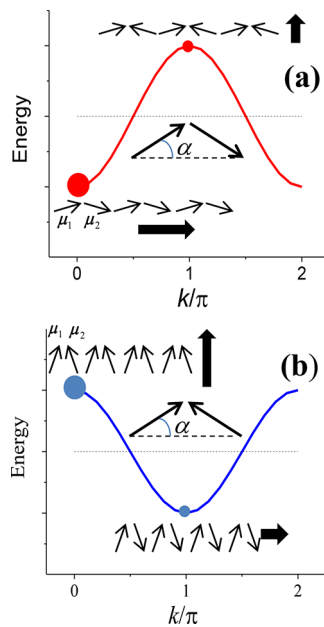


**Figure 45.** Exciton dispersion curves for J-type (a) and H-type (b) linear aggregates with two molecules in a unit cell. In J-type aggregates,  $\alpha < \pi/4$ , whereas in H-type aggregates,  $\alpha > \pi/4$ . Thick arrows indicate the polarization and approximate relative intensity of the respective transition. Note that, in both cases, the band-bottom exciton has a transition parallel to the aggregate axis. The dots indicate states with allowed transitions from  $|G\rangle$  with radii proportional to the oscillator strength. When  $\alpha = \pi/4$ , there is no difference in the aggregate photophysics for J- vs H-types (both polarized transitions have equal intensity).

side” H-type aggregates of Figure 45b ( $\alpha > \pi/4$ ), the Coulomb coupling is positive,  $J_C = \mu^2(1 + \cos^2 \alpha)/4\pi e d^3$ , resulting in the  $k = 0$  exciton residing at the top of the band. Because in both aggregate types the nearest-neighbor coupling is uniform along the chain (because  $d$  is constant), the exciton eigen structure is unchanged from a linear aggregate with just one molecule per unit cell. Hence, as in refs 165, 167, and 168, we can continue to define the (free) excitons according to eq 3 with  $k$  ranging from  $-\pi$  to  $\pi$  (or 0 to  $2\pi$ ) in units of  $d^{-1}$ . With the Brillouin zone so defined, the aggregates in Figure 45 support two transitions: one to the  $k = 0$  exciton with an oscillator strength proportional to  $|\mu_1 + \mu_2|^2$  and polarized parallel to the aggregate axis in J-type aggregates (normal to the axis in H-type aggregates), and the second to the  $k = \pi$  exciton with an oscillator strength proportional to  $|\mu_1 - \mu_2|^2$  and polarized normal to the aggregate axis in J-type aggregates (parallel to the axis in H-type aggregates).

**4.6.1. Polarized Absorption and the Ratio Formula.** Generally, the two excitons with orthogonal polarizations are revealed in aligned samples by measuring the absorption spectrum with the exciting electric field aligned along ( $\parallel$ ) and normal ( $\perp$ ) to the aggregate axis. When vibronic coupling is included, each polarized component of the spectrum contains additional vibronic structure as demonstrated in Figure 46 for the two aggregate types of Figure 45. The calculated J- and H-type spectra in Figure 46a and b correspond to aggregates with  $N = 6$  chromophores and hence reduce exactly to the corresponding ideal (i.e., one molecule per unit cell) J- and H-aggregate spectra in Figure 17c and h as  $\alpha$  approaches zero (J-type) and  $\pi/2$  (H-type). Interestingly, the dominant (minor) polarization component in the J-type aggregate has the same

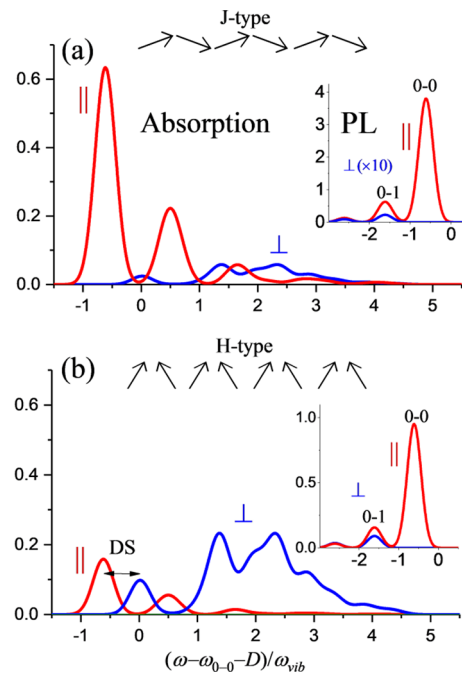


**Figure 46.** Calculated polarized absorption spectra for (a) a J-type aggregate with  $\tan \alpha = 1/2$  and (b) an H-type aggregate with  $\tan \alpha = 2$ . Each aggregate contains three unit cells ( $N = 6$ ). Spectra are based on the Holstein Hamiltonian with  $W = 2\omega_{\text{vib}} = 0.34$  eV,  $\lambda^2 = 1$ , and n.n coupling only.

vibronic line shape as exists in the ideal J-aggregate (H-aggregate) spectrum. A similar correspondence holds for the H-type aggregates. Even though the aggregates are finite ( $N = 6$ ), the J-type spectrum in Figure 46a still manages to qualitatively capture the essential spectral features in the measured PIC spectrum in Figure 44 as was also originally recognized by Scherer and Fischer.<sup>165</sup> Better agreement with experimental results requires a large  $N$  limit, indeed, the J-polymer spectrum in Figure 27 strongly resembles the spectrum polarized parallel to the aggregate axis in PIC. Using the parameters of Scherer and Fischer ( $J_C = -0.5\omega_{\text{vib}}$ ,  $\omega_{\text{vib}} = 1368$  cm<sup>-1</sup>, and  $\lambda^2 = 0.6$ ) in the inset formula in Figure 27 gives  $I_{\text{SB}}/I_{A_{\text{max}}} \approx 0.22$  in good agreement with the experimental value.

For either aggregate type (J- or H-), the transition to the lowest energy exciton, also referred to as the lower Davydov component (LDC), is polarized along the aggregate axis and displays J-like vibronic signatures (i.e.,  $R_{\text{abs}}$  is larger than the monomer value), and the transition to the highest-energy exciton (the upper Davydov component or UDC) is polarized normal to the axis and displays H-type vibronic signatures in agreement with the measured and calculated PIC spectrum in Figure 44. The difference in energy between the two Davydov components is referred to as the Davydov splitting (DS).<sup>25</sup> When vibronic coupling is pronounced, as it is for PIC aggregates, the DS is defined relative to the lowest-energy vibronic peaks of the two components as indicated in Figure 46b. Hence, the DS is  $\sim 1500$  cm<sup>-1</sup> for the PIC aggregates in Figure 44.

One can show quite generally that, for any packing architecture, the red-shifted Davydov component (due strictly to excitonic interactions) exhibits J-like vibronic signatures, and the blue-shifted component exhibits H-like vibronic signatures. This was discussed for herringbone-type packing by Kistler et al.<sup>309</sup> and is embodied in the ratio formula adapted for packing

arrangements with two molecules per unit cell. For the spectrum polarized like the lower (L) and upper (U) Davydov component, the ratio of the first two vibronic peaks is

$$R_{\text{abs}}^{\text{L/U}} \approx \frac{[1 - e^{-\lambda^2} G(0; \lambda^2) J_{\text{L/U}} / \omega_{\text{vib}}]^2}{\lambda^2 [1 - e^{-\lambda^2} G(1; \lambda^2) J_{\text{L/U}} / \omega_{\text{vib}}]^2} \quad (107)$$

where  $J_{\text{L}}$  ( $J_{\text{U}}$ ) is the free-exciton shift of the lower (upper) Davydov component. Hence, for the J-type aggregates in Figure 45a, we have  $J_{\text{L}} = J_{k=0} = 2J_{\text{C}}$  and  $J_{\text{U}} = J_{k=\pi} = -2J_{\text{C}}$  with  $J_{\text{C}} < 0$ . For the H-type aggregates in Figure 45b,  $J_{\text{L}} = J_{k=\pi} = -2J_{\text{C}}$  and  $J_{\text{U}} = J_{k=0} = 2J_{\text{C}}$  with  $J_{\text{C}} > 0$ .

Eq 107 reveals an important correlation between the excitonic spectral shift of the Davydov component and the value of the ratio  $R_{\text{abs}}$  compared to the monomer value ( $1/\lambda^2$ ): a negative shift gives  $R_{\text{abs}} > 1/\lambda^2$ , and a positive shift gives  $R_{\text{abs}} < 1/\lambda^2$ . More interesting cases arise when beyond nearest neighbor coupling is included, especially in two- or three-dimensional lattices. Under certain conditions, the coupling between translationally equivalent molecules can exceed that between the translationally inequivalent molecules, the latter of which defines the DS. In such cases, the two Davydov components can be spectrally shifted in the same direction: if they are both red-shifted, then one can expect J-like vibronic signatures for both components; if they are both blue-shifted, then they should display H-like vibronic signatures.

**4.6.2. Polarized PL and the Ratio Rule.** The origin of polarized PL from linear aggregates with two molecules per unit cell is qualitatively similar to that of herringbone aggregates considered in refs 13, 283, and 298. In the J- and H-type aggregates in Figure 45, emission derives from the band-bottom  $k = 0$  and  $k = \pi$  excitons, respectively, which are also responsible for the LDC. Representative PL spectra for J- and H-type aggregates are shown in the insets of Figure 46. For both aggregate types, the emission polarized parallel to the long molecular axis is J-like with a dominant 0–0 peak followed by weak sidebands. By contrast, the emission polarized normal to the aggregate axis is H-like, lacking entirely the 0–0 peak. For both aggregate types, the PL spectrum reduces to characteristic “pure” J- and H-aggregate spectra when the angle  $\alpha$  tends to zero (J-type) and  $\pi/2$  (H-type). The H-type aggregate emission is especially interesting: as shown in Figure 46b, the emission is almost entirely J-like with a dominant 0–0 emission band polarized along the aggregate axis.

The PL spectra for the two aggregate types are readily understood using the exciton–phonon basis set,<sup>176</sup> where a general form for the emitting (band bottom) exciton is

$$|\psi_{\kappa=0(\kappa=\pi)}^{\text{em,J(H)}}\rangle = |\tilde{0}\rangle \otimes \sum_k \sum' c_{k;n_{q_1},n_{q_2},\dots}^{\text{em}} |k; n_{q_1}, n_{q_2} \dots n_{q_{N-1}}\rangle \quad (108)$$

The prime on the summation indicates that the total momentum (see eq 24) is equal to  $\kappa = \pi$  for H-type aggregates and  $\kappa = 0$  for J-type aggregates. A parallel derivation can also be made using the multiparticle basis set as has been conducted for herringbone aggregates.<sup>13,283,298</sup> On the basis of the emitting state in eq 108, the 0–0 line strength for both aggregate types (disorder-free and at low temperature) is

$$I_{\parallel,\text{J}}^{0-0} = NF_{\text{J}} \frac{|\mu_1 + \mu_2|^2}{4\mu^2} \quad (109)$$

$$I_{\parallel,\text{H}}^{0-0} = NF_{\text{H}} \frac{|\mu_1 - \mu_2|^2}{4\mu^2} \quad (110)$$

where the generalized FC factors are given by,  $F_{\text{J}} = e^{-\lambda^2/N}|c_{k=0,0,\dots}^{\text{em}}|^2$  and  $F_{\text{H}} = e^{-\lambda^2/N}|c_{k=\pi,0,\dots}^{\text{em}}|^2$ .<sup>176</sup> In both aggregate types, 0–0 emission is polarized parallel to the aggregate axis consistent with the polarization of the band-bottom exciton in Figure 45 and is coherently enhanced by a factor of  $N$  as in ideal J-aggregates. Surprisingly, even dominant H-type aggregates with  $|\mu_1 - \mu_2| \ll \mu$  display J-like emission (ultimately due to the positive band curvature at the band bottom) and can be superradiant in a manner analogous to herringbone aggregates.<sup>298</sup> However, because of the dependence of the 0–0 intensity on the difference,  $|\mu_1 - \mu_2| < \mu$ , “superradiant H-aggregates” require a threshold number of chromophores  $N_{\text{th}}$  before the radiative decay rate exceeds that of a single molecule. This occurs approximately when  $N > N_{\text{th}}$  with  $N_{\text{th}} \equiv 4 \mu^2 [F_{\text{H}} |\mu_1 - \mu_2|^2]^{-1}$ .<sup>118,120,178,217</sup>

Following along the same lines as in ref 176, the 0–1 line strength for light polarized parallel to the aggregate axis is

$$I_{\parallel,\text{J}}^{0-1} = \lambda^2 F_{\text{J}} \frac{|\mu_1 + \mu_2|^2}{4\mu^2} \quad (111)$$

$$I_{\parallel,\text{H}}^{0-1} = \lambda^2 F_{\text{H}} \frac{|\mu_1 - \mu_2|^2}{4\mu^2} \quad (112)$$

for J- and H-aggregates, respectively. Unlike 0–0 emission, there is no enhancement by the number of chromophores,  $N$ . Eqs 109–112 lead directly to the ratio rule modified to include two molecules per unit cell

$$R_{\text{PL}}^{\parallel} \equiv \frac{I_{\parallel,\text{J}}^{0-0}}{I_{\parallel,\text{J}}^{0-1}} = \frac{I_{\parallel,\text{H}}^{0-0}}{I_{\parallel,\text{H}}^{0-1}} = \frac{N}{\lambda^2} \quad (113)$$

which is exact in the absence of disorder and at sufficiently low temperatures. The validity of eq 113 can be appreciated from the inset spectra in Figure 46 where  $R_{\text{PL}}^{\parallel}$  is exactly  $N$  ( $= 6$ ) because  $\lambda^2 = 1$  for either aggregate type. Hence, as long as the transition to the band-bottom exciton has oscillator strength from the vibrationless ground state, the ratio rule applies for PL polarized in the direction defined by the lower Davydov component. As with linear aggregates with one molecule per unit cell, a more general but approximate form of the ratio rule follows when disorder and higher temperatures are included by replacing  $N$  in eq 113 with the coherence number

$$R_{\text{PL}}^{\parallel} \approx \frac{N_{\text{coh}}}{\lambda^2} \quad (114)$$

In particular, when there is no disorder,  $N_{\text{coh}} = N_{\text{T}}$ . In this case, eq 97 still applies in the thermodynamic limit but using the curvature evaluated at the  $k$  vector corresponding to the band-bottom exciton.

Further use of the form of the emitting exciton in eq 108 shows that for either aggregate type sideband emission also contains a component polarized normal to the aggregate axis. For example, in H-type aggregates where the momentum of the emitting exciton is  $\kappa = \pi$ , the term in the sum with  $k = 0$  and one (nontotally symmetric) phonon with  $q = \pi$  contributes to sideband (0–1) emission polarized normal to the aggregate axis. For the J-type aggregate, the emitting exciton has  $\kappa = 0$ , which allows a contribution from the state having  $k = \pi$  and a

phonon with  $q = \pi$ , which is again polarized normal to the aggregate axis. When the exciton coupling is large ( $W \gg \lambda^2 \omega_{\text{vib}}$ ), such intensity borrowing can be understood in terms of HT coupling of section 4.2.7. For emission polarized normal to the aggregate axis (in both aggregate types), the line strength is given by

$$I_{\perp,J}^{0-1} = \frac{|\mu_1 - \mu_2|^2}{4\mu^2} e^{-\lambda^2/N} \frac{\lambda^2 \omega_{\text{vib}}^2}{(W + \omega_{\text{vib}})^2} \quad (115)$$

$$I_{\perp,H}^{0-1} = \frac{|\mu_1 + \mu_2|^2}{4\mu^2} e^{-\lambda^2/N} \frac{\lambda^2 \omega_{\text{vib}}^2}{(W + \omega_{\text{vib}})^2} \quad (116)$$

Finally, the presence of both polarizations in the 0–1 emission allows one to also define a “mixed” ratio as discussed in ref 176,  $R_{\text{PL}}^M \equiv I_{\parallel}^{0-0}/I_{\perp}^{0-1}$ . The mixed PL ratio is particularly useful for analyzing herringbone aggregates as discussed in greater detail in section 4.7.

#### 4.7. Herringbone Aggregates

Herringbone (HB) packing in the solid phase is ubiquitous among rod-shaped conjugated organic chromophores such as unsubstituted (or end-substituted) oligophenylenevinylenes (OPVn’s),<sup>128,353,354</sup> oligothiophenes (OTn’s),<sup>102,355–358</sup> dinaphtho-thieno-thiophenes (DNTT’s),<sup>346</sup> and oligoacenes.<sup>359</sup> Here, the “n” in OPVn and OTn indicates the number of phenyl and thiophene rings, respectively. The photophysics and transport properties of OTn<sup>92–120</sup> and OPVn<sup>92,93,121–138</sup> aggregates, thin films, and crystals has received a great deal of attention over the years, motivated primarily by applications in organic electronics. Recently, DNTT has emerged as an excellent hole-transporting material,<sup>360–362</sup> which like OTn and OPVn exhibits photophysics unique to HB packing.<sup>346</sup> Theoretical analyses related to the special attributes of HB lattices and the related molecular “pinwheel” aggregates have also been plentiful.<sup>13,120,183,260–262,283–287,298,299,314–316,333,363–367</sup> In this section, we briefly review the photophysics of a two-dimensional HB lattice, such as that illustrated in Figure 47. Here, we focus on systems where the coupling between chromophores is mainly Coulombic, as in OPVn and OTn lattices, driven by a large  $S_0 \rightarrow S_1$  molecular transition dipole moment (~10 D) directed along the long molecular axis. This contrasts with the oligoacenes (discussed in section 5.10), where the much weaker short-axis polarized  $S_0 \rightarrow S_1$  transition results in a reduction in the Coulomb coupling by 2 orders of magnitude, thereby allowing the short-range CT-mediated interactions to dominate. Because the fundamental photophysics of OPVn and OTn HB lattices have already been reviewed in ref 13, we outline here just some of the novel H- and J-aggregate behaviors distinguishing HB packing from the simpler linear lattices considered in section 4.6.

The photophysical properties of OTn and OPVn ordered phases can be understood from the simplified HB lattice introduced in ref 183 and illustrated in Figure 47. Such approximate lattices are square along the  $x$  and  $y$  directions defined in the figure, with the long molecular axis taken to be normal to the page, i.e., along the  $c$  axis. The two molecules in the unit cell are therefore oriented in a “side-by-side” fashion but with a relative twist by  $\phi$  about the  $c$ -axis. Hence, for OPVn and OTn in which the  $S_0 \rightarrow S_1$  transition dipole moment is oriented mainly along the long molecular axis, Kasha theory predicts H-like behavior, as verified in Figure 48 for *p*-distyrylbenzene (OPV3) nanodispersions measured by Oelkrug

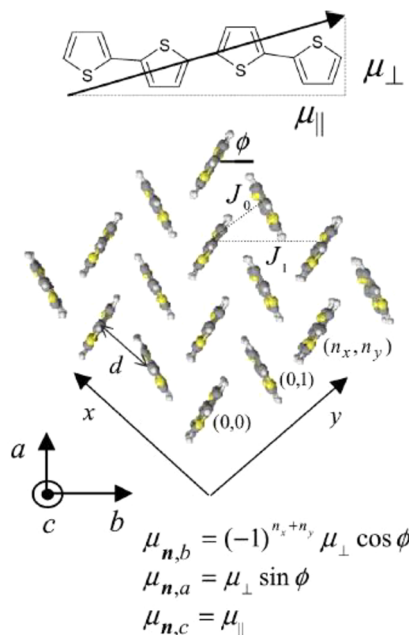


**Figure 47.** (top) An OT4 molecule with the transition dipole moment indicated by the arrow. (bottom) A  $4 \times 4$  HB lattice of OT4 molecules. The nearest neighbor ( $J_0$ ) and next nearest neighbor ( $J_1$ ) couplings are indicated. The equations for the transition dipole moments along each crystal axis are also shown. Reprinted with permission from ref 183. Copyright 2007, AIP Publishing.

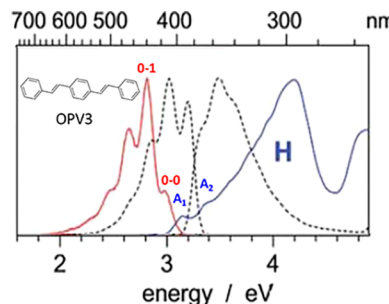


**Figure 48.** Experimental absorption and PL spectra for OPV3 in solution (dotted curves) and for OPV3 nanoaggregate suspensions (solid curves) from ref 127. Adapted with permission from ref 127. Copyright 2013, The Royal Society of Chemistry.

et al.<sup>93</sup> Compared to the monomer (unaggregated) absorption spectrum (dotted curve), the main peak (“H”) in the nanoaggregate spectrum is strongly blue-shifted by ~1 eV. Note also the strong attenuation of the 0–0 peak in the PL spectrum, also characteristic of H-aggregates, although the origin of 0–0 emission in packing structures with two (or more) molecules per unit cell can be more complex, as discussed earlier for linear aggregates, see section 4.6.

Interestingly, the transition dipole moments of the two molecules in the unit cell are not exactly parallel for OPVn’s and even numbered OTn’s due to the existence of a small off-axis component,  $\mu_{\perp}$ , indicated in Figure 47. In such molecules, the  $C_{2h}$  point group symmetry precludes the long molecular axis, which can be identified with a principle axis of inertia, from being a symmetry axis. Hence, the transition dipole is not constrained to lie along the long axis. By contrast, for OTn’s with an odd number of thiophene rings, the point group changes to  $C_{2v}$ ; the long axis is now a well-defined symmetry

axis along which the transition dipole moment lies. Hence, the OTn's with odd  $n$  display classic H-aggregate behavior according to the Kasha theory, and indeed, the absorption spectrum for OTS nanoaggregates is characterized by a strong blue-shifted H-band by almost 1 eV<sup>92</sup> with a spectral line shape very similar to that of OPV3 in Figure 48; by contrast, the OTn's (with  $n$  even) and OPVn's exhibit two Davydov components, a strongly allowed, high-energy upper Davydov component (UDC) polarized in the  $ac$  plane (the H-band in Figure 48), and a weakly allowed low-energy Davydov component (LDC) polarized along the  $b$ -axis (the J-band)<sup>99,100</sup> with the ratio of H- to J-band oscillator strengths proportional to  $(\mu_{||}/\mu_{\perp})^2$ . The J-band for OPV3 nanoaggregates is too weak to be clearly observed in Figure 48 because  $(\mu_{||}/\mu_{\perp})^2 \approx 0.01$  but is discernible in more crystalline, thin-film spectra with narrower line widths,<sup>122</sup> where it appears several hundred wave numbers below the  $A_1$  band in Figure 48. In OPV3, the Davydov splitting is therefore quite large,  $\sim 1$  eV.<sup>283,284</sup> Likewise, for OT4 and OT6 the weak J-band is readily detected in crystalline samples,<sup>99,100,114,118,120,183</sup> and the Davydov splitting is also  $\sim 1$  eV.<sup>364,365</sup> In the OPVn's and OTn's, there are also  $ac$ -polarized peaks near the absorption origin ("false origins")<sup>99,100,114,118,120,183</sup> clearly discernible in Figure 48 ( $A_1$  peak) due to an aggregate version of HT coupling (see section 4.2.7).<sup>284,314,316</sup>

Meinardi et al.<sup>107</sup> showed that PL from thin OTn films is markedly different for even and odd values of  $n$ . OTn's with odd  $n$  lack the 0–0 PL origin, as one would expect in disorder-free H-aggregates where 0–0 emission is strictly symmetry-forbidden; only sideband emission is observed in OTS as shown in Figure 49a dominated by the quinoidal-aromatic

stretching mode (with energy of 0.17 eV). By contrast, in OT4 the 0–0 emission is clearly identified at low temperatures. Moreover, the 0–0 peak occurs at practically the same energy as the  $b$ -polarized absorption origin (J-band) observed in the OT4 crystal spectrum.<sup>100</sup> Hence, emission derives from the LDC.<sup>108</sup> For OPV3, the 0–0 peak is also clearly defined at low temperatures in crystalline samples and is polarized mainly along the  $b$ -axis.<sup>317</sup>

**4.7.1. Exciton Band Structure in HB Lattices.** The exciton band structure responsible for the aforementioned spectral attributes of OPVn and OTn aggregates, thin films, and crystals is easiest to understand using the approximate HB crystal lattices, taken as square along the  $x$  and  $y$  directions with lattice spacing  $d$ ,<sup>183,260–262</sup> as depicted in Figure 47. (Interactions between HB planes are weak and can be neglected.) Assuming as in section 4.6 that each chromophore is equivalent with regard to the coupling with its neighbors,<sup>260</sup> one can define the Brillouin zone  $k \equiv (k_x, k_y)$  based on just one molecule per unit cell. Hence, for the UDC exciton with  $(k_x, k_y) = (0,0)$ , all transition dipoles are oscillating in phase with respect to the long-axis component of the transition dipole moment, giving rise to the dominant blue-shifted H-band polarized normal to the HB plane (along  $c$  in the simplified lattice). By contrast, in the LDC exciton with  $k = (\pi, \pi)$  the  $n$ -dependent wave function coefficients alternate in phase as  $(-1)^{n_x + n_y}$  so that only the off-axis component of  $\mu$  can constructively interfere along the  $b$ -axis. For example, assuming free excitons and referring to Figure 47, we have

$$\langle g|\mu|k = (\pi, \pi) \rangle = \sum_{n_x} \sum_{n_y} \frac{(-1)^{n_x + n_y}}{\sqrt{N}} (\mu_{||c} + \mu_{\perp} \sin \phi \mathbf{a} + (-1)^{n_x + n_y} \mu_{\perp} \cos \phi \mathbf{b}) = \sqrt{N} \mu_{\perp} \cos \phi \mathbf{b}$$

Hence, transitions to the  $k = (\pi, \pi)$  exciton are allowed and give rise to the low-energy  $b$ -polarized J-band (LDC). Note that in the more conventional definition of the Brillouin zone in molecular crystals, the UDC and LDC excitons would both have  $k = (0,0)$  but with symmetric and antisymmetric phase relations, respectively, between the two molecules within the unit cell.

Free-exciton dispersion curves for the simplified HB lattice in Figure 47 were evaluated in refs 183 and 260–262. For the exciton with wave vector  $k$ , the dispersive component is

$$J_k = 2J_0(\cos k_x + \cos k_y) + 2J_1[\cos(k_x + k_y) + \cos(k_x - k_y)] \quad (117)$$

where  $J_0 (>0)$  is the Coulomb coupling corresponding to the four nearest-neighbors, assumed to be equivalent, and  $J_1 (>0)$  represents the Coulomb coupling corresponding to the four next nearest neighbors also taken to be equivalent, see Figure 47. Within our truncated Coulomb-coupling treatment,  $J_1$  can be considered as an effective coupling that accounts for the sum of all beyond nearest neighbor couplings. Figure 50 shows the exciton dispersion curves based on eq 117 using  $J_1 = 0.4J_0$ . Note the similarity to the exciton bands in the linear H-type aggregates of Figure 45b. Figure 50 identifies the LDC (red dot), UDC (blue dot), and the energy difference between them,  $W$ , defining the Davydov splitting, which also coincides with the exciton bandwidth  $W = 8J_0$ . Notably, the DS depends only on the magnitude of the n.n. coupling  $J_0$ , whereas the asymmetry of the splitting (relative to  $\omega_{0-0} + D$ ) is determined by  $J_1$ . To appreciate the latter, note that the blue shift of the H-

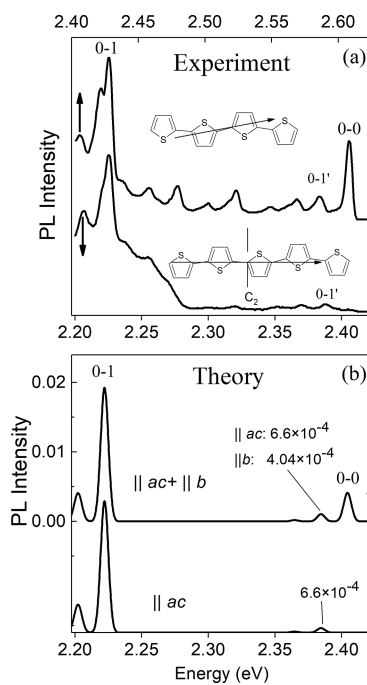


**Figure 49.** (a) Experimental ( $T = 5\text{K}$ , unpolarized) and (b) simulated OT4 and OT5 thin film PL spectra. 0–0 emission is observed only in OT4. In OT4 and OT5, sideband (0–1) emission is dominated by the high-energy aromatic-quinoidal stretching mode with energy of 0.17 eV. Weaker sidebands with lower mode energies also appear in both the OT4 and OT5 spectra. Adapted with permission from ref 262. Copyright (2007), American Chemical Society.

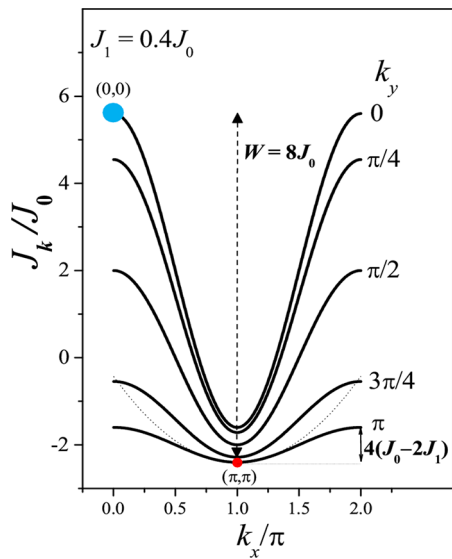


**Figure 50.** Exciton dispersion for the simplified HB aggregate of Figure 47. Each curve corresponds to a given value of  $k_y$ . Oscillator strength is concentrated primarily in the  $\mathbf{k} = (0,0)$  exciton responsible for the H-band (blue dot), although the slight misalignment of transition dipoles also makes the band-bottom exciton (red dot) symmetry allowed. Note the similarity to the dispersion of Figure 44b for H-type linear aggregates with two molecules per unit cell. Reprinted with permission from ref 183. Copyright 2007, AIP Publishing.

band,  $4|J_0 + J_1|$ , is larger than the red-shift of the J-band,  $4|J_0 + J_1|$  in agreement with what is observed in OTn and OPVn solid phases where the magnitude of the H-band blue shift is several times larger than the J-band red-shift (see Figure 48).

Taking the second derivative of eq 117 with respect to either  $k_x$  or  $k_y$  at  $\mathbf{k} = (\pi, \pi)$  gives  $\omega_c = J_0 - 2J_1$  as the curvature at the LDC. Hence, as long as  $J_1 < J_0/2$ , the curvature is positive and the LDC defines the bottom of the band, allowing the equivalency between the Davydov splitting and the exciton bandwidth,  $W$ . This is consistent with experimental evidence in crystalline OT4: the existence of a 0–0 PL peak, which decreases with increasing temperature, and the absence of any appreciable Stokes shift from the LDC indicates a positive curvature at the band bottom.<sup>108</sup> The relation  $J_1 = 0.4J_0$  used in Figure 50 is close to what is needed to reproduce experimental details.<sup>260,262</sup> For example, in OT4, the curvature is estimated to be only 6 meV, far smaller than the exciton bandwidth of close to 1 eV.<sup>120,183</sup>

As emphasized in refs 120, 183, and 260–262, the small value of the exciton band curvature at the band bottom compared to the bandwidth  $W$  in OPVn and OTn crystals necessitates a reclassification of the exciton coupling regimes, especially for the low-energy emitting excitons. Here, the definition of weak and strong exciton coupling regimes must be based on the free exciton curvature  $\omega_c$ , which determines the exciton's effective mass and not the total bandwidth  $W$  as is the case for the classification schemes based on the work of Simpson and Peterson.<sup>301</sup> The latter works well for linear aggregates where the next nearest neighbor is twice as far as the nearest neighbor, making  $J_1$  several times smaller than  $J_0$ . In such cases, the curvature remains approximately one-fourth of the bandwidth. However, the two-dimensional nature of HB aggregates allows the next nearest neighbor distance to get closer to the nearest neighbor distance, creating band

curvatures  $\omega_c = J_0 - 2J_1$ , which can be vanishingly small or (even negative) compared to the bandwidth  $W = 8J_0$ . In ref 183, a classification scheme was presented for HB lattices based on both the band-bottom band curvature  $\omega_c$  and bandwidth  $W$ . In terms of the relative strength of the exciton–phonon (EP) coupling, represented by the last term in the Hamiltonian of eq 18, the various regimes are

$$\omega_{\text{vib}}\lambda^2 \ll 4\pi\omega_c \quad \text{weak EP coupling}$$

$$\omega_{\text{vib}}\lambda^2 \approx 4\pi\omega_c \quad \text{intermediate I EP coupling}$$

$$W \gg \omega_{\text{vib}}\lambda^2 \gg 4\pi\omega_c \quad \text{strong I EP coupling}$$

$$W \approx \omega_{\text{vib}}\lambda^2 \gg 4\pi\omega_c \quad \text{intermediate II EP coupling}$$

$$\omega_{\text{vib}}\lambda^2 \gg W \quad \text{strong II EP coupling}$$

Note that for linear aggregates it is more conventional to define the coupling regimes with respect to the exciton coupling (i.e., Coulomb coupling) as opposed to the EP coupling (governed by  $\omega_{\text{vib}}\lambda^2$ ). Hence, the strong exciton coupling regime of section 4.2.1 is equivalent to the weak EP coupling regime here. We also point out that the classification described above is strictly applicable for single-mode vibronic coupling, involving, for example, the aromatic-quinoidal stretching mode in OPVn and OTn. However, by replacing the free-exciton curvature,  $\omega_c$ , with the curvature renormalized by coupling to the  $1400 \text{ cm}^{-1}$  mode,  $\tilde{\omega}_c$ , the resulting EP coupling regimes can be used to study the impact of additional vibrational modes, such as the low-frequency modes in OTn.<sup>120,183</sup>

**4.7.2. Polarized Photoluminescence.** A theoretical description of the polarized emission bands in HB lattices appeared in refs 260–262, 283, 284, and 298 and closely resembles that needed to understand the linear H-type aggregates with two molecules per unit cell discussed in section 4.6. In these works, dominant vibronic coupling to the aromatic-quinoidal stretching mode (0.17 eV,  $\lambda^2 \approx 1$ ) was assumed. The general form for the 0–0 emission, strictly valid for defect-free lattices at temperatures low enough to ensure emission from only the band bottom  $\mathbf{k} = (\pi, \pi)$  exciton (which requires that  $T$  approaches 0 K for arbitrarily large  $N$ ), has the form<sup>260,261,283,284</sup>

$$I_b^{0-0} = FN \frac{\mu_\perp^2}{\mu^2} \cos^2 \phi \quad (118)$$

As in linear aggregates, the  $N$ -fold enhancement of the 0–0 emission is sourced by a coherent superposition of molecular transition dipole moments. The 0–0 emission can therefore also drive superradiance<sup>298,368</sup> but is limited by the dependence of  $I_b^{0-0}$  on the small off-axis component of the transition dipole moment projected along  $b$  as well as the generalized FC factor  $F$ .<sup>260,261</sup> In the multiparticle basis set,  $F$  is generally a function of one-particle coefficients, the form of which can be found in refs 260–262.  $F$  is sensitive to the band bottom curvature, which as noted above can be much smaller than the bandwidth  $W$ ;  $F$  ranges from  $\exp(-\lambda^2)$  in the strong I EP coupling regime ( $\omega_{\text{vib}}\lambda^2 \gg 4\pi\omega_c$ ) to  $\exp(-\lambda^2/N)$  in the weak EP coupling regime ( $\omega_{\text{vib}}\lambda^2 \ll 4\pi\omega_c$ ). An alternate form for  $F$ <sup>176</sup>

$$F = e^{-\lambda^2/N} |c_{k=(\pi,\pi);0,0,\dots}^{\text{em}}|^2 \quad (119)$$

follows after expanding the emitting  $\mathbf{k} = (\pi, \pi)$  exciton in the exciton–phonon basis set, as was done in eq 108 for H-type linear aggregates with two molecules per unit cell.

In contrast to the 0–0 emission, the incoherent sidebands contain both *b*-polarized and *ac*-polarized contributions. For 0–1 emission, the line strengths take the form

$$I_b^{0-1} = F\lambda^2 \frac{\mu_{\perp}^2}{\mu^2} \cos^2 \phi \quad (120)$$

$$I_c^{0-1} = \frac{\mu_{\parallel}^2}{\mu^2} \frac{\lambda^2 \omega_{\text{vib}}^2}{(W + \omega_{\text{vib}})^2} \quad W \gg \lambda^2 \omega_{\text{vib}} \quad (121)$$

(The *a*-polarized line strength,  $I_a^{0-1}$ , is found by replacing  $\mu_{\perp}^2$  with  $\mu_{\perp}^2 \sin^2 \phi$  on the rhs of eq 121). Earlier works<sup>260–262</sup> assumed that eq 120 was restricted to the strong exciton coupling regime  $W \gg \lambda^2 \omega_{\text{vib}}$ , where  $F$  reduces to  $\exp(-\lambda^2/N)$ . However, in ref 176 it was shown that eq 120 remains exact, independent of the exciton coupling, with  $F$  given by eq 119, a result with very important implications for the PL ratio rule (see below). By contrast, the *c*-polarized line strength in eq 121, derived in ref 260, is specific to the strong exciton coupling limit relevant for OTn and OPVn lattices where the exciton bandwidth  $W \approx 1$  eV is ~6-times greater than the nuclear relaxation energy,  $\lambda^2 \omega_{\text{vib}}$ , derived mainly from the aromatic-quinoidal mode. The sideband is labeled 0–1 in Figure 49. The quadratic dependence on  $\omega_{\text{vib}}$  in eq 121 is responsible for the much smaller *ac*-polarized component of the 0–1' sideband derived from the low-energy symmetric mode ( $\omega_{\text{vib}}' \approx 0.02$  eV,  $HR' \approx 1$ ) in Figure 49. An alternate form for  $I_c^{0-1}$  derived using the multiparticle basis set consists of a destructive interference between one- and two-particle contributions in the emitting exciton.<sup>260,261,283,284</sup> For completeness, it should be pointed out that a general expression for the *c*-polarized emission (independent of the exciton coupling regime) can also be derived in the exciton–phonon basis set and is obtained by replacing  $\omega_{\text{vib}}^2/(W + \omega_{\text{vib}})^2$  in eq 121 with  $e^{-\lambda^2/N} c_{k=0,0,q=(\pi,\pi),0,\dots}^{\text{em}}$ . This form emphasizes that the *c*-polarized 0–1 line strength requires the emitting exciton to borrow intensity from the much higher energy  $\mathbf{k} = (0,0)$  exciton (coupled with a  $q = (\pi, \pi)$  phonon), a form of Herzberg–Teller coupling.

Because the 0–0 emission in eq 118 is marginalized by the small off-axis component of the transition dipole moment,  $N$  must exceed a threshold number of coherently coupled chromophores,  $N_{\text{th}} = [F(\mu_{\perp}^2/\mu^2)\cos^2 \phi]^{-1}$ , before the 0–0 line strength surpasses unity. This is approximately the condition for the radiative decay rate to exceed that of a single molecule, i.e., superradiance.<sup>13,260,261,283,284,298</sup> For the OPVn's and OTn's,  $N_{\text{th}}$  has been estimated to be several hundred molecules;<sup>284</sup> however, this is still small in comparison to the total number of chromophores of order  $O[10^5]$  in a square (optical) wavelength of crystalline OTn or OPVn (or  $O[10^7]$  in a cubic wavelength). Hence, despite the small off-axis component of the transition dipole moment appearing in eq 118, the 0–0 peak should dominate the PL spectrum in OTn (n even) and OPVn in direct contradiction to experimental observations where the 0–0 band is only appreciable at low temperatures<sup>107,108,317,368</sup> and even then is a relatively minor component, see Figure 49 (top). Such a concern was recently raised by Wykes in their analysis of HT coupling in OPV3.<sup>311</sup>

As shown in refs 260 and 261, the resolution of the above conundrum is straightforward and is a direct consequence of

the weak but positive curvature of the exciton band at  $\mathbf{k} = (\pi, \pi)$ , see Figure 50, leading to a dramatic decrease of just the 0–0 emission relative to the rest of the progression with increasing temperature. Assuming a Boltzmann population of emitting excitons, the steady-state 0–0 emission takes the form<sup>260–262,333</sup>

$$I_b^{0-0} = FN_{\text{T},2D} \frac{\mu_{\perp}^2}{\mu^2} \cos^2 \phi \quad (122)$$

where  $N_{\text{T},2D}$  is the two-dimensional thermal coherence number introduced for isotropic square lattices in section 4.4. When  $T$  is near 0 K, then  $N_{\text{T},2D} = N$  and eq 118 is recovered. As with linear aggregates, increasing temperature leads to a decrease in the population of the band-bottom exciton ( $\mathbf{k} = (\pi, \pi)$ ), the only exciton capable of providing *b*-polarized 0–0 emission. In the thermodynamic limit, the thermal coherence number becomes<sup>260,261</sup>

$$N_{\text{T},2D} = 1 + \frac{4\pi\tilde{\omega}_c}{k_B T} \quad 4\pi\tilde{\omega}_c > k_B T \gg \frac{4\pi\tilde{\omega}_c}{N} \quad (123)$$

after also invoking the parabolic band approximation.  $N_{\text{T},2D}$  in eq 123 differs from the expression in eq 100 with the inclusion of “1” added to the right-hand-side, an approximation made to reproduce the high temperature limit.<sup>242</sup> Note that eq 123 assumes isotropic Coulombic interactions within the HB plane, which is an excellent approximation for OTn and OPVn lattices where the dominant Coulomb couplings involving the four nearest neighbors are roughly equal.<sup>283</sup> The curvature at the band minimum  $\tilde{\omega}_c$  is therefore independent of direction within the *ab* plane, as is the case for a parabolic “bowl”. Finally, the impact of vibronic coupling appears in the renormalized band curvature,  $\tilde{\omega}_c$  (note the tilde), as was also the case for the linear aggregate in eq 97.

Eq 123 shows that the thermal coherence number scales linearly with the band curvature  $\tilde{\omega}_c$  and inversely with temperature. Hence, the weak curvature of the J-band in OTn HB lattices is very likely the culprit responsible for the aforementioned marginalized 0–0 peak, as demonstrated in ref 262 for OT4. In contrast, by the same arguments made in section 4.6 regarding linear aggregates, the sideband line strengths are very nearly independent of temperature. Interestingly, in HB aggregates the dominant *c*-polarized sideband emission (0–1, 0–2, ...) is far more sensitive to bandwidth ( $W$ ) than to the curvature, see eq 121. With all of the above considerations taken into account, the theoretical spectrum in Figure 49 does a reasonable job in reproducing the relative intensity of the 0–0 and 0–1 peaks observed experimentally at  $T = 5$  K in OT4 when using a value of only 50 cm<sup>-1</sup> for the band-bottom curvature.<sup>260–262</sup> The theory is also consistent with the monotonic decrease in the 0–0 peak with increasing temperature beyond 5 K.<sup>108</sup>

With regard to OPV3, the experimental PL spectra obtained by Wu et al. for crystalline samples show a greatly diminished *b*-polarized 0–0 peak at 1.4 K, which actually increases with temperature, peaking at ~50 K and then decreasing at higher temperatures with an apparent activation energy of ~11 meV. Such behavior may arise from a small negative curvature at the point  $\mathbf{k} = (\pi, \pi)$ , which arises if  $J_0 - 2J_1$  becomes slightly negative so that the band minima are now located at  $\mathbf{k} = (0, \pi)$  and  $(\pi, 0)$ , as can be appreciated from Figure 50. Excitons with these wave vectors cannot source 0–0 emission; the latter requires thermal activation to the exciton with  $\mathbf{k} = (\pi, \pi)$ .

Figure 51, adapted from ref 261, demonstrates the overall temperature dependence of the polarized PL in HB aggregates

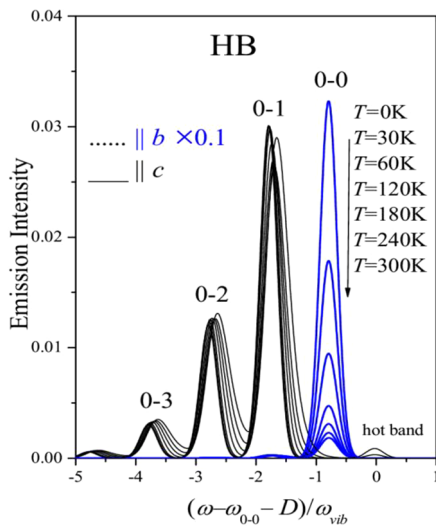


**Figure 51.** Calculated temperature-dependent PL spectra corresponding to 10 by 10 HB aggregates based on the packing arrangement in Figure 47 with  $\mu_{\perp} = 0.1 \mu$  and vibronic coupling defined by  $\omega_{\text{vib}} = 0.17 \text{ eV}$  ( $1400 \text{ cm}^{-1}$ ) and  $\lambda^2 = 1$ . The excitonic couplings are  $J_0 = 0.5 \omega_{\text{vib}}$ , and  $J_1 = 0.4J_0$ . Figure reprinted with permission from ref 261. Copyright (2005), American Physical Society.

with nonzero  $\mu_{\perp}$ . The calculated spectra pertain to a  $10 \times 10$  model aggregate containing  $N = 100$  chromophores. On the basis of the parameters reported in the figure caption, the threshold number,  $N_{\text{th}}$ , is  $\sim 300$ . Hence, at  $T = 0 \text{ K}$ ,  $I_b^{0-0} = N/N_{\text{th}} \approx 0.3$ , which works out to be  $\sim 10$ -times larger than the  $c$ -polarized 0–1 sideband (note the reduction of the 0–0 peak by a factor of 10 in the figure). Further analysis in ref 261 reveals that, beyond  $T = 30 \text{ K}$ , the 0–0 intensity scales as  $1/T$  as predicted by eq 123 in the thermodynamic limit. In sharp contrast, the 0–1, 0–2, ... sidebands are practically temperature independent, although there is a slight blue shift with temperature due to emission from thermally populated excitons. We note that the free-exciton curvature,  $\omega_c = J_0 - 2J_1 = 140 \text{ cm}^{-1}$  assumed in the figure is 3-times larger than that used to model the OTn aggregates in Figure 49.<sup>262</sup> Reducing the curvature by three (by slightly increasing  $J_1$ ) would also reduce the 0–0 emission by a factor of 3 for  $T > 30 \text{ K}$  but would hardly affect the sideband intensities because they are mainly sensitive to exciton bandwidth  $W$  (and not the curvature).

Tanaka et al.<sup>346</sup> measured a similar temperature-dependent PL line shape in DNNT and C<sub>10</sub>-DNNT HB aggregates. As shown in Figure 52, the spectra behave qualitatively as described above; increasing temperature leads to a sharp decrease in the 0–0 emission, whereas the sideband intensity is practically independent of temperature. This observation further requires that the (dominant) nonradiative decay rate is independent of temperature (see section 4.4), as is demonstrated in Figure 52c. The decrease in the overall fluorescence decay rate with increasing temperature in Figure 52d is due to the enhanced radiative component at low temperatures. Detailed analysis of the PL spectral line shape showed that the coherence numbers,  $N_{\text{coh}}$ , are roughly 15 and 30 for DNNT and C<sub>10</sub>-DNNT, respectively, at temperatures near 50 K. The authors concluded that alkyl substitution at the

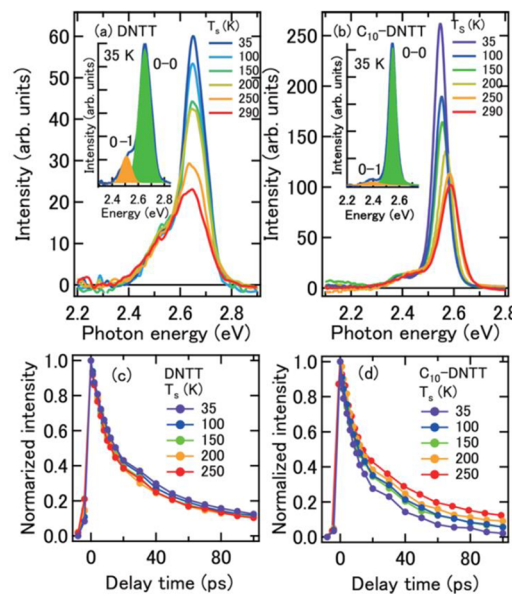


**Figure 52.** Temperature-dependent PL spectra and fluorescent decay profiles for DNNT and C<sub>10</sub>-DNNT measured in ref 346. Reprinted with permission from ref 346. Copyright (2016), American Chemical Society.

chain ends enhances order, leading to larger coherence numbers.

In ref 176, it was shown that the J-like behavior of the lowest exciton band in HB aggregates leads directly to the PL ratio rule. In general, for emission polarized along the direction defined by the LDC, which for OTn (with n even) and OPVn HB aggregates is along the *b*-axis, one obtains<sup>176</sup>

$$R_{\text{PL}} \equiv \frac{I_b^{0-0}}{I_b^{0-1}} \approx \frac{N_{\text{T},2D}}{\lambda^2} \quad (124)$$

Eq 124 follows by dividing eq 122 by eq 120 and is rigorously exact at  $T = 0 \text{ K}$  (where  $N_{\text{T},2D} = N$ ), independent of exciton coupling, an important property not fully appreciated for HB-aggregates until 2011, when a detailed derivation of eq 124 appeared in ref 176 using the exciton–phonon basis set. As with linear aggregates, including disorder allows a further generalization of eq 124 where  $N_{\text{T},2D}$  is replaced by the coherence number,  $N_{\text{coh}}$ . In addition to the OPVn's and OTn's, the PL ratio rule also applies to the oligoacenes-like tetracene, where the LDC is also polarized along the crystallographic *b*-axis<sup>369</sup> and is the source of superradiance.<sup>344,370,371</sup> The robustness of the PL ratio rule in oligoacenes<sup>342</sup> is especially interesting because the exciton bandwidth is dominated by Frenkel/CT mixing and not Coulomb couplings,<sup>209,224</sup> see section S.10 for a more detailed discussion.

Notwithstanding its simplicity, eq 124 is difficult to apply for the  $1400 \text{ cm}^{-1}$  vibrational mode in OTn where the 0–1 *b*-polarized emission peak is spectrally buried underneath the dominant 0–1 *ac*-polarized peak, as can be appreciated from Figure 51. As a result, earlier works<sup>260,261,283,284,364</sup> focused instead on the mixed PL ratio defined by  $R_{\text{PL}}^M \equiv I_b^{0-0}/I_c^{0-1}$ , which using eqs 121–123 is approximately given by

$$R_{\text{PL}}^M \equiv \frac{I_b^{0-0}}{I_c^{0-1}} = \frac{FN_{\text{T},2D}\mu_{\perp}^2(W + \omega_{\text{vib}})^2 \cos^2 \phi}{\mu_{\parallel}^2 \lambda^2 \omega_{\text{vib}}^2} \quad (125)$$

where more information is required to extract the coherence number. Fortunately, the simpler ratio rule in eq 124 remains valid in the presence of multiple mode vibronic coupling as is discussed in greater detail in section 4.9. Thus, eq 124 can be applied to the low-energy vibrational modes observed as sidebands in the measured PL spectrum of OT4 films shown in Figure 49, for example, the  $160\text{ cm}^{-1}$  mode labeled as 0–1'. In other words, the *b*-polarized component of any vibrational sideband can be used to determine the coherence size directly through eq 124, as was done in ref 262, although the analysis there was limited to the weak EP coupling regime. Together, the PL ratios in eqs 124 and 125 along with the polarized absorption spectrum offer an effective means with which to experimentally determine the important properties of the band-bottom excitons in HB lattices given the molecular properties ( $\omega_{\text{vib}}$ ,  $\lambda^2$ ,  $\mu_\perp$ ,  $\mu_\parallel$ ) and HB angle ( $\phi$ ). The exciton coherence number and band curvature follow directly from the *b*-polarized PL ratio using eqs 123 and 124, whereas the generalized FC factor can be deduced from the mixed PL ratio after first determining the Davydov splitting (which is equal to the exciton bandwidth  $W$ ) from the polarized absorption spectrum.

Before leaving this section, we emphasize that the weak band-bottom curvature  $\tilde{\omega}_c$  in OTn and OPVn HB assemblies made possible by the 2D nature of the beyond near-neighbor interactions renders the steady-state exciton coherence number  $N_{\text{coh}}$  highly susceptible to disorder and thermal fluctuations, as reflected in a compromised 0–0 emission peak. This occurs despite a very large Davydov splitting on the order of 1 eV. As discussed in section 4.3 for linear aggregates, strong localization follows when the disorder width  $\sigma_{\text{sd}}$  and/or temperature obey

$$k_B T, \sigma_{\text{sd}} \gg 4\pi\tilde{\omega}_c$$

Importantly, the right-hand side of the inequality does not involve the free-exciton bandwidth  $W$ , which is orders of magnitude larger than the curvature in OTn and OPVn lattices. Structural defects such as stacking faults and dislocations have a similar impact on reducing the coherence length and have been extensively studied for HB lattices of OTn's and OPVn's.<sup>13,283,364</sup>

#### 4.8. Segregated HJ-Aggregates and “Null” Aggregates

An interesting situation, originally considered in ref 249, arises in aggregates that contain both negative (J-promoting) and positive (H-promoting) nearest neighbor couplings, such as those shown in Figure 53a. Coulomb coupling dictates that the head-to-tail orientation between nearest neighbors along the *y*-axis creates J-chains with an intrachain coupling  $J_{\text{intra}} < 0$ . Conversely, the side-by-side orientation between adjacent chromophores on neighboring chains leads to positive couplings,  $J_{\text{inter}} > 0$ . In the example shown in Figure 53b, the opposing couplings are divided between the four J-like nearest neighbor couplings and the two H-like second-nearest neighbor couplings, an arrangement that successfully accounts for the photophysics of lutein diacetate aggregates.<sup>91</sup> Such a brick-wall packing arrangement was proposed early on for cyanine (PIC) J-aggregates by Czilkely et al.<sup>53</sup> and merocyanine J-aggregates by Wolthaus et al.<sup>61</sup> An important recent example involves a PTCDA monolayer on a KCl substrate,<sup>338,343</sup> which is discussed in greater detail below. In such “HJ”-aggregates how does one reconcile the photophysical response—is it J-like, H-like, or something in between? This is especially interesting with respect to the radiative decay rate; in ref 249, it was shown that HJ-aggregates display thermally activated superradiant

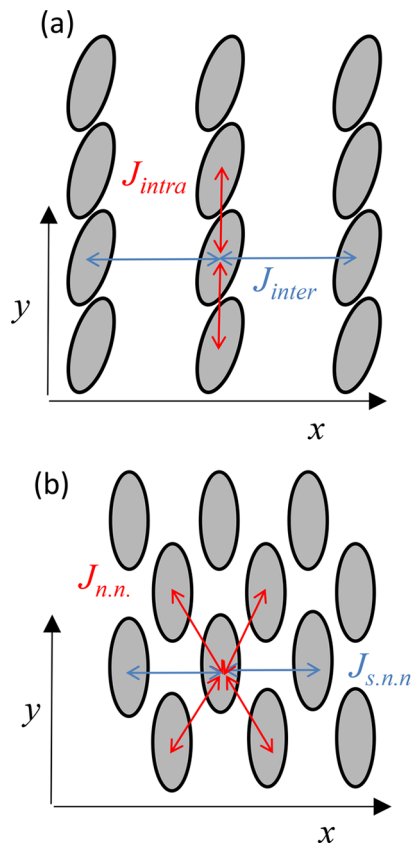


**Figure 53.** A segregated HJ-aggregate consisting of a stack of J-chains. The n.n. coupling along the *y*-axis is J-like ( $J_{\text{intra}} < 0$ ), whereas the n.n. coupling along the *x*-axis is H-like ( $J_{\text{inter}} > 0$ ). In (b), the HJ nature is established by four J-like nearest neighbor interactions and two H-like second-nearest neighbor interactions. The HJ-aggregates have one molecule per unit cell.

behavior; at low temperatures, the radiative decay rate is suppressed (H-like) but becomes more J-like (superradiant) with increasing temperature. The effect of segregated H- and J-couplings on exciton transport has also been considered.<sup>372</sup>

Because the H- and J- couplings occur between different pairs of chromophores (for example, the intra- and interchain couplings in Figure 53a), the aggregates in Figure 53 are referred to as *segregated* HJ-aggregates.<sup>15,249,275,308,327</sup> In the simplest manifestation, the H- and J-couplings derive from Coulomb interactions as in Kasha aggregates. More general treatments also consider short-range CT-mediated couplings, or superexchange couplings, which derive from wave function overlap between neighboring chromophores.<sup>233,235</sup> The inclusion of two different coupling sources allows also for *integrated* HJ-aggregates, discussed in section 5.6, where the opposing J- and H-couplings, one Coulombic and the other superexchange, compete within the same pair of chromophores.

The most well-studied manifestation of segregated HJ-aggregates are conjugated polymer  $\pi$ -stacks,<sup>15,249,275,308,327,373</sup> where single polymer chains can be considered as J-chains in which repeat-unit chromophores interact via covalent (through-bond) coupling (see section 5.8.2),<sup>242–244</sup> whereas neighboring polymers interact with each other with H-promoting (positive) Coulombic coupling.<sup>125,144</sup> Such aggregates therefore pack in a manner similar to Figure 53a. In P3HT  $\pi$ -stacks, the interchain interactions may also derive from wave function overlap as neighboring chains are only 3.8 Å apart, resulting in a

superexchange interaction that is also H-like<sup>223</sup> according to intermolecular orientations derived from X-ray diffraction studies.<sup>374</sup> (Interestingly, small longitudinal slips along the polymer axis can change the sign of the superexchange coupling; if the magnitude of the latter exceeds the H-promoting Coulomb coupling, the result would be a P3HT “JJ”-aggregate.<sup>223</sup>) HJ-aggregation may also account for the unusual PL spectral line shapes observed by core–shell assemblies of alkoxy-substituted OPVs in THF/water solvent mixtures.<sup>375–377</sup>

In ref 249, the photophysics of segregated HJ-aggregates with n.n. electronic couplings arranged as in Figure 53a were investigated. For an  $N_x \times N_y$  HJ-aggregate with  $N_x, N_y > 2$ , the free-exciton energies (in the absence of vibronic coupling) depend on the wave vector ( $k_x, k_y$ )

$$E(k_x, k_y) = E_M + D + 2J_{\text{intra}} \cos k_y + 2J_{\text{inter}} \cos k_x \quad (126)$$

where  $k_{x(y)} = 0, \pm 2\pi/N_{x(y)}, \dots, \pi$ . The expression holds in the dimer limit of two J-chains ( $N_x = 2$ ) if  $2J_{\text{inter}}$  is replaced by  $J_{\text{inter}}$  and in the limit of two H-chains ( $N_y = 2$ ) if  $2J_{\text{intra}}$  is replaced by  $J_{\text{intra}}$ . Representative energy surfaces for two  $10 \times 10$  HJ-aggregates are shown in Figure 54. Because of the opposing

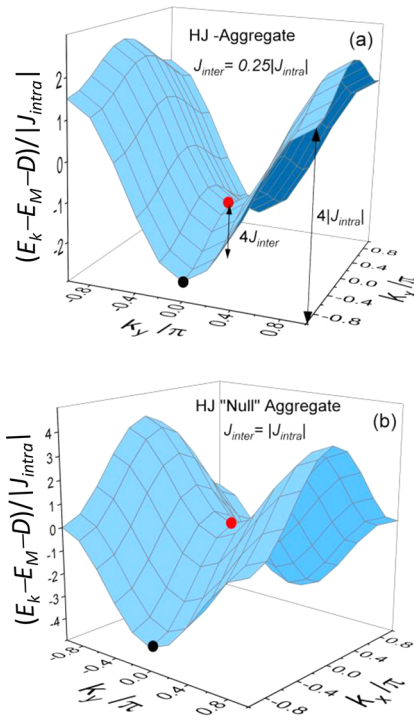


**Figure 54.** (a) Free-exciton energies for HJ-aggregates dominated by the  $J$ -coupling along  $y$  with  $|J_{\text{intra}}| = 4J_{\text{inter}}$ . In the “null” aggregate in (b),  $|J_{\text{intra}}| = J_{\text{inter}}$  and the absorption spectrum resembles a monomer (see text). Energy units are in  $|J_{\text{intra}}|$ . The full bandwidth ( $W$ ) obtained from eq 128 is  $5|J_{\text{intra}}|$  in (a) and  $8|J_{\text{intra}}|$  in (b).

signs of the intra- and interchain couplings, the energy surface resembles a saddle; the saddle point defined by  $(k_x, k_y) = (0,0)$  and depicted by the red dot in Figure 54 corresponds to the bright exciton, which captures all of the oscillator strength from the vibrationless ground state. (There is only one molecule per unit cell, so there is not a second Davydov component.) In Figure 54a, the  $J$ -couplings are dominant, and the bright exciton undergoes an exciton-induced red shift relative to the monomer,  $J_{k=0} = 2J_{\text{intra}} + 2J_{\text{inter}} < 0$ , as in a J-aggregate.

However, unlike a true J-aggregate, the absorbing exciton resides in the interior of the band; it no longer defines the band-bottom state (indicated by the black dot) as in ideal J-aggregates. Hence, HJ-aggregates are expected to show very different PL signatures as discussed below. In Figure 54b, the magnitudes of the inter- and intrachain couplings are equal; in this case, the bright exciton is exactly in the middle of the band, and there is no exciton-induced shift at all. In ref 91, such an aggregate was referred to as a “null” aggregate due to the cancellation of couplings.

Figure 55 shows how the (reduced) absorption spectrum evolves with increasing  $J_{\text{inter}}$  in a  $4 \times 4$  HJ-aggregate. The HR

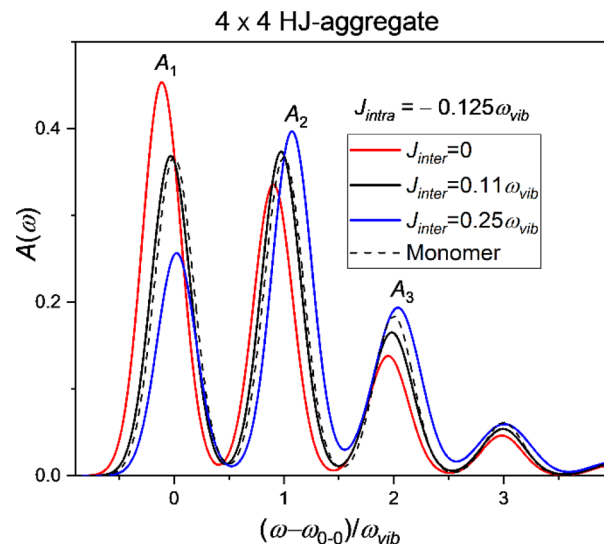


**Figure 55.** Absorption spectrum for a  $4 \times 4$  HJ-aggregate with  $J_{\text{intra}} = -0.125 \omega_{\text{vib}}$  and for several values of  $J_{\text{inter}}$ . The HR factor,  $\lambda^2$ , is set to unity so that the first two vibronic peaks are equal in the monomer spectrum (dashed line). Spectra were evaluated using the Holstein Hamiltonian under the TPA and assuming periodic boundary conditions.

factor was set to unity so that in the monomer spectrum (dashed line) the peaks  $A_1$  and  $A_2$  are of equal intensity. In addition, the gas-to-crystal shift  $D$  was set to zero to more easily compare the aggregate and monomer spectra. When  $J_{\text{inter}} = 0$ , the spectra corresponds to a linear J-aggregate with  $N = 4$ . Note that  $R_{\text{abs}}$  is significantly greater than the monomer value,  $1/\lambda^2 (= 1)$ , and the  $0-0$  peak is red-shifted relative to the monomer. Increasing  $J_{\text{inter}}$  results in increasing H-aggregate character;  $R_{\text{abs}}$  decreases, and the  $A_n$  peaks blue-shift. Interestingly, when  $J_{\text{inter}}$  is  $\sim 0.85|J_{\text{intra}}|$ , the ratio  $R_{\text{abs}}$  becomes unity, the spectral shift vanishes, and the entire spectral line shape becomes practically identical to the monomer. At this point, the H and J influences have effectively canceled out.

The competition between H- and J-promoting couplings can be appreciated quantitatively in the weak exciton coupling regime<sup>249</sup> ( $W \ll \lambda^2 \omega_{\text{vib}}$ ), where  $R_{\text{abs}}$  is given by the ratio formula in eq 55 after replacing  $J_{k=0}$  with  $2J_{\text{intra}} + 2J_{\text{inter}}$ . In particular, the ratio formula predicts that  $R_{\text{abs}}$  is equal to the monomer value exactly at the null condition,  $J_{\text{inter}} = |J_{\text{intra}}|$ . This weak coupling prediction differs slightly from what was found for the  $4 \times 4$  aggregates in Figure 55 because the exciton bandwidth is just beyond the perturbative regime ( $W = \lambda^2 \omega_{\text{vib}}$  when  $J_{\text{inter}} = |J_{\text{intra}}| = 0.125 \lambda^2 \omega_{\text{vib}}$ ).

Null aggregates were first introduced to describe the absorption spectral line shape of lutein diacetate assemblies,<sup>91</sup> where all of the extended J- and H-like Coulombic couplings in the packing arrangement of Figure 53b were shown to practically cancel for the  $k = (0,0)$  exciton. Calculations for a chiral stack of such aggregates accounted for the overall H-like absorption spectral line shape obtained experimentally due almost entirely to interplanar positive couplings. Interestingly, such H-aggregates are still red-shifted most likely due to a substantial gas-to-crystal spectral shift.<sup>91</sup>

Note that in the segregated null aggregates considered so far the cancellation of H- and J-couplings is limited to the excitonic contribution to the  $k = (0,0)$  exciton's energy and does not imply a collapse of the entire exciton bandwidth. Indeed, at the null condition ( $J_{\text{intra}} = -J_{\text{inter}}$ ), the free exciton bandwidth is  $8|J_{\text{intra}}|$  from eq 126. Because the bandwidth dictates transport, the exciton mobility is not adversely affected at the null condition. This is quite different from integrated null aggregates where the cancellation occurs within the same set of chromophores, for example, in integrated HJ-aggregates where Coulomb and short-range couplings effectively cancel out between neighboring chromophores in a  $\pi$ -stack (see section 5.7).<sup>225,238</sup> In such aggregates, one can achieve an effective cancellation of the Coulomb-derived exciton band (including extended couplings) with the exciton band derived from the short-range couplings leading to substantial overall band narrowing and a reduction in exciton mobility.<sup>225,238</sup>

The competition between H- and J-promoting couplings in HJ-aggregates can also be observed in the PL spectrum. Consistent with Kasha's rule, PL derives from the lowest-energy exciton(s). In HJ-aggregates, the lowest energy exciton is a dark exciton with  $k_y = 0$ ,  $k_x = \pi$ , as indicated by the black dot in Figure 54. As in linear aggregates, 0–0 emission can only derive from the nodeless (bright) exciton indicated by the red dot, which has energy  $\Delta E = 4J_{\text{inter}}$  relative to the band bottom. When vibronic coupling is included,  $\Delta E$  is approximately equal to  $4FJ_{\text{inter}}$ , where  $F$  is the generalized FC factor. (Note that for the HJ dimers in ref 249,  $\Delta E = 2FJ_{\text{inter}}$ ). Hence, when the temperature is low enough to ignore thermal excitations, 0–0 emission is strictly forbidden, resulting in an H-like vibronic progression in the PL spectrum devoid of the origin (0–0) peak. As temperature increases and  $k_B T$  approaches  $\Delta E$ , the 0–0 emission from the bright exciton with  $k = (0,0)$  becomes thermally activated. (Conversely, all excitons, independent of wave vector, contribute to sideband emission, see section 4.4.) The overall effect is an initial H-like increase of  $I^{0-0}$  and  $R_{\text{PL}}$  with temperature. Both quantities reach their maximum values when  $k_B T$  is approximately  $\Delta E$  and subsequently diminish with further increases in temperature as the population of the  $k = (0,0)$  exciton is thermally depleted, as is characteristic of J-aggregates. The overall "HJ" behavior was evaluated in ref 249 for an HJ dimer consisting of two interacting J-chains packed as in Figure 53a. The numerical results (colored dots), shown in Figure 56, are well-captured by the analytical expression (colored lines) obtained under the parabolic band approximation and in the thermodynamic limit<sup>249,308</sup>

$$R_{\text{PL}} = \frac{2}{\lambda^2} \frac{e^{-\Delta E/k_B T}}{1 + e^{-\Delta E/k_B T}} \sqrt{\frac{4\pi F|J_{\text{intra}}|}{k_B T}} \quad N > \sqrt{\frac{4\pi F|J_{\text{intra}}|}{k_B T}} > 1 \quad (127)$$

where  $\Delta E = 2FJ_{\text{inter}}$  for a dimer and the generalized FC factor,  $F$ , ranges from  $\exp(-\lambda^2)$  for weak exciton coupling to

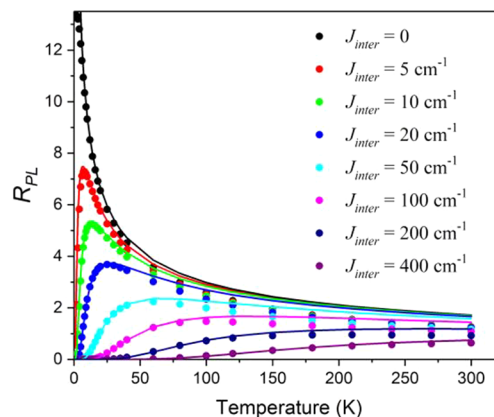


**Figure 56.** PL ratio  $R_{\text{PL}}$  vs temperature for an HJ dimer with  $J_{\text{intra}} = -325 \text{ cm}^{-1}$  and  $\lambda^2 = 1$  from ref 249. Several values of the interchain coupling are shown. The circles represent the numerically calculated ratio while the solid lines are determined from eq 127. Reprinted with permission from ref 249. Copyright 2012, AIP Publishing.

approximately unity for strong exciton coupling. Analysis of eq 127 shows that the peak occurs when  $T = T_p$  with  $T_p \approx 1.3\Delta E/k_B$  for an HJ dimer. Beyond  $T_p$ , the ratio decreases as  $T^{-1/2}$  as expected for a single J-chain. In the fully two-dimensional HJ-aggregate depicted in Figure 53a, making the parabolic band approximation in both directions results in a form similar to eq 127 but with an overall  $1/T$  dependence for  $T > T_p$ .<sup>249</sup> More accurate numerical evaluations for  $R_{\text{PL}}$  in 2D HJ-aggregates parametrized for P3HT (which do not invoke the parabolic band approximation) are presented by Paquin et al.<sup>327</sup> and display temperature dependences qualitatively similar to those in Figure 56.

Because the radiative decay rate,  $\gamma_R$ , approximately tracks the 0–0 line strength (when the 0–0 peak is dominant), it will also initially increase with temperature, peak, and then decrease. Hence, HJ-aggregates display the unusual phenomenon of thermally activated superradiance,<sup>249</sup> which has not yet been observed in polymer HJ-aggregates, most likely due to the obstructive influence of disorder.<sup>308,327</sup> The maximum enhancement of the radiative rate for the HJ dimers of ref 249 occurs when  $T = T_p$ , at which point<sup>249</sup>

$$(\gamma_R/\gamma_{\text{mon}})_{\text{max}} \approx 1.4F \sqrt{\frac{|J_{\text{intra}}|}{J_{\text{inter}}}} \quad (128)$$

where  $\gamma_{\text{mon}}$  is the single-molecule radiative decay rate. Hence, strong superradiant behavior,  $(\gamma_R/\gamma_{\text{mon}})_{\text{max}} \gg 1$ , is expected whenever the intrachain coupling is much larger than the interchain coupling consistent with dominant J-aggregate behavior.

Evidence for thermally activated superradiance has very recently been obtained by Eisfeld et al.<sup>338</sup> for the perylene derivative PTCDA deposited as a monolayer on a KCl substrate. The well-ordered "brick-wall" aggregates, shown in the inset to Figure 57, are similar to those in Figure 53b. Using the point-dipole approximation, Eisfeld et al.<sup>338</sup> showed that the intermolecular coupling between the four nearest neighbors is negative whereas that between the two next nearest (side-by-side) neighbors is positive. Figure 57 shows the radiative enhancement factor derived from the 0–0/0–1 PL ratio as a function of temperature, illustrating activated behavior followed by an approximately  $1/T$  temperature dependence. As shown

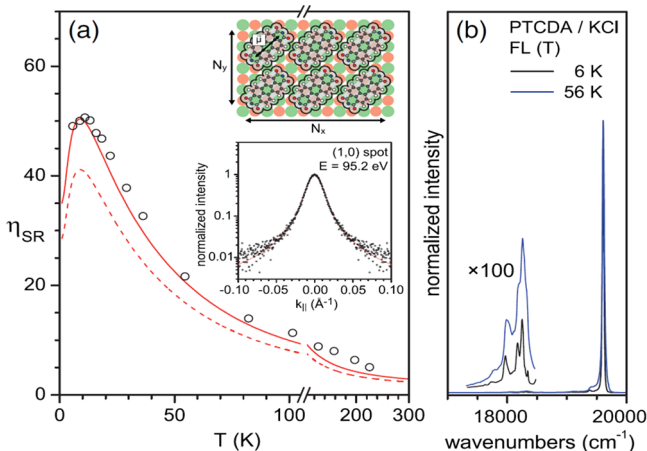


**Figure 57.** (a) Superradiance enhancement factor (the 0–0/0–1 ratio) as a function of temperature for the PTCDA monolayer on KCl from ref 338. (b) The PL spectral line shape normalized to the 0–0 peak at two temperatures. Reprinted figure with permission from ref 338. Copyright (2017), American Physical Society.

by Eisfeld et al., the activated dependence derives from the presence of dark states below the bright exciton, as is characteristic of HJ-aggregates, where the bright exciton no longer resides at the band edges. On the basis of the peak temperature ( $T_p \approx 15$  K) in Figure 57a, one can estimate that the bright exciton is only  $\approx 10$  cm<sup>-1</sup> displaced from the bandbottom. Figure 57b shows the enormous enhancement of the PL ratio ( $R_{PL}$ ) at two selected temperatures. The enhancement is the largest measured for a molecular ensemble and reflects similarly large exciton coherence numbers ( $O[10^2]$ ) obtained at low temperatures. It should be cautioned, however, that extracting  $N_{coh}$  from  $R_{PL}$  is strictly valid when the lowest exciton is optically allowed to the vibrationless ground state as in a J-aggregate. When the band bottom is defined by dark states, H-aggregate behavior prevails at low temperatures ( $T < T_p$ ) and  $N_{coh}$  no longer scales as  $R_{PL}$ , see section 4.5. Only when J-aggregate behavior is recovered at higher temperatures can one safely use  $R_{PL}$  to extract  $N_{coh}$ .

#### 4.9. Multiple Mode Vibronic Coupling

In this section we review some of the basic photophysics resulting from vibronic coupling involving two or more modes. The inclusion of extra vibrational modes was found to be necessary in understanding the polarized absorption and PL spectra of oligothiophenes and oligophenylene aggregates and crystals,<sup>120,183,262,314,316</sup> where, in addition to the usual aromatic-quinoidal stretching mode with energy  $\approx 0.18$  eV, there exist lower energy modes (starting at  $\approx 0.02$  eV) which create even finer vibronic structure, most apparent near the absorption origin. The existence of two or more modes is also interesting from a fundamental viewpoint, as synergies between modes may develop such that the spectral impact is not additive; for example, the presence of one mode may alter the exciton-coupling regime “felt” by another mode.<sup>120,183,262,378</sup> In the case of quaterthiophene herringbone aggregates considered already in section 4.7 the presence of the 0.18 eV mode renormalizes the lowest exciton band making it flatter; lowering the curvature allows the low-frequency modes to experience a reduced “effective” exciton coupling which leads to substantial changes in the polarized absorption<sup>120,183</sup> and PL spectra.<sup>262</sup>

Inclusion of vibronic coupling involving  $M$  total vibrational modes in the Frenkel–Holstein Hamiltonian is straightforward;

the single-mode Hamiltonian in eq 13 is generalized to read<sup>120,183,262,314,316,378</sup>

$$H_{FH} = H_{ex} + \sum_{i=1}^M \sum_n \omega_{vib}^i b_{n,i}^\dagger b_{n,i} + \sum_{i=1}^M \sum_n \{\lambda_i \omega_{vib}^i (b_{n,i}^\dagger + b_{n,i}) + \lambda_i^2\} |n\rangle \langle n| \quad (129)$$

where  $b_{n,i}^\dagger$  is the creation operator corresponding to the  $i$ th vibrational mode on the  $n$ th chromophore and  $\omega_{vib}^i$  is the frequency of mode  $i$ . The Hamiltonian treats all  $M$  modes as symmetric (relative to the point group of the molecule) because only symmetric modes can undergo a shift in their equilibrium positions subsequent to electronic excitation. The shift for the  $i$ th mode is dictated by the HR factor  $\lambda_i^2$ .

One difficulty in working with the Hamiltonian in eq 129 is the large basis set necessary to account for the many ways of distributing multiple quanta over  $M$  modes and  $N$  sites. The problem is exacerbated if the mode couplings are spread throughout the different regimes of exciton-vibrational coupling. For example, the aforementioned vibrational modes in oligothiophenes have energies spanning 0.02–0.2 eV with comparable HR factors of order unity; hence, the exciton bandwidth  $W$  ( $\sim 0.5$ –1 eV) is very large relative to the nuclear relaxation energy of the lowest-energy modes, making the exciton–phonon basis set the most efficient basis for evaluating the impact of such modes. However,  $W$  is comparable to the nuclear relaxation energy of the highest energy modes, making the multiparticle basis set under the two-particle approximation the best basis for evaluating the impact of these modes. In ref 316, the dilemma was resolved by introducing a hybrid basis set to simultaneously treat the two classes of modes. In this way, the authors were able to capture the vibronic fine structure in the measured absorption spectrum of quarter-thiophene thin films in agreement with a Herzberg–Teller analysis of Petelenz and Andrzejak.<sup>314</sup>

The polarized PL from OTn herringbone lattices including multimode vibrational coupling was also investigated theoretically.<sup>262</sup> As reviewed in section 4.7, the 0–0 emission from herringbone lattices is uniquely polarized along the direction defined by the lowest Davydov component (the  $b$ -axis for OTn’s), but the 0–1 emission has components polarized along all directions. As shown in Figure 49, the aforementioned low-energy modes contribute pronounced sidebands in the PL spectrum, the lowest such peak is only  $\sim 160$  cm<sup>-1</sup> to the red of the 0–0 PL origin. As hinted at in ref 262 and shown rigorously below, the PL ratio rule applies individually to all such modes, making them ideal for extracting exciton coherence numbers as described in section 4.5.

In ref 378, it was shown that interesting synergies can develop between low and high frequency modes of comparable relaxation energies, which are directly relevant for treating low-energy torsional modes in coexistence with the higher-energy vinyl-stretching modes in *p*-oligophenylens<sup>379–381</sup> and other conjugated oligomers. The low-energy torsional modes, which are more accurately described using a double-well potential in either the ground or excited electronic states, were instead described using displaced ground and excited harmonic wells with large HR factors of order ten. One of the interesting findings concerns the radiative efficiency related to the band-integrated PL. As shown in Figure 58 for an H dimer, the radiative efficiency when both modes are simultaneously present is twice as large as the sum of the single-mode efficiencies. The figure further shows that adding the torsional degree of freedom triples the photon output. Much of the effect

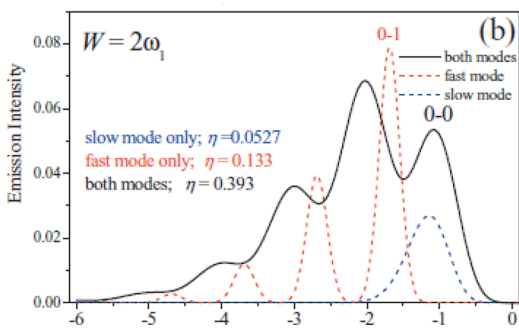


**Figure 58.** PL spectrum of an H dimer with vibronic coupling to a single fast mode ( $\omega_{\text{vib}} = 1400 \text{ cm}^{-1}, \lambda^2 = 1$ ), a single slow mode ( $\omega_{\text{vib}} = 140 \text{ cm}^{-1}, \lambda^2 = 10$ ), and coupling to both modes. The inset shows the radiative efficiencies  $\eta$ . Reprinted with permission from ref 378. Copyright 2010, AIP Publishing.

is due to the ability of the torsional mode to activate emission in the spectral region labeled as “0–0” in the figure; without the torsional mode, 0–0 emission corresponding to the high-frequency mode is disallowed by symmetry. The effect can be understood as a form of symmetry breaking; the torsional mode is so slow as to be considered static on the time scale of emission. The resulting static disorder then allows 0–0 emission from the high-frequency mode in much the same way that the 0–0 emission in H-aggregates increases with inhomogeneous disorder. The intermode synergy is actually slightly more complex as discussed at length in ref 378.

We conclude the section by once again demonstrating the robustness of the PL ratio rule for J-aggregates or any aggregate in which the lowest energy optical transition is symmetry allowed (for example, HB aggregates), this time in the presence of multiple-mode vibronic coupling. The derivation follows from a straightforward generalization of the single-mode proof outlined in ref 176. The lowest energy exciton can be expressed in a multimode generalization of the exciton–phonon wave function of section 3.3

$$|\psi_{\text{em}}\rangle = |\tilde{\mathbf{0}}_1, \tilde{\mathbf{0}}_2, \dots, \tilde{\mathbf{0}}_M\rangle \otimes \sum_{k, n_{q_1}^1, n_{q_2}^1, \dots} c_{k; n_{q_1}^1, n_{q_2}^1, \dots}^{\text{em}} |k; n_{q_1}^1, n_{q_2}^1, \dots, n_{q_{N-1}}^1; n_{q_1}^2, \dots\rangle \quad (130)$$

where we have accounted for  $M$  totally symmetric (progression-building) vibrational modes. The first ket indicates that there are no vibrational quanta in any of the totally symmetric ( $q = 0$ ) modes. The ket in the summand indicates the value of the exciton wave vector ( $k$ ) as well as the number of quanta in the nontotally symmetric modes ( $q \neq 0$ ) of the  $i$ th

vibration (indicated by the superscript). For ideal J-aggregates with one molecule per unit cell, the prime constrains the sum to include only states with zero total quasi-momentum,  $\kappa$ , i.e.,

$$\kappa \equiv k + \sum_{i=1}^M \sum_{l=1}^{N-1} n_{q_l}^i q_l = 0$$

However, for H-type aggregates with two molecules per unit cell, the prime indicates that  $\kappa$  must equal  $\pi$  in linear aggregates and  $(\pi, \pi)$  in HB aggregates.<sup>176</sup>

The evaluation of the 0–0 intensity proceeds along the same lines described in ref 176. For linear J-aggregates, we obtain

$$I^{0-0} = FN \quad (131)$$

where the FC factor is generalized in a straightforward manner to include all  $M$  modes

$$F \equiv \exp[-(\lambda_1^2 + \lambda_2^2 + \dots + \lambda_M^2)/N] |c_{k=0,0,\dots,0}^{\text{em}}|^2 \quad (132)$$

The line-strength of the first sideband of mode  $i$  has the form

$$I_i^{0-1} = F \lambda_i^2, \quad i = 1, 2, \dots, M \quad (133)$$

so that, for the  $i$ th mode, the ratio rule becomes

$$R_{\text{PL}}^{(i)} \equiv \frac{I_i^{0-0}}{I_i^{0-1}} = \frac{N}{\lambda_i^2} \quad \text{J-aggregates} \quad (134)$$

**Eq 134** represents the most general form of the PL ratio rule for linear J-aggregates. For H-type aggregates with two molecules per unit cell,  $F$  is obtained from **eq 132** by replacing  $c_{k=0,0,\dots,0}^{\text{em}}$  with  $c_{k=\pi,0,\dots,0}^{\text{em}}$  for linear aggregates and  $c_{k=(\pi,\pi),0,\dots,0}^{\text{em}}$  for 2D aggregates. The ratio rule that follows, applies to emission polarized in the same direction ( $\beta$ ) as the lower Davydov component

$$R_{\text{PL},\beta}^{(i)} \equiv \frac{I_{\beta}^{0-0}}{I_{i,\beta}^{0-1}} = \frac{N}{\lambda_i^2} \quad \text{H-type(two-mol/unit cell)} \quad (135)$$

As discussed in earlier sections, the ratio rule can also be readily extended to include disordered lattices with thermally excited populations. In such cases, **eqs 134** and **135** remain valid but with  $N$  replaced by the coherence number  $N_{\text{coh}}$ . Referring again to the experimentally determined PL spectrum for OT4 in **Figure 49**, the most direct way of determining  $N_{\text{coh}}$  is from the ratio of the  $b$ -polarized 0–0 peak and the first vibronic sideband with energy only 0.02 eV below the 0–0 peak from which one can estimate a value of 10 for  $N_{\text{coh}}$ .<sup>262</sup>

A more useful form of the ratio rule also follows from **eqs 134** and **135**. As often happens in conjugated molecules, there

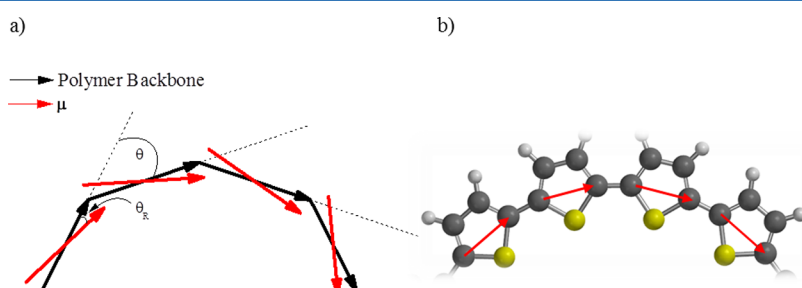


**Figure 59.** (a) Schematic representation of a bent polymer chain. Each monomer unit is represented by a black arrow, and the transition dipole moment of each unit is represented by a red arrow. The bend angle  $\theta$  is the angle between adjacent monomer vectors. (b) A segment of a polythiophene chain in the all-syn conformation. The vector model in (a) can be easily mapped onto the polythiophene chain segment in (b). Adapted with permission from ref 177. Copyright (2014), American Chemical Society.

are a cluster of modes with similar frequencies that contribute sideband peaks that cannot be resolved and together form a broad sideband ("0–1") peak. The integrated band scales as  $\sum_i I_i^{0-1} = F \sum_i \lambda_i^2$ . Here,  $\sum_i \lambda_i^2$  can be thought of as the effective HR factor for the collection of closely spaced modes. Hence, for linear J-aggregates, the modified ratio rule becomes

$$R_{PL} \equiv \frac{I^{0-0}}{\sum_i I_i^{0-1}} = \frac{N}{\sum_i \lambda_i^2} \quad (136)$$

where, as usual,  $R_{PL}$  is determined experimentally from the ratio of integrated areas. For H-type aggregates, a form similar to eq 136 results but for the component of PL polarized along  $\beta$ .

#### 4.10. Curved Aggregates

Polarized absorption and emission studies of bent or curved molecular aggregates and polymers have provided additional insight into exciton localization and photophysics.<sup>382–391</sup> In this regard, conjugated polymers (CPs) can be effectively modeled as linear J-aggregates ("J-chains"), where each repeat unit represents a chromophore as depicted in Figure 59.<sup>15,207–213</sup> The uniform chain bend is quantified by the angle  $\theta$  between adjacent repeat unit (transition) dipole moment vectors; in the all-syn conformation of P3HT shown in Figure 59,  $\theta$  is well-defined. However, even ostensibly "straight" polymers (for example, all-anti-P3HT) can undergo long-range bending stress, which induces a curved topology. The impact of uniform bending on the absorption and PL spectrum has been analyzed theoretically by Hestand and Spano<sup>177</sup> as well as Barford and Marcus.<sup>244,248</sup> A uniform bend is still an ordered morphology; allowing the repeat units to also rotate out of the plane as occurs when torsional disorder is present is an additional and important consideration. Such conformational disorder was originally treated theoretically by Rossi et al.<sup>392</sup> and Soos and Schweizer.<sup>393</sup>

In CPs, the J-aggregate nature derives mainly from the negative short-range coupling between neighboring repeat units arising primarily from p-orbital overlap.<sup>15,242–248</sup> This is entirely consistent with direct bandgap semiconductors in which the optical gap transition is optically allowed with no change in wave vector  $k$  (see section 5.8.2). Longer-range Coulomb coupling due to the repeat unit transition dipoles is of secondary importance and usually absorbed into an effective nearest neighbor coupling. As for the case of "straight" aggregates considered so far, the steady-state absorption and PL spectral line shapes of curved J-chains depend on the exciton coupling regime defined by comparing the exciton bandwidth  $W$  to the nuclear relaxation energy  $\lambda^2 \omega_{vib}$ .

In the weak-to-intermediate exciton coupling regime considered in ref 177 ( $W < \lambda^2 \omega_{vib}$ ), the PL spectrum was shown to be particularly sensitive to chain bending while the absorption spectrum was shown to be rather insensitive. Figure 60 shows how the absorption and PL spectra respond to the bend angle in weakly coupled J-chains with  $J_C = -200 \text{ cm}^{-1} = 0.14 \omega_{vib}$ . (Note that, here,  $J_C$  can be considered as an effective coupling composed of both Coulombic and short-range superexchange interactions, see section 5 for further details). The HR factor was set to  $\lambda^2 = 1$  so that in the monomer spectrum the first two vibronic peaks in either spectrum are of equal intensity. As can be seen from the figure, the absorption spectrum is almost independent of  $\theta$  in part due to the neglect of any  $\theta$ -dependent changes in  $J_C$  ( $\theta$  increases to only  $2\pi/40$  in Figure 60). However, bending still leads to oscillator strength redistribution to higher energy excitons; in straight J-chains, the

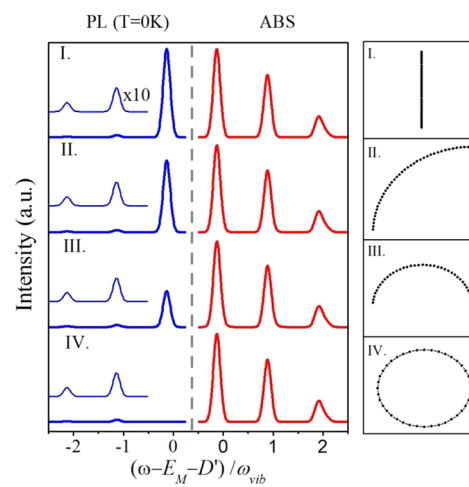


**Figure 60.** Absorption and PL spectra of bent J-chains with  $N = 40$  chromophore units and  $\lambda^2 = 1$ . Note that the spectra for each configuration look nearly identical with the exception of the 0–0 peak in the PL spectrum. Reprinted with permission from ref 177. Copyright (2014), American Chemical Society.

0–0 oscillator strength resides entirely in the transition to the lowest energy ( $k = 0$ ) exciton, whereas in circular or ring aggregates, oscillator strength resides in the higher-energy  $k = \pm 2\pi/N$  excitons. As shown by Spitz et al.,<sup>69</sup> the  $k = 0$  exciton in ring aggregates acquires oscillator strength when the transition dipole moment has a component normal to the plane of the ring, which is not the case here. The blue shift, which results from the transfer of oscillator strength from the  $k = 0$  to the  $k = \pm 2\pi/N$  excitons, is of the order  $4\pi^2 |J_C|/N^2$ , which is only  $5 \text{ cm}^{-1}$  for the J-chains in Figure 60 with  $N = 40$  and therefore not observable. However, for much larger values of  $|J_C|$  ( $\gtrsim 1000 \text{ cm}^{-1}$ ) typically encountered in CPs (which also exhibit conjugation lengths of  $N = 10$  repeat units or less), the blue-shift is clearly observed.<sup>177</sup> This is consistent with the work of Soos and Schweizer<sup>393</sup> who showed that, in conformationally disordered polymers where the spatial correlation of the transition dipole moment vector is defined by a persistent length  $\xi_p$ , the absorption spectrum blue-shifts (and broadens) with decreasing  $\xi_p$ , although here the inherent disorder allows oscillator strength to be distributed over a range of  $k$  values. In CP chains, the blue shift can increase to almost 20% of the (straight-chain) optical gap as  $\xi_p$  is reduced to the length of a repeat unit. Rossi et al.<sup>392</sup> also studied the relationship between the conjugation length and persistent length in several CPs, showing in particular how sensitive the persistence length is to details of the torsional potential.

In sharp contrast, the PL spectrum is extremely sensitive to bending as observed in Figure 60. The spectra were calculated in the low temperature limit so that emission derives entirely from the lowest energy ( $k = 0$ ) exciton. Hence,  $R_{PL}$  is equal to  $N/\lambda^2 (= 40)$  in the straight chains in panel I (see eq 58) but is driven to zero in the circular chains (panel IV) where the 0–0 line strength involving the lowest-energy exciton is exactly zero. As shown in ref 177, the PL ratio is almost entirely driven by changes in the 0–0 intensity, which is coherently enhanced and hence sensitive to the  $\theta$ -dependent sum of repeat unit transition dipole moments. In the weak-to-intermediate exciton coupling regime, the PL ratio was shown to be given by<sup>177</sup>

$$R_{\text{PL}} \approx \frac{\csc^2(\theta/2)\sin^2(N\theta/2)}{N\lambda^2} \quad k_{\text{B}}T \ll 4\pi\tilde{\alpha}_c/N^2 \quad (137)$$

which reduces to  $N/\lambda^2$  for straight chains ( $\theta = 0$ ) and to zero for circular chains ( $\theta = 2\pi/N$ ). It should be noted that the ratio  $R_{\text{PL}} \equiv I^{0-0}/I^{0-1}$  involves the line strengths, which are derived from the measured spectra after removing the cubic frequency dependency stemming from the density of photon states. The ratio of line intensities with the cubic frequency retained is therefore  $R_{\text{PL}} \times [\omega_{0-0}/(\omega_{0-0} - \omega_{\text{vib}})]^3$ , which is roughly 30% greater than  $R_{\text{PL}}$  for typical values encountered in conjugated polymers ( $\omega_{0-0} = 2 \text{ eV}$ ,  $\omega_{\text{vib}} = 0.17 \text{ eV}$ ).

For increasing temperatures, the emitting ensemble consists of a Boltzmann distribution of the lowest energy excitons. Maintaining the weak-to-intermediate exciton coupling limit, the ratio becomes<sup>177</sup>

$$R_{\text{PL}} \approx \frac{N_{\text{T}}}{\lambda^2} c(\theta, T) \quad (138)$$

where  $N_{\text{T}}$  is the thermal coherence number defined in eq 97 and  $c(\theta, T)$  is a morphology-dependent factor. In perfectly straight J-chains,  $c(\theta, T) = 1$  independent of temperature so that eq 138 reduces to eq 99. In the opposite extreme of ring aggregates,  $c(\theta, T)$  is zero at low temperature because the 0–0 transition involving the lowest-energy exciton (with  $k = 0$ ) is zero. However, increasing the temperature in ring aggregates allows thermal excitation of the bright  $k = \pm 2\pi/N$  excitons, thereby increasing the thermally averaged 0–0 transition intensity.  $c(\theta, T)$  increases to unity in the high-temperature limit of circular aggregates.

Barford and Marcus<sup>244,248</sup> also considered the photophysics of bent CPs, relating the PL ratio  $R_{\text{PL}}$  directly to the participation number. Using an exciton–phonon basis set similar to that in eq 21, they showed that in the strong coupling regime ( $4\pi^2|J_{\text{C}}|/N^2 \gg \omega_{\text{vib}}$ ) the PL ratio becomes completely insensitive to bending. In particular, they derived the simple relation

$$R_{\text{PL}} = \frac{\text{PN}}{\lambda^2}, \quad 4\pi^2|J_{\text{C}}|/N^2 \gg \omega_{\text{vib}} \quad (139)$$

where the participation number, PN, was defined by  $\text{PN} \equiv 1/\sum_n |c_n^{\text{em}}|^4$  with  $c_n^{\text{em}} = \langle n; 0, 0, \dots 0 | \psi_{\text{em}} \rangle$  (note the difference from the IPR definition in eq 36). For aggregates with periodic boundary conditions, eq 139 further reduces to  $R_{\text{PL}} = N/\lambda^2$ , a limit that also follows directly from the analysis in ref 177 when the strong excitonic coupling condition is applied to eq S10 of that paper. Barford and Marcus<sup>248</sup> also considered what they called the “anti-adiabatic” regime equivalent to the weak exciton coupling,  $4\pi^2|J_{\text{C}}|/N^2 \ll \omega_{\text{vib}}$ , in which the PL ratio becomes very sensitive to bending, similar to the behavior demonstrated in Figure 60.

The PL ratio has been used by experimentalists to determine the impact of bending on exciton delocalization.<sup>388–390</sup> For oligothiophene chains and macrocycles containing 10 thiophene rings, Kim et al.<sup>390</sup> observed an inversion of the 0–0/0–1 PL intensity ratio in going from the linear conformer, where the ratio is approximately 2, to the macrocycles where the ratio drops to only 0.80. Because the experiments were conducted at room temperature, the nonzero value of the 0–0 PL intensity for the macrocycles is likely due to thermal excitation effects (see eq 138) along with localization due to torsional disorder.

Interestingly, the latter effect was suspected in larger macrocycles containing up to 30 thiophene units.

#### 4.11. Chiral H-Aggregates

An important class of helical H-aggregates are comprised of  $\pi$ -stacked, hydrogen-bonded chromophores in which neighboring molecules are related through a twist angle  $\phi$  about the aggregate axis, as demonstrated in Figure 61 for the

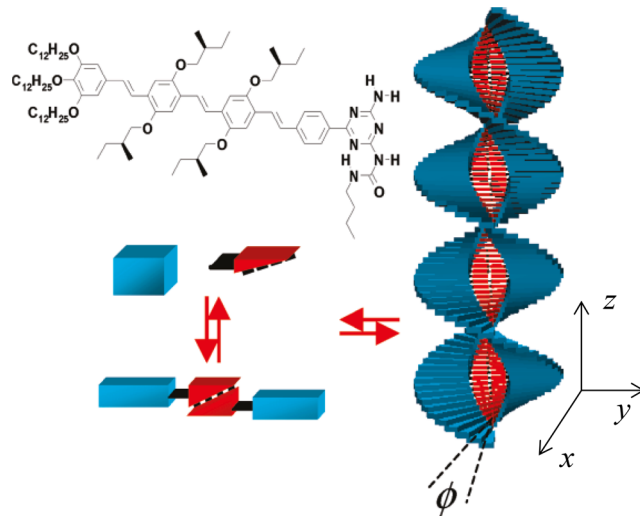


**Figure 61.** Left-handed helical aggregate of MOPV4 with  $\phi = 14$  degrees. Reprinted with permission from ref 182. Copyright 2008, AIP Publishing.

chromophore MOPV4 shown in the inset. Left- and right-handed helices correspond to  $\phi > 0$  and  $\phi < 0$ , respectively. Examples of chromophores that engage in helical aggregate formation include perylene derivatives,<sup>33,37</sup> functionalized OPVn's,<sup>131,181,394–399</sup> functionalized OTn's,<sup>112,115,116,400,401</sup> and certain carotenoids.<sup>89,90,402–404</sup> Chiral aggregates absorb and emit right- and left-handed circularly polarized light differently, giving rise to differential absorption or circular dichroism (CD) and differential emission or circularly polarized luminescence (CPL). The associated absorption and luminescence dissymmetries,  $g_{\text{abs}}(\omega)$  and  $g_{\text{lum}}(\omega)$  follow by dividing the differential absorption and luminescence spectra by the total absorption and luminescence cross sections, respectively. The intensive observables  $g_{\text{abs}}(\omega)$  and  $g_{\text{lum}}(\omega)$  along with the total absorption and PL spectral line shapes considered so far provide four spectral observables with which to rigorously test theories for vibronically coupled molecular aggregates.<sup>91,169,181,182,309,405–415</sup> In addition,  $g_{\text{abs}}(\omega)$  and  $g_{\text{lum}}(\omega)$  provide additional information; for example, extreme sensitivity of  $g_{\text{abs}}(\omega)$  and  $g_{\text{lum}}(\omega)$  to distant interchromophore separations<sup>181,407,408,416–419</sup> allows for novel ways to probe the nature of intermolecular interactions.

**4.11.1. Unpolarized Absorption and PL.** The unpolarized absorption and photoluminescence spectra of an isotropic distribution of the helical aggregates shown in Figure 61 has been described in detail in refs 91 and 181. In such aggregates, the  $S_0 \rightarrow S_1$  transition dipole moment lies along the long molecular axis that is normal to the helical (z) axis; for the  $n$ th chromophore, the transition dipole moment is

$$\mu_n \equiv \mu \cos(\phi n) \mathbf{i} - \mu \sin(\phi n) \mathbf{j} \quad (140)$$

where  $i$  and  $j$  are unit vectors in the  $x$  and  $y$  directions, respectively. Hence, ideal H-aggregates are obtained when  $\phi = 0$  with oscillator strength confined to the  $k = 0$  exciton located at the top of the band. When  $\phi$  is nonzero and in the limit of large aggregates ( $N \gg M$ , where  $M$  is the number of molecules per complete turn) oscillator strength is instead divided between the two excitons with wave vectors  $k = \pm 2\pi/M$  ( $= \pm\pi\phi/180$ ), where  $\phi$  is in degrees) with energy given by<sup>91</sup>

$$J_\phi = 2 \sum_{s>0} J_{n,n+s} \cos(\phi s) \quad (141)$$

Under the point dipole approximation (see eq 1), the Coulomb coupling between two chromophores separated by a distance  $ds$ , where  $d$  is the nearest neighbor separation, is

$$J_{n,n+s} = \frac{\mu^2}{4\pi\epsilon(ds)^3} \cos(\phi s) \quad (142)$$

Inserting eq 142 into eq 141 shows that  $J_\phi > 0$  for any  $\phi$ . Hence, the helical aggregates in Figure 61 resemble Kasha H-aggregates with respect to absorption and PL. More accurate evaluations of the Coulomb coupling using atomic transition charges also supports H-like aggregates.<sup>91</sup> When vibronic coupling is absent, the absorption spectrum consists of a single blue-shifted peak at an energy,  $\omega_{0-0} + D + J_\phi$ , equally polarized along  $i$  and  $j$ . As in classic H-aggregates, PL, which originates from the band-bottom ( $k = \pi$ ) exciton, vanishes due to symmetry.

The absorption spectra of lutein and lutein diacetate aggregates measured by Zsila et al.<sup>89</sup> provide excellent examples of chiral H-aggregates in the strong  $W \gg \lambda^2\omega_{\text{vib}}$  and weak  $W \lesssim \lambda^2\omega_{\text{vib}}$  exciton coupling regimes, respectively. As demonstrated in Figure 62, the unsubstituted lutein aggregates exhibit a

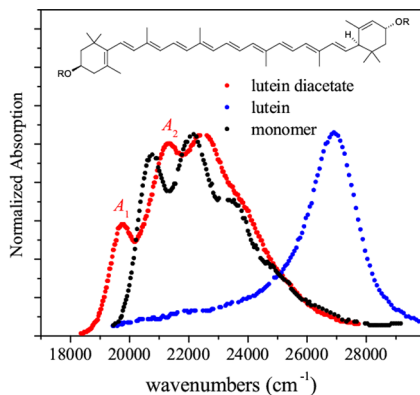


**Figure 62.** Lutein and lutein diacetate aggregate spectra measured in ref 89 along with the monomer in solution (which is essentially the same spectrum for both molecules). Adapted with permission from ref 91. Copyright (2009), American Chemical Society.

dominant peak in the absorption spectrum, blue-shifted by  $\sim 5000 \text{ cm}^{-1}$  from the monomer peak. Such aggregates are believed to be tightly packed with  $\phi \approx 20^\circ$  due to efficient hydrogen bonding between neighboring molecules. By contrast, lutein diacetate can no longer exploit hydrogen bonding and forms more loosely bound aggregates. Consequently, the absorption spectrum in Figure 62 assumes the classic form of a weakly coupled H-aggregate with an attenuated value of  $R_{\text{abs}}$  relative to the monomer. For chiral aggregates, the ratio rule for absorption derives from the general form in eq 55 after

replacing  $J_{k=0}$  with  $J_\phi$ . Because  $J_\phi > 0$ , the first vibronic peak ( $A_1$ ) is increasingly attenuated relative to the second peak ( $A_2$ ) with increasing exciton bandwidth, as is consistent with H-aggregation. In the limit of strong excitonic coupling ( $W \gg \lambda^2\omega_{\text{vib}}$ ), the vibronic structure is lost entirely and the absorption spectrum reduces to a single, strongly blue-shifted peak at  $\omega_{0-0} + D + \lambda^2\omega_{\text{vib}} + J_\phi$ <sup>91</sup> as observed for the unsubstituted lutein aggregates in Figure 62.

The steady-state PL spectrum for the chiral aggregates of Figure 61 is also H-like; when the exciton coupling is weak and disorder is absent, the vibronic progression is preserved but without the 0–0 peak. Moreover, the entire spectrum vanishes in the limit of strong exciton coupling as discussed in section 4.2.1 for ideal H-aggregates. Unfortunately, in the lutein derivatives and carotenoids in general, the state  $S_1$  is optically dark, making them essentially nonfluorescent. (The absorption spectra in Figure 62 originate from the  $S_2$  exciton.) This is not the case, however, in MOPV4 aggregates where the  $S_1$  state is strongly allowed, thereby leading to the structured PL shown in Figure 63a. However, MOPV4 aggregates have inherent

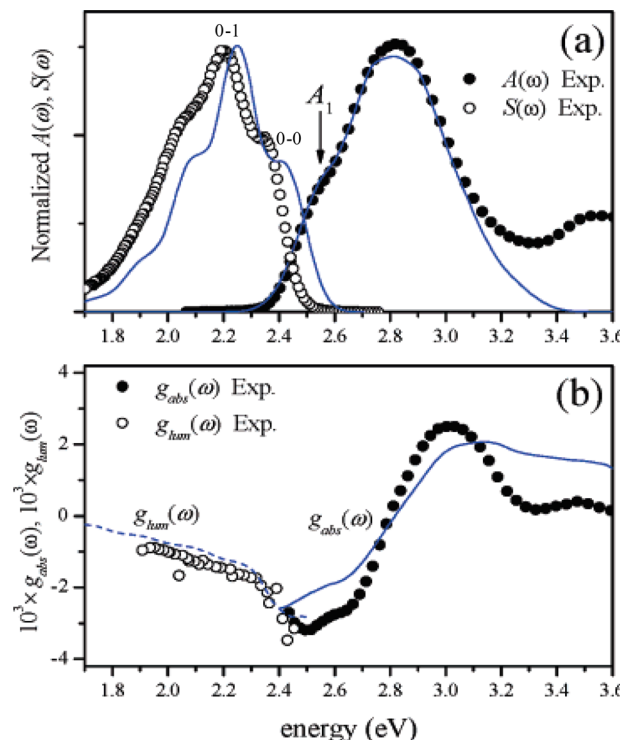


**Figure 63.** (a) Experimental absorption and emission spectra of MOPV4 helical aggregates at  $T = 288 \text{ K}$  along with corresponding absorption and luminescence dissymmetries in (b). Theoretical results are shown as solid lines assuming  $\phi = +14$  degrees and  $\lambda^2 = 1.2$ . Reprinted with permission from ref 181. Copyright (2007), American Chemical Society.

disorder due largely to thermal fluctuations, which creates a distribution of transition frequencies. As discussed in ref 181, the presence of symmetry-breaking disorder leads to the substantial 0–0 emission in Figure 63a.

For dimers and aggregates too small to contain a complete helical turn, the excitons responsible for absorption and PL are no longer nearly degenerate. In the case of a chiral dimer treated by Kistler et al.,<sup>309</sup> both chromophores are related via a  $C_2$  rotation with oscillator strength divided among the

symmetric and antisymmetric excitons separated in energy by the Davydov-like splitting. In bichromophoric PDI complexes, the splitting has been measured by Langhals et al. to be several hundred wave numbers.<sup>420</sup> As shown by Kistler et al., the lower energy component displays J-type vibronic signatures ( $R_{\text{abs}}$  is larger than the monomer value), whereas the higher-energy component displays H-type vibronic signatures ( $R_{\text{abs}}$  is smaller than the monomer value) in a manner identical to that described in section 4.6 for the Davydov components in crystals hosting two molecules per unit cell. The correlation between spectral shift and the vibronic peak ratio  $R_{\text{abs}}$  is readily appreciated from the form of the ratio formula of eq 55. Of course, resolving the H- and J-type spectral components would require an oriented sample of PDI bichromophores, which is contrary to the isotropic distribution found in solution. Increasing the number of chromophores  $N$  beyond  $N = 2$  while maintaining the helical pitch causes the two orthogonal transitions to move closer in energy, eventually yielding the chiral H-aggregate behavior described above.

Interestingly, if there was a component of the molecular transition dipole moment along the aggregate ( $z$ ) axis, the  $k = 0$  exciton would also acquire oscillator strength but polarized along the  $z$ -axis, i.e., orthogonal to the transition derived from the radially directed transition dipole moment considered so far.<sup>69</sup> Such is the case in the amphiphilic cyanine dyes, which form chiral tubular aggregates investigated by Eisele, Knoester, and co-workers.<sup>70–72</sup>

**4.11.2. Optical Activity.** Circular dichroism derives from the differential absorption of left- vs right-circularly polarized light. For the helical aggregates depicted in Figure 61, the CD response in the spectral region corresponding to the main UV-vis absorption band takes on a bisignate line shape, the Cotton effect, an important signature for excitons.<sup>421</sup> This is readily observed in Figure 63b and Figure 64 for MOPV4 and lutein

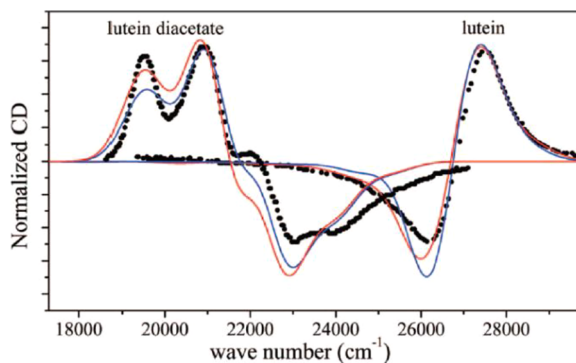


**Figure 64.** Measured CD spectra for lutein and lutein diacetate aggregates (black dots) from ref 89 along with theoretical spectra (red and blue curves) from ref 91. See ref 91 for details. Adapted with permission from ref 91. Copyright (2009), American Chemical Society.

aggregates, respectively. For the chiral H-aggregates in Figure 63b and Figure 64, the Cotton effect is manifest as a negative to positive sign change in the CD signal with increasing energy for left-handed helices, which inverts for right-handed helices. Hence, lutein and MOPV4 form predominantly left-handed helical H-aggregates. (Note, the original assignment of  $\phi$  in MOPV4 helices in ref 181 was corrected in ref 422). Figure 64 also includes the more complex CD line shape for the lutein diacetate aggregate. Here, the vibronic features arise because

the excitonic coupling in these non-hydrogen bonded helices is sufficiently weak. Unlike unsubstituted lutein, lutein diacetate forms right-handed helical aggregates.

The CD response of the chiral aggregates is governed by the rotational line strengths,  $R_j$ , according to the Rosenfeld expression<sup>421</sup>

$$R_j = (i/c\mu^2) \langle \psi_j | \hat{\mathbf{M}} | G \rangle \cdot \langle G | \hat{\mathbf{m}} | \psi_j \rangle \quad (143)$$

$R_j$ , reported here in dimensionless units, is directly proportional to the dot product of the electric and magnetic dipole moments of the  $|G\rangle \rightarrow |\psi_j\rangle$  transition. For the chiral H-aggregates in Figure 61, the (transition) electric dipole moment operator is  $\hat{\mathbf{M}} = \sum_n \mu_n |g\rangle \langle nl + h.c.$  with  $\mu_n$  given by eq 140. The magnetic dipole moment operator,  $\hat{\mathbf{m}}$ , is sensitive to the “circular” motion of electrons and takes the form<sup>421</sup>

$$\hat{\mathbf{m}} = \frac{ick_\lambda}{2} \sum_n |ln\rangle \langle gl | \mathbf{r}_n \times \mu_n + h.c. \quad (144)$$

where  $\mathbf{r}_n$  is the center of mass of the  $n$ th chromophore and  $k_\lambda = \omega_{0-0}/c$ . Eq 144 neglects the intrinsic contribution from individual chromophores, an excellent approximation for chromophores like MOPV4, where the CD response in Figure 63b is entirely aggregation induced.<sup>89,90,181</sup> Inserting eq 144 into the Rosenfeld expression shows that  $R_j$  depends entirely on the cross-products between the molecular electric transition dipole moments<sup>421</sup>

$$R_j = \frac{k_\lambda}{4\mu^2} \sum_{n,n'} (\mu_n^{j,G} \times \mu_{n'}^{G,j}) \cdot (\mathbf{r}_n - \mathbf{r}_{n'}) \quad (145)$$

where  $\mu_n^{j,G} \equiv \langle \psi_j | \hat{\mu}_n | G \rangle$  is a matrix element of the local operator  $\hat{\mu}_n \equiv \mu_n \{ g \rangle \langle nl + ln \rangle \langle gl \}$ .

The rotational line strengths in eq 145<sup>423</sup> form the basis of the CD spectrum, which is expressed as

$$\text{CD}(\omega) = \sum_j R_j W_{\text{LS}}(\omega - \omega_j) \quad (146)$$

where  $\omega_j$  is the transition frequency of the  $j$ th exciton and  $W_{\text{LS}}$  is the line shape function from eq 41. (Note that the spectrum in eq 146 is reduced as described in section 4.1.3.) Recognizing that the rotational line strengths are peaked for transitions with frequencies near  $\omega_\phi$  ( $= \omega_{0-0} + D + J_\phi$  with  $J_\phi$  defined in eq 141), Harada et al.<sup>418</sup> showed that the CD spectrum can be further simplified by expanding the Gaussian line shape function  $W_{\text{LS}}(\omega - \omega_j)$  around  $\omega_\phi$ . For a disorder-free helical aggregate with sufficiently large  $N$  (to eliminate size effects) and with no vibronic coupling, the spectrum in eq 146 reduces to

$$\text{CD}(\omega) = k_\lambda d S_j \frac{\omega - \omega_\phi}{2\Gamma_{\text{H}}^2} W_{\text{LS}}(\omega - \omega_\phi) \quad (147)$$

The excitonic Cotton effect derives from the product  $(\omega - \omega_\phi) W_{\text{LS}}(\omega - \omega_\phi)$ , which drives the CD to zero at the peak in the absorption spectrum ( $\omega = \omega_\phi$ ). The prefactor in eq 147 contains the  $s \sin(\phi s)$  modulated interaction sum

$$S_j \equiv \sum_{n,s>0} J_{n,n+s} s \cdot \sin(\phi s) \quad (148)$$

Forms similar to eq 147 have been obtained by Didraga et al.<sup>424</sup> and Burin et al.<sup>425</sup> in excitonic systems that lack vibronic coupling. In the presence of vibronic coupling, Spano and co-workers<sup>91,407</sup> showed that eq 147 describes the CD spectrum in

the limit of strong excitonic coupling with  $\omega_\phi$  replaced by the vertical transition frequency  $\omega_\phi + \lambda^2\omega_{\text{vib}}$ . They also derived an expression in the weak coupling limit ( $W \ll \lambda^2\omega_{\text{vib}}$ ) in which  $S_j$  remains a prefactor but with a bisignate line shape for each vibronic peak (along with other nuances as well as described in ref 91). As shown in Figure 64, the theoretical line shapes agree well with the measured line shapes for lutein and lutein diacetate aggregates.

As demonstrated in refs 91 and 407, the summand in eq 148 converges rather slowly with increasing  $s$ , allowing the CD signal to be measurable even for distant pairs of chromophores. The long-range behavior of CD has been appreciated for some time;<sup>416–419</sup> a more recent example involves two porphyrin chromophores covalently bound to an oligonaphthalene scaffold, where a CD Cotton effect was detectable for intermolecular separations as high as 70 Å.<sup>419</sup> The extreme sensitivity to distant couplings is also manifest in helical H-aggregates; for MOPV4 aggregates, it was demonstrated theoretically that setting the Coulombic couplings to zero after the sixth nearest neighbor results in a 30% increase in the peak magnitudes of  $g_{\text{abs}}$  and  $g_{\text{lum}}$  even though excitons in these strongly disordered systems are localized to only a couple of chromophores.<sup>181,182,408</sup> Finally, the slow convergence of the summand in eq 148 is related to a similarly slow convergence of the CD response with the number of chromophores,  $N$ , as noted by Didraga et al.<sup>424,426</sup> and by Van Dijk et al.<sup>407</sup> in their theoretical analyses of helical cylindrical aggregates and chiral H-aggregates, respectively.

The dependence of the CD response on the interaction sum  $S_j$  is also robust to disorder and vibronic coupling. Somsen et al.<sup>427</sup> and Burin et al.<sup>425</sup> showed that the first spectral moment of the CD spectrum, defined here as  $M_{\text{CD}}^1 \equiv \int \omega \text{CD}(\omega) d\omega / \int A(\omega) d\omega$ , is directly proportional to  $S_j$  in eq 148 independent of the presence of energetic disorder. This prompted Van Dijk et al. to further analyze the CD response in the presence of disorder and vibronic coupling showing that, quite generally, the first moment is entirely independent of both effects, i.e.  $M_{\text{CD}}^1 = c \times S_j$ .<sup>407</sup> This is an extremely useful result, making it possible to measure extended electronic couplings in size-controlled helical aggregates without any information about disorder or vibronic coupling by simply comparing the measured values of  $M_{\text{CD}}^1$  for dimers, trimers, tetramers, and so on. The ability to map out extended intermolecular couplings within molecular aggregates would shed light on the mechanism of dielectric screening and the nature (i.e., pairwise and beyond) of intermolecular coupling.

We conclude this section by briefly discussing some unusual features related to circularly polarized luminescence in chiral H-aggregates, focusing again on the MOPV4 aggregates shown in Figure 61. The different efficiencies for right- and left-handed CPL in chiral aggregates gives rise to a nonzero value for the luminescence dissymmetry,  $g_{\text{lum}}$ , defined as<sup>428</sup>

$$g_{\text{lum}}(\omega) = 2 \frac{S_L(\omega) - S_R(\omega)}{S_L(\omega) + S_R(\omega)} \quad (149)$$

where  $S_{L(R)}(\omega)$  is the steady-state PL spectrum for left-handed (right-handed) circularly polarized light. A similar construct for the absorption dissymmetry  $g_{\text{abs}}(\omega)$  is obtained by replacing  $S_L(\omega)$  and  $S_R(\omega)$  in eq 149 with  $A_L(\omega)$  and  $A_R(\omega)$ , respectively. The  $g_{\text{lum}}(\omega)$  and  $g_{\text{abs}}(\omega)$  spectra for left-handed MOPV4 helices, as measured in ref 181, are shown in Figure 63b. The magnitude of the luminescence dissymmetry peaks

around the energy of the 0–0 transition with  $g_{\text{lum}} \approx -3 \times 10^{-3}$ , thereafter decreasing monotonically with decreasing energy.

A quantitative appreciation for the behavior of  $g_{\text{lum}}(\omega)$  in MOPV4 helices requires inclusion of vibronic coupling. The theory for  $g_{\text{lum}}$  in vibronically coupled chiral aggregates was introduced in ref 405 and developed further in subsequent works.<sup>181,182,408</sup> Optical activity in emission is governed by the rotational line strengths for transitions from an excited electronic state (usually the lowest energy exciton) to the vibrationless ground electronic state as well as the many purely vibrationally excited states within the ground electronic manifold. (This is entirely analogous to the case for photoluminescence considered in section 4.1.) The rotational line strength between the  $j$ th electronic excited state,  $|\psi_j\rangle$ , and the electronic ground state  $|g; v_1, v_2, \dots, v_N\rangle$  hosting a distribution of purely vibrational excitations in the unshifted  $S_0$  nuclear potential is given by<sup>408</sup>

$$R_{j,\{g;v_m\}} = \frac{k_\lambda}{4\mu^2} \sum_{n,n'} (\boldsymbol{\mu}_n^{j,\{g;v_m\}} \times \boldsymbol{\mu}_n^{\{g;v_m\},j}) \cdot (\mathbf{r}_n - \mathbf{r}_{n'}) \quad (150)$$

where  $\{g;v_m\}$  is short-hand notation for  $|g; v_1, v_2, \dots, v_N\rangle$  and  $\boldsymbol{\mu}_n^{j,\{g;v_m\}} \equiv \langle \psi_j | \hat{\boldsymbol{\mu}}_n | g; v_1, v_2, \dots, v_N \rangle$  is the matrix element of the local transition dipole moment operator,  $\hat{\boldsymbol{\mu}}_n$ , defined after eq 145. On the basis of eqs 149 and 150, the luminescence dissymmetry is<sup>408</sup>

$$g_{\text{lum}}(\omega) = \frac{4}{S(\omega)} \sum_{v_t=0,1,2,\dots} R_{\text{lum}}^{0-v_t} W_{\text{LS}}(\omega - \omega_{\text{em}} + v_t \omega_{\text{vib}}) \quad (151)$$

where  $R_{\text{lum}}^{0-v_t} \equiv \sum'_{\{v_n\}} R_{j,\{g;v_m\}}$  with the prime indicating the constraint  $\sum_m v_m = v_t$ .<sup>429</sup> The  $R_{\text{lum}}^{0-v_t}$  in eq 151 are the rotational line strength equivalents of the PL line strengths,  $I_{\text{PL}}^{0-v_t}$ , in eqs 43–45.

Good agreement between the calculated  $g_{\text{lum}}(\omega)$  using eq 151 and the measured spectrum for MOPV4 was reported in ref 181 and shown in Figure 63b. As indicated earlier, the simulated spectrum requires significant energetic site disorder ( $\sigma_d = 0.085$  eV and  $l_0 = 4.5$ , see section 4.3) to reproduce the experimental values.  $g_{\text{lum}}(\omega)$  (as well as  $g_{\text{abs}}(\omega)$ ) are particularly challenging to account for theoretically because they are intensive quantities (unlike absorption and PL) and therefore cannot be renormalized to agree with the experiment. Indeed, it is quite reassuring that satisfactory agreement between experiment and theory is obtained for all four spectral observables shown in Figure 63b using a common parameter set.

Interestingly, the vibronic/vibrational states (alias two-particle states) play a crucial role in accounting for the  $g_{\text{lum}}$  line shape. Although the 0–0 line strength,  $R_{\text{lum}}^{0-0}$ , depends entirely on the one-particle coefficients of the emitting exciton  $|\psi_j\rangle$  in eq 150, the line strengths  $R_{\text{lum}}^{0-v_t}$  for sideband transitions ( $v_t \geq 1$ ) depend on the product of one- and two-particle coefficients.<sup>408</sup> Hence, without two-particle states, the  $g_{\text{lum}}$  signal would vanish to the red of the 0–0 transition, making  $g_{\text{lum}}(\omega)$  a direct probe of the two-particle component of the emitting exciton. Because the two-particle component also contributes to the radius of the “excitonic polaron”,  $g_{\text{lum}}(\omega)$  can be used to obtain information about the spatial extent of the phonon cloud surrounding the central electronic excitation. As shown in ref 181, the excitonic polaron corresponding to the lowest-energy excited state in MOPV4 has significant nuclear

distortion not only on the chromophore hosting the electronic excitation but also on its two nearest neighbors. Finally, numerical calculations of Tempelaar et al.<sup>408</sup> showed that, like the CD spectrum in eq 147,  $g_{\text{lum}}(\omega)$  also scales with the  $s \sin(\phi s)$  modulated interaction sum in eq 148 despite the presence of strong localizing disorder and vibronic coupling, thereby accounting for its extreme sensitivity to extended intermolecular couplings. In summary, the additional spectral observables  $g_{\text{lum}}(\omega)$  and  $g_{\text{abs}}(\omega)$  for chiral aggregates allow for much greater interrogation of fundamental excitonic properties, especially extended (Coulombic) interactions.

## 5. THE IMPACT OF INTERMOLECULAR CHARGE TRANSFER ON J- AND H-AGGREGATE BEHAVIOR

The role of intermolecular charge-transfer (CT) in defining the photophysics of organic semiconductors has received a considerable amount of attention over the past several decades. For example, in the late twentieth century, interest in organic photoconducting materials for xerography spurred a significant amount of research concerning photoinduced charge generation in organic semiconductors.<sup>430–434</sup> Around the same time, Kazmaier and Hoffmann showed<sup>210</sup> that the valence and conduction bandwidths in molecular crystals originate from a quantum interference effect among the overlapping frontier molecular orbitals, thereby accounting for the phenomenon of crystallochromy,<sup>435–442</sup> the extreme sensitivity of a crystal's color to intermolecular packing. More recently, interest in singlet-fission as a possible route to overcome the Shockley–Queisser limit<sup>443,444</sup> in solar cells has led to scrutiny of CT states, which are believed to serve as intermediates in the fission process.<sup>239,445–454</sup>

In organic systems, the valence and conduction bands that support electron and hole transport are formed mainly from the frontier molecular orbitals of the constituent molecules. Close intermolecular distances ( $\sim 3.5$ –4 Å), such as those found in molecular  $\pi$ -stacks, facilitate large spatial overlap between the highest occupied and lowest unoccupied molecular orbitals (HOMOs and LUMOs, respectively) on neighboring molecules. In such closely packed systems, the main approximation of Kasha's exciton model,<sup>20–24</sup> namely that "electron overlap between the light absorbing units must be small",<sup>20</sup> breaks down and the excited states responsible for the absorption and photoluminescence spectra are no longer accurately described by the vibronic Frenkel exciton Hamiltonian in eq 13. The electronic excited states are bound electron/hole pairs with radii depending on the depth of the Coulomb binding well; shallow wells promote large-radius Wannier-like excitons, whereas deep wells lead to tightly bound excitons with large Frenkel character. Mixed Frenkel/CT excitons have optical properties that generally differ from pure Frenkel excitons. Indeed, many authors including Kazmaier and Hoffmann,<sup>210</sup> Soos and co-workers,<sup>211–213</sup> Gisslen and Scholz,<sup>214,215</sup> Hoffmann et al.,<sup>216</sup> Spano and co-workers,<sup>223–230</sup> Gao et al.,<sup>455</sup> Scholes and co-workers,<sup>231,232</sup> and Reineker and co-workers<sup>456,457</sup> have shown that CT interactions can have a profound impact on the absorption spectra of molecular aggregates and crystals.

The effects of CT-mediated interactions on photoluminescence is a more complex matter as significant wave function overlap between neighboring chromophores may lead to the formation of low-energy excimers<sup>30–36,127</sup> from which emission originates. Excimers are common in perylene<sup>31–37</sup> and oligo-phenylenevinylene-based  $\pi$ -stacks<sup>127</sup> and form when there is

substantial mixing between Frenkel and CT states as well as a harmonic-like (binding) dependence of the resulting state energy on an intermolecular coordinate  $q$  (which is lacking in the ground state). Relaxation along  $q$  subsequent to optical excitation results in broad, red-shifted emission that competes with<sup>455,458</sup> and often dominates the structured FC emission derived from intramolecular modes (vinyl stretching, aromatic-quinooidal). Excimers and CT states in general can act as efficient traps preventing efficient energy transfer.<sup>455,458–462</sup> There is evidence that excimer emission is more pronounced when the cofacial overlap between neighboring chromophores is largest, for example, in H-like rather than J-like cofacial orientations.<sup>35,37</sup> However,  $\pi$ -stacks of 7,8,15,16-tetraazaterrylene (TAT) exhibit structured vibronic emission (no excimers)<sup>225,463</sup> despite strong wave function overlap. P3HT  $\pi$ -stacks also show no evidence of excimer emission despite nearest neighbor contacts of 0.38 nm. For P3HT, the CT state is sufficiently high in energy relative to the Frenkel exciton<sup>464</sup> as to prevent the strong Frenkel/CT exciton mixing required for excimer formation.<sup>225</sup> This is not the case, however, in TAT. Predicting excimer formation is a complex task, requiring a detailed analysis of Frenkel-CT state mixing and the coupling of such excitons to intermolecular vibrational modes.<sup>458</sup>

In this section, we review the current understanding of the role CT-mediated interactions play in determining the photophysics and band structures of tightly  $\pi$ -stacked systems. Owing to the complexities introduced by excimers, we limit the PL analysis to molecules like TAT and P3HT that form  $\pi$ -stacks but show no evidence of excimer formation. We focus specifically on the role that CT interactions play in determining the J- or H-aggregate nature of a molecular ensemble and leave the more general topic of charge transport in organic semiconductors to other excellent reviews.<sup>4,11,16,465–467</sup>

### 5.1. Frenkel–Holstein Hamiltonian with Charge transfer

The first generalization of the Frenkel exciton model to account for charge transfer in molecular crystals was developed by Merrifield<sup>196</sup> in the early 1960s. Merrifield's model considers both Frenkel and charge transfer excitons in a one-dimensional crystal in the absence of vibronic coupling. For a linear array of  $N$ -coupled chromophores, Merrifield's Hamiltonian can be divided as

$$H_{\text{el}} = H_{\text{ex}} + H_{\text{CT}} \quad (152)$$

where  $H_{\text{ex}}$  is the usual Frenkel exciton Hamiltonian

$$H_{\text{ex}} = E_{S_1} \sum_n |n\rangle\langle n| + \sum_{m,n} J_{m,n} |m\rangle\langle n| \quad (153)$$

and  $H_{\text{CT}}$  accounts for charge transfer

$$\begin{aligned} H_{\text{CT}} = & t_e \sum_n \sum_{s=0,\pm 1,\dots} \{|n, n+s\rangle\langle n, n+s+1| + |n, n+s\rangle\langle n, n+s-1|\} + \text{h. c.} \\ & - t_h \sum_n \sum_{s=0,\pm 1,\dots} \{|n, n+s\rangle\langle n+1, n+s| \\ & + |n, n+s\rangle\langle n-1, n+s|\} + \text{h. c.} + \sum_{n,s \neq 0} E_{\text{CT}}(s) |n, n+s\rangle\langle n, n+s| \end{aligned} \quad (154)$$

The basis set in  $H_{\text{ex}}$  and  $H_{\text{CT}}$  is constructed from the HOMO and LUMO levels on each chromophore. In this realization, a local excitation ( $S_1$ ) is represented by a single electron residing in both the HOMO and LUMO of a particular chromophore. Molecules in which the first electronic transition is dominated by the HOMO-LUMO transition have been denoted as Class 1

by Smith and Michl.<sup>446</sup> Accordingly, the state  $|n\rangle$  in  $H_{\text{ex}}$  consists of a local molecular ( $S_1$ ) excitation on chromophore  $n$  while all other molecules remain in their electronic ground states. The associated energy is denoted as  $E_{S_1}$ . As it appears in eq 153,  $E_{S_1}$  also includes nonresonant interactions between the local excited state and higher energy aggregate states (excluding the CT states already included in  $H_{\text{CT}}$ ). Resonant interactions derived from transition dipole–dipole interactions are included in  $J_{\text{mr}}$ . In  $H_{\text{CT}}$ , the state  $|n,n+s\rangle$  with  $s = \pm 1, \pm 2, \dots$  represents a charge-separated state in which site  $n$  hosts a cation and site  $n+s$  hosts an anion. A cation or “hole” results from the removal of a HOMO electron from a neutral ground-state molecule, whereas an anion or “electron” results from the addition of a LUMO electron. Charge-transfer (or “charge-separated”) states in which the anion and cation are on neighboring sites, as in  $|n,n \pm 1\rangle$ , are sometimes referred to as charge-resonance states.<sup>445,468,469</sup> The Hamiltonian in eq 154 also admits the states  $|n,n+s\rangle$  with  $s = 0$ , where the electron and hole appear on the same site ( $n$ ); the state  $|n,n\rangle$  is therefore the neutral ( $S_1$ ) excitation, identical to the Frenkel state  $|n\rangle$ . An important distinction between CT and Frenkel states is that CT states have negligible oscillator strengths compared to those of Frenkel states.<sup>214,215</sup> Finally, under the assumed periodic boundary conditions, the state  $|n,n+s\rangle$  identifies with  $|n,n+s-N\rangle$  if  $n+s > N$  and with  $|n,n+s+N\rangle$  if  $n+s < 0$ .

The first two terms in eq 154 account for nearest-neighbor electron and hole transfer (“hopping”). Charge mobility is governed by the electron and hole transfer integrals,  $t_e$  and  $t_h$ , respectively, which are defined by the matrix elements

$$t_e = \langle \phi_1^L | \hat{h} | \phi_2^L \rangle \quad (155)$$

$$t_h = -\langle \phi_1^H | \hat{h} | \phi_2^H \rangle \quad (156)$$

where  $\hat{h}$  is the single electron Hamiltonian operator, and  $\phi_n^{H(L)}$  is the HOMO (LUMO) wave function on molecule  $n$  ( $= 1, 2$ ). When calculating  $t_e$  and  $t_h$  based on eqs 155 and 156, it is important that the molecular orbitals  $\phi_1^{H(L)}$  and  $\phi_2^{H(L)}$  be orthogonal for the charge-transfer integrals to be well-defined and independent of the reference energy.<sup>11,470–472</sup> Note also that the negative sign in eq 156 reflects the fact that the hole corresponds to the absence of an electron.<sup>473,214,215</sup> The electron and hole integrals defined above give rise to the conduction and valence bands with  $4|t_e|$  and  $4|t_h|$  defining the associated bandwidths.

The first two terms in eq 154 not only account for electron and hole transfer but also include the important coupling between a localized Frenkel exciton  $|n,n\rangle$  (or  $|n\rangle$ ) and the nearest neighbor charge-separated states  $|n,n \pm 1\rangle$  and  $|n \pm 1,n\rangle$  derived from electron and hole dissociation. The Hamiltonian in eq 154 therefore assumes the dissociation integrals  $D_e$  and  $D_h$  are equal to  $t_e$  and  $t_h$ , respectively, which is a good approximation.<sup>446,447</sup> The last term in eq 154 assigns the energies of the charge-separated states, which are determined from  $E_{\text{CT}}(s) = I_p - E_A + P + V(s)$ , where  $I_p$  is the ionization potential,  $E_A$  is the electron affinity,  $P$  is the polarization energy, and  $V(s) = -e^2/4\pi\epsilon_0\epsilon_s l sd$  is the Coulomb binding energy between the electron and hole, where  $d$  is the nearest neighbor intermolecular distance.

Soon after its inception, Choi and co-workers employed Merrifield’s model to calculate optical spectra in molecular crystals<sup>197,198</sup> and Petelenz extended the model to account for systems with two molecules per unit cell.<sup>199,200</sup> Vibronic

coupling was later incorporated first by Petelenz and co-workers when investigating the electro absorption spectra of polyacene<sup>203,474</sup> and sexithiophene<sup>205</sup> crystals and later by Hennessy et al.<sup>212,213</sup> who used a vibronically coupled dimer variant of Merrifield’s model to investigate the absorption spectra of perylenetetracarboxylic acid (PTCDA). Others, including Hoffmann et al.,<sup>216</sup> Hoffmann and Soos,<sup>211</sup> Gisslen and Scholz,<sup>214,215</sup> Heinemeyer et al.,<sup>475</sup> Spano and co-workers,<sup>223–230</sup> Stradomska et al.,<sup>287,367</sup> Gao et al.,<sup>455</sup> and Reineker and co-workers<sup>456,457</sup> have used similar models based on vibronically coupled Frenkel and charge-separated excitons. In the spirit of Holstein, vibronic coupling is accounted for by adding to Merrifield’s Hamiltonian the term

$$\begin{aligned} H_{\text{vib}} = & \omega_{\text{vib}} \sum_n b_n^\dagger b_n + \omega_{\text{vib}} \sum_n \{\lambda(b_n^\dagger + b_n) + \lambda^2\} |n\rangle \langle n| \\ & + \omega_{\text{vib}} \sum_{n,s \neq 0} \{(b_n^\dagger + b_n)\lambda_+ + \lambda_+^2\} |n; n+s\rangle \langle n; n+s| \\ & + \omega_{\text{vib}} \sum_{n,s \neq 0} \{(b_{n+s}^\dagger + b_{n+s})\lambda_- + \lambda_-^2\} |n; n+s\rangle \langle n; n+s| \end{aligned} \quad (157)$$

where we continue to set  $\hbar = 1$ . Here,  $\lambda_+$  and  $\lambda_-$  are the cationic and anionic Huang–Rhys factors, which quantify the nuclear deformation of the ionic states relative to the ground state, and  $\lambda_+^2\omega_{\text{vib}}$  and  $\lambda_-^2\omega_{\text{vib}}$  account for the cationic and anionic nuclear relaxation energies, respectively. All other parameters have been defined previously (see section 3.1). Taken together, the Hamiltonian

$$H = H_{\text{el}} + H_{\text{vib}} \quad (158)$$

is well suited to describe the excited states of tightly packed molecular systems such as  $\pi$ -stacks.

## 5.2. The Multiparticle Basis Set for Charge-Transfer States

Eigenstates of the Frenkel–CT Holstein Hamiltonian of eq 158 can be expressed in a multiparticle basis set composed of both Frenkel and CT multiparticle states. Under the TPA, the  $\alpha$ th eigenstate can be expanded in the local basis as

$$\begin{aligned} |\psi_\alpha\rangle = & \sum_n \sum_{\tilde{v}=0,1,\dots} c_{n,\tilde{v}}^\alpha |n, \tilde{v}\rangle + \sum_n \sum_{\tilde{v}=0,1,\dots} \sum_{n'} \sum_{v'=1,2,\dots} c_{n,\tilde{v};n',v'}^\alpha |n, \tilde{v}; n', v'\rangle \\ & + \sum_n \sum_{v^+=0,1,\dots} \sum_{s=\pm 1, \pm 2, \dots} \sum_{v^- = 0,1,\dots} d_{n,v^+,s,v^-}^\alpha |n, v^+; n+s, v^-\rangle \end{aligned} \quad (159)$$

where the first two terms correspond to one- and two-particle Frenkel excitons, respectively, of section 3.2, and the last term introduces two-particle charge-separated states,  $|n, v^+; n+s, v^-\rangle$ , in which  $v^+$  vibrational quanta reside on the cation and  $v^-$  vibrational quanta reside on the anion, see Figure 65. (Note, because an ionic state counts as a “particle”, there are no one-particle charge-separated states.) In most cases relevant to

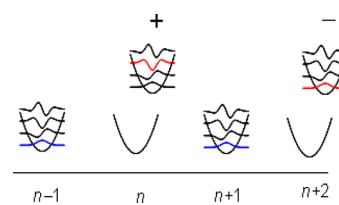


**Figure 65.** Two-particle charge-separated state,  $|n, v^+; n+s, v^-\rangle$ . The shifted potentials are governed by the ionic HR factors.

molecular crystals and aggregates, the TPA is sufficient for spectroscopic convergence, although in some cases, particularly when  $|t_e|, |t_h| \gg |E_{CT}(1) - E_{S_1}|$ , three-particle and higher states can be important.<sup>285,342</sup>

Given translational symmetry, the exciton's wave vector  $k$  is a good quantum number and the  $\alpha$ th eigenstate with wave vector  $k$  can be expanded as

$$\begin{aligned} |\psi_k^\alpha\rangle = & \sum_{\tilde{v}=0,1,\dots} c_{k,\tilde{v}}^\alpha |k, \tilde{v}\rangle + \sum_{\tilde{v}=0,1,\dots} \sum_{s=\pm 1,\pm 2,\dots} \sum_{v=1,2,\dots} c_{k,\tilde{v};s,v}^\alpha |k, \tilde{v}; s, v\rangle \\ & + \sum_{v^+=0,1,\dots} \sum_{s=\pm 1,\pm 2,\dots} \sum_{v^- = 0,1,\dots} d_{k,v^+;s,v^-}^\alpha |k, v^+; s, v^-\rangle \end{aligned} \quad (160)$$

The  $k$ -dependent multiparticle Frenkel exciton wave functions were defined in eqs 16 and 17, and the  $k$ -dependent two-particle CT wave function is

$$\begin{aligned} |k, v^+; s, v^-\rangle \equiv & \frac{1}{\sqrt{N}} \sum_n e^{ikn} |n, v^+; n+s, v^-\rangle \\ k = & 0, \pm 2\pi/N, \pm 4\pi/N, \dots, \pi \end{aligned} \quad (161)$$

Generalizations of eqs 159 and 160 to include three-particle and higher basis states are straightforward.<sup>229,230</sup>

### 5.3. Charge-Transfer Excitons

Most organic aggregates and crystals are characterized by a small static dielectric constant, resulting in a large Coulomb binding energy that typically restricts the excitons to small electron–hole radii with charges separated over at most one or two chromophores. Such mixed Frenkel/CT excitons are usually referred to simply as CT-excitons. For linear aggregates, the binding potential appearing in eq 154 can be simplified to allow for only nearest neighbor charge separation

$$E_{CT}(s) = \begin{cases} E_{CT} & |s| = 1 \\ \infty & |s| > 1 \end{cases} \quad (162)$$

To study the spectral response in more general cases where shallow binding potentials necessarily involve states with electron/hole separations well beyond nearest neighbors, one needs to utilize the proper  $1/|s|$  binding potential, as enacted by Merrifield<sup>196</sup> and Hernandez and Choi.<sup>197</sup> Merrifield obtained exact solutions for the energies of bound and unbound excitons (without vibrations) in infinite chains using special (hypergeometric) functions.

In the limit where eq 162 applies and maintaining translational symmetry, the eigenstates of the Frenkel/CT Hamiltonian  $H_{el}$  in eq 152 can be obtained exactly.<sup>227,228,230</sup> The electronic Hamiltonian is first represented in the symmetry-adapted basis of  $k$ -dependent Frenkel and CT states

$$\begin{aligned} |k\rangle \equiv & \frac{1}{\sqrt{N}} \sum_n e^{ikn} |n\rangle \\ |k, \pm\rangle \equiv & \frac{1}{\sqrt{2N}} \sum_n \{e^{ikn+i\theta(k)} |n; n+1\rangle \pm e^{ikn-i\theta(k)} |n; n-1\rangle\} \end{aligned} \quad (163)$$

where the  $+$  ( $-$ ) sign refers to the symmetric (antisymmetric) linear combination of nearest neighbor CT states. The phase angle,  $\theta(k)$ , depends on the asymmetry of the electron and hole transfer integrals

$$e^{i\theta(k)} = (t_e + t_h e^{ik}) / |t_e + t_h e^{ik}| \quad (164)$$

Others, including Hennessy et al.,<sup>212,213</sup> Hoffmann et al.,<sup>216</sup> and Gisslen and Scholz<sup>214</sup> have employed similar transformations to simplify the Hamiltonian.

The Frenkel and CT states that appear in eq 163 are sometimes loosely referred to as the *diabatic* Frenkel and CT excitons as they are not yet mixed together via  $t_e$  and  $t_h$ . (The diabatic label anticipates the inclusion of vibronic coupling within the Frenkel and CT bands.) In the diabatic basis of eq 163, the electronic Hamiltonian is block diagonal in  $k$ , and each sub block is a  $3 \times 3$  matrix defined by

$$\begin{aligned} H_{el}(k) = & E_k |k\rangle\langle k| + E_{CT}(|k, +\rangle\langle k, +| + |k, -\rangle\langle k, -|) \\ & + \sqrt{2} |t_e + t_h e^{ik}| (|k\rangle\langle k, +| + |k, +\rangle\langle k|) \end{aligned} \quad (165)$$

where  $E_k = E_{S_1} + J_k$  with  $J_k$  defined in eq 5. Notably, only the  $|k, +\rangle$  charge-transfer states couple to the Frenkel excitons  $|k\rangle$  while the  $|k, -\rangle$  charge-transfer states remain uncoupled.<sup>216</sup> The form of eq 165 further reveals that the Frenkel/CT mixing depends on a  $k$ -dependent interference between the electron and hole transfer integrals, as emphasized by Hennessy et al.<sup>213</sup> and Gisslen and Scholz.<sup>214</sup> The optically allowed  $k = 0$  Frenkel states mix strongly with the  $|k, +\rangle$  charge-transfer states when  $t_e$  and  $t_h$  add constructively, but mix weakly when  $t_e$  and  $t_h$  add destructively.<sup>213</sup> As detailed later, this interference has profound implications for the system photophysics. Diagonalization of eq 165 yields the free exciton dispersions

$$\begin{aligned} E_{\alpha=1}(k) = & \frac{E_{CT} + E_k}{2} - \sqrt{\left(\frac{E_{CT} - E_k}{2}\right)^2 + 2(t_e^2 + t_h^2 + 2t_e t_h \cos(k))} \\ E_{\alpha=2}(k) = & E_{CT} \\ E_{\alpha=3}(k) = & \frac{E_{CT} + E_k}{2} + \sqrt{\left(\frac{E_{CT} - E_k}{2}\right)^2 + 2(t_e^2 + t_h^2 + 2t_e t_h \cos(k))} \end{aligned} \quad (166)$$

where the excitons corresponding to the  $\alpha = 1$  and  $\alpha = 3$  bands have mixed Frenkel ( $|k\rangle$ ) and charge-transfer ( $|k, +\rangle$ ) character, whereas the excitons responsible for the  $\alpha = 2$  band have pure charge-transfer ( $|k, -\rangle$ ) character.<sup>216</sup> As the CT states carry negligible oscillator strength,<sup>214,215</sup> only the  $\alpha = 1$  and  $\alpha = 3$  bands contribute to the optical absorption spectrum.

### 5.4. Charge-Transfer Induced J- and H-Aggregate Behavior in the Perturbative Regime

On the basis of the pioneering work of Kasha,<sup>20–24</sup> it is by now well-known that intermolecular Coulomb coupling leads to J- or H-aggregate behavior in molecular aggregates and crystals. As shown in section 2, such coupling can induce a positive (J) or negative (H) curvature in the exciton band at  $k = 0$ , which is manifest spectroscopically via spectral shifts and vibronic signatures. Perhaps somewhat less well-known is that intermolecular charge-transfer can also induce J- and H-aggregate behavior with very similar spectral signatures.<sup>223</sup>

When the diabatic (premixed) CT and Frenkel bands are energetically well-separated,  $|E_{CT} - E_{S_1}| \gg |t_e|, |t_h|, W, \omega_{vib}$ , a second-order perturbative approach that treats the charge-transfer states as virtual excitations can be employed on the Hamiltonian in eq 158 to derive an effective Frenkel/Holstein Hamiltonian given by

$$\begin{aligned} H_{eff} = & E_{S_1} + \Delta_{CT} + \sum_{m,n} (J_{m,n} + J_{CT} \delta_{n,m\pm 1}) |lm\rangle\langle nl| \\ & + \omega_{vib} \sum_n b_n^\dagger b_n + \omega_{vib} \sum_n \{\lambda(b_n^\dagger + b_n) + \lambda^2\} |n\rangle\langle n| \end{aligned} \quad (167)$$

where  $J_{CT}$  is the charge-transfer-mediated intermolecular coupling or superexchange coupling<sup>232–237</sup>

$$J_{CT} = -2 \frac{t_e t_h}{E_{CT} - E_{S_1}} \quad (168)$$

and  $\Delta_{CT}$  is the self-energy correction

$$\Delta_{CT} = -2 \frac{t_e^2 + t_h^2}{E_{CT} - E_{S_1}} \quad (169)$$

$J_{CT}$  describes an energy-transfer process that proceeds through a virtual charge-separated state, as depicted in Figure 66. The

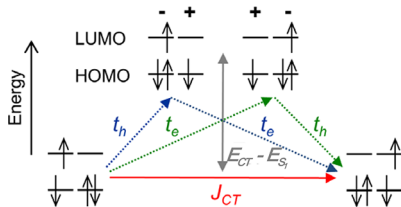


**Figure 66.** A diagram depicting origin of the charge-transfer-mediated exciton coupling,  $J_{CT}$ . See text for details. Reprinted with permission from ref 228. Copyright (2017), American Chemical Society.

exciton, originally localized on a single molecule, first dissociates by transferring an electron (or hole) to its neighbor, creating the higher-energy charge-transfer state. The charges can then recombine to form a local exciton on the neighbor. The net result of this two-step process, often called superexchange,<sup>233,235</sup> is energy transfer between neighboring molecules. In contrast, the self-energy correction,  $\Delta_{CT}$ , derives from dissociation and subsequent back recombination on the initially excited molecule. Note that eq 169, which assumes  $N > 2$ , is a factor of 2 larger than the analogous dimer ( $N = 2$ ) expression in ref 223 because when  $N > 2$  each molecule has two neighbors that are involved in the dissociation/recombination event.

Eq 168 shows that both the Coulomb coupling and superexchange coupling determine the net excitonic coupling between molecular neighbors. Moreover,  $J_{CT}$  is positive (H-promoting) whenever  $t_e$  and  $t_h$  have opposite signs and negative (J-promoting) whenever  $t_e$  and  $t_h$  have the same sign (assuming  $E_{CT} > E_{S_1}$ ). The J/H-assignment is consistent with a determination of the signs of  $t_e$  and  $t_h$  based on translational symmetry. Section 5.8.3 discusses in greater detail how the phase convention impacts the H- and J-promoting interpretation of  $J_{CT}$ . Notwithstanding the phase assignment (which cannot have any effect on the system observables), in the perturbative regime, charge-transfer interactions alone can induce J- and H-aggregate behavior.

The eigenvalues of just the electronic part of the effective Hamiltonian in eq 167 are given by

$$E_{\alpha=1}(k) = E_{S_1} + \Delta_{CT} + 2J_{CT}\cos k + J_k \quad (170)$$

where  $J_k$  derives from Coulomb coupling defined in eq 5 and generally includes extended (beyond nearest neighbor) interactions. Eq 170 can also be derived from the  $E_{\alpha=1}(k)$  dispersion in eq 166 in the limit of well-separated Frenkel and CT bands ( $|E_{CT} - E_{S_1}| \gg |t_e|, |t_h|, W$ ).<sup>228</sup> Importantly, eq 170 reveals how the interference between the two coupling sources impacts the band dispersion, as investigated in greater detail in section 5.6. This is more readily appreciated when the Coulomb coupling is restricted to nearest neighbors, an

approximation that is fairly accurate for linear aggregates such as  $\pi$ -stacks. In this case,  $J_k = 2J_C\cos(k)$  and eq 170 reduces to

$$E_{\alpha=1}(k) = E_{S_1} + \Delta_{CT} + 2(J_{CT} + J_C)\cos k \quad (171)$$

Interestingly, the aggregation-induced absorption spectral shift from eq 170, given by  $\Delta_{CT} + 2J_{CT} + J_{k=0}$ , complicates the Kasha signatures for H-aggregates because  $\Delta_{CT}$  induces a uniform redshift (assuming, as we are, that  $E_{CT} > E_{S_1}$ ). As shown in greater detail below, CT-mediated interactions admit the possibility of red-shifted H-aggregates.

Because the entire structure of the effective Hamiltonian in eq 167 can be mapped directly onto the usual Frenkel–Holstein Hamiltonian in eq 13, all of the vibronic signatures that apply to the conventional Coulomb-coupled H- and J-aggregates also apply in the more general situation in which Coulomb coupling and CT-mediated superexchange couplings coexist. For example, the perturbative expression for the ratio  $R_{abs}$  in the absorption spectrum, introduced in section 4.2, becomes

$$R_{abs} \approx \frac{[1 - e^{-\lambda^2} G(0; \lambda^2)[J_{k=0} + 2J_{CT}]/\omega_{vib}])^2}{\lambda^2 [1 - e^{-\lambda^2} G(1; \lambda^2)[J_{k=0} + 2J_{CT}]/\omega_{vib}])^2} \quad (172)$$

valid in the limit that the total exciton bandwidth is smaller than the nuclear relaxation energy. Once again, the interference between the Coulombic and CT-mediated couplings is evident. For example, if the two sources cancel,  $J_{k=0} + 2J_{CT} \approx 0$ , the absorption ratio remains unchanged from the monomer value ( $1/\lambda^2$ ). Turning now to PL, the ratio rule  $R_{PL} = N_{coh}/\lambda^2$  also holds in the presence of both coupling sources as long as the coupling is overall negative as in a J-aggregate,  $J_{k=0} + 2J_{CT} < 0$ . In the absence of disorder and at low temperature, the ratio is exactly given by  $N/\lambda^2$ .

For the remainder of this section and in section 5.5, we will neglect the Coulomb couplings by setting  $J_{n,m} = 0$  in order to focus on the interesting case of J- and H-aggregates derived solely from CT-mediated interactions. Although this may seem unrealistic, it is actually a fairly good approximation for materials like tetracene and pentacene crystals where weakly allowed  $S_0 \rightarrow S_1$  transitions and sufficient intermolecular wave function overlap result in photophysics dominated by Frenkel/CT exciton mixing.<sup>224</sup> We will reintroduce the Coulombic coupling later on in section 5.6 when discussing in greater detail the interference between the Coulombic and charge-transfer coupling.

In the absence of Coulomb coupling, eq 170 shows that the allowed exciton ( $k = 0$ ) resides at the bottom of the exciton band when  $J_{CT} < 0$  and at the top of the band when  $J_{CT} > 0$ . The former situation is consistent with J-aggregation, and the latter is consistent with H-aggregation. In refs 223, 227, and 228, the spectral responses of CT-mediated J- and H-aggregates were investigated in the perturbative limit, examples of which are shown in Figure 67. Although the calculated spectra were based on the Frenkel/CT Holstein Hamiltonian in eq 158, they are identical to those calculated using the simpler effective Hamiltonian in eq 167, since the diabatic CT state is taken far from resonance with a local excitation. As apparent from the figure, all of the vibronic signatures derived for Kasha aggregates<sup>14</sup> apply to the CT aggregates. Namely,  $R_{abs}$  is substantially larger than the monomer value,  $1/\lambda^2$  (which is unity in the figure) in the CT J-aggregate in Figure 67a and substantially smaller than  $1/\lambda^2$  in the CT H-aggregate in Figure

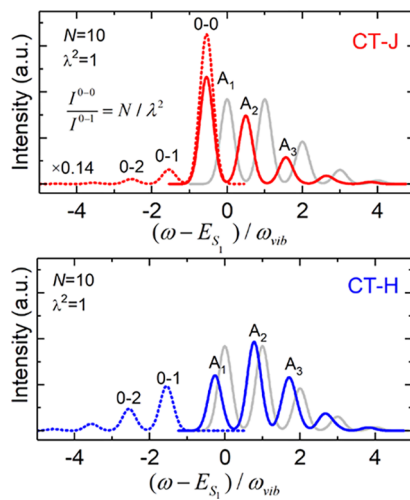


**Figure 67.** Absorption (solid) and PL spectrum (dashed) of a charge-transfer-mediated J-aggregate with  $t_e = t_h = \omega_{vib}$  (top) and an H-aggregate with  $t_e = -t_h = \omega_{vib}$  (bottom). In both cases,  $N = 10$ ,  $E_{CT} - E_{S_1} = 10\omega_{vib}$ , and the Coulomb coupling is neglected along with all nonresonant interactions not involving CT. In addition, the neutral and ionic HR factors are set to unity and one-half, respectively, and  $T = 0$  K. The monomer absorption spectrum is shown in gray for reference. Reprinted with permission from ref 228. Copyright (2017), American Chemical Society.

67b. Because the free-exciton bandwidth,  $W = 4|J_{CT}|$  ( $= 0.8\omega_{vib}$ ), is smaller than the nuclear relaxation energy,  $\lambda^2\omega_{vib}$ , eq 172 (or eq 57 with  $W = 0.8\omega_{vib}$ <sup>227</sup>) reproduces the value of  $R_{abs}$ . Furthermore, just as in Coulomb-coupled aggregates, the PL ratio at  $T = 0$  K is  $R_{PL} = N/\lambda^2$  for CT J-aggregates and  $R_{PL} = 0$  for CT H-aggregates.<sup>14</sup> We emphasize that in the perturbative regime the CT state is only weakly coupled to the Frenkel exciton so that excimers can be safely neglected.

Interestingly, the  $A_1$  absorption peak is red-shifted for the CT H-aggregate in Figure 67b. The red-shift does not contradict the H-aggregate assignment; the  $k = 0$  exciton still lies at the top of the exciton band although red-shifted due to  $\Delta_{CT}$ . In CT H- and J-aggregates, the overall spectral shift is given by  $\Delta_{CT} + 2J_{CT}F$ , where  $F$  is the generalized Franck–Condon factor ranging from  $\exp(-\lambda^2)$  in the weak exciton coupling limit to  $\exp(-\lambda^2/N)$  in the strong coupling limit. Using eqs 168 and

169, the spectral shift induced entirely by (virtual) CT-mediated interactions is

$$\Delta_{CT} + 2J_{CT}F = -2 \frac{(t_e + t_h)^2 + 2t_e t_h(F - 1)}{E_{CT} - E_{S_1}} \quad (173)$$

which is universally negative for J-aggregates ( $t_e t_h > 0$ ) but also for H-aggregates ( $t_e t_h < 0$ ) when  $F < 1$ . Even if  $F = 1$ , H-aggregates remain red-shifted due to the CT-mediated red-shift with the exception of the special case when  $t_e = -t_h$  at which point the red-shift is exactly zero. The red-shift of the H-aggregate in Figure 67b of approximately  $-0.2\omega_{vib}$  is consistent with eq 173 using the numerically obtained value,  $F \approx 0.5$ . This example illustrates the danger in assigning H- and J-aggregates based solely on spectral shifts. Instead, H- and J-aggregates are reliably distinguished by the band curvature at  $k = 0$ ; for CT aggregates, the curvature is  $-FJ_{CT}$ , which is positive for J-aggregates and negative for H-aggregates.

### 5.5. Charge-Transfer Induced J- and H-Aggregate Behavior in the Resonance Regime

When the energy gap between the diabatic (premixed) Frenkel and charge-transfer bands is small compared to the magnitude of the CT integrals, the perturbative limit no longer applies, and the analysis based on the effective Hamiltonian in eq 167 breaks down. In this regime, which we refer to as the “resonance regime”, CT states need to be considered explicitly to fully describe the system photophysics. Most previous treatments of the effect of intermolecular charge-transfer on the absorption spectrum of molecular aggregates are nonperturbative and generally have obtained very good agreement with experiment, most notably the works of Soos and co-workers,<sup>211–213</sup> Gisslen and Scholz,<sup>214,215</sup> Spano and co-workers,<sup>223–230</sup> Gao et al.,<sup>455</sup> Reineker and co-workers,<sup>456,457</sup> and Hoffman et al.<sup>216</sup>

Figure 68 illustrates the free-exciton band dispersions before and after CT/Frenkel mixing and in the absence of Coulomb coupling. Before mixing, the Frenkel and CT bands are comprised of the states  $|k\rangle$  and  $|k, \pm\rangle$  in eq 163 with energies  $E_{S_1}$  and  $E_{CT}$ , respectively, whereas after mixing the states are divided among the  $\alpha = 1, 2$ , and 3 bands in eq 166. In the figure, the  $\alpha = 2$  band, which consists of pure CT states, is omitted. As the  $\alpha = 2$  band remains uncoupled from the Frenkel band, it cannot acquire oscillator strength and therefore has no impact on the absorption spectrum. Furthermore, in the perturbative regime considered up until now, the Frenkel/CT

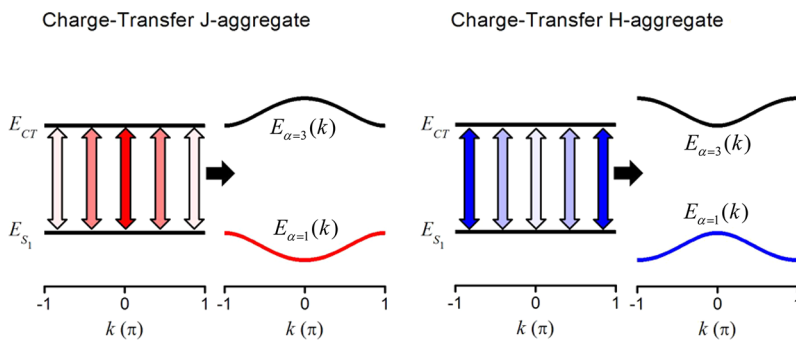


**Figure 68.** Exciton dispersion curves of a charge-transfer J-aggregate when  $t_e$  and  $t_h$  are in-phase (left) and a charge-transfer H-aggregate when  $t_e$  and  $t_h$  are out-of-phase (right). The dispersion curves on the left of each panel consider the system before Frenkel/CT state mixing (“diabatic”), whereas those on the right of each panel consider the system after Frenkel/CT mixing. The stronger shading of the double-sided arrows indicates stronger Frenkel/CT mixing. In the resonance regime, the diabatic bands are sufficiently close in energy so that both ( $\alpha = 1, 3$ ) bands contain strong Frenkel and CT character. See text for further discussion. Adapted with permission from ref 228. Copyright (2017), American Chemical Society.

exciton mixing is weak so that only the Frenkel-dominated ( $\alpha = 1$ ) band contributes to both absorption and emission. J- or H-aggregation is therefore defined solely by the  $\alpha = 1$  band; when the  $k = 0$  exciton resides at the bottom (top) of the band, the system is a J- (H-) aggregate. In the resonance regime, however, the mixing is strong and both  $\alpha = 1$  and  $\alpha = 3$  bands have significant Frenkel character. In the resonance regime, the aggregate type is based on the position of the  $k = 0$  exciton in the *lowest* energy ( $\alpha = 1$ ) band. This definition ensures that the characteristics historically associated with each aggregate type, such as super- and subradiance for J- and H- aggregates, respectively, are maintained (because emission proceeds primarily from the lower band). In the left panel of Figure 68, the charge transfer integrals are in phase causing the  $k = 0$  exciton to move to the bottom of the  $\alpha = 1$  band, thereby creating a J-aggregate. The right panel shows the situation when the charge transfer integrals are out of phase; the  $k = 0$  exciton now resides at the top of the lower energy band as defines an H-aggregate.

The origin of the band dispersions in Figure 68 can be understood by analyzing the  $k$ -dependent Frenkel/CT matrix element in eq 165. The magnitude of the interaction, which determines the magnitude of the CT-induced energy splitting, is indicated by the shading of the arrows in Figure 68 with darker shading indicating a stronger interaction. When  $t_e$  and  $t_h$  have the same sign, the interaction, which is proportional to  $|t_e + t_h e^{ikl}|$ , is maximum for the  $k = 0$  excitons and decreases with increasing wave vector, reaching the minimum for the  $k = \pi$  excitons. Conversely, when  $t_e$  and  $t_h$  have opposite signs, the Frenkel/CT interaction is minimal for the  $k = 0$  excitons and increases with increasing wave vector until reaching the maximum for the  $k = \pi$  excitons. In the resonance regime, when  $|t_e + t_h| > |t_e - t_h|$ , the  $k = 0$  exciton will lie at the bottom of the lower energy band (J-aggregate), whereas when  $|t_e + t_h| > |t_e - t_h|$ , the  $k = 0$  exciton will lie at the top of the band (H-aggregate).<sup>227,228</sup> Note that this is equivalent to the condition  $-t_e t_h < 0$  for J-aggregate behavior and  $-t_e t_h > 0$  for H-aggregate behavior regardless of the sign of  $E_{CT} - E_{S_1}$ . Hence, in the resonance regime, J- and H-aggregation depends only on the relative sign of  $t_e$  and  $t_h$ , whereas in the perturbative regime, it also depends on the sign of  $E_{CT} - E_{S_1}$ , as is evident in the form of  $J_{CT}$  in eq 168.

The changes in the CT J- and H-aggregate spectra in going from the perturbative to the resonance regimes were explored in refs 227 and 228. Figure 69 shows the absorption and emission spectra for J- and H-aggregates in the resonance regime with  $E_{CT} - E_{S_1} = 0$ , which is the only parameter that differentiates these aggregates from those in the perturbative regime in Figure 67. Comparison of the two figures reveals substantial spectroscopic differences, especially for CT J-aggregates, where the absorption spectrum in the resonance regime is characterized by two main absorption bands, consistent with the well-separated  $k = 0$  excitons in the  $\alpha = 1$  and 3 exciton bands in Figure 68. The appearance of two absorption bands results from a constructive interference between  $t_e$  and  $t_h$ <sup>214</sup> which enhances the coupling amongst the (diabatic)  $k = 0$  Frenkel and CT excitons, resulting in oscillator strength being effectively shared between the ( $k = 0$ )  $\alpha = 1$ , and  $\alpha = 3$  excitons in Figure 68. Interestingly, both bands contain vibronic structure with vibronic signatures reflective of the band curvatures; in the lower band, which has positive curvature at  $k = 0$ ,  $R_{abs}$  is enhanced relative to the monomer,

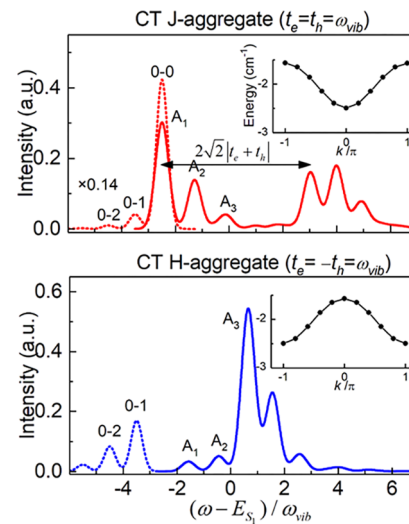


**Figure 69.** Simulated absorption (solid curves) and PL spectra (dashed curves) at 0 K for charge-transfer (a) J-aggregates where  $t_e = t_h = \omega_{vib}$  and (b) H-aggregates where  $t_e = -t_h = \omega_{vib}$ . In both cases,  $N = 10$ ,  $E_{CT} - E_{S_1} = 0$ ,  $\lambda^2 = 2\lambda_{\pm}^2 = 1$ , and  $J_C = 0$ . The dispersions of the lowest energy excitons appear in the inset. Adapted with permission from ref 228. Copyright (2017), American Chemical Society.

whereas in the upper band, which has negative curvature,  $R_{abs}$  is attenuated (recall that it is the lower band that characterizes J- or H-aggregate behavior). In marked contrast, the absorption spectrum for the CT H-aggregate in Figure 69b is dominated by a single blue-shifted band with a reduced value of  $R_{abs}$ . The single-band structure arises because the coupling between the diabatic  $k = 0$  Frenkel and CT excitons is reduced via destructive interference between  $t_e$  and  $t_h$ ; in the special case,  $t_e = -t_h$  and  $E_{CT} - E_{S_1} = 0$ , which defines the H-aggregate in Figure 69b, the  $\alpha = 1$  and 3 exciton bands in Figure 68 actually intersect at  $k = 0$ . The result is an absorption and PL spectrum characteristic of a strongly coupled H-aggregate.

For the CT J-aggregate in Figure 69a, the peak-to-peak splitting between the two-bands is approximately equal to  $2\sqrt{2}|t_e + t_h|$ , the exciton splitting obtained in the absence of vibronic coupling (when  $E_{CT} - E_{S_1} = 0$ ).<sup>227</sup> Hence, the peak-to-peak splitting appears to be relatively insensitive to vibronic coupling, thereby providing a qualitative measure of  $|t_e + t_h|$  in the general case. A second, and perhaps more robust, measure of  $|t_e + t_h|$  is the second central moment of the absorption spectrum, which provides information about the spectral width. Gisslen and Scholz showed<sup>214</sup> that, for the Frenkel/CT Holstein Hamiltonian, the second central moment is given by

$$\langle (\Delta E)^2 \rangle = \frac{\sum_i |\langle G|\hat{M}|\psi_i\rangle|^2 E_i^2}{\sum_i |\langle G|\hat{M}|\psi_i\rangle|^2} = 2(t_e + t_h)^2 + \lambda^2 \omega_{vib}^2 \quad (174)$$

(Note that the first moment is insensitive to charge transfer, see eq 51.<sup>214</sup>) Hence, given the Huang–Rhys factor and vibrational energy, both of which can be easily extracted from the solution (monomer) spectrum, one can readily determine  $|t_e + t_h|$  from eq 174. In contrast to the peak-to-peak splitting method, the second moment can be used to extract  $|t_e + t_h|$  from experiment even for systems with merged two-band structures, such as

TAT,<sup>225</sup> and for charge-transfer H-aggregates, such as those in Figure 69b, where there is no discernible splitting.

The relationship between the second central moment and the charge transfer integrals corresponds well to Kazmaier and Hoffmann's observation<sup>210</sup> that photoconducting systems exhibiting broadened absorption spectra—including perylene,<sup>210</sup> squaraine,<sup>476</sup> thiopyrylium,<sup>477</sup> and diketopyrrolo dyes—have the highest photosensitivities. The charge-transfer integrals responsible for the broadening of the spectra are also responsible for exciton dissociation and charge generation. As discussed in detail by Hestand et al.<sup>230</sup> and later in section 5.7, not only are the individual magnitudes of  $t_e$  and  $t_h$  important factors in determining photosensitivity and conductivity but also their relative phases, which dictate the coupling between the optically allowed Frenkel exciton and CT states via the matrix element  $|t_e + t_h|$ .

In ref 230, it was found that asymmetries in the two-band line shape in charge-transfer J-aggregates reveal the relative (diabatic) Frenkel and CT exciton energies,  $E_{k=0}$  and  $E_{CT}$ , respectively. When the majority of oscillator strength is concentrated in the lower (upper) energy band in the absorption spectrum, the diabatic  $k = 0$  Frenkel exciton has lower (higher) energy than the charge-transfer excitons. Figure 70 illustrates how the absorption asymmetry depends on  $E_{k=0}$

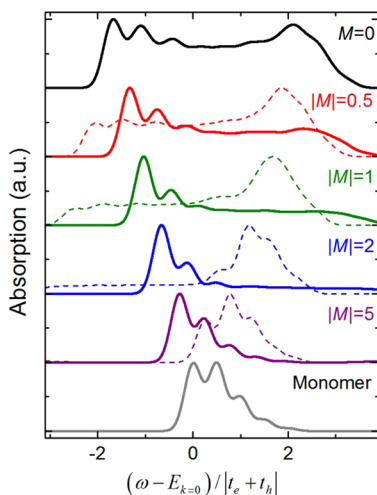


**Figure 70.** Simulated absorption spectra as a function of the relative energy difference between the diabatic Frenkel and charge-transfer states. Solid (dashed) curves correspond to positive (negative) values of  $M$ . In addition,  $\omega_{\text{vib}} = 0.5|t_e + t_h|$  and  $\lambda^2 = 1$ . See ref 230 for further details. Reprinted with permission from ref 230. Copyright (2016), American Chemical Society.

and  $E_{CT}$  for several values of the mixing parameter  $M = (E_{CT} - E_{k=0})/|t_e + t_h|$ . The sign of  $M$  indicates the relative order of  $E_{k=0}$  and  $E_{CT}$ , whereas  $|M|$  indicates the asymmetry magnitude. The spectral asymmetry is a qualitative measure of the relative energy difference between the (diabatic) Frenkel and CT states and must be applied with care; for systems having relatively strong vibronic coupling with  $\lambda^2 \geq 1$ , vibronic effects can complicate the interpretation of the spectrum (see ref 230 for further discussion). A more robust measure of the Frenkel/CT energy separation =  $(E_{CT} - E_{k=0})$  is the third central moment of the absorption spectrum, which characterizes the skewness of the spectrum. A straightforward calculation yields

$$\langle (\Delta E)^3 \rangle = \frac{\sum_i |\langle G|\hat{M}|\psi_i\rangle|^2 E_i^3}{\sum_i |\langle G|\hat{M}|\psi_i\rangle|^2} = (\omega_{\text{vib}}\lambda)^2(\omega_{\text{vib}} - J_k + 2(t_e + t_h)^2(E_{CT} - E_{k=0} + \omega_{\text{vib}}(\lambda_-^2 + \lambda_+^2 - \lambda^2))) \quad (175)$$

Notably, all of the terms appearing in eq 175, with the exception of  $E_{CT}$ ,  $\lambda_-^2$ , and  $\lambda_+^2$ , can be determined either from the (monomer) solution spectrum or the first or second moment of the aggregate absorption spectrum. Furthermore, the approximate sum rule<sup>214</sup>  $\lambda_-^2 + \lambda_+^2 = \lambda^2$  yields  $E_{CT}$  as the only remaining unknown. Hence,  $E_{CT}$  and  $(E_{CT} - E_{k=0})$  can be extracted from the third central moment of the absorption spectrum for any aggregate exhibiting charge-transfer so long as  $t_e \neq -t_h$ .

In the resonant regime, the PL spectra of CT J-aggregates also show a small but notable departure from the PL spectra of Coulombically coupled J-aggregates (or from CT J-aggregates in the perturbative regime); at  $T = 0$  K and in the absence of disorder,  $R_{\text{PL}}$  is no longer rigorously equal to  $N/\lambda^2$  over the entire phase space of the Hamiltonian in eq 152. Instead, significant charge-transfer character within the emitting state results in a dependence of the PL ratio on the ionic nuclear geometries and hence the ionic Huang–Rhys parameters. This dependence is illustrated in the simulated dimer spectra in Figure 71 for a trio of  $\lambda_+^2$  and  $\lambda_-^2$  values. The deviation of the PL

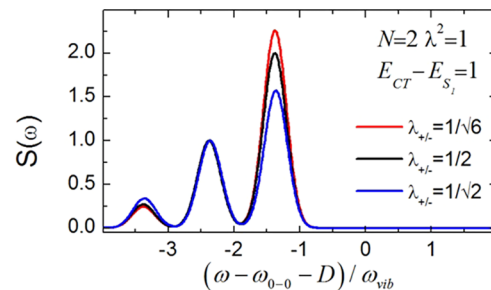


**Figure 71.** Simulated PL dimer spectra for CT-mediated J-aggregates for selected values of  $\lambda_{\pm}^2$  as noted in the legend. The spectra are normalized to the 0–1 peak so that the PL ratio  $R_{\text{PL}}$  can be readily appreciated. In all cases,  $J_C = 0$ ,  $\lambda^2 = 1$ ,  $E_{CT} - E_{S_i} = \omega_{\text{vib}}$ , and  $t_e = t_h = \omega_{\text{vib}}$ . Reprinted with permission from ref 342. Copyright 2016, Elsevier.

ratio from  $N/\lambda^2$  was first noted in ref 243 in an investigation of the photophysics of practically defect-free polydiacetylene chains prepared by Schott and co-workers.<sup>334–336</sup> In the presence of strong Frenkel/CT coupling, the PL ratio rule is modified by a multiplicative factor,  $\kappa_0$ , such that

$$R_{\text{PL}} = \kappa_0 N/\lambda^2 \quad (176)$$

The  $\kappa_0$  factor was observed to exceed unity for weak ionic vibronic coupling (i.e., small  $\lambda_{\pm}^2$ ) and falls below unity for strong ionic vibronic coupling. Regardless, it was concluded in ref 243 that the PL ratio, modified by the  $\kappa_0$  factor, is still able to accurately track the thermal coherence number  $N_{\text{coh}}$ , i.e.,  $R_{\text{PL}} = \kappa_0 N_{\text{coh}}/\lambda^2$ .

In a later study,<sup>342</sup> the  $\kappa_0$  factor was shown to be a temperature-independent function of the HR factors and the Frenkel exciton admixture,  $\langle \text{FE} \rangle$ , within the emitting exciton

$$\kappa_0 \approx [\langle \text{FE} \rangle + (1 - \langle \text{FE} \rangle)(\lambda_+ + \lambda_-)^2/\lambda^2]^{-1} \quad (177)$$

Eq 177 shows that, whenever  $|\lambda_+ + \lambda_-| < |\lambda|$  ( $|\lambda_+ + \lambda_-| > |\lambda|$ ), the factor  $\kappa_0$  in the  $R_{PL}$  ratio formula will be greater (less) than one, in agreement with the earlier conclusions.<sup>243</sup> Notably, whenever  $\lambda_+ + \lambda_- = \lambda$ ,  $\kappa_0$  in eq 177 reduces to unity and the original PL ratio rule of eq 58 is recovered exactly.<sup>342</sup>

We again note that utilizing the PL ratio as a measure of exciton coherence relies on structured emission spectra where the 0–0 and 0–1 peaks are well resolved. High charge-transfer character in the emitting states, such as that which would be expected in the resonance regime, may lead to excimer formation and the associated broad and unstructured emission spectra,<sup>30–36,141</sup> thereby preventing straightforward extraction of the coherence number from the PL spectrum. However, there are systems, such as TAT,<sup>225,463</sup> that show structured emission regardless of the strong charge-transfer character in the emitting states. In such systems, the PL spectrum can provide a simple measure of the exciton coherence number.

### 5.6. Interference between Coulombic and CT-Mediated Coupling

As originally recognized by Yamagata et al.,<sup>225</sup> in general, the J- or H-nature of a molecular aggregate, and in particular a  $\pi$ -stack, derives from a competition between the Coulombic and CT-mediated intermolecular interactions. This is most easily appreciated in the perturbative limit where the effective Hamiltonian in eq 167 describes the system photophysics. When the Coulombic coupling is restricted to nearest neighbors, the free-exciton band (i.e., in the absence of vibronic coupling) is given in eq 171, showing that the H- and J-aggregate behavior is governed by an interference between the CT-mediated couplings,  $J_{CT}$ , and the Coulomb coupling,  $J_C$ . Overall, H-like behavior results when  $J_{CT} + J_C > 0$ , and J-like behavior results when  $J_{CT} + J_C < 0$ . Because the signs of  $J_{CT}$  and  $J_C$  can vary independently, there arises the possibility of integrated HJ, JH, JJ, and HH aggregates where the first (second) letter corresponds to the Coulombic (CT-mediated) coupling. When  $J_{CT}$  and  $J_C$  have the same sign (HH or JJ) the couplings reinforce one another, leading to exaggerated H- or J-like behavior. On the other hand, when  $J_{CT}$  and  $J_C$  have opposite signs (HJ or JH), the couplings interfere destructively, leading to suppressed H- or J-like behavior with the overall nature of the system determined by the coupling with the largest magnitude. To indicate the relative magnitude of the couplings, lower and upper case letters can be used<sup>227,228</sup> with comparable couplings defaulting to upper case. Hence, hJ-aggregates are Kasha H-aggregates with regard to just the Coulomb coupling, but because the CT-mediated coupling is J-like and dominant, the overall aggregate behaves like a J-aggregate. We emphasize that because the interference is confined to the same molecular pair (i.e., nearest neighbors) the HJ-aggregates described in this section are fundamentally different from the segregated HJ-aggregates discussed in section 4.8, where the H- and J-interactions are spatially distinct (i.e., intra- vs interchain). Moreover, the interference described here is also fundamentally different from the aforementioned interference between diabatic Frenkel and CT excitons introduced by Gisslen and Scholz<sup>214</sup> (and dictated by the relative signs of  $t_e$  and  $t_h$ ) to explain the broadened spectra observed in several perylene derivatives. Finally, when extended couplings are included within a  $\pi$ -stack, the J- and H-nature is determined by the sign of  $J_{CT} + J_C + \sum_{n \geq 2} J_{n,n+1} = J_{CT} + J_C^{\text{eff}}$ , where  $J_C^{\text{eff}}$  is an effective nearest neighbor coupling that includes the influence of extended interactions.

The competition between  $J_{CT}$  and  $J_C$  (or  $J_C^{\text{eff}}$ ) is illustrated in Figure 72. Like Figure 68, Figure 72 shows the free exciton

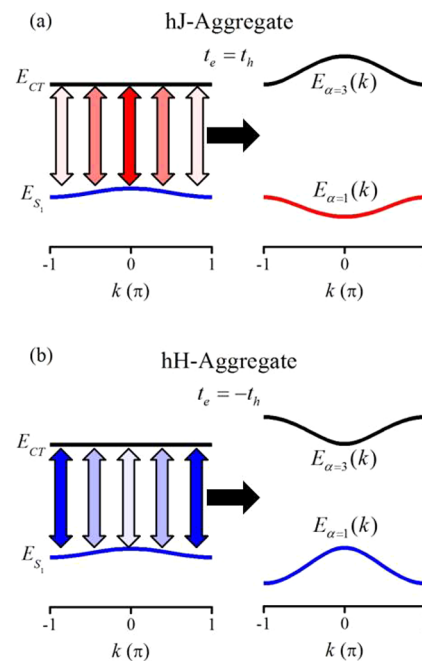


**Figure 72.** Exciton bands before (left) and after (right) Frenkel/CT mixing when  $t_e = t_h$  in (a) and  $t_e = -t_h$  in (b). In both cases, the Coulomb coupling is positive ( $J_C > 0$ ), leading to H-like Frenkel bands (colored blue) before mixing. In both (a) and (b),  $|J_{CT}| > J_C$ . The double-sided arrows indicate the strength of the Frenkel/CT exciton mixing with darker shading indicating stronger mixing. Adapted with permission from ref 228. Copyright (2017), American Chemical Society.

band dispersions before and after Frenkel/charge-transfer mixing, the difference here being that the Coulombic coupling is now included in the Frenkel band,  $E_k = E_{S_1} + 2J_C$ . In Figure 72a and b, the Coulombic coupling ( $J_C$ ) was chosen to be positive so that the curvature of the Frenkel band, shown in blue, is negative as in an H-aggregate. In Figure 72a, the electron and hole integrals ( $t_e$  and  $t_h$ ) were taken to be in phase, making the CT-mediated interaction  $J_{CT}$  in eq 168 negative (J-like). If  $|J_{CT}|$  exceeds  $J_C$ , as in the hJ-aggregate in Figure 72a, the low-energy ( $\alpha = 1$ ) band, shown in red, is J-like with positive curvature. Hence, in hJ-aggregates, Frenkel/CT mixing reverses the curvature of the exciton band.

Conversely, if  $t_e$  and  $t_h$  are out of phase as in Figure 72b,  $J_{CT}$  is positive and H-promoting. There is now a constructive interference between the Coulomb and CT-induced couplings. Rather than reordering the excitons as in the hJ-aggregates of Figure 72a, the effect of Frenkel/charge-transfer mixing is to preserve the negative curvature of the exciton band and enhance its bandwidth, note the increased bandwidth of the low-energy  $\alpha = 1$  band leading to enhanced H-aggregate behavior. Although our description is so far limited to the perturbative regime, similar interference effects are expected in the resonance regime, although there the relative magnitudes of the Coulomb and charge-transfer couplings are harder to quantify.

Significantly, the interference between Coulombic and charge-transfer interactions in  $\pi$ -stacked systems can disrupt the photophysical behavior that is expected based on

Coulombic coupling alone. For example, it is conceivable that a system would behave photophysically like a J-aggregate even though the Coulombic coupling predicts H-like behavior, as in the hJ-aggregate in the top panel of Figure 72. As discussed in section 5.8, the geometries associated with Kasha's J- and H-aggregates, which were derived based on Coulombic coupling alone, are not accurate predictors of H- and J-aggregate behavior in many  $\pi$ -stacked systems. For quantitative descriptions of the photophysics, both the Coulombic and charge-transfer interactions need be taken into account.

### 5.7. Interference Effects in Energy and Charge Transport

Materials that are able to rapidly transport energy and charge are desirable for electronics applications. For example, in bulk heterojunction photovoltaic cells,<sup>479</sup> the absorbing material must be able to transport the absorbed energy to the heterojunction interface where charge separation can occur before the energy is lost to either radiative or nonradiative decay processes. After separation, the charges must then proceed to the electrodes where they enter the circuit. In this section, we briefly review two important interference effects that influence energy and charge-transport dynamics<sup>4,8–12,16,17</sup> in  $\pi$ -stacked organic systems. We first discuss the results presented in ref 238, which show that the interference between Coulomb and CT-mediated couplings can substantially impact energy transfer dynamics. Next, we consider how the interference between the CT integrals,  $t_e$  and  $t_h$ , affects the dynamics of charge separation subsequent to absorption.<sup>230</sup> Recently, Tempelaar et al.<sup>480</sup> have shown that such interferences also play a decisive role in charge recombination at a heterojunction interface.

In ref 238, Hestand et al. demonstrated that the interference between the Coulomb ( $J_C$ ) and charge transfer ( $J_{CT}$ ) couplings may significantly alter the dynamics of energy transfer. Using the insight gained from the effective Hamiltonian in eq 167, they proposed that because the rate of energy transport correlates to the exciton bandwidth, rapid energy transport should be realized when the Coulomb and CT couplings interfere constructively, whereas a suppressed rate should result when the couplings interfere destructively. Furthermore, as the total exciton coupling, including its sign, is reflected in the value of  $R_{abs}$ , see eq 172, the absorption spectrum should provide an efficient means of screening for materials with efficient energy transport.

In ref 238, trajectories were calculated for an initially localized exciton within a linear  $\pi$ -stack of TAT molecules by solving the Schrodinger equation using the vibronic Frenkel/CT Hamiltonian in eq 152. The results, shown in the top panel of Figure 73, indicate that excitons in TAT  $\pi$ -stacks are practically immobile due to an efficient destructive interference between the H-promoting Coulomb coupling  $J_C^{\text{eff}}$  (which includes all extended interactions) and the J-promoting CT-mediated coupling, such that the net exciton bandwidth is substantially reduced. Note that TAT aggregates are not strictly in the perturbative regime because  $|t_e|$  and  $|t_h|$  are only a factor of  $\sim 3$  smaller than  $E_{CT} - E_{S_i}$ . Regardless, a comparison of  $J_{CT}$  vs  $J_C^{\text{eff}}$  still provides insight into the approximate degree of interference between the two coupling sources. In ref 238 it was further demonstrated that a sign change in  $t_e$  (and therefore  $J_{CT}$ ), which can be achieved in TAT by a sub-Å short- or long-axis slip in the  $\pi$ -stacking geometry, results in a substantially enhanced rate of excitation transport (see the middle panel of Figure 73). Furthermore, the energy transfer rate within this

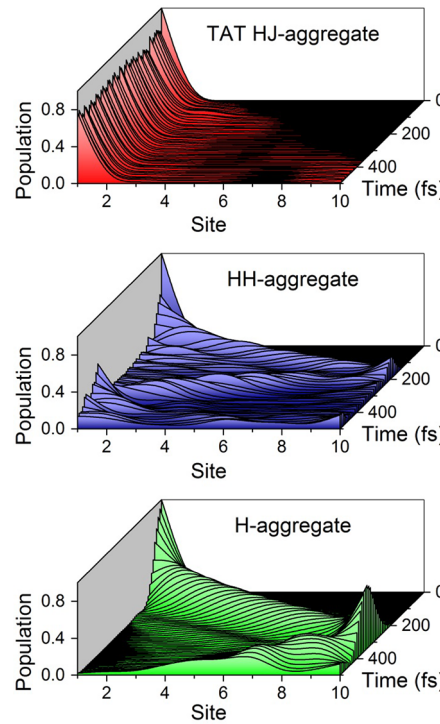


**Figure 73.** Exciton population on each site in a  $\pi$ -stack of 10 molecules as a function of time in a TAT HJ aggregate (top), a hypothetical TAT HH aggregate (middle), and in a Kasha H-aggregate (bottom). See ref 238 for parameters. Top/middle figures: Reprinted with permission from ref 238. Copyright (2015), by the American Physical Society.

hypothetical TAT HH-aggregate is also enhanced relative to a traditional Kasha H-aggregate defined to include only Coulomb coupling (compare the middle and bottom panels of Figure 73). These results suggest a design principle for enhancing energy transfer in  $\pi$ -stacked materials, namely optimizing the  $\pi$ -stacking structure so that the Coulomb and CT-mediated interactions interfere constructively (see section 5.8 for a detailed discussion on the spatial dependence of the Coulomb and charge-transfer interactions).

The simulations in Figure 73 consider ideal, isolated systems such that the dynamics are not subject to the effects of disorder or thermal fluctuations. However, in ref 238, the interference effect was demonstrated to be robust against such interactions in TAT, after incorporating static disorder, and treating thermal fluctuations using an overdamped Brownian oscillator model. Also relevant are the recent works by Troisi and co-workers<sup>481–483</sup> who showed that low frequency ( $\sim 100 \text{ cm}^{-1}$ ) intramolecular vibrations can lead to substantial thermal fluctuations in the total coupling ( $J_{CT} + J_C^{\text{eff}}$ ) in organic crystals. Fluctuations in the total coupling were found to arise mainly from the short-range (CT-mediated) component with the standard deviation of the total coupling generally found to be  $\sim 1/5$  of its mean value,<sup>482,483</sup> although in extreme cases the standard deviation can exceed the mean.<sup>481</sup> Such fluctuations are expected to impact the energy transport dynamics, for example, by leading to enhanced mobility through partial mitigation of the destructive interference present in HJ-aggregates but reduced mobility in HH-aggregates where the interference is constructive. More studies are needed to test the robustness of the constructive interference, especially at room

temperature, to guide the optimization of materials for rapid energy transport.

Spectral signatures for rapid energy transfer are correlated to the vibronic signatures of charge-transfer mediated H- and J-aggregates. For example, whenever the vibronic ratio  $R_{\text{abs}}$  is near the monomer value, the net exciton coupling is near zero, and the exciton should be relatively immobile. Conversely, a large deviation of the ratio  $R_{\text{abs}}$  indicates a large exciton bandwidth and rapid energy transport. Hence,  $R_{\text{abs}}$  can serve as a simple probe of exciton mobility, which may be useful for large throughput screening for high-mobility aggregates.

We now turn to another important interference effect that concerns the rate of charge separation in  $\pi$ -stacked systems. In ref 230, it was observed that, after optical excitation to the  $k = 0$  Frenkel exciton, the rate of electron/hole separation depends on an interference between the charge transfer integrals  $t_e$  and  $t_h$ . In ref 230, the restriction of charge-separated states to just nearest neighbors was relaxed, and as a result, the diabatic CT states with  $k = 0$  were dispersed over a band of width  $4|t_e + t_h|$ . As noted in section 5.3, the  $k$ -dependent Frenkel/CT mixing is proportional to  $t_e + t_h e^{ik}$ ; strong mixing of the optically bright ( $k = 0$ ) Frenkel exciton and the  $k = 0$  CT excitons results when  $t_e$  and  $t_h$  interfere constructively and weak mixing results when  $t_e$  and  $t_h$  interfere destructively.<sup>214,215</sup> The effect of this interference (as well as the interference present in the CT bandwidth) on the charge-separation dynamics is illustrated in Figure 74, which shows the electron/hole separation as a

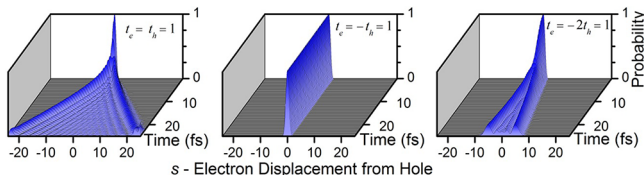


**Figure 74.** Expected distance ( $s$ ) between electron and hole after excitation to the  $k = 0$  Frenkel exciton for various charge-transfer aggregates. At  $t = 0$ , the system is in the state defined by the  $k = 0$  Frenkel exciton. In all cases, the nuclear degrees of freedom were neglected ( $\lambda^2 = \lambda_+^2 = \lambda_-^2 = 0$ ) and only nearest neighbor charge-transfer interactions, as indicated in the insets in units of  $1400 \text{ cm}^{-1}$ , were considered. Additionally, the Frenkel and charge transfer states were assumed to be resonant ( $E_{\text{CT}} - E_{S_1} = 0$ ), and an infinite dielectric was assumed so that no Coulomb barrier had to be overcome for charge separation. Adapted with permission from ref 230. Copyright (2016), American Chemical Society.

function of time in a rigid  $\pi$ -stack of 50 molecules placed in a medium with a high dielectric constant. At  $t = 0$ , the system is in the  $k = 0$  Frenkel exciton state, and the electron and hole are therefore localized to the same molecule ( $s = 0$ ). Notably, when  $t_e = t_h$  (constructive interference), the electron and hole rapidly separate, whereas when  $t_e = -t_h$  (destructive interference), the charges remain bound and no separation occurs. For more moderate destructive interferences,  $t_e = -2t_h$ , the charges do separate but significantly slower than in the constructively interfering case. Interestingly, it was also observed that vibronic coupling interrupts the perfect destructive interference occurring when  $t_e = -t_h$ , leading to an enhanced charge separation rate that is only several times slower than the maximum rate (when  $t_e = t_h$ ).<sup>230</sup> Enhanced energy transport<sup>484–488</sup> and charge separation<sup>489,490</sup> within photosynthetic systems have also been attributed to vibronic coupling effects, although those enhancements are due to resonantly enhanced

coherences rather than the aforementioned interference. Disorder and thermal fluctuations are also expected to modulate the interference such that the results presented in ref 230 likely represent the upper limit of the interference effects. Nevertheless, this interference effect can likely be exploited to optimize charge separation in organic materials through control over the packing structure. Section 5.8 discusses how the charge-transfer integrals respond to the packing geometry.

The charge-separation dynamics can also be linked to spectroscopic signatures. Specifically, when  $t_e$  and  $t_h$  interfere constructively (destructively), a CT-mediated J-aggregate (H-aggregate) results. The spectroscopic signatures associated with resonant charge-transfer J- and H-aggregates (see section 5.5) can therefore be used to discriminate between materials based on their expected exciton dissociation rate subsequent to optical absorption. Namely, the absorption spectrum of systems exhibiting the fastest rates (CT J-aggregates) should exhibit a broad, two-band absorption spectrum with a large band-to-band separation (see, e.g., the top panel of Figure 69). Finally, we note that in addition to constructively interfering charge-transfer integrals, separation beyond nearest neighbors also requires that the charges can overcome the Coulomb binding energy, a condition that can be easily met in systems with high-dielectric constants,<sup>230</sup> but one that is not usually met within bulk organic crystals.

## 5.8. Dependence of Coulomb and Charge-Transfer Interactions on Molecular Packing

The relationship between packing geometry and photophysics established by Kasha's analysis of the Coulombic coupling is relatively simple: molecules packed such that the transition dipole moments are oriented "side-by-side" form H-aggregates, whereas those packed with the transition dipole moments related "head-to-tail" form J-aggregates (see section 2). However, because of the interference between Coulomb and CT interactions described in section 5.6, full appreciation of how geometry relates to photophysics in molecular  $\pi$ -stacks also requires an understanding of how the CT integrals  $t_e$  and  $t_h$  depend on packing geometry.

Kazmaier and Hoffmann's seminal work<sup>210</sup> concerning crystallochromy in perylene pigments provided the theoretical foundation for understanding geometric dependencies of the CT integrals. In their work, they debunked the idea that the valence and conduction band widths, which are determined by  $t_h$  and  $t_e$ , respectively, depend solely on the "area overlap" between the HOMO and LUMO wave functions on adjacent molecules. Instead, they showed that the bandwidth, and hence the integrals, depend on a quantum interference effect that is extremely sensitive to small changes in the packing geometry. Kazmaier and Hoffmann utilized their theory to explain the broad range of colors observed in a series of perylene derivatives<sup>435–440</sup> despite similar solution spectra and only slight differences in molecular packing. Gisslen and Scholz<sup>214,215</sup> expanded upon Kazmaier and Hoffman's theory by showing how the coupling between the (diabatic)  $k = 0$  Frenkel and CT excitons, dictated by the sum  $t_e + t_h$ , impacts the absorption spectrum. More recently, crystallochromy has also been observed in a variety of tetracene derivatives by Kitamura et al.<sup>441,442</sup>

Straightforward application of Kazmaier and Hoffmann's theory has led to relationships between the packing geometry and CT-induced J- and H-aggregation in several chemical

systems including perylene,<sup>227,228</sup> terrylene,<sup>225,238</sup> and polythiophene.<sup>223</sup> Significantly, it was shown that, in contrast to the Coulombic coupling, which is known to change from H- to J-like upon packing displacements on the order of half a molecular length,<sup>127,263,271</sup> the superexchange CT coupling,  $J_{CT}$ , is sensitive to displacements on the order of a carbon–carbon bond length.<sup>227,228,238</sup> The details of the geometric dependence of the interference, as well as the nature of the CT couplings, are described below.

**5.8.1. Geometric Dependence of Charge-Transfer Integrals.** Kazmaier and Hoffmann's description of the charge-transfer interactions within an ethylene dimer provides an excellent introduction for understanding how the CT integrals,  $t_e$  and  $t_h$ , derive from the relative orientations of the HOMOs and LUMOs on neighboring molecules.<sup>210</sup> Of particular interest is the relative sign between  $t_e$  and  $t_h$ , which dictates the H- or J-like behavior of the CT-mediated exciton couplings, as discussed in sections 5.4 and 5.5. We begin this section by summarizing Kazmaier and Hoffmann's results concerning an ethylene dimer.

The HOMO and LUMO of ethylene are shown in Figure 75; in both the HOMO and LUMO, the molecular plane

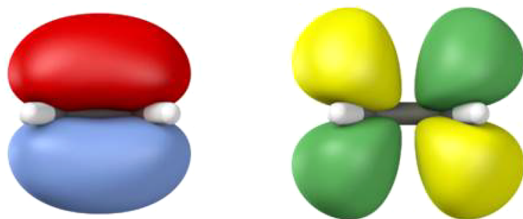


Figure 75. HOMO (left) and LUMO (right) of ethylene.

containing all of the atoms is a nodal plane. The LUMO has an additional nodal plane that bisects the molecule.  $t_e$  and  $t_h$  defined in eqs 155 and 156 represent interaction energies between adjacent molecular LUMOs and HOMOs, respectively, within the dimer. Hence, the signs of  $t_e$  and  $t_h$  can be readily determined using intuition from molecular orbital theory. When the dimer is in an eclipsed packing geometry (Figure 76, top left), a nodal plane divides the molecular HOMOs, implying an antibonding (high-energy) intermolecular interaction and therefore a negative value for  $t_h$  (recall  $t_h \equiv -\langle \phi_1^H | \hat{h} | \phi_2^H \rangle$ , see eq 156). The figure shows that as the two ethylene molecules are slipped along their long molecular axes  $t_h$  remains negative due to the antibonding nature of the intermolecular interaction; however, the interaction energy is expected to decrease as the spatial overlap between ethylene HOMOs diminishes.

The situation differs for the interaction between ethylene LUMOs. At the eclipsed geometry (Figure 76, bottom left), there is an obvious nodal plane dividing the molecular LUMOs implying an antibonding (high-energy) interaction and therefore a positive value for  $t_e$  ( $\equiv \langle \phi_1^L | \hat{h} | \phi_2^L \rangle$ ). However, when the relative slip reaches  $\sim 1.6$  Å, the bonding and antibonding interactions cancel each other and the net interaction goes to zero. As emphasized by Kazmaier and Hoffmann,<sup>210</sup> this quantum interference results in the total collapse of the conduction bandwidth even though there is still substantial “area” overlap between adjacent LUMOs. At larger slip distances ( $> 1.6$  Å), the adjacent LUMOs exhibit a bonding (low-energy) intermolecular interaction, implying a negative  $t_e$ .

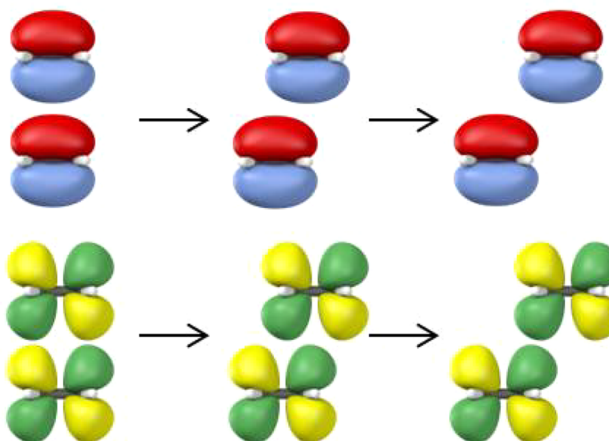


Figure 76. Ethylene HOMOs (upper) and LUMOs (lower) in an ethylene dimer as a function of long-axis displacement. Adapted with permission from ref 210. Copyright (1994), American Chemical Society.

Hence,  $t_e$  but not  $t_h$  undergoes a sign change as the two ethylenes are slipped along their long axes. A similar analysis of  $t_e$  and  $t_h$  as a function of short-axis displacement reveals that the sign of each integral remains constant.<sup>210</sup>

The qualitative description above is placed on a more quantitative footing in Figure 77, which shows the electron and

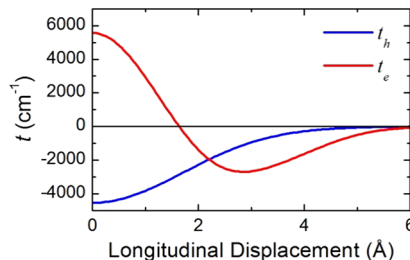
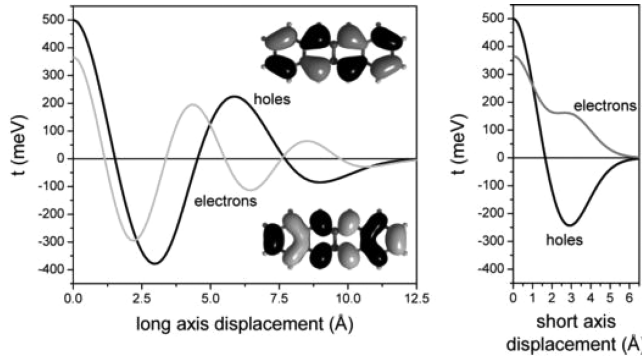


Figure 77. Electron and hole transfer integrals in an ethylene dimer as a function of longitudinal (long-axis) slip. The  $\pi$ -stacking distance was set to 3.5 Å.

hole integrals in an ethylene dimer as a function of longitudinal (long-axis) displacement. As expected,  $t_h$  is negative over the entire range of longitudinal displacements, and the sign of  $t_e$  changes from positive to negative as the molecules are displaced from the eclipsed geometry. These integrals were evaluated from ab initio calculations using the energy splitting method.<sup>11,214,491–497</sup> We note that, when using the energy splitting method to determine  $t_h$  and  $t_e$ , care must be taken to assign the correct signs.<sup>214,223,492,493</sup> The latter can usually be determined by visual inspection of the dimer HOMO and LUMO: whenever the dimer HOMO or LUMO is symmetric under the relevant symmetry operation (see section 5.8.3), the sign of  $t_h$  and  $t_e$  is negative. The symmetry operation used should also be consistent with the phase assigned to the transition dipoles (see section 5.8.3).

The relationship between packing geometry and the signs of  $t_e$  and  $t_h$  can be extended to molecules with more complex HOMO and LUMO nodal patterns. Kazmaier and Hoffman noted that<sup>210</sup> “if a given monomer MO has  $n$  longitudinal nodes and  $m$  transverse nodes, there should be in the bandwidth versus offset graph  $n$  and  $m$  points of zero

bandwidth.” (Note that the “transverse” direction defined in ref 210 corresponds to the short-axis direction.) The points of zero bandwidth correspond to the points at which  $t_e$  or  $t_h$  change sign. Hence, for a HOMO (LUMO) with  $n$  longitudinal and  $m$  transverse nodes, the sign of  $t_h$  ( $t_e$ ) will change  $n$ - and  $m$ -times as the molecules are displaced longitudinally (along the long axis) and transversely (along the short axis), respectively, from the eclipsed geometry. This behavior is illustrated for a tetracene dimer in Figure 78.<sup>11</sup> The tetracene HOMO contains



**Figure 78.** Charge-transfer integrals in a tetracene dimer as a function of (left) long-axis and (right) short-axis displacements. The tetracene HOMO and LUMO are shown as the top and bottom inset, respectively. Reprinted with permission from ref 11. Copyright (2007), American Chemical Society.

3 longitudinal nodes and 1 transverse node. Hence,  $t_h$  changes sign 3 times as a function of longitudinal displacement and 1 time as a function of transverse displacement. In contrast, the tetracene LUMO has 5 longitudinal nodes and 0 transverse nodes. The sign of  $t_e$ , therefore, changes 5 times as a function of longitudinal displacement and 0 times as a function of transverse displacement.

As a second example, the HOMO and LUMO of perylene and the spatial dependence of the CT integrals are shown in Figure 79a–d. The HOMO of perylene has 3 longitudinal nodes and 1 transverse node, and the LUMO has 0 longitudinal and 3 transverse nodes. Hence, the sign of  $t_h$  ( $t_e$ ) changes 3 (0) times as the molecules are displaced longitudinally and 1 (3) time as the molecules are displaced transversally. In Figure 79b, the third sign change in  $t_e$  occurs after a transverse displacement of greater than 4 Å and is not shown.

**5.8.2. Conjugated Polymers as J-Aggregates.** In section 5.8.1, we discussed the geometric dependence of  $t_e$  and  $t_h$  for  $\pi$ -stacked geometries. Charge-transfer interactions also occur between chromophores arranged head to tail, the most notable example of which is a conjugated polymer chain (CPC), where the repeat units are considered to be the coupled chromophores. For emissive conjugated polymers like polydiacetylene,<sup>334–336</sup> the CPC behaves photophysically like a linear J-aggregate. The similarities between emissive conjugated polymers and molecular J-aggregates have been pointed out by Spano and co-workers<sup>15,242,243,249,275,308,327</sup> and Barford and co-workers;<sup>244,498</sup> both CPCs and molecular J-aggregates exhibit (1) increasingly red-shifted absorption spectra with increasing chain/aggregate size, (2) enhanced radiative decay rates relative to a single chromophore (repeat unit or molecule), and similar vibronic signatures including (3) an increased vibronic ratio  $R_{\text{abs}}$  with increasing exciton bandwidth and (4) a PL ratio ( $R_{\text{PL}}$ ) proportional to the exciton coherence length.<sup>242</sup> Despite their

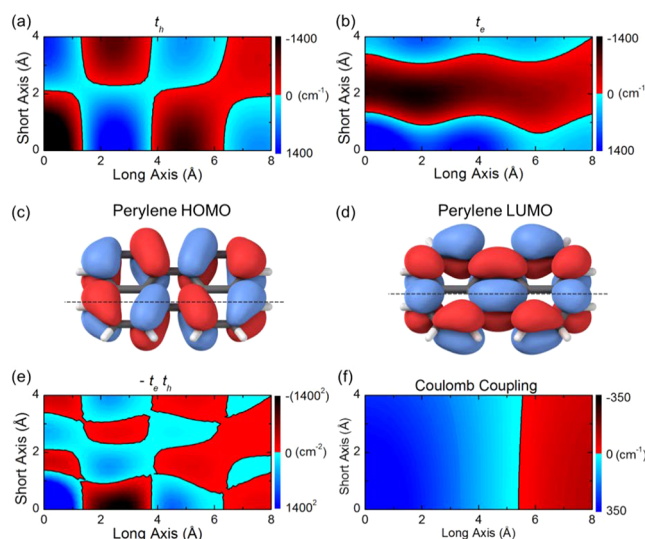


**Figure 79.** (a)  $t_h$  and (b)  $t_e$  within a  $\pi$ -stacked perylene dimer (3.5 Å stacking distance) as a function of short- and long-axis displacements. (c) The HOMO and (d) LUMO of perylene. (e) The product  $-t_e t_h (\propto J_{\text{CT}})$  and (f)  $J_C$  as a function of short- and long-axis displacements. Red regions indicate a negative coupling (J-aggregation), and blue regions indicate a positive coupling (H-aggregation). The Coulomb coupling is evaluated using atomic transition charges and scaled by 1/3 to approximate the effects of dielectric screening. The wave function phase is determined using translational symmetry, see top of Figure 82. Reprinted with permission from ref 228. Copyright (2017), American Chemical Society.

similarities, however, the J-aggregate behavior of CPCs and conventional “Kasha” J-aggregates derive from entirely different physical processes.

Conventional “Kasha” J-aggregation results from through-space Coulomb interactions between head-to-tail aligned transition dipole moments. Conversely, CPCs derive their J-aggregate behavior from a combination of Coulombic (through-space) and through-bond interactions.<sup>242,244</sup> In CPCs, the through-space interaction is usually J-like (negative) due to the head-to-tail alignment of neighboring monomer units. However, the through-bond (or superexchange) interaction, which depends on  $t_e$  and  $t_h$  through eq 168, is dominant, and J-like whenever the (diabatic)  $k = 0$  Frenkel-like excitation lies lower in energy than the charge-transfer excitation. This arises because CPCs are one-dimensional, direct band-gap semiconductors,<sup>499</sup> resulting in an in-phase relationship between  $t_e$  and  $t_h$ . The latter can be appreciated by considering the valence and conduction bands of a polyene shown in Figure 80.<sup>499</sup> The conduction and valence bands have opposite curvatures implying that  $t_e$  and  $t_h$  have the same sign. (Note that the sign of the hole transfer integral,  $t_h$ , is opposite to that of the transfer integral for an electron in the valence band, see eq 156.) Accordingly, so long as the (diabatic) CT state is higher in energy than the Frenkel-like excitation, as is usually the case in emissive CPs like polydiacetylene,<sup>334–336</sup> eq 168 predicts that the superexchange coupling will induce J-aggregate behavior. Interestingly, the class of nonemissive CPs such as polyacetylene, show more H-like behavior, likely due to the (diabatic) CT state lying below the Frenkel state. This is consistent with the existence of a dark S1 state found in many polyene-based molecules like carotenoids.<sup>89,90</sup>

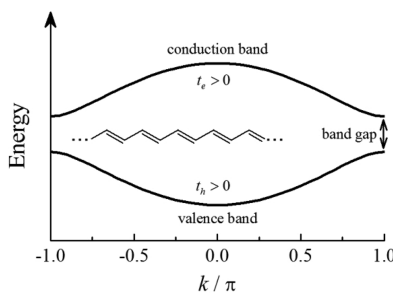


**Figure 80.** Valence and conduction bands of a one-dimensional direct band gap semiconductor such as the trans-polyene shown in the inset. The valence and conduction bands have opposite curvatures giving rise to electron and hole transfer integrals having the same sign.

The relative sign between  $t_e$  and  $t_h$  in CPCs can be further appreciated by analyzing the interaction energy between frontier molecular orbitals localized on nearest neighbor units, as was done in section 5.8.1 for  $\pi$ -stacked molecules. Figure 81 shows the localized HOMOs and LUMOs of four

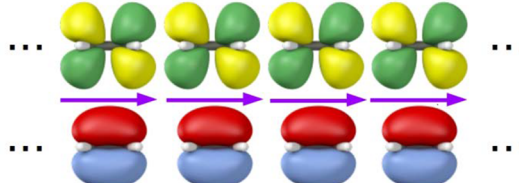


**Figure 81.** Ethylene LUMOs (top) and HOMOs (bottom) in a head-to-tail geometry based on the HOMO–LUMO transition dipole moment shown as purple arrows. The linear array is an approximation for polyacetylene.

ethylene molecules, which form the basis for polyacetylene, oriented in a head-to-tail fashion, based on the direction of the monomeric HOMO–LUMO transition dipole moment shown as purple arrows. The figure shows that there are no nodes between the neighboring HOMOs indicative of a bonding type interaction and a positive  $t_h$  (again, recall the negative sign in eq 156). In contrast, a node exists between neighboring LUMOs, indicating an antibonding interaction and a positive  $t_e$ . Hence, both integrals have the same sign, and assuming  $E_{CT} > E_{S_p}$ , the charge-transfer-mediated interaction in eq 168 will be J-like. Such an analysis can be generalized to other CP monomer repeat units as well.

**5.8.3. The Assignment of Phase.** As discussed in sections 5.4 and 5.5 and shown explicitly in eq 168, the H- or J-like nature of the charge-transfer interaction depends on the relative sign of  $t_e$  and  $t_h$  through the product  $t_e t_h$ . However, the choice of phase is arbitrary and one may wonder how eq 168 can continue to predict H- and J-aggregate behavior under arbitrary phase changes. For example, in a molecular dimer, changing the phase (sign) of the LUMO of just one of the molecules will result in a sign change of  $t_e$ . According to eq 168, does this mean a conversion between H- and J-aggregate behavior? This obviously cannot be the case; the system physics must be invariant to phase assignment. During their investigation of polythiophene dimers, Yamagata et al.<sup>223</sup> showed that the choice of phase does not impact the photophysics of the system so long as it is consistently applied. However, the issue of phase can be confusing and thus warrants a brief discussion; in this

section, we will continue to use the ethylene dimer as an illustration.

Figure 82 shows the local molecular orbitals of an ethylene dimer where the phase of each individual molecular orbital has

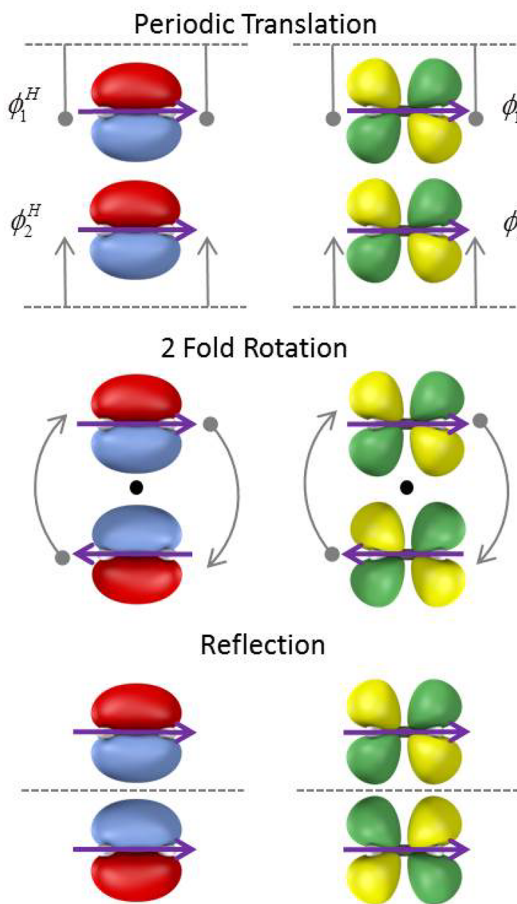


**Figure 82.** (left) HOMOs and (right) LUMOs of ethylene monomers in a dimer configuration. The relative phases of the individual molecular orbitals were assigned according to the given symmetry operation. The transition dipole moments are indicated by purple arrows. Note that the  $C_2$  phase assignment is unconventional since the symmetric exciton ( $k = 0$ ) is optically dark.

been assigned according to a specific symmetry operation as indicated. In the top panel, the phases of the HOMOs and LUMOs have been chosen so that the system is symmetric under periodic translation

$$\hat{T}\phi_1^{H(L)} = \phi_2^{H(L)} \quad (178)$$

where  $\hat{T}$  is the translation operator. With this choice of phase, the HOMOs and LUMOs are in an antibonding configuration resulting in a negative  $t_h$  and positive  $t_e$ . (Recall the definitions of the CT integrals in eqs 155 and 156.) Thus, according to eq 168,  $J_{CT} > 0$  whenever  $E_{CT} > E_{S_p}$ . Furthermore, the molecular transition dipole moments  $\mu_1$  and  $\mu_2$  with  $\mu_n \equiv \langle \phi_n^H | -e\mathbf{r} | \phi_n^L \rangle$  are aligned (see the purple arrows in Figure 82) and hence add constructively in the “bright”  $k = 0$  exciton,  $\{|\phi_1^H \phi_1^L\rangle + |\phi_2^H \phi_2^L\rangle\}/\sqrt{2}$ , which resides at the top of the band because  $J_{CT} > 0$ . Conversely, the dark  $k = \pi$  exciton,  $\{|\phi_1^H \phi_1^L\rangle - |\phi_2^H \phi_2^L\rangle\}/\sqrt{2}$ , resides at the bottom of the band. Accordingly, in the eclipsed geometry shown in the figure, the CT interaction induces H-aggregate photophysical behavior.

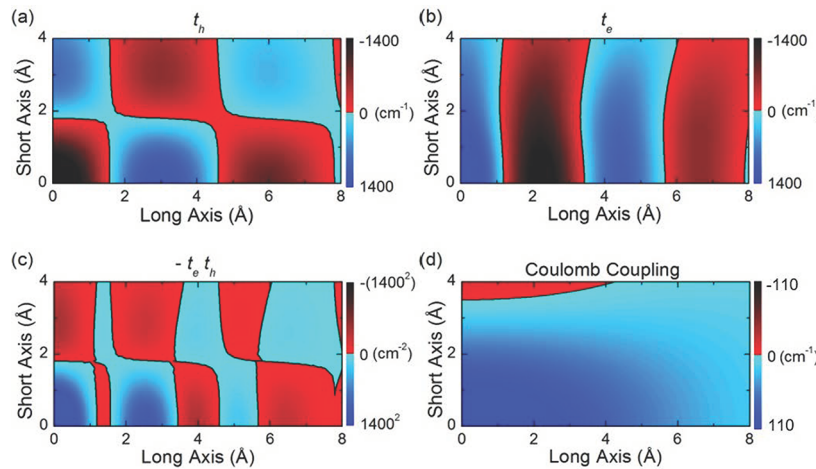


**Figure 83.** (a)  $t_h$  and (b)  $t_e$  within a  $\pi$ -stacked tetracene dimer (3.74 Å stacking distance) as a function of short- and long-axis displacements. (c) The product  $-t_e t_h$  ( $\propto J_{\text{CT}}$ ) and (d)  $J_C$  as a function of short- and long-axis displacements. Red regions indicate a negative coupling (J-aggregation), and blue regions indicate a positive coupling (H-aggregation). CT integrals and Coulomb couplings were computed as in Figure 79. The phase convention is also the same as in Figure 79.

Consider now a different assignment of phase exploiting the 2-fold rotational symmetry demonstrated in the middle panel of Figure 82. In this case, the phase of the MOs is determined by a rotation about the axis indicated by the black dot

$$\hat{C}_2 \phi_1^{\text{H(L)}} = \phi_2^{\text{H(L)}} \quad (179)$$

where  $\hat{C}_2$  is the 2-fold rotation operator. With this choice of phase, the HOMOs are in a bonding configuration and the LUMOs are in an antibonding configuration resulting in positive signs for both  $t_h$  and  $t_e$ . Thus,  $J_{\text{CT}} < 0$  whenever  $E_{\text{CT}} > E_{S_i}$  (see eq 168), opposite in sign to the previous case where phase was based on translation symmetry. However, we still have an H-aggregate because under the present ( $C_2$ ) phase convention, the transition dipole moments are antiparallel in the symmetric exciton  $\{|\phi_1^{\text{H}}\phi_1^{\text{L}}\rangle + |\phi_2^{\text{H}}\phi_2^{\text{L}}\rangle\}/\sqrt{2}$ , which is therefore dark and lowest in energy (because  $J_{\text{CT}} < 0$ ), whereas the antisymmetric exciton  $\{|\phi_1^{\text{H}}\phi_1^{\text{L}}\rangle - |\phi_2^{\text{H}}\phi_2^{\text{L}}\rangle\}/\sqrt{2}$  is bright and highest in energy. Hence, the choice of phase has absolutely no impact on photophysics. Before continuing, we note that phase assignments like those determined by  $C_2$  are unconventional in the sense that the symmetric exciton ( $k = 0$ ) is optically dark, due to the occurrence of antiparallel dipole moments. They are therefore inconsistent with the usual phase convention for defining J and H-aggregates and not typically used.

Finally, in the bottom panel of Figure 82, the phase is chosen based on reflection symmetry about the mirror plane separating the two molecules

$$\hat{R} \phi_1^{\text{H(L)}} = \phi_2^{\text{H(L)}} \quad (180)$$

where  $\hat{R}$  is the reflection operator. With this choice of phase, the HOMOs and LUMOs are in bonding configurations resulting in a positive value for  $t_h$  and negative value for  $t_e$ . Thus,  $J_{\text{CT}} > 0$  whenever  $E_{\text{CT}} > E_{S_i}$  (see eq 168). Because the transition dipole moments are aligned and parallel under reflection, the symmetric exciton is bright, and the antisymmetric exciton is dark. Because  $J_{\text{CT}} > 0$ , the symmetric exciton resides at the top of the band (see eq 170), resulting in H-aggregate behavior. Hence, in all three phase conventions described above, the charge-transfer interactions induce H-like

behavior at the eclipsed geometry (assuming  $E_{\text{CT}} > E_{S_i}$ ). The phase convention has no impact on the physical properties.

**5.8.4. Comparing the Geometric Dependencies of  $J_{\text{CT}}$  and  $J_C$ .** The competition between the Coulomb and CT (superexchange) couplings discussed in section 5.6 depends sensitively on the packing geometry. The geometric dependence of  $J_C$  is less sensitive to the molecular details of the system; according to Kasha,  $J_C$  induces H-like photophysics when the molecular transition dipole moments are parallel and side-by-side and J-like photophysics when the molecular transition dipole moments are parallel and head-to-tail. Importantly, the sign of  $J_C$  changes only once as the molecules are displaced from an eclipsed geometry to a head-to-tail geometry. When molecules are separated by lengths much greater than the size of the molecule (or, more accurately, the spatial extent of the transition dipole moment), the point-dipole approximation is valid, and the sign of  $J_C$  changes when  $\theta$  in Figure 1 goes through the “magic angle” of roughly 54 degrees. For intermolecular distances consistent with  $\pi$ -stacking ( $\sim 3\text{--}4$  Å), the sign change occurs at displacements of approximately half the molecular length.<sup>127,263,271</sup> On the other hand, the geometric dependence of  $J_{\text{CT}}$  depends sensitively on the molecular details and can undergo several sign changes upon long- and short-axis slips and even rotational displacements.<sup>227,228,238</sup> Such sign changes often correspond to packing displacements on the order of a bond length, which is usually much smaller than half the molecular length. The different length scales of interconversion between J- and H-like behavior for  $J_C$  and  $J_{\text{CT}}$  facilitate a rich phase space of interferences that can be exploited to control the total exciton coupling via crystal engineering. As discussed in section 5.7, such engineering could result in improved exciton mobility and more efficient solar cells, as one example.

The contour plots in Figure 79e and f illustrate the geometric dependencies of  $J_C$  and  $-t_e t_h$  for perylene  $\pi$ -stacks as a function of long- and short-axis displacements. (Recall from eq 168 the dependence of  $J_{\text{CT}}$  on  $-t_e t_h$ .) Blue regions of the plots indicate H-like interactions where the couplings are positive whereas red regions indicate J-like (negative) interactions. For  $J_{\text{CT}}$ , the sign assignment further assumes, as usual, that  $E_{\text{CT}} > E_{S_i}$ , see eq 168, and the normal phase convention in which the symmetric

exciton ( $k = 0$ ) carries the oscillator strength, see top of Figure 82). As can be appreciated from the figure, the nature of the Coulombic coupling is relatively insensitive to changes in packing geometry. A longitudinal displacement of more than 5 Å from the totally eclipsed geometry is required to convert the coupling from H- to J-like (the transition dipole moment of perylene is parallel to the long axis). Short-axis displacements lead to a reduction in the magnitude of  $J_C$ , but the sign remains unchanged. In comparison, the product  $-t_e t_h$ , which determines the H- or J-like nature of the CT-induced coupling, is far more sensitive to changes in the packing structure; from the eclipsed geometry, displacements of  $\sim 1.6$  Å along either the long or short axis convert the coupling from H- to J-like. Additional sign changes are observed at further displacements due to the nodal structures of  $t_e$  and  $t_h$  (see Figure 79a and b).

As a comparison, the contour plots in Figure 83 show how the Coulomb and CT-mediated couplings depend on the packing geometry in  $\pi$ -stacked tetracene systems. (Note that the phase convention used to determine the sign of  $t_e$  and  $t_h$  in Figure 83 is consistent with parallel transition dipole moments in the symmetric exciton, as in Figure 79, whereas in Figure 78, the phase convention is consistent with antiparallel transition dipole moments; importantly, the J- or H-like photophysical behavior is entirely independent on the choice of phase, see section 5.8.3 for further discussion.) In tetracene, the  $S_0 \rightarrow S_1$  transition dipole moment is parallel to the short molecular axis leading to a single sign change in  $J_C$  upon a short-axis displacement of  $\sim 3.5$  Å and no sign change at all for long-axis displacements. Overall, the Coulombic coupling in tetracene is relatively weak (compare with perylene in Figure 79) and insensitive to changes in packing geometry, and H-like interactions are expected at most geometries. On the other hand, the CT-mediated coupling dictated by  $-t_e t_h$  shows several variations in sign as a function of geometry. Notably, the contour plot of  $-t_e t_h$  exhibits a very different geometric dependence than was found in perylene due to the different nodal structures of  $t_e$  and  $t_h$  in the two systems (compare Figure 79a and b and Figure 83). Interestingly, in tetracene the signs of  $t_e$  and  $t_h$  change nearly simultaneously at longitudinal displacements of approximately 1.3 and 7.9 Å, leading to regions of H- or J-like behavior of varying size, as opposed to the more regular variations observed in perylene. The different geometric dependencies of  $J_{CT}$  between perylene and tetracene highlights the sensitivity of  $J_{CT}$  to molecular details.

It is also interesting to consider how rotational displacements impact the competition between the Coulomb and charge-transfer couplings because many  $\pi$ -stacked systems are helical or form crystals in which the molecules comprising the unit cell are twisted relative to each other.<sup>37,75,131,229,394,500</sup> According to the point-dipole approximation (eq 1),  $J_C$  will be at a maximum when two molecules are side by side with parallel dipole moments and diminish to zero as the molecules are rotated 90 degrees about the axis connecting their centers. More detailed calculations give qualitatively similar results.<sup>219,265</sup> On the other hand, the behavior of  $t_e$ ,  $t_h$ , and  $J_{CT}$  will depend on the details of the molecules involved. Ide et al.<sup>240</sup> and Hestand and Spano<sup>227</sup> investigated how the CT integrals depend on the twist angle  $\theta$  for two  $\pi$ -stacked perylene chromophores with  $\theta = 0$  corresponding to an eclipsed configuration. Figure 84 shows how the relevant quantities,  $t_e$ ,  $t_h$ ,  $J_{CT}$ , and  $J_C$  change as a function of  $\theta$ . As expected,  $J_C$  is H-like when the molecules are parallel and diminishes to zero as the molecules are rotated to 90 degrees. The electron and hole integrals are far more

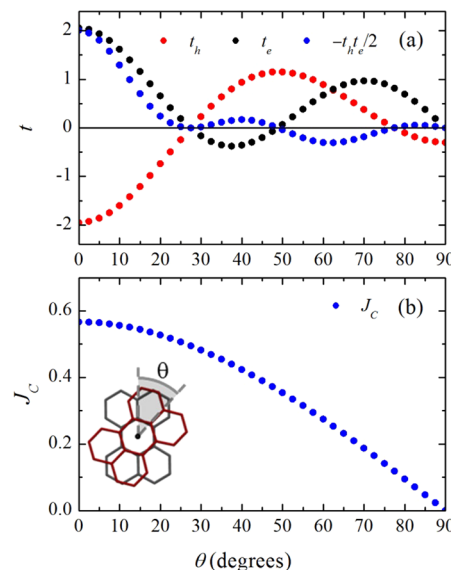


**Figure 84.** (a) The electron and hole transfer integrals as well as the product  $-t_e t_h / 2 (\propto J_{CT})$  within a perylene dimer as a function of relative rotation. (b) The Coulomb coupling as a function of rotation. In both cases, the  $\pi$ -stacking distance is 3.5 Å, and all energies are expressed in units of 1400 cm<sup>-1</sup>. Adapted with permission from ref 227. Copyright (2015), AIP Publishing.

sensitive to  $\theta$  as they depend on wave function overlap. The associated charge-transfer coupling  $J_{CT}$  is H-like when the molecules are eclipsed, assuming  $E_{CT} > E_{S_1}$  (see eq 168) but is driven to zero at a critical angle of  $\sim 28$  degrees. At this angle, both  $t_h$  and  $t_e$  go to zero, effectively shutting off charge-transfer and creating an aggregate driven entirely by Coulombic couplings, i.e., an ideal Kasha aggregate. Such behavior is manifest in the conventional H-aggregate spectrum measured by Sarbu et al.<sup>81</sup> in helical  $\pi$ -stacks of a perylene bisimide derivative. Beyond the critical angle, the CT integrals maintain their opposite phases so that  $J_{CT}$  remains H-like. This continues until  $\sim 50$  degrees, whereupon only  $t_e$  changes sign, finally forcing  $J_{CT}$  to become negative or J-like until  $\theta$  reaches 78 degrees, at which point there is another sign change in  $J_{CT}$ . Hence, the competition between Coulomb and charge-transfer couplings can also be tuned via molecular rotations.

As observed for both perylene and tetracene, the Coulomb and CT-mediated couplings change sign on different length scales. Hence, both constructive and destructive interference between  $J_C$  and  $J_{CT}$  are possible, and in principle, the total coupling can be tuned via the packing geometry. To date, control over the packing structure has been achieved through chemical tuning of the side chains<sup>77,441,500–502</sup> and covalent linking using variable length spacer groups.<sup>34,35,141,453</sup> Mechanical techniques have also been used; Giri et al. demonstrated a reduction in the  $\pi$ -stacking distance in 6,13-bis(triisopropylsilylethynyl) (TIPS) pentacene by 0.2 Å using a solution-shearing technique,<sup>503</sup> and more recently, Molina-Lopez et al. demonstrated control over the packing geometry in TIPS pentacene and 2,7-diethyl [1] benzothieno [3,2-*b*] [1] benzothiophene (C8-BTBT) using dielectrophoresis coupled with solution shearing.<sup>504</sup> Admittedly, control over the packing geometry is still a challenging goal, but continuing advances in the aforementioned areas and in the field of self-assembly<sup>505</sup> should hopefully lead to more precise control in the near future.

## 5.9. Generalized J- and H-Aggregates: Selected Examples

So far in section 5 we have discussed, largely theoretically, how intermolecular charge transfer impacts the photophysics of tightly packed  $\pi$ -stacked molecular aggregates and crystals. In the current section, we provide some real-world examples, including (1) the H- to J-aggregate transformations observed for several perylene-based systems,<sup>76,81,241,506,507</sup> (2) the HJ-aggregate nature of 7,8,15,16-tetraazaterrylene (TAT),<sup>225</sup> (3) the enhanced Davydov splitting observed in *N,N'*-bis(3-pentyl)-perylene-3,4,9,10-bis(dicarboximide) (B2) crystals,<sup>229</sup> and (4) the photophysics of oligoacene crystals. The first three examples highlight the competition between the Coulomb and CT-mediated (superexchange) coupling as well as the sensitivity of the CT interactions to slight (subangstrom) changes in the packing geometry. In crystalline tetracene and pentacene, considered separately in section 5.10, the photophysics and transport properties are dominated by CT interactions due to the relatively weak Coulombic coupling derived from the short-axis polarized  $S_0 \rightarrow S_1$  transition. However, even without Coulomb coupling, the H- and J-aggregate behavior inherent to the CT-mediated coupling is clearly present.

**5.9.1. H- to J-Aggregate Transformations.** An illustration of the interplay between Coulombic and CT-mediated interactions is provided by the so-called H- to J-aggregate transformation observed by Yagai et al. and Sarbu et al. in systems based on hydrogen bonding perylene derivatives.<sup>76,81</sup> In Yagai's experiments (see Figure 85a), a reversible trans-

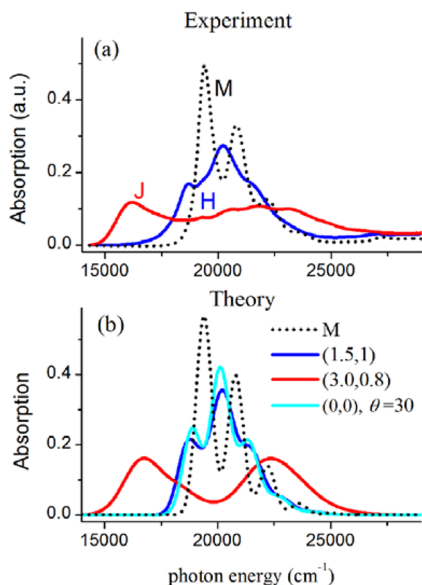


**Figure 85.** (a) Measured absorption spectrum of the monomer (M), J- and H-aggregate forms of the perylene derivatives from ref 76. (b) The corresponding simulations from ref 227. The coordinates in the legends correspond to the potential energy minima in Figure 86. Reprinted with permission from ref 227. Copyright (2015), AIP Publishing.

formation between H- and J-forms was observed upon changing the molar ratio between the perylene derivative and a hydrogen bonding complexing agent. Complexation results in changes to the intermolecular hydrogen bonding patterns and the molecular packing structure between adjacent perylene molecules.<sup>76</sup> In Sarbu's experiments, a reversible H- to J-

aggregate transformation was achieved by thermal annealing and contact with an organic nonsolvent. As in the experiments of Yagai, the transformation derives from a reorganization of the hydrogen bonding patterns and molecular packing structure.<sup>81</sup> For both systems, the absorption spectrum of the H-form is characterized by a single absorption band with well-pronounced vibronic structure. The vibronic ratio  $R_{\text{abs}}$  is clearly diminished in the H-complex compared to the monomer in solution, as is typical of H-aggregates (see section 4.2). In marked contrast, the absorption spectrum of the J-form is comprised of two broad, featureless bands (see Figure 85a) with the low-energy band very strongly red-shifted by  $\sim 3000 \text{ cm}^{-1}$  from the main absorption peak in the monomer. The large red shift was the main reason for identifying the complex as a J-aggregate by the authors of refs 76 and 81. The two-band line-shape is, however, the hallmark signature of CT-mediated J-aggregation in the Frenkel/CT resonance regime, as described in section 5.5. The red-shift derives from the mixing between (diabatic) Frenkel and CT excitons induced by a strong in-phase relationship between  $t_e$  and  $t_h$  and has virtually nothing to do with Coulombic coupling.

The H- and J-aggregate spectra measured by Yagai (see Figure 85a) were simulated in ref 227 based on geometries that minimize the ground state energy of a perylene bisimide dimer according to DFT calculations by Fink et al.,<sup>458</sup> see Figure 86.

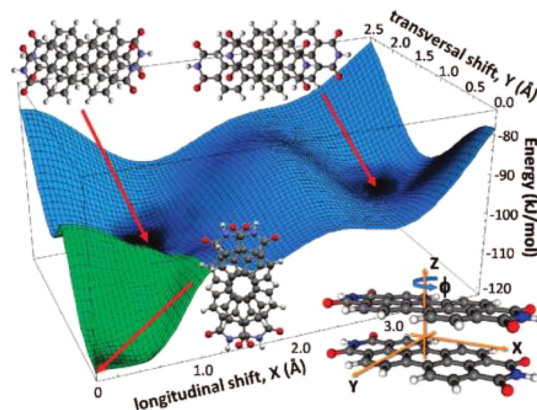


**Figure 86.** Computed potential energy surface of a  $\pi$ -stacked perylene dimer. Reprinted with permission from ref 458. Copyright (2008), American Chemical Society.

The simulated spectra are shown in Figure 85b and capture all of the salient features that appear in the measured spectra. The spectrum of the H-form was found to be consistent with two of the three minima predicted by Fink et al.,<sup>458</sup> a local minimum corresponding to a slightly offset parallel packing arrangement at (1.5 Å, 1 Å), where the first (second) entry indicates the long-axis (short-axis) offset and the global minimum corresponding to a relative twist of  $\sim 30^\circ$  about the  $\pi$ -stacking axis (see Figure 86). At both minima, the CT-mediated coupling is negligible (see Figures 79 and 84) and the photophysics are dominated by the H-like Coulomb coupling. Conversely, the J-form was found to be consistent with the third minimum predicted by Fink et al.,<sup>458</sup> a slip-stacked orientation defined by (3.0 Å, 0.8 Å), where the large in-phase values for  $t_e$  and  $t_h$  promote strong CT-mediated coupling, giving rise to the observed two-band J-aggregate absorption spectrum (see section 5.5). Although the geometry of the J-form differs from the slipped H-form by a longitudinal displacement of only

1.5 Å, it is enough to dramatically change the nature of the charge-transfer interaction. It is worth noting that Coulomb coupling alone predicts H-aggregate behavior at all three minima (see Figures 84 and 79f), underscoring the importance of incorporating charge-transfer excitations for these closely packed systems.

The geometries of the H- and J-aggregate forms predicted in ref 227 correlate well to observations made in similar systems by other groups. For example, Gregg and Kose<sup>241</sup> discovered a reversible transformation between a black phase and red phase of a perylene diimide liquid crystal upon exposure to water vapor. The spectrum of the red phase (so-called due to strong absorption between 450 and 500 nm) strongly resembles the H-form spectrum measured by Yagai et al.<sup>76</sup> and Sarbu et al.,<sup>81</sup> whereas the spectrum of the black phase is strikingly similar to the J-form spectrum. Importantly, using X-ray diffraction, Gregg and Kose measured a translational packing displacement of 1.6 Å between the red and black phases, consistent with 1.5 Å difference between H- and J-aggregate geometries proposed in ref 227. Moreover, Gregg and Kose assigned the transitions associated with the red phase (H-form) as arising mainly from Frenkel excitons and those associated with the black phase (J-form) as arising from mixed Frenkel/CT excitons, in agreement with the analysis in ref 227.

Other H-to J-transformations have been observed by Mizuguchi and Tojo<sup>506</sup> and more recently by Lambrecht et al.<sup>507</sup> Mizuguchi and Tojo observed a color change from red to black in a perylene (PB31) film after deposition via evaporation and subsequent thermal annealing. Though this transformation was not reversible, the spectra associated with the red (H) and black (J) phase are remarkably similar to the spectra of the H- and J-aggregate forms of Yagai and Sarbu (see Figure 87). Lambrecht et al. observed a reversible color change from red to

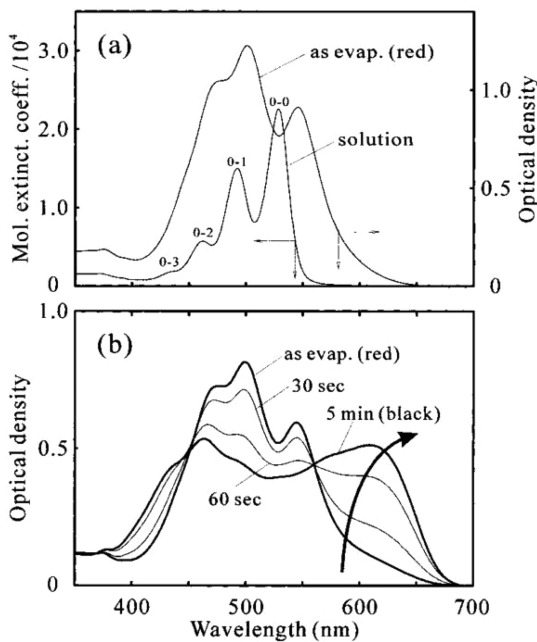


**Figure 87.** Irreversible H- to J-aggregate transformation in the perylene derivative PB31. (a) The solution spectrum and H-like spectrum of the film as deposited. (b) Thermal annealing at 100 °C facilitates transformation to a new species that exhibits a J-like spectrum. Reprinted with permission from ref 506. Copyright (2002), American Chemical Society.

black in perylene-based nanowires depending on the composition of the atmosphere; in air, the perylene nanowires exhibited a red color (H), whereas under solvent atmosphere, the nanowires exhibited a black color (J). Remarkably, the nanowires also showed self-healing behavior (due to packing rearrangement) when exposed to solvent vapor, underscoring the correlation between changes in the packing structure and the absorption spectrum. We anticipate that color changes in the experiments of both Mizuguchi and Tojo and Lambrecht et al. are due to changes in the nature of the charge-transfer interaction because the J-forms are associated with a two-band absorption line shape, whereas the H-forms are associated with single band line shapes. The two-band absorption line shape is a unique characteristic of charge-transfer J-aggregation that is not observed in Coulombically coupled linear aggregates.

**5.9.2. TAT Nanopillars.** Strong evidence of destructively interfering Coulombic and CT-mediated couplings was obtained for crystalline nanopillars of 7,8,15,16-tetraazaterrylene (TAT),<sup>225</sup> a material introduced by Briseno and Wudl as an efficient electron acceptor for OPV applications.<sup>463,508</sup> The absorption spectrum of TAT, shown in Figure 88a, exhibits a

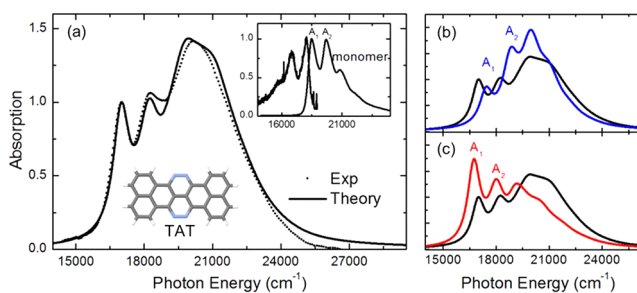


**Figure 88.** Experimental and simulated absorption spectrum of TAT from ref 225. Adapted with permission from ref 225. Copyright (2017), American Chemical Society.

s somewhat merged, two-band structure with a red-shifted absorption origin and blue-shifted absorption maximum compared to the monomer. Such behaviors are characteristic of J- and H-aggregates, respectively, suggesting that both J- and H-like couplings are simultaneously present within the crystal. Moreover, the vibronic ratio  $R_{\text{abs}}$ , introduced in section 4.2, is essentially unchanged with respect to the monomer, suggesting a destructive interference between J- and H-promoting couplings. As described in section 5.6,  $R_{\text{abs}}$  responds to the total coupling,  $J_C + J_{\text{CT}}$ , see for example eq 172; a substantial deviation  $R_{\text{abs}}$  from the monomer signifies a large value for  $|J_C + J_{\text{CT}}|$ , whereas a negligible divergence signifies a negligible net coupling,  $|J_C + J_{\text{CT}}| \ll \omega_{\text{vib}}$ .<sup>225,227,228,238</sup> Moreover, an increase (decrease) in  $R_{\text{abs}}$  indicates overall J-like (H-like) behavior. Because the vibronic ratio in the absorption spectrum of TAT nanopillars does not change relative to the monomer in solution,  $J_C + J_{\text{CT}}$  is likely small.

Within the nanopillars, TAT molecules pack in a slightly offset  $\pi$ -stacked geometry with nearest neighbor molecules aligned parallel to one another.<sup>508</sup> There are two molecules per unit cell giving rise to two translationally inequivalent  $\pi$ -stacks. As illustrated by Yamagata et al., the photophysics of the nanopillars can be modeled as a single  $\pi$ -stack (Figure 88a), indicating that the strongest intermolecular interactions occur between molecules within the same stack.<sup>225</sup> Further support for strong intrastack CT interactions were provided by Labastide et al., who showed that charge separation in TAT

crystals occurs preferentially along the  $\pi$ -stacking axis due to strong intrastack charge transfer.<sup>509</sup> Within a TAT  $\pi$ -stack, the side-by-side packing gives rise to H-like Coulombic interactions, and the slight offset between neighboring molecules facilitates J-like charge-transfer interactions.<sup>225,238</sup> Moreover, calculations reveal that the magnitudes of the two coupling sources are comparable, resulting in an effective destructive interference that suppresses energy transfer.<sup>225,238</sup> TAT is thus classified as an HJ-aggregate.

Panels b and c in Figure 88 illustrate the competition between the two coupling sources and their individual effects on the absorption spectrum. When only the Coulombic coupling is considered (Figure 88b), the spectrum exhibits a one-band, H-like spectrum with a vibronic ratio  $R_{\text{abs}}$  significantly less than that of the monomer. Alternatively, when only the CT interactions are considered (Figure 88b), the spectrum exhibits a J-like two-band line shape (slightly merged) with an absorption ratio  $R_{\text{abs}}$  significantly greater than that of the monomer. Only when both interactions are considered do the simulations reproduce the experimentally measured spectrum (Figure 88a).

Subsequent calculations by Hestand et al. predicted that TAT should exhibit slow exciton transport as a result of the destructively interfering couplings, see section 5.7.<sup>238</sup> They further showed that a short- or long-axis displacement of less than 0.5 Å converts the CT-mediated coupling from J- to H-like while the Coulombic coupling remains H-like; i.e., the aggregate converts from HJ to HH. The resulting constructive interference boosts the exciton velocity from near zero in the HJ case to  $2 \times 10^4$  m/s in the HH case. Such predictions are certainly best-case scenarios as they exclude dephasing due to system–bath interactions and have yet to be experimentally verified in TAT (as there is no straightforward method to induce a small change in crystal packing). Instead of trying to create an HH-aggregate from TAT, a better strategy would be to screen TAT derivatives (or other compounds) for those in which  $R_{\text{abs}}$  in the crystalline absorption spectrum differs substantially from the monomer value.

### 5.9.3. Giant Davydov Splitting in Isopentyl Perylene-bisimide.

Evidence for constructively interfering Coulombic and CT-mediated interactions was recently obtained in crystals of the perylene derivative *N,N'*-bis(3-pentyl)-perylene-3,4,9,10-bis(dicarboximide) (**B2**) by Austin et al.<sup>229</sup> The crystal structure of **B2** consists of four translationally inequivalent  $\pi$ -stacks with the individual  $\pi$ -stacks exhibiting a twisted sandwich structure<sup>510</sup> as depicted in Figure 89. The twisted structure gives rise to two orthogonally polarized transitions that are responsible for the upper and lower Davydov components observed in the polarized absorption spectrum (see Figure 90). As for TAT, the dominant intermolecular interactions occur between nearest neighbor  $\pi$ -stacked molecules.<sup>229</sup> We note that, although TAT has two molecules per unit cell, the weak coupling between inequivalent molecules, which reside in separate  $\pi$ -stacks, results in a negligible Davydov splitting. This is in contrast to **B2** in which two inequivalent molecules are nearest neighbors within the same  $\pi$ -stack, giving rise to an exceptionally large Davydov splitting ( $A_1 - B_1$ ) of approximately  $1230 \text{ cm}^{-1}$ . The maximum-to-maximum ( $A_1 - B_2$ ) splitting is even larger,  $\sim 3040 \text{ cm}^{-1}$ , and is responsible for the vivid pleochromism observed in **B2**.<sup>229</sup> Similarly, large Davydov splittings have recently been observed in aniline squaraine dyes.<sup>352</sup>

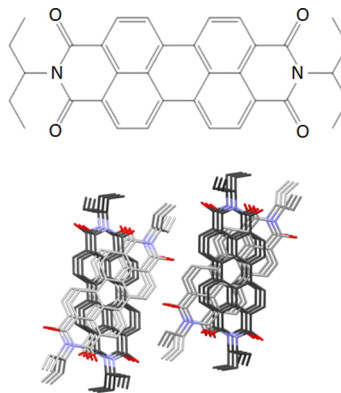


**Figure 89.** (top) Molecular structure of **B2**. (bottom) **B2** crystal packing as viewed along the  $\pi$ -stacking axis. Only two of the four translationally inequivalent stacks are shown.

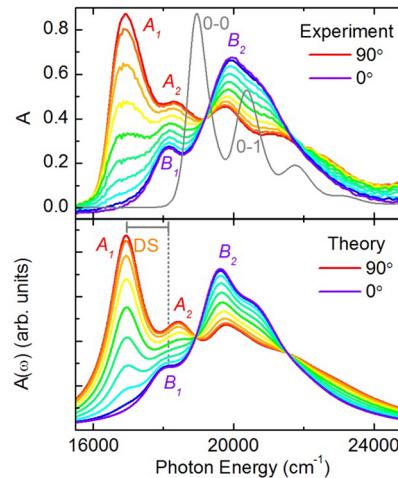


**Figure 90.** (top) The experimentally measured polarized **B2** spectrum and (bottom) simulated **B2** spectrum in 10 degree increments. Note that the solution spectrum (gray) has been normalized to the  $A_1$  peak. Reprinted with permission from ref 229. Copyright (2017), American Chemical Society.

The simulated polarized spectra in the bottom panel of Figure 90 are based on the full Frenkel/CT Holstein Hamiltonian in eq 158 with structural parameters deduced from structural analysis. The simulations include the full extended range of (screened) Coulomb couplings as well as a nonperturbative treatment of Frenkel/CT mixing, see ref 229 for more details. Further analysis revealed that the Davydov splitting results from a constructive interference between the Coulombic and CT-mediated couplings.<sup>229</sup> This is illustrated in Figure 91a–c, which compares the simulated spectra to experimental results when the coupling sources are alternatively turned off. When only Coulombic interactions are considered (Figure 91b), the simulations predict a Davydov splitting of  $\sim 500 \text{ cm}^{-1}$ . Alternatively, when only CT-mediated interactions are retained (Figure 91c), the simulations predict a Davydov splitting of  $910 \text{ cm}^{-1}$ . Hence, when either coupling source is neglected, the simulations predict a considerably smaller Davydov splitting than the experimentally measured value of  $1230 \text{ cm}^{-1}$ . Only when both sources are included is the Davydov splitting quantitatively reproduced by the simulations.

The large Davydov splitting in **B2** is a manifestation of the more general competition between Coulomb and CT-mediated

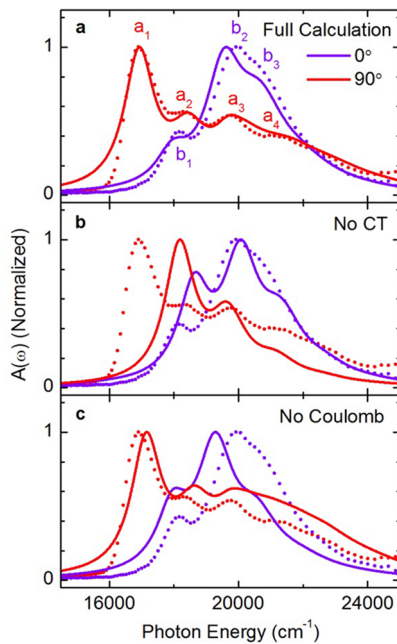


**Figure 91.** (a) The simulated (solid lines) B2 upper and lower Davydov components are compared directly to experiment (dots). (b) The simulations compared to experiment when charge transfer is neglected. (c) The simulations compared to experiment when Coulomb interactions are neglected. Reprinted with permission from ref 229. Copyright (2017), American Chemical Society.

couplings occurring in a linear aggregate or  $\pi$ -stack with two molecules per unit cell. This competition can be easily appreciated by taking the perturbative limit for CT-mediated coupling (i.e., by using  $J_{\text{CT}}$  from eq 168) and considering only nearest neighbor Coulomb coupling,  $J_{\text{C}}$ . In this simplified picture, the free exciton band dispersion is described in eq 171 with the Davydov components given by the  $k = 0$  and  $k = \pi$  excitons, see section 4.6. (In the more conventional molecular crystal approach, both Davydov components have  $k = 0$  but correspond to symmetric and antisymmetric combinations of the unit cell molecular excitations.) The Davydov splitting, defined as the energetic difference between the  $k = 0$  and  $k = \pi$  excitons, is then simply given by  $4|J_{\text{C}} + J_{\text{CT}}|$  in the absence of vibronic coupling. Hence, when the Coulombic and CT-mediated couplings interfere constructively, as in B2, the Davydov splitting is enhanced. Alternatively, opposite signs for  $J_{\text{CT}}$  and  $J_{\text{C}}$  result in destructive interference, which reduces the Davydov splitting; in the most dramatic case, the DS can vanish if  $J_{\text{C}} + J_{\text{CT}} = 0$  despite large individual couplings.

Other interesting features of the polarized B2 spectra involve the vibronic signatures of the upper and lower Davydov components. The lower Davydov component, polarized at  $90^\circ$  to the long crystal axis, exhibits signatures of J-aggregation including an increased  $A_1/A_2$  ratio relative to the monomer, whereas the upper Davydov component, polarized at  $0^\circ$ , exhibits signatures of H-aggregation including a decreased  $B_1/B_2$  ratio relative to the monomer. Similar vibronic signatures have been noted for Scheibe aggregates,<sup>165</sup> see section 4.6 as well as for crystalline pentacene<sup>224,226</sup> as described in the following section. Kistler et al showed that, for Coulombically coupled systems with two molecules per unit cell, the lower Davydov component will always display J-aggregate signatures and the upper Davydov component will always display H-aggregate signatures so long as the coupling between

inequivalent molecules is larger (in magnitude) than the coupling between equivalent molecules.<sup>309</sup> Kistler's result can be generalized for systems exhibiting both Coulombic and CT-mediated interactions by replacing the Coulombic coupling between inequivalent molecules with the total coupling between inequivalent molecules.

### 5.10. The Oligoacenes

Over the past several years, the oligoacene series and derivatives thereof have received considerable attention as promising materials for electronic and solar cell applications.<sup>511–517</sup> The oligoacenes have also served as benchmark materials for singlet fission,<sup>446,447,450–452,518–540</sup> a process which has the potential to substantially increase the efficiency of solar cells.<sup>444</sup> Superradiance from anthracene<sup>345</sup> and tetracene<sup>344,370,371,541</sup> has also been observed. In this section, we briefly review the absorption and photoluminescence spectra of anthracene, tetracene, and pentacene and discuss their spectral signatures within the context of J- and H-aggregation.

The oligoacenes pack in a herringbone motif with two translationally inequivalent molecules per unit cell as demonstrated in Figure 92 for triclinic pentacene. The

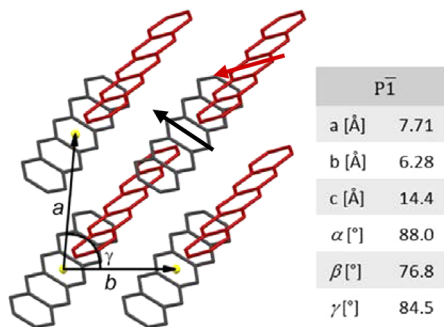


**Figure 92.** (left) Crystal packing in triclinic pentacene as viewed down the  $c$ -axis. The sublattices are colored differently for easier viewing. The short-axis polarized transition dipole moments are also indicated. (right) The unit cell parameters. Note that the  $b$ -axis is defined to be the axis containing the closest neighbors. Reprinted with permission from ref 226. Copyright (2015), American Chemical Society.

photophysics of herringbone aggregates were considered in section 4.7. However, unlike the chromophores treated in section 4.7, the  $S_0 \rightarrow S_1$  transition dipole moment in the oligoacenes is oriented along the short molecular axis, as indicated in Figure 92, and is comparatively weak. The two molecules in the unit cell give rise to two orthogonally polarized optical transitions, the upper and lower Davydov components, for excitation normal to the ( $ab$ ) herringbone plane. In the oligoacenes, the lower Davydov component is polarized mainly parallel to the crystalline  $b$  axis (the axis that includes the closest neighbors), whereas the upper Davydov component is polarized mainly perpendicular to the crystalline  $b$  axis. Interestingly, the Davydov splitting (DS) increases with increasing oligoacene length:  $\sim 200 \text{ cm}^{-1}$  in anthracene,<sup>542,543</sup>  $\sim 630 \text{ cm}^{-1}$  in tetracene,<sup>369,544</sup>  $\sim 1100 \text{ cm}^{-1}$  in pentacene,<sup>226,545,546</sup> and  $\sim 1400 \text{ cm}^{-1}$  in hexacene.<sup>547</sup> Larger Davydov splittings involving higher-energy transitions have also been observed; most notably, a DS of  $\sim 3500 \text{ cm}^{-1}$  has been measured in norbornyl-bridged tetracene dimers due to the long-axis polarized  $S_0 \rightarrow S_3$  transition.<sup>537,538</sup>

Because of the important role CT states play in singlet excitation fission,<sup>239,445–454,523,536</sup> renewed interest has arisen

concerning the nature of the excited state responsible for the absorption origin (the lower Davydov component), especially in pentacene,<sup>527</sup> which displays the greatest fission rate. Thus far, theoretical predictions fall into several categories: those that support (1) a state with dominant CT character,<sup>548–550</sup> (2) a state with minor CT character (10–30%),<sup>527</sup> (3) a state with negligible CT character,<sup>533</sup> and (4) a state with a roughly even admixture of CT and Frenkel character.<sup>224,226,239,450,536</sup> Recent, strong support for (4) comes from detailed analyses of the absorption spectral line shapes of thin pentacene films.<sup>226,239,450,536</sup> Convincing experimental evidence for substantial Frenkel/CT mixing also comes from measurements of the exciton band dispersion using electron energy loss spectroscopy by Knupfer and co-workers.<sup>551,552</sup>

In contrast to the OTn and OPVn aggregates discussed in section 4.7 and the B2 crystals discussed in section 5.9.3, and in accordance with the conclusions reached in refs 224, 226, 239, and 450, Frenkel/CT mixing induced by substantial in-phase electron and hole transfer integrals between nearest neighbor chromophores drives the Davydov splitting in tetracene and pentacene. Only in anthracene is the Coulomb coupling competitive. Accordingly, the exciton responsible for the *b*-polarized origin in the UV-vis spectrum maintains 10–15% CT character in anthracene, 25–30% CT character in tetracene,<sup>224,450,536</sup> and near 50% CT character in pentacene. Hence, oligoacene crystals are expected to behave like the linear CT H- and J-aggregates of section 5.4 and 5.5 but with additional complexity arising from crystal packing with two molecules per unit cell.

Petelenz et al. was the first to recognize the importance of Frenkel/CT mixing in the oligoacenes, arguing that Coulombic coupling alone was insufficient for obtaining the DS.<sup>209</sup> This represented a strong departure from the commonly perceived view at the time that the DS was entirely due to Coulomb coupling, supported by extensive theoretical calculations of Schlosser and Philpott,<sup>276</sup> who invoked interband exciton coupling and fictitious high energy states (for pentacene) to achieve reasonable agreement with experimental results. In addition, they used unscreened Coulomb couplings, which overestimate the actual couplings by a factor of 2 or 3 given a dielectric (screening) constant of  $\sim 3$ . However, by introducing Frenkel/CT mixing, one can obtain excellent agreement with experimental results using properly screened Coulombic potentials and without having to introduce extra Frenkel exciton bands.<sup>224,226,239</sup> As the  $\pi$ -conjugation size of the oligoacene increases, the resulting decrease (increase) in the molecular ionization potential (electron affinity) lowers the Frenkel/CT energy gap from  $\sim 0.4$  eV in anthracene<sup>553</sup> to 0.29 eV in pentacene,<sup>554</sup> resulting in larger Frenkel/CT mixing and a concomitant increase in the DS.

A quantitative account of the DS as well as the polarized absorption spectral line shapes requires not only Frenkel/CT exciton mixing but also local vibronic coupling involving the prominent  $\sim 1200$ –1400 symmetric stretching mode. This was accomplished in refs 224, 226, 239, and 536 by using the Frenkel/CT Holstein Hamiltonian represented in a one- and two-particle basis set and by Berkelbach and Reichman using a similar Hamiltonian with a Redfield approach to account for system–bath interactions.<sup>450–452</sup> Figure 93 shows the measured and calculated absorption spectra of crystalline pentacene taken from ref 226. Also shown is the solution spectrum displaying the pronounced vibronic progression from the symmetric stretching mode. Although both Coulombic coupling and

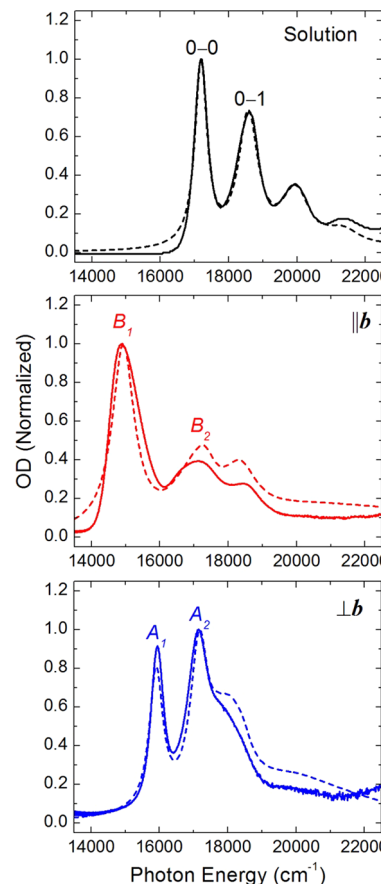


**Figure 93.** Absorption spectrum of (top) pentacene in solution and crystalline pentacene polarized (middle) parallel to *b* and (bottom) perpendicular to *b*. Experimental spectra are shown as solid lines, and simulations are shown as dashes. Reprinted with permission from ref 226. Copyright (2015), American Chemical Society.

Frenkel/CT exciton mixing are included in the simulated spectra, a more detail analysis reveals that Frenkel/CT mixing is primarily responsible for the strong deviations in the absorption line shape upon crystallization and especially the ( $A_1$ – $B_1$ ) DS of  $\sim 1000$  cm<sup>−1</sup>. Similarly accurate reproductions of the absorption spectra for anthracene and tetracene have also been obtained using the same theoretical approach.<sup>224</sup>

In the oligoacenes, electroabsorption experiments place the charge-transfer excitons higher in energy than the Frenkel excitons,<sup>553,554</sup> the latter of which possesses the bulk of the oscillator strength when  $k = 0$ . The mixing between the (diabatic) Frenkel and CT excitons is indicated in Figure 94. Because the HB lattice hosts two molecules per unit cell, there are symmetric (+) and antisymmetric (−) excitons with  $k = 0$ ; the Frenkel states  $|FE\rangle_{k=0,+}$  and  $|FE\rangle_{k=0,-}$  derive from neutral excitations, whereas  $|CTE\rangle_{k=0,+}$  and  $|CTE\rangle_{k=0,-}$  derive from charge-transfer excitons. The symmetry is defined with respect to an operation that takes one sublattice of translationally equivalent molecules into the other. For example, in a monoclinic unit cell, the two sublattices are related by a 2-fold screw rotation along the *b*-axis, see ref 224 for a more detailed discussion. Accordingly,  $|FE\rangle_{k=0,+}$  absorbs *b*-polarized light, whereas  $|FE\rangle_{k=0,-}$  absorbs light polarized perpendicular to *b*. The symmetry operation also determines the phases of the electron and hole transfer integrals,  $t_e$  and  $t_h$ , as well as the sign of the Coulombic coupling, all of which must be assigned

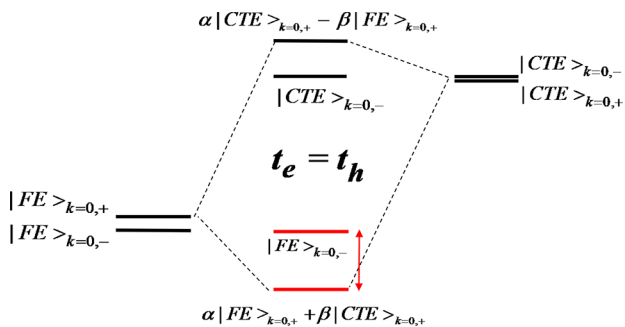


**Figure 94.** Approximate energy level diagram demonstrating the mixing of (diabatic) Frenkel and CT excitons to create Davydov splitting in oligoacenes.

consistently. (Note that as triclinic pentacene lacks a symmetry operation to connect the two sublattices, the mechanism described in Figure 94 should be considered qualitative).

The Frenkel states on the left side of Figure 94 are slightly split by the small Coulomb coupling characterizing the acenes. In tetracene, for example, the calculated Coulomb-induced DS is  $<100\text{ cm}^{-1}$  and leads to an incorrect ordering;<sup>224</sup> the  $b$ -polarized state  $|FE\rangle_{k=0,+}$  is *higher* in energy, as indicated in the figure. The correct ordering and the much larger measured DS relies on substantial Frenkel/CT mixing. The coupling between the ( $k = 0$ ) symmetric Frenkel and CT excitons is equal to  $2(t_e + t_h)$ , a factor of  $\sqrt{2}$  larger than found in the one-dimensional lattices<sup>226</sup> in section 5.3, see eq 165. (Here, we have approximated the Frenkel dissociation integrals  $D_e$  and  $D_h$  with  $t_e$  and  $t_h$ , respectively, see ref 224.) In contrast, the coupling between the antisymmetric Frenkel and CT excitons is governed by the difference  $2(t_e - t_h)$ . For the oligoacenes,  $t_e$  and  $t_h$  are in-phase (based on a the 2-fold screw rotation along the  $b$ -axis) leading to a much stronger interaction among the symmetric ( $b$ -polarized) vs antisymmetric ( $\perp b$ -polarized) excitons. This is most dramatic when  $t_e = t_h$  as assumed in Figure 94, where the antisymmetric Frenkel and CT  $k = 0$  excitons do not mix at all and the symmetric Frenkel and CT excitons are very strongly mixed. Overall, the Frenkel/CT coupling results in a large red-shift of the symmetric Frenkel/CT exciton, pushing it much lower in energy than the unmixed antisymmetric Frenkel/CT exciton, creating a substantial DS.

As demonstrated in ref 224, the Frenkel/CT coupling diminishes as the magnitude of the reciprocal lattice vector increases in the  $ab$ -plane for symmetric excitons and increases for the antisymmetric excitons, leading to a positive (negative) curvature evaluated at  $k = 0$  for the band containing the lower (upper) Davydov component. Recently, Roth et al. measured the low energy exciton dispersion of crystalline pentacene using electron energy loss spectroscopy, see Figure 95.<sup>552</sup> Consistent with theory, the exciton responsible for the lower Davydov component is located at the bottom of the band with the momentum vector parallel to the reciprocal  $b$  axis,  $k \parallel K_b$ , while the exciton responsible for the upper Davydov component is located at the top of the band with the momentum vector parallel to the reciprocal  $a$  axis,  $k \parallel K_a$ . Theoretical calculations by Yamagata et. al show that tetracene and anthracene are characterized by similar exciton dispersions; the exciton responsible for the lower (upper) Davydov component lies at the bottom (top) of the relevant band.<sup>224</sup>

Because of the positive band curvature, the  $b$ -polarized lower Davydov component and its vibronic satellites should exhibit J-

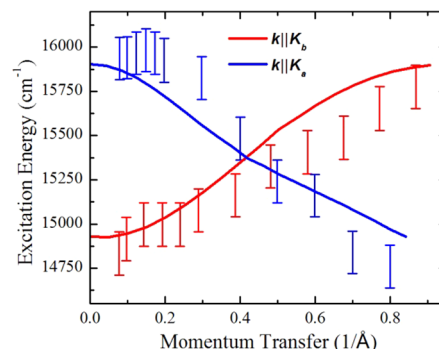


**Figure 95.** Experimentally measured (ref 552) and simulated dispersion curve of crystalline pentacene. Note that the  $k = 0$  exciton responsible for the lower Davydov component lies at the bottom of the band (J-like), whereas the  $k = 0$  exciton responsible for the upper Davydov component lies at the top of the band (H-like). Reprinted with permission from ref 226. Copyright (2015), American Chemical Society.

like signatures, whereas the  $\perp b$ -polarized upper Davydov component and its vibronic satellites should exhibit H-like signatures. The predicted behavior is borne out by the measured absorption spectrum as demonstrated in Figure 93 for pentacene. The  $b$ -polarized spectrum exhibits considerable spectroscopic distortions relative to the solution spectra including a substantial increase in the vibronic ratio ( $R_{\text{abs}}$ ) and a sizable redshift, both hallmarks of J-aggregation. These features are also characteristic of the  $b$ -polarized spectrum in anthracene and tetracene.<sup>224</sup> In contrast, the  $\perp b$ -polarized spectrum, which includes the upper Davydov component, exhibits only minor distortions of  $R_{\text{abs}}$  relative to the isolated molecules in anthracene and tetracene.<sup>224</sup> In pentacene, where the Frenkel-CT coupling is strongest,  $R_{\text{abs}}$  decreases substantially relative to the isolated molecules (see Figure 93c), indicating pronounced H-aggregate behavior. It is also noteworthy that the upper Davydov components are redshifted relative to the isolated molecules, likely due to a combination of the solution-to-crystal red-shift and the red-shift induced by the Frenkel/charge-transfer interaction<sup>227</sup> as discussed in section 5.4.

The band structure of Figure 95 also has implications for the J- or H-character of the steady-state PL spectrum. Recall that a positive curvature for the low-energy band at  $k = 0$  indicates J-aggregate emission characterized by a dominant  $0-0$  component that decreases with increasing temperature. The temperature dependence of the PL spectrum of pentacene has been measured by several groups;<sup>553–557</sup> the measurement of Anger et al. is reproduced in Figure 96. There, the peak labeled  $A_1$  is the only main peak present at room temperature and corresponds to the ( $S_1 \rightarrow S_0$ )  $0-0$  transition. As noted in the inset, there is also a weak vibronic progression (VP) accompanying the main  $A_1$  band at room temperature (representing the  $0-1$ ,  $0-2$ , ... transitions). Notably, the vibronic ratio  $R_{\text{PL}}$  is quite large at room temperature, consistent with J-aggregate behavior and a sizable room temperature exciton coherence (see section 4.5). Interestingly, as the temperature decreases, the  $A_1$  band gains intensity while that of the vibronic sidebands remains low.<sup>558</sup> Such J-like behavior can be attributed to an increase in the population of the band-bottom exciton and a concomitant increase in the exciton's coherence length as discussed in section 4.4. Unfortunately, at low temperatures, the vibronic ratio is obscured by additional

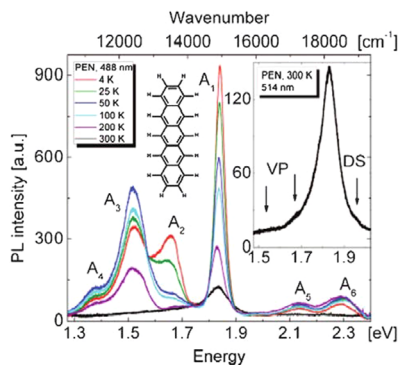


**Figure 96.** Temperature-dependent PL spectra of pentacene. The  $A_1$  peak corresponds to emission from the  $S_1 \rightarrow S_0$  transition, whereas the other peaks belong to other transitions from other states such as self-trapped excitons. Reprinted with permission from ref 555. Copyright (2012), AIP Publishing.

peaks, presumably arising from self-trapped or defect excitons,<sup>555</sup> thereby precluding a precise measurement of the exciton coherence length from the PL ratio. Regardless, the qualitative trend remains quite clear.

Conveniently, the PL spectra of tetracene, shown in Figure 97,<sup>344</sup> exhibit no such additional peaks at low temperatures,

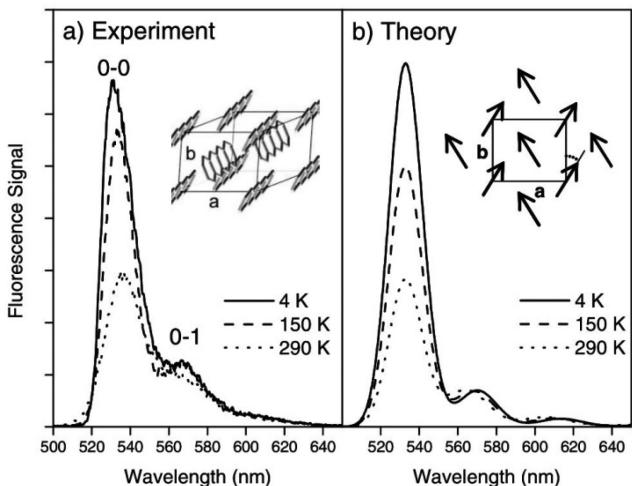


**Figure 97.** PL spectrum of tetracene. The PL ratio  $R_{PL}$  decreases with temperature as expected of a J-aggregate. Theoretical spectra were modeled with the exciton Hamiltonian of eq 13 modified for two-dimensional herringbone aggregates. Additional modification to include charge transfer should lead to similar behavior. Reprinted with permission from ref 344. Copyright (2004), American Physical Society.

thereby allowing for straightforward application of the ratio rule to extract the exciton's coherence number. Indeed, on the basis of the PL ratio at 4 K and the ratio rule derived from the Frenkel/CT Hamiltonian (see section 5.5), the estimated coherence number is  $N_{coh} \approx 5.7$ .<sup>342</sup> Interestingly, the original interpretation of the temperature-dependent  $R_{PL}$  in tetracene relied on a pure Frenkel exciton description using unphysically large nearest neighbor Coulomb couplings derived by fitting the Davydov splitting. Using the Holstein Hamiltonian, the coherence number of  $N_{coh} \approx 5$  at 4 K was obtained, very close to the value obtained using the Frenkel/CT Holstein

Hamiltonian and showing that the PL ratio rule is also robust against the nature of the coupling.

Additional evidence for the H/J aggregate interpretation of oligoacene photophysics can be found in the norbornyl-bridged tetracene dimers of Cook et al.,<sup>537,538</sup> where as indicated in Figure 98 the two tetracene transition dipole moments are parallel and “side-by-side” as in an ideal H-aggregate. Indeed, the absorption spectrum shows a clear reduction by  $\sim 20\%$  in  $R_{abs}$  in the dimer complex BT1 relative to the monomer Tc-e. Moreover, the PL ratio  $R_{PL}$  is also significantly reduced but is not expected to be zero even in the absence of disorder because of thermally activated 0–0 emission in H-aggregates. The excitonic bandwidth is likely sourced by the weak Coulombic coupling between the short-axis polarized transition dipole moments, enabling  $k_B T$  at room temperature to become comparable to the excitonic bandwidth,<sup>537</sup> see section 4.4 and Figure 39.

## 6. SUMMARY AND FUTURE DIRECTIONS

The purpose of the review was to highlight the success of an expanded exciton theory for J- and H-aggregates that incorporates long-range Coulomb coupling, short-range CT-mediated coupling, and vibronic coupling in understanding the photophysics of organic molecules assembled in a wide array of architectures. The simultaneous presence of both short- and long-range couplings allows for a broad range of photophysical behaviors, some of which defy explanation based on conventional Kasha theory. Perhaps the most dramatic example involves the hydrogen bonding perylene diimide derivatives involved in H- to J-aggregate transformations.<sup>76,81</sup> Frenkel/CT exciton coupling in the slipped-stacked geometry of the J-form not only accounts for the enormous red-shift of the absorption spectrum but also the presence of the second, higher energy band of comparable oscillator strength to the red-shifted band.<sup>227</sup> Coulomb coupling, which is the basis of the Kasha model, makes only a minor contribution and is actually positive, promoting H-like behavior. In general, H- and J-aggregates, which derive from an interference between the two coupling sources, can exhibit unorthodox “non-Kasha” geometries that in some cases contradict the long-held association of “side-by-side” H-aggregates and “head-to-tail” J-aggregates. Importantly, the vibronic signatures for assigning J- and H-aggregation based on the spectral ratios  $R_{abs}$  and  $R_{PL}$ , which were originally derived for Coulomb-coupled aggregates,<sup>14</sup> continue to hold when both CT-mediated and Coulomb couplings are present.<sup>223,225,227,228</sup> The two ratios provide complementary information about the underlying excitons:  $R_{abs}$  reports on the exciton bandwidth, and  $R_{PL}$  reports on the exciton coherence number. This complementarity is evident in the simple “ratio formulas” in eqs 55 and 105 and is demonstrated in Figure 24.

Early on, Kasha showed that the true distinction between J- and H-aggregates lies in the relative position of the nodeless ( $k = 0$ ) “bright” exciton within the exciton band; in J-aggregates, the bright exciton defines the band minimum, whereas in H-aggregates, it defines the band maximum. This definition remains valid independent of the coupling source, be it Coulombic, CT-mediated, or a combination thereof. When Coulomb coupling prevails, as in the Kasha theory, the bright exciton is shifted to higher energies relative to the monomer energy in H-aggregates and to lower energies in J-aggregates, thereby providing the basis for the celebrated spectral shift signatures for H- and J-aggregates. However, these signatures are no longer generally true in the presence of CT-mediated

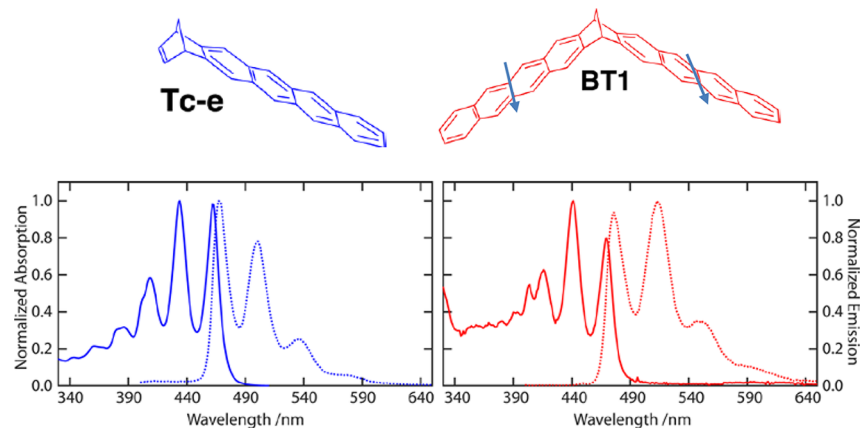


**Figure 98.** Absorption and emission spectra of (a) Tc-e and (b) BT1 in toluene at room temperature. Reprinted with permission from ref 537. Copyright (2016), American Chemical Society.

coupling. A fascinating example is the CT H-aggregate of section 5.4, where the interactions between Frenkel excitons and virtual CT excitons result in the bright exciton lying at the top of the band, as unambiguously defines H-aggregates. However, the CT-mediated interactions also cause an overall red-shift ( $\Delta_{CT}$ ) of all excitons independent of  $k$ , resulting in an oxymoronic “red-shifted H-aggregate”. Importantly, such aggregates display all the correct H-like vibronic signatures;  $R_{abs}$  is less than the monomer value, and  $R_{PL}$  is zero when there is no disorder and  $T = 0$  K. There are examples in the literature of H-aggregates in which the first vibronic peak ( $A_1$ ) is red-shifted, for example, the perylene diimide dimers<sup>35</sup> in Figure 20 and the lutein diacetate aggregates<sup>91</sup> of Figure 62, both of which also display H-aggregate vibronic signatures. The red-shift is likely due to nonresonant dispersion forces responsible for the gas-to-crystal shift (which derives, in part, from  $\Delta_{CT}$ ). A related example is the nonfluorescent squaraine J-aggregate reported by Zhang et al.,<sup>558</sup> which was recently revealed to be a red-shifted H-aggregate as the lowest energy excited state is optically dark.<sup>559</sup> Obviously, caution needs to be exercised when assigning J- or H-aggregation based on solely spectral shifts.

Coulombic and CT-mediated couplings impact not only the nature of the optical response, be it J-like, H-like, or a hybrid thereof, but also play an important role in exciton dynamics. The exciton mobility is enhanced (HH) or suppressed (HJ) depending on a constructive or destructive interference, respectively, between the two coupling sources,<sup>225,238</sup> and the rate at which excitons dissociate into charges (“exciton splitting”) further depends on an interference between the CT integrals ( $t_e$  and  $t_h$ ).<sup>230</sup> Recent theoretical investigations have also revealed a coherent suppression of the singlet exciton–exciton annihilation rate in H- but not J-aggregates<sup>560</sup> and a strong dependence of the singlet exciton fission rate on the aggregate type (J or H).<sup>561</sup> Conveniently, quantum interference effects, which derive from the H- or J-aggregate nature of the aggregate, can be effectively screened for using the optical response, in particular the vibronic ratios  $R_{abs}$  and  $R_{PL}$ .

One of the basic assumptions of exciton theory is that the total number of excitations is a well-defined quantum number; eigenstates with different numbers of excitations do not mix. In fact, throughout the review we have considered Hamiltonians in a basis set containing a single electronic excitation, be it Frenkel, CT, or a mixture thereof. Such states suffice for evaluating the linear optical susceptibility. Hamiltonians based

on more general exciton creation and annihilation operators readily accommodate multiple electronic excitations that are essential for evaluating the nonlinear optical response;<sup>282</sup> for example, the so-called two-exciton states and biexciton states, which are unbound and bound states, respectively, comprised of two Frenkel excitations are required for evaluating the third order nonlinear susceptibilities in molecular aggregates.<sup>282,320,562,563</sup> A natural extension of such theories would be the incorporation of local vibronic coupling as in the Holstein Hamiltonian. It would be extremely interesting to see how vibronic coupling modulates exciton–exciton interactions, impacting exciton binding as well as dynamical processes such as exciton–exciton annihilation.

There are also very important examples of dipolar and quadrupolar chromophores dominated by intramolecular charge-transfer transitions that give rise to Hamiltonians in which the excitation number is no longer well-defined. Interestingly, cyanine dyes, which are most often treated using the Frenkel exciton model, fall into this class. Painelli and co-workers<sup>559,564–569</sup> and Egorov and Al'fimov<sup>570</sup> introduced models that more accurately treat the intramolecular CT character of the monomer transition to account for solvochromism, symmetry-breaking, and two-photon absorption in monomeric and aggregated forms of such chromophores. In particular, the essential states model pioneered by Painelli<sup>559,564–569</sup> describes each chromophore with a set of diabatic states with intermixing dictated not only by (intramolecular) charge transfer but also by intermolecular Coulomb coupling arising from the large transition dipole moments. The mixing is also susceptible to intermolecular charge transfer, which was shown to be responsible for the “double-hump” spectrum exhibited by aggregates of certain squaraine derivatives.<sup>571</sup> The spectral shape bears an uncanny resemblance to the two-band spectrum associated with the J-form of the hydrogen bonded perylene diimide complexes that undergo J- to H-aggregate transformations (see section 5.9.1),<sup>76,81</sup> which similarly derives from intermolecular CT. Interestingly, the essential states model also shows that there generally is no correlation between spectral shifts and H/J-aggregation<sup>559</sup> in stark contrast to conventional Kasha theory. This needs to be further investigated, especially because the Kasha model has been so successful in treating the photophysical response of highly dipolar cyanine dye aggregates. It would also be quite interesting to explore vibronic signatures for J- and H-aggregation within the essential states model.

Perhaps the most interesting future applications of the expanded exciton theory outlined in this review pertain to exciton coherence. As established in refs 145, 176, 182, 195, 327, and 342, the PL ratio  $R_{PL}$  is a reliable reporter of the exciton coherence number  $N_{coh}$ ; generally,  $R_{PL}$  decreases with  $N_{coh}$  in H-aggregates and increases with  $N_{coh}$  in J-aggregates. In J-aggregates or generally any packing geometry in which the 0–0 transition involving the band-bottom exciton is symmetry allowed (for example, in herringbone aggregates),  $N_{coh}$  is simply obtained by multiplying  $R_{PL}$  by the HR factor  $\lambda^2$ .  $R_{PL}$  obtained from steady-state PL responds to the coherence number contributed by an equilibrium distribution of band-bottom (emitting) excitons, whereas  $R_{PL}(t)$  for PL following impulsive excitation tracks the evolution of spatial coherence;<sup>36,195</sup> for example,  $R_{PL}(t)$  will shrink in response to exciton localization. Future applications of these simple relationships may help to unravel the nature of coherent exciton transport, an issue of very pressing concern especially in applications involving biological light harvesting.<sup>18,189–194</sup> Measuring spatial (and temporal) coherence is just the first step in manipulating coherence for function.<sup>189</sup> Controlling and enhancing coherence in molecular assemblies can be achieved, for example, by using optical microcavities<sup>572–574</sup> to couple excitons to optical cavity modes with much larger coherence lengths.<sup>575</sup> In this manner, enhanced energy transfer was observed between J-aggregates,<sup>574</sup> and a 10-fold increase in conductivity was observed in organic semiconductors.<sup>576</sup> Several groups have also realized strong coupling between excitons in J-aggregates and surface plasmon modes in metal nanoparticles.<sup>577–579</sup> One may also be able to use appropriately tuned microcavity modes and/or surface plasmon resonances to control the mixing between CT and Frenkel excitons, thereby also controlling the magnitude and sign of the short-range excitonic coupling (and ultimately transport). There are also more fundamental theoretical issues regarding the composite nature of the excited states in the presence of cavity/plasmon-mode coupling; such particles are generally composed of excitons, photons, and phonons,<sup>580–582</sup> offering a rich phase space ripe for exploration. Considering the progress already made since Michael Kasha's curious observation regarding the enhancement of phosphorescence upon aggregation of dye molecules some six decades ago, the future for the field of "excitonics" is certainly bright, and we can no doubt expect significant advances in the upcoming years driven by fundamental curiosity as well as practical applications in organic electronics.

## AUTHOR INFORMATION

### Corresponding Author

\*E-mail: spano@temple.edu.

### ORCID

Nicholas J. Hestand: 0000-0001-7522-2466

Frank C. Spano: 0000-0003-3044-6727

### Notes

The authors declare no competing financial interest.

### Biographies

**Nicholas J. Hestand** studied Chemistry and Mathematics at Evangel University in Springfield, Missouri, graduating with a B.S. in 2012. He subsequently moved to Temple University in Philadelphia, PA to pursue his Ph.D. in Theoretical Chemistry under the supervision of Professor Frank C. Spano. His Ph.D. research focused on the

spectroscopic signatures and dynamics of charge-transfer excitons in molecular aggregates. After graduating in 2017, Nicholas moved to the Institute for Molecular Engineering at the University of Chicago where he is currently a postdoctoral scholar working with Professor James L. Skinner.

**Frank C. Spano** received an Associates in Science degree from Middlesex County College in 1980 and a B.S. in Engineering Physics from Lehigh University in 1982. He pursued Chemistry at Princeton University receiving a Ph.D. in 1988 under the advisement of Warren S. Warren. He worked as a postdoctoral fellow for Shaul Mukamel at the University of Rochester from 1988 to 1990. He is currently a professor in the Department of Chemistry at Temple University.

## ACKNOWLEDGMENTS

F.C.S. is supported by the NSF, grant no. DMR-1505437.

## REFERENCES

- (1) Reineke, S.; Thomschke, M.; Lüssem, B.; Leo, K. White Organic Light-Emitting Diodes: Status and Perspective. *Rev. Mod. Phys.* **2013**, *85*, 1245–1293.
- (2) *Organic Light-Emitting Diodes (Oleds): Materials, Devices and Applications*; Buckley, A., Ed.; Woodhead Publishing: Cambridge, 2013.
- (3) *The Wspc Reference on Organic Electronics: Organic Semiconductors*; Bredas, J.-L., Marder, S. R., Eds.; World Scientific Publishing Co: Singapore, 2016.
- (4) Ostroverkhova, O. Organic Optoelectronic Materials: Mechanisms and Applications. *Chem. Rev.* **2016**, *116*, 13279–13412.
- (5) Clarke, T. M.; Durrant, J. R. Charge Photogeneration in Organic Solar Cells. *Chem. Rev.* **2010**, *110*, 6736–6767.
- (6) Trung, T. Q.; Lee, N. E. Recent Progress on Stretchable Electronic Devices with Intrinsically Stretchable Components. *Adv. Mater.* **2017**, *29*, 1603167.
- (7) Chen, D.; Pei, Q. Electronic Muscles and Skins: A Review of Soft Sensors and Actuators. *Chem. Rev.* **2017**, *117*, 11239–11268.
- (8) Bardeen, C. J. The Structure and Dynamics of Molecular Excitons. *Annu. Rev. Phys. Chem.* **2014**, *65*, 127–148.
- (9) Bredas, J. L.; Beljonne, D.; Coropceanu, V.; Cornil, J. Charge-Transfer and Energy-Transfer Processes in Pi-Conjugated Oligomers and Polymers: A Molecular Picture. *Chem. Rev.* **2004**, *104*, 4971–5003.
- (10) Schroter, M.; Ivanov, S. D.; Schulze, J.; Polyutov, S. P.; Yan, Y.; Pullerits, T.; Kuhn, O. Exciton-Vibrational Coupling in the Dynamics and Spectroscopy of Frenkel Excitons in Molecular Aggregates. *Phys. Rep.* **2015**, *567*, 1–78.
- (11) Coropceanu, V.; Cornil, J.; da Silva, D. A.; Olivier, Y.; Silbey, R.; Bredas, J. L. Charge Transport in Organic Semiconductors. *Chem. Rev.* **2007**, *107*, 926–952.
- (12) Scholes, G. D.; Rumbles, G. Excitons in Nanoscale Systems. *Nat. Mater.* **2006**, *5*, 683–696.
- (13) Spano, F. C. Excitons in Conjugated Oligomer Aggregates, Films, and Crystals. *Annu. Rev. Phys. Chem.* **2006**, *57*, 217–243.
- (14) Spano, F. C. The Spectral Signatures of Frenkel Polarons in H- and J-Aggregates. *Acc. Chem. Res.* **2010**, *43*, 429–439.
- (15) Spano, F. C.; Silva, C. H- and J-Aggregate Behavior in Polymeric Semiconductors. *Annu. Rev. Phys. Chem.* **2014**, *65*, 477–500.
- (16) Troisi, A. Charge Transport in High Mobility Molecular Semiconductors: Classical Models and New Theories. *Chem. Soc. Rev.* **2011**, *40*, 2347–2358.
- (17) Brixner, T.; Hildner, R.; Köhler, J.; Lambert, C.; Würthner, F. Exciton Transport in Molecular Aggregates – from Natural Antennas to Synthetic Chromophore Systems. *Adv. Energy Mater.* **2017**, *7*, 1700236.
- (18) Scholes, G. D. Long-Range Resonance Energy Transfer in Molecular Systems. *Annu. Rev. Phys. Chem.* **2003**, *54*, 57–87.

- (19) Saikin, S. K.; Eisfeld, A.; Valleau, S.; Aspuru-Guzik, A. Photonics Meets Excitonics: Natural and Artificial Molecular Aggregates. *Nanophotonics* **2013**, *2*, 21–38.
- (20) Kasha, M.; Rawls, H. R.; El-Bayoumi, M. A. *The Exciton Model in Molecular Spectroscopy*; Butterworths: London, U.K., 1965; Vol. 11.
- (21) Kasha, M. Energy Transfer Mechanisms and the Molecular Exciton Model for Molecular Aggregates. *Radiat. Res.* **1963**, *20*, 55–70.
- (22) Hochstrasser, R. M.; Kasha, M. Application of the Exciton Model to Monomolecular Lamellar Systems. *Photochem. Photobiol.* **1964**, *3*, 317–331.
- (23) McRae, E. G.; Kasha, M. Enhancement of Phosphorescence Ability Upon Aggregation of Dye Molecules. *J. Chem. Phys.* **1958**, *28*, 721–722.
- (24) Kasha, M. Relation between Exciton Bands and Conduction Bands in Molecular Lamellar Systems. *Rev. Mod. Phys.* **1959**, *31*, 162–169.
- (25) Davydov, A. S. *Theory of Molecular Excitons*; Plenum: New York, NY, 1971.
- (26) Kasha, M. Characterization of Electronic Transitions in Complex Molecules. *Discuss. Faraday Soc.* **1950**, *9*, 14–19.
- (27) Dicke, R. H. Coherence in Spontaneous Radiation Processes. *Phys. Rev.* **1954**, *93*, 99–110.
- (28) Sundstrom, V.; Gillbro, T.; Gadonas, R. A.; Piskarskas, A. Annihilation of Singlet Excitons in J-Aggregates of Pseudoisocyanine (Pic) Studied by Picosecond and Subpicosecond Spectroscopy. *J. Chem. Phys.* **1988**, *89*, 2754–2762.
- (29) Scheblykin, I. G.; Varnavsky, O. P.; Bataiev, M. M.; Sliusarenko, O.; Van der Auweraer, M.; Vitukhnovsky, A. G. Non-Coherent Exciton Migration in J-Aggregates of the Dye Thiats: Exciton-Exciton Annihilation and Fluorescence Depolarization. *Chem. Phys. Lett.* **1998**, *298*, 341–350.
- (30) Birks, J. B. Excimers. *Rep. Prog. Phys.* **1975**, *38*, 903.
- (31) Ahrens, M. J.; Sinks, L. E.; Rybtchinski, B.; Liu, W. H.; Jones, B. A.; Giaimo, J. M.; Gusev, A. V.; Goshe, A. J.; Tiede, D. M.; Wasielewski, M. R. Self-Assembly of Supramolecular Light-Harvesting Arrays from Covalent Multi-Chromophore Perylene-3,4:9,10-Bis(Dicarboximide) Building Blocks. *J. Am. Chem. Soc.* **2004**, *126*, 8284–8294.
- (32) Neuteboom, E. E.; Meskers, S. C. J.; Meijer, E. W.; Janssen, R. A. J. Photoluminescence of Self-Organized Perylene Bisimide Polymers. *Macromol. Chem. Phys.* **2004**, *205*, 217–222.
- (33) Lim, J. M.; Kim, P.; Yoon, M. C.; Sung, J.; Dehm, V.; Chen, Z.; Würthner, F.; Kim, D. Exciton Delocalization and Dynamics in Helical Pi-Stacks of Self-Assembled Perylene Bisimides. *Chem. Sci.* **2013**, *4*, 388–397.
- (34) Liu, H.; Shen, L.; Cao, Z.; Li, X. Covalently Linked Perylenetetracarboxylic Diimide Dimers and Trimers with Rigid "J-Type" Aggregation Structure. *Phys. Chem. Chem. Phys.* **2014**, *16*, 16399–16406.
- (35) Margulies, E. A.; Shoer, L. E.; Eaton, S. W.; Wasielewski, M. R. Excimer Formation in Cofacial and Slip-Stacked Perylene-3,4:9,10-Bis(Dicarboximide) Dimers on a Redox-Inactive Triptycene Scaffold. *Phys. Chem. Chem. Phys.* **2014**, *16*, 23735–23742.
- (36) Sung, J.; Kim, P.; Fimmel, B.; Würthner, F.; Kim, D. Direct Observation of Ultrafast Coherent Exciton Dynamics in Helical Pi-Stacks of Self-Assembled Perylene Bisimides. *Nat. Commun.* **2015**, *6*, 8646.
- (37) Würthner, F.; Saha-Möller, C. R.; Fimmel, B.; Ogi, S.; Leowanawat, P.; Schmidt, D. Perylene Bisimide Dye Assemblies as Archetype Functional Supramolecular Materials. *Chem. Rev.* **2016**, *116*, 962–1052.
- (38) Deboer, S.; Wiersma, D. A. Dephasing-Induced Damping of Superradiant Emission in J-Aggregates. *Chem. Phys. Lett.* **1990**, *165*, 45–53.
- (39) Fidder, H.; Knoester, J.; Wiersma, D. A. Superradiant Emission and Optical Dephasing in J-Aggregates. *Chem. Phys. Lett.* **1990**, *171*, 529–536.
- (40) Fidder, H.; Knoester, J.; Wiersma, D. A. Optical Properties of Disordered Molecular Aggregates - a Numerical Study. *J. Chem. Phys.* **1991**, *95*, 7880–7890.
- (41) Potma, E. O.; Wiersma, D. A. Exciton Superradiance in Aggregates: The Effect of Disorder, Higher Order Exciton-Phonon Coupling and Dimensionality. *J. Chem. Phys.* **1998**, *108*, 4894–4903.
- (42) Moll, J.; Daehne, S.; Durrant, J. R.; Wiersma, D. A. Optical Dynamics of Excitons in J-Aggregates of a Carbocyanine Dye. *J. Chem. Phys.* **1995**, *102*, 6362–6370.
- (43) Scheblykin, I. G.; Bataiev, M. M.; Van der Auweraer, M.; Vitukhnovsky, A. G. Dimensionality and Temperature Dependence of the Radiative Lifetime of J-Aggregates with Davydov Splitting of the Exciton Band. *Chem. Phys. Lett.* **2000**, *316*, 37–44.
- (44) Kamalov, V. F.; Struganova, I. A.; Tani, T.; Yoshihara, K. Temperature Dependence of Superradiant Emission of Bic J-Aggregates. *Chem. Phys. Lett.* **1994**, *220*, 257–261.
- (45) Spano, F. C.; Kuklinski, J. R.; Mukamel, S. Temperature Dependent Superradiant Decay of Excitons in Small Aggregates. *Phys. Rev. Lett.* **1990**, *65*, 211–214.
- (46) Spano, F. C.; Kuklinski, J. R.; Mukamel, S. Cooperative Radiative Dynamics in Molecular Aggregates. *J. Chem. Phys.* **1991**, *94*, 7534–7544.
- (47) Chernyak, V.; Meier, T.; Tsiper, E.; Mukamel, S. Scaling of Fluorescence Stokes Shift and Superradiance Coherence Size in Disordered Molecular Aggregates. *J. Phys. Chem. A* **1999**, *103*, 10294–10299.
- (48) Jolley, E. E. Spectral Absorption and Fluorescence of Dyes in the Molecular State. *Nature* **1936**, *138*, 1009–1010.
- (49) Scheibe, G. Reverseible Polymerisation as a Reason for New Types Absorption Bands Form Coloured Materials. *Colloid Polym. Sci.* **1938**, *82*, 1–14.
- (50) Scheibe, G.: *Optische Anregungen Organischer Systeme*; Forst, W., Ed.; Verlag Chemie: Weinheim, Germany, 1966; pp 109.
- (51) Daltrozzi, E.; Scheibe, G.; Gschwind, K.; Haimerl, F. Structure of J-Aggregates of Pseudoisocyanine. *Phot. Sci. Eng.* **1974**, *18*, 441–450.
- (52) Möbius, D. Scheibe Aggregates. *Adv. Mater.* **1995**, *7*, 437–444.
- (53) Czikkely, V.; Forsterling, H. D.; Kuhn, H. Light Absorption and Structure of Aggregates of Dye Molecules. *Chem. Phys. Lett.* **1970**, *6*, 11–14.
- (54) J-Aggregates; Kobayashi, T., Ed.; World Scientific: Singapore, 1996; pp 228.
- (55) Cooper, W. Multiplet Structure of Aggregated States in 1,1'-Diethyl-2,2'-Cyanine Dye. *Chem. Phys. Lett.* **1970**, *7*, 73–77.
- (56) Kopainsky, B.; Hallermeier, J. K.; Kaiser, W. The 1st Step of Aggregation of Pic - the Dimerization. *Chem. Phys. Lett.* **1981**, *83*, 498–502.
- (57) Möbius, D.; Kuhn, H. Monolayer Assemblies of Dyes to Study the Role of Thermal Collisions in Energy Transfer. *Isr. J. Chem.* **1979**, *18*, 375–384.
- (58) Möbius, D.; Kuhn, H. Energy Transfer in Monolayers with Cyanine Dye Scheibe Aggregates. *J. Appl. Phys.* **1988**, *64*, 5138–5141.
- (59) Fidder, H. Absorption and Emission Studies on Pure and Mixed J-Aggregates of Pseudoisocyanine. *Chem. Phys.* **2007**, *341*, 158–168.
- (60) Herz, A. H. Aggregation of Sensitizing Dyes in Solution and Their Adsorption onto Silver-Halides. *Adv. Colloid Interface Sci.* **1977**, *8*, 237–298.
- (61) Wolthaus, L.; Schaper, A.; Möbius, D. Brickstone Arrangement in J-Aggregates of an Amphiphilic Merocyanine Dye. *Chem. Phys. Lett.* **1994**, *225*, 322–326.
- (62) Bialas, D.; Zitzler-Kunkel, A.; Kirchner, E.; Schmidt, D.; Würthner, F. Structural and Quantum Chemical Analysis of Exciton Coupling in Homo- and Heteroaggregate Stacks of Merocyanines. *Nat. Commun.* **2016**, *7*, 11.
- (63) Liess, A.; Lv, A.; Arjona-Estebar, A.; Bialas, D.; Krause, A. M.; Stepanenko, V.; Stolte, M.; Würthner, F. Exciton Coupling of Merocyanine Dyes from H- to J-Type in the Solid State by Crystal Engineering. *Nano Lett.* **2017**, *17*, 1719–1726.

- (64) Kulinich, A. V.; Ishchenko, A. A. Merocyanine Dyes: Synthesis, Structure, Properties and Applications. *Russ. Chem. Rev.* **2009**, *78*, 141–164.
- (65) Kawaguchi, T.; Iwata, K. Merocyanine J-Aggregates - Formation and Structural Change on Chemical and Thermal Treatments. *Thin Solid Films* **1990**, *191*, 173–191.
- (66) Scheblykin, I. G.; Varnavsky, O. P.; Verbouwe, W.; De Backer, S.; Van der Auweraer, M.; Vitukhnovsky, A. G. Relaxation Dynamics of Excitons in J-Aggregates Revealing a Two-Component Davydov Splitting. *Chem. Phys. Lett.* **1998**, *282*, 250–256.
- (67) Herz, A. H. Dye-Dye Interactions of Cyanines in Solution and at AgBr Surfaces. *Photogr. Sci. Eng.* **1974**, *18*, 323–335.
- (68) Ozcelik, S.; Akins, D. L. Superradiance of Aggregated Thiacyarbocyanine Molecules. *J. Phys. Chem. B* **1999**, *103*, 8926–8929.
- (69) Spitz, C.; Knoester, J.; Ouart, A.; Daehne, S. Polarized Absorption and Anomalous Temperature Dependence of Fluorescence Depolarization in Cylindrical J-Aggregates. *Chem. Phys.* **2002**, *275*, 271–284.
- (70) Eisele, D. M.; Knoester, J.; Kirstein, S.; Rabe, J. P.; Vanden Bout, D. A. Uniform Exciton Fluorescence from Individual Molecular Nanotubes Immobilized on Solid Substrates. *Nat. Nanotechnol.* **2009**, *4*, 658–663.
- (71) Eisele, D. M.; Cone, C. W.; Bloemsma, E. A.; Vlaming, S. M.; van der Kwaak, C. G. F.; Silbey, R. J.; Bawendi, M. G.; Knoester, J.; Rabe, J. P.; Vanden Bout, D. A. Utilizing Redox-Chemistry to Elucidate the Nature of Exciton Transitions in Supramolecular Dye Nanotubes. *Nat. Chem.* **2012**, *4*, 655–662.
- (72) Eisele, D. M.; Arias, D. H.; Fu, X. F.; Bloemsma, E. A.; Steiner, C. P.; Jensen, R. A.; Rebentrost, P.; Eisele, H.; Tokmakoff, A.; Lloyd, S.; et al. Robust Excitons Inhabit Soft Supramolecular Nanotubes. *Proc. Natl. Acad. Sci. U. S. A.* **2014**, *111*, E3367–E3375.
- (73) Friedl, C.; Renger, T.; Berlepsch, H. V.; Ludwig, K.; Busch, M. S. A.; Megow, J. Structure Prediction of Self-Assembled Dye Aggregates from Cryogenic Transmission Electron Microscopy, Molecular Mechanics, and Theory of Optical Spectra. *J. Phys. Chem. C* **2016**, *120*, 19416–19433.
- (74) Kaiser, T. E.; Stepanenko, V.; Würthner, F. Fluorescent J-Aggregates of Core-Substituted Perylene Bisimides: Studies on Structure-Property Relationship, Nucleation-Elongation Mechanism, and Sergeants-and-Soldiers Principle. *J. Am. Chem. Soc.* **2009**, *131*, 6719–6732.
- (75) Ghosh, S.; Li, X.-Q.; Stepanenko, V.; Würthner, F. Control of H- and J-Type P Stacking by Peripheral Alkyl Chains and Self-Sorting Phenomena in Perylene Bisimide Homo- and Heteroaggregates. *Chem. - Eur. J.* **2008**, *14*, 11343–11357.
- (76) Yagai, S.; Seki, T.; Karatsu, T.; Kitamura, A.; Würthner, F. Transformation from H- to J-Aggregated Perylene Bisimide Dyes by Complexation with Cyanurates. *Angew. Chem., Int. Ed.* **2008**, *47*, 3367–3371.
- (77) Hartnett, P. E.; Timalsina, A.; Matte, H. S. S. R.; Zhou, N.; Guo, X.; Zhao, W.; Facchetti, A.; Chang, R. P. H.; Hersam, M. C.; Wasielewski, M. R.; et al. Slip-Stacked Perylenediimides as an Alternative Strategy for High Efficiency Nonfullerene Acceptors in Organic Photovoltaics. *J. Am. Chem. Soc.* **2014**, *136*, 16345–16356.
- (78) Yoo, H.; Furumaki, S.; Yang, J.; Lee, J.-E.; Chung, H.; Oba, T.; Kobayashi, H.; Rybtchinski, B.; Wilson, T. M.; Wasielewski, M. R.; et al. Excitonic Coupling in Linear and Trefoil Trimer Perylenediimide Molecules Probed by Single-Molecule Spectroscopy. *J. Phys. Chem. B* **2012**, *116*, 12878–12886.
- (79) Pochas, C. M.; Kistler, K. A.; Yamagata, H.; Matsika, S.; Spano, F. C. Contrasting Photophysical Properties of Star-Shaped Vs Linear Perylene Diimide Complexes. *J. Am. Chem. Soc.* **2013**, *135*, 3056–3066.
- (80) Wilson, T. M.; Tauber, M. J.; Wasielewski, M. R. Toward an N-Type Molecular Wire: Electron Hopping within Linearly Linked Perylenediimide Oligomers. *J. Am. Chem. Soc.* **2009**, *131*, 8952–8957.
- (81) Sarbu, A.; Biniek, L.; Guenet, J.-M.; Mesini, P. J.; Brinkmann, M. Reversible J- to H-Aggregate Transformation in Thin Films of a Perylenebisimide Organogelator. *J. Mater. Chem. C* **2015**, *3*, 1235–1242.
- (82) Ohno, O.; Kaizu, Y.; Kobayashi, H. J-Aggregate Formation of a Water-Soluble Porphyrin in Acidic Aqueous Media. *J. Chem. Phys.* **1993**, *99*, 4128–4139.
- (83) Steinbeck, C. A.; Ernst, M.; Meier, B. H.; Chmelka, B. F. Anisotropic Optical Properties and Structures of Block Copolymer/Silica Thin Films Containing Aligned Porphyrin J-Aggregates. *J. Phys. Chem. C* **2008**, *112*, 2565–2573.
- (84) Vlaming, S. M.; Augulis, R.; Stuart, M. C. A.; Knoester, J.; van Loosdrecht, P. H. M. Exciton Spectra and the Microscopic Structure of Self-Assembled Porphyrin Nanotubes. *J. Phys. Chem. B* **2009**, *113*, 2273–2283.
- (85) Würthner, F.; Kaiser, T. E.; Saha-Moller, C. R. J-Aggregates: From Serendipitous Discovery to Supramolecular Engineering of Functional Dye Materials. *Angew. Chem., Int. Ed.* **2011**, *50*, 3376–3410.
- (86) Bricks, J. L.; Slominskii, Y. L.; Panas, I.; Demchenko, A. Fluorescent J-Aggregates of Cyanine Dyes: Basic Research and Applications Review. *Methods Appl. Fluoresc.* **2018**, *6*, 012001.
- (87) Duan, H. G.; Nalbach, P.; Prokhorenko, V. I.; Mukamel, S.; Thorwart, M. On the Origin of Oscillations in Two-Dimensional Spectra of Excitonically-Coupled Molecular Systems. *New J. Phys.* **2015**, *17*, 9.
- (88) Halpin, A.; Johnson, P. J. M.; Tempelaar, R.; Murphy, R. S.; Knoester, J.; Jansen, T. L. C.; Miller, R. J. D. Two-Dimensional Spectroscopy of a Molecular Dimer Unveils the Effects of Vibronic Coupling on Exciton Coherences. *Nat. Chem.* **2014**, *6*, 196–201.
- (89) Zsila, F.; Bikadi, Z.; Keresztes, Z.; Deli, J.; Simonyi, M. Investigation of the Self-Organization of Lutein and Lutein Diacetate by Electronic Absorption, Circular Dichroism Spectroscopy, and Atomic Force Microscopy. *J. Phys. Chem. B* **2001**, *105*, 9413–9421.
- (90) Zsila, F.; Deli, J.; Bikadi, Z.; Simonyi, M. Supramolecular Assemblies of Carotenoids. *Chirality* **2001**, *13*, 739–744.
- (91) Spano, F. C. Analysis of the UV/Vis and Cd Spectral Line Shapes of Carotenoid Assemblies: Spectral Signatures of Chiral H-Aggregates. *J. Am. Chem. Soc.* **2009**, *131*, 4267–4278.
- (92) Gierschner, J.; Egelhaaf, H.-J.; Oelkrug, D. Absorption, Fluorescence and Light Scattering of Oligothiophene and Oligophenylenevinylene Nanoaggregates. *Synth. Met.* **1997**, *84*, 529–530.
- (93) Oelkrug, D.; Egelhaaf, H.-J.; Gierschner, J.; Tompert, A. Electronic Deactivation in Single Chains, Nano-Aggregates and Ultrathin Films of Conjugated Oligomers. *Synth. Met.* **1996**, *76*, 249–253.
- (94) Fichou, D.; Horowitz, G.; Xu, V.; Garnier, F. Low Temperature Optical Absorption of Polycrystalline Thin Films of a-Quaterthiophene, a-Sexithiophene and a-Octithiophene, Three Model Oligomers of Polythiophene. *Synth. Met.* **1992**, *48*, 167–179.
- (95) Egelhaaf, H. J.; Bauerle, P.; Rauer, K.; Hoffmann, V.; Oelkrug, D. UV/Vis and IR Spectroscopic Studies on Molecular Orientation in Ultrathin Films of Polythiophene Model Compounds. *J. Mol. Struct.* **1993**, *293*, 249–252.
- (96) Bosisio, R.; Botta, C.; Colombo, A.; Destri, S.; Porzio, W.; Grilli, E.; Tubino, R.; Bongiovanni, G.; Mura, A.; Di Silvestro, G. Excitonic Effects in Thiophene Oligomers. *Synth. Met.* **1997**, *87*, 23–29.
- (97) Gebauer, W.; Sokolowski, M.; Umbach, E. Optical Processes in Ultrathin Oligothiophene Films on Well-Defined Substrates. *Chem. Phys.* **1998**, *227*, 33–48.
- (98) Muccini, M.; Lunedei, E.; Bree, A.; Horowitz, G.; Garnier, F.; Taliani, C. Polarized Fluorescence in a-Sexithiophene Single Crystal at 4.2 K. *J. Chem. Phys.* **1998**, *108*, 7327–7333.
- (99) Muccini, M.; Lunedei, E.; Taliani, C.; Beljonne, D.; Cornil, J.; Bredas, J. L. Interchain Interaction in a Prototypical Conjugated Oligomer from Polarized Absorption at 4.2K: A-Sexithiophene Single Crystal. *J. Chem. Phys.* **1998**, *109*, 10513–10520.
- (100) Muccini, M.; Schneider, M.; Taliani, C.; Sokolowski, M.; Umbach, E.; Beljonne, D.; Cornil, J.; Bredas, J. L. Effect of Wave-Function Delocalization on the Exciton Splitting in Organic

- Conjugated Materials. *Phys. Rev. B: Condens. Matter Mater. Phys.* **2000**, *62*, 6296–6300.
- (101) DiCesare, N.; Belletete, M.; Marrano, C.; Leclerc, M.; Durocher, G. Intermolecular Interactions in Conjugated Oligothiophenes. I. Optical Spectra of Terthiophene and Substituted Terthiophenes Recorded in Various Environments. *J. Phys. Chem. A* **1999**, *103*, 795–802.
- (102) *Handbook of Oligo and Polythiophenes*; Taliani, C., Gebauer, W., Eds.; Wiley-VCN: Weinheim, Germany, 1999.
- (103) Kouki, F.; Spearman, P.; Valat, P.; Horowitz, G.; Garnier, F. Experimental Determination of Excitonic Levels in  $\alpha$ -Oligothiophenes. *J. Chem. Phys.* **2000**, *113*, 385–391.
- (104) Moller, S.; Weiser, G.; Garnier, F. Electric Field Effects on the Davydov Components of a Strong Intramolecular Transition:  $\alpha$ -Sexithiophene Single Crystals. *Phys. Rev. B: Condens. Matter Mater. Phys.* **2000**, *61*, 15749–15755.
- (105) Sassella, A.; Borghesi, A.; Meinardi, F.; Tubino, R.; Gurioli, M.; Botta, C.; Porzio, W.; Barbarella, G. Optical Properties of Highly Oriented Quaterthiophene Thin Films Grown by Organic Molecular-Beam Deposition. *Phys. Rev. B: Condens. Matter Mater. Phys.* **2000**, *62*, 11170–11176.
- (106) Meinardi, F.; Borghesi, A.; Cerminara, M.; Sassella, A.; Tavazzi, S.; Tubino, R.; Gurioli, M.; Mura, A.; Bongiovanni, G. The Origin of Radiative Emission of Quaterthiophene Ultra-Thin Films. *Synth. Met.* **2001**, *121*, 1355–1356.
- (107) Meinardi, F.; Cerminara, M.; Sassella, A.; Borghesi, A.; Spearman, P.; Bongiovanni, G.; Mura, A.; Tubino, R. Intrinsic Excitonic Luminescence in Odd and Even Numbered Oligothiophenes. *Phys. Rev. Lett.* **2002**, *89*, 157403–157401–157403–157404.
- (108) Meinardi, F.; Cerminara, M.; Blumstengel, S.; Sassella, A.; Borghesi, A.; Tubino, R. Broad and Narrow Bands in the Photoluminescence Spectrum of Solid-State Oligothiophenes: Two Marks of an Intrinsic Emission. *Phys. Rev. B: Condens. Matter Mater. Phys.* **2003**, *67*, 184205.
- (109) Apperloo, J. J.; Janssen, R. A. J.; Malenfant, P. R. L.; Frechet, J. M. J. Interchain Delocalization of Photoinduced Neutral and Charged States in Nanoaggregates of Lengthy Oligothiophenes. *J. Am. Chem. Soc.* **2001**, *123*, 6916–6924.
- (110) Loi, M. A.; Martin, C.; Chandrasekhar, H. R.; Chandrasekhar, M.; Graupner, W.; Garnier, F.; Mura, A.; Bongiovanni, G. Primary Optical Excitations and Excited-State Interaction Energies in Sexithiophene. *Phys. Rev. B: Condens. Matter Mater. Phys.* **2002**, *66*, 113102.
- (111) Schneider, M.; Brinkmann, M.; Muccini, M.; Biscarini, F.; Taliani, C.; Gebauer, W.; Sokolowski, M.; Umbach, E. Morphology and Trap Luminescence in Thin Oligothiophene Films on Hopg. *Chem. Phys.* **2002**, *285*, 345–353.
- (112) Schenning, A. P. H. J.; Kilbinger, A. F. M.; Biscarini, F.; Cavallini, M.; Cooper, H. J.; Derrick, P. J.; Feast, W. J.; Lazzaroni, R.; Leclere, M.; McDonell, L. A.; et al. Supramolecular Organization of  $\alpha,\alpha'$ -Disubstituted Sexithiophenes. *J. Am. Chem. Soc.* **2002**, *124*, 1269–1275.
- (113) Gebauer, W.; Langner, A.; Schneider, M.; Sokolowski, M.; Umbach, E. Exciton Dispersion in a  $\Pi$ -Conjugated Oligomer Film: A Quaterthiophene on Highly Oriented Pyrolytic Graphite and Ag(111). *Phys. Rev. B: Condens. Matter Mater. Phys.* **2004**, *69*, 125420.
- (114) Tavazzi, S.; Borghesi, A.; Laicini, M.; Spearman, P. Polarized Absorption of Quaterthiophene Single Crystals. *J. Chem. Phys.* **2004**, *121*, 8542–8546.
- (115) Leclere, P.; Surin, M.; Verville, P.; Lazzaroni, R.; Kilbinger, A. F. M.; Henze, O.; Feast, W. J.; Cavallini, M.; Biscarini, F.; Schenning, A. P. H. J.; et al. About Oligothiophene Self-Assembly: From Aggregation in Solution to Solid-State Nanostructures. *Chem. Mater.* **2004**, *16*, 4452–4466.
- (116) Westenhoff, S.; Abrusci, A.; Feast, W. J.; Henze, O.; Kilbinger, A. F. M.; Schenning, A.; Silva, C. Supramolecular Electronic Coupling in Chiral Oligothiophene Nanostructures. *Adv. Mater.* **2006**, *18*, 1281–1285.
- (117) Raimondo, L.; Laicini, M.; Spearman, P.; Tavazzi, S.; Borghesi, A. Effect of Static and Dynamic Disorder on Exciton Mobility in Oligothiophenes. *J. Chem. Phys.* **2006**, *125*, 024702.
- (118) Tavazzi, S.; Campione, M.; Laicini, M.; Raimondo, L.; Borghesi, A.; Spearman, P. Measured Davydov Splitting in Oligothiophene Crystals. *J. Chem. Phys.* **2006**, *124*, 194710.
- (119) Raimondo, L.; Campione, M.; Laicini, M.; Moret, M.; Sassella, A.; Spearman, P.; Tavazzi, S. Absorption Spectra of Polycrystalline Samples and Twinned Crystals of Oligothiophenes. *Appl. Surf. Sci.* **2006**, *253*, 271–274.
- (120) Silvestri, L.; Tavazzi, S.; Spearman, P.; Raimondo, L.; Spano, F. C. Exciton-Phonon Coupling in Molecular Crystals: Synergy between Two Intramolecular Vibrational Modes in Quaterthiophene Single Crystals. *J. Chem. Phys.* **2009**, *130*, 234701.
- (121) Oelkrug, D.; Tompert, A.; Egelhaaf, H.-J.; Hanack, M.; Steinhuber, E.; Hohloch, M.; Meier, H.; Stalmach, U. Towards Highly Luminescent Phenylene Vinylene Films. *Synth. Met.* **1996**, *83*, 231–237.
- (122) Oelkrug, D.; Tompert, A.; Gierschner, J.; Egelhaaf, H.-J.; Hanack, M.; Hohloch, M.; Steinhuber, E. Tuning of Fluorescence in Films and Nanoparticles of Oligophenylenevinylenes. *J. Phys. Chem. B* **1998**, *102*, 1902–1907.
- (123) Gierschner, J.; Mack, H.-G.; Luer, L.; Oelkrug, D. Fluorescence and Absorption Spectra of Oligophenylenevinylenes: Vibronic Coupling, Band Shapes, and Solvatochromism. *J. Chem. Phys.* **2002**, *116*, 8596–8609.
- (124) Gierschner, J.; Oelkrug, D. Optical Properties of Oligophenylenevinylenes. In *Encyclopedia of Nanoscience and Nanotechnology*; Nalwa, H., Ed.; American Scientific Publishers, 2004; Vol. 8, pp 219–238.
- (125) Gierschner, J.; Huang, Y. S.; Van Averbeke, B.; Cornil, J.; Friend, R. H.; Beljonne, D. Excitonic Versus Electronic Couplings in Molecular Assemblies: The Importance of Non-Nearest Neighbor Interactions. *J. Chem. Phys.* **2009**, *130*, 044105.
- (126) Gierschner, J.; Luer, L.; Milian-Medina, B.; Oelkrug, D.; Egelhaaf, H. J. Highly Emissive H-Aggregates or Aggregation-Induced Emission Quenching? The Photophysics of All-Trans Para-Distyrylbenzene. *J. Phys. Chem. Lett.* **2013**, *4*, 2686–2697.
- (127) Gierschner, J.; Park, S. Y. Luminescent Distyrylbenzenes: Tailoring Molecular Structure and Crystalline Morphology. *J. Mater. Chem. C* **2013**, *1*, S818–S832.
- (128) Wu, C. C.; Delong, M. C.; Vardeny, Z. V.; Ferraris, J. P. Structural and Optical Studies of Distyrylbenzene Single Crystals. *Synth. Met.* **2003**, *137*, 939–941.
- (129) Osterbacka, R.; Wohlgemant, M.; Shkunov, M.; Chinn, D.; Vardeny, Z. V. Excitons, Polarons, and Laser Action in Poly(P-Phenylen Vinylene) Films. *J. Chem. Phys.* **2003**, *118*, 8905–8916.
- (130) Wu, C. C.; Ehrenfreund, E.; Gutierrez, J. J.; Ferraris, J. P.; Vardeny, Z. V. Apparent Vibrational Side Bands in Pi-Conjugated Systems: The Case of Distyrylbenzene. *Phys. Rev. B: Condens. Matter Mater. Phys.* **2005**, *71*, 081201.
- (131) Schenning, A. P. H. J.; Jonkheijm, P.; Peeters, E.; Meijer, E. W. Hierarchical Order in Supramolecular Assemblies of Hydrogen-Bonded Oligo(P-Phenylen Vinylene)S. *J. Am. Chem. Soc.* **2001**, *123*, 409–416.
- (132) Meskers, S. C. J.; Bender, M.; Hubner, J.; Romanovskii, Y. V.; Oestreich, M.; Schenning, A. P. H. J.; Meijer, E. W.; Bässler, H. Interchromophoric Coupling in Oligo(P-Phenylenevinylen)-Substituted Poly(Propyleneimine) Dendrimers. *J. Phys. Chem. A* **2001**, *105*, 10220–10229.
- (133) Narwark, O.; Meskers, S. C. J.; Peetz, R.; Thorn-Csanyi, E.; Bässler, H. Spectroscopic Characterization of P-Phenylen Vinylene (Pv) Oligomers. Part I: A Homologous Series of 2,5-Diheptyloxy Substituted Pv-Oligomers. *Chem. Phys.* **2003**, *294*, 1–15.
- (134) Narwark, O.; Gerhard, A.; Meskers, S. C. J.; Brocke, S.; Thorn-Csanyi, E.; Bässler, H. Spectroscopic Characterization of P-Phenylen Vinylene (Pv) Oligomers. Part II: Selected 2,5-Diheptyl Substituted Pv-Oligomers. *Chem. Phys.* **2003**, *294*, 17–30.

- (135) Claudio, G. C.; Bittner, E. R. Excitation Transfer in Aggregated and Linearly Confined Poly(P-Phenylene Vinylene) Chains. *J. Phys. Chem. A* **2003**, *107*, 7092–7100.
- (136) Bjorklund, T. G.; Lim, S.-H.; Bardeen, C. J. The Optical Spectroscopy of Poly(P-Phenylene Vinylene)/Polyvinyl Alcohol Blends: From Aggregates to Isolated Chromophores. *Synth. Met.* **2004**, *142*, 195–200.
- (137) Beljonne, D.; Hennebicq, E.; Daniel, C.; Herz, L. M.; Silva, C.; Scholes, G. D.; Hoeben, F. J. M.; Jonkheijm, P.; Schenning, A. P. H. J.; Meskers, S. C. J.; et al. Excitation Migration Along Oligophenylenevinylene-Based Chiral Stacks: Delocalization Effects on Transport Dynamics. *J. Phys. Chem. B* **2005**, *109*, 10594–10604.
- (138) Lim, S.-H.; Bjorklund, T. G.; Bardeen, C. J. Characterization of Individual Submicron Distyrylbenzene Aggregates Using Temperature Dependent Picosecond Fluorescence and Atomic Force Microscopy. *J. Phys. Chem. B* **2004**, *108*, 4289–4295.
- (139) Shaller, A. D.; Wang, W.; Gan, H. Y.; Li, A. D. Q. Tunable Molecular Assembly Codes Direct Reaction Pathways. *Angew. Chem., Int. Ed.* **2008**, *47*, 7705–7709.
- (140) Chen, Z. J.; Stepanenko, V.; Dehm, V.; Prins, P.; Siebbeles, L. D. A.; Seibt, J.; Marquetand, P.; Engel, V.; Wurthner, F. Photoluminescence and Conductivity of Self-Assembled Pi-Pi Stacks of Perylene Bisimide Dyes. *Chem. - Eur. J.* **2007**, *13*, 436–449.
- (141) Giaimo, J. M.; Lockard, J. V.; Sinks, L. E.; Scott, A. M.; Wilson, T. M.; Wasielewski, M. R. Excited Singlet States of Covalently Bound, Cofacial Dimers and Trimers of Perylene-3,4:9,10-Bis(Dicarboximide)S. *J. Phys. Chem. A* **2008**, *112*, 2322–2330.
- (142) Hariharan, M.; Zheng, Y.; Long, H.; Zeidan, T. A.; Schatz, G. C.; Vura-Weis, J.; Wasielewski, M. R.; Zuo, X.; Tiede, D. M.; Lewis, F. D. Hydrophobic Dimerization and Thermal Dissociation of Perylenediimide-Linked DNA Hairpins. *J. Am. Chem. Soc.* **2009**, *131*, 5920–5929.
- (143) Clark, J.; Chang, J. F.; Spano, F. C.; Friend, R. H.; Silva, C. Determining Exciton Bandwidth and Film Microstructure in Polythiophene Films Using Linear Absorption Spectroscopy. *Appl. Phys. Lett.* **2009**, *94*, 163306.
- (144) Clark, J.; Silva, C.; Friend, R. H.; Spano, F. C. Role of Intermolecular Coupling in the Photophysics of Disordered Organic Semiconductors: Aggregate Emission in Regioregular Polythiophene. *Phys. Rev. Lett.* **2007**, *98*, 206406.
- (145) Spano, F. C.; Clark, J.; Silva, C.; Friend, R. H. Determining Exciton Coherence from the Photoluminescence Spectral Line Shape in Poly(3-Hexylthiophene) Thin Films. *J. Chem. Phys.* **2009**, *130*, 074904.
- (146) Spano, F. C. Modeling Disorder in Polymer Aggregates: The Optical Spectroscopy of Regioregular Poly(3-Hexylthiophene) Thin Films. *J. Chem. Phys.* **2005**, *122*, 234701.
- (147) Spano, F. C. Absorption in Regioregular Poly(3-Hexylthiophene) Thin Films: Fermi Resonances, Interband Coupling and Disorder. *Chem. Phys.* **2006**, *325*, 22–35.
- (148) Panzer, F.; Bassler, H.; Lohwasser, R.; Thelakkat, M.; Kohler, A. The Impact of Polydispersity and Molecular Weight on the Order-Disorder Transition in Poly(3-Hexylthiophene). *J. Phys. Chem. Lett.* **2014**, *5*, 2742–2747.
- (149) Panzer, F.; Sommer, M.; Bassler, H.; Thelakkat, M.; Kohler, A. Spectroscopic Signature of Two Distinct H-Aggregate Species in Poly(3-Hexylthiophene). *Macromolecules* **2015**, *48*, 1543–1553.
- (150) Fulton, R. L.; Gouterman, M. Vibronic Coupling 0.1. Mathematical Treatment for 2 Electronic States. *J. Chem. Phys.* **1961**, *35*, 1059–1071.
- (151) Fulton, R. L.; Gouterman, M. Vibronic Coupling 0.2. Spectra of Dimers. *J. Chem. Phys.* **1964**, *41*, 2280–2286.
- (152) McRae, E. G. Molecular Vibrations in the Exciton Theory for Molecular Aggregates. I. General Theory. *Aust. J. Chem.* **1961**, *14*, 329–343.
- (153) McRae, E. G. Molecular Vibrations in the Exciton Theory for Molecular Aggregates III: Polymeric Systems. *Aust. J. Chem.* **1961**, *14*, 354–371.
- (154) McRae, E. G. Vibronic Interactions in the Theory for Molecular Crystals. *J. Chem. Phys.* **1963**, *39*, 2974–2982.
- (155) McRae, E. G.; Siebrand, W. Vibronic Coupling Criteria in Molecular Crystals. *J. Chem. Phys.* **1964**, *41*, 905–906.
- (156) Witkowski, A.; Moffitt, W. Electronic Spectra of Dimers - Derivation of the Fundamental Vibronic Equation. *J. Chem. Phys.* **1960**, *33*, 872–875.
- (157) Merrifield, R. E. Vibrational Structure of Molecular Exciton States. *J. Chem. Phys.* **1964**, *40*, 445–450.
- (158) Merrifield, R. E. Vibronic States of Dimers. *Radiat. Res.* **1963**, *20*, 154–158.
- (159) Forster, T. *Delocalized Excitation and Excitation Transfer*; Florida State University, Tallahassee, FL, 1965.
- (160) Philpott, M. R. Theory of Coupling of Electronic and Vibrational Excitations in Molecular Crystals and Helical Polymers. *J. Chem. Phys.* **1971**, *55*, 2039–2054.
- (161) Briggs, J. S.; Herzenberg, A. Bandshapes in Polymer Spectra. *Mol. Phys.* **1971**, *21*, 865–879.
- (162) Briggs, J. S.; Herzenberg, A. Sum Rules for Vibronic Spectra of Helical Polymers. *J. Phys. B: At. Mol. Phys.* **1970**, *3*, 1663–1676.
- (163) Levinson, Y. B.; Rashba, E. I. Electron-Phonon and Exciton-Phonon Bound States. *Rep. Prog. Phys.* **1973**, *36*, 1499–1565.
- (164) Hemenger, R. P. Theory of Optical Absorption by Aggregates of Large Molecules. *J. Chem. Phys.* **1977**, *66*, 1795–1801.
- (165) Scherer, P. O. J.; Fischer, S. F. On the Theory of Vibronic Structure of Linear Aggregates. Application to Pseudoisocyanin (Pic). *Chem. Phys.* **1984**, *86*, 269–283.
- (166) Knapp, E. W.; Scherer, P. O. J.; Fischer, S. F. On the Lineshapes of Vibronically Resolved Molecular Aggregate Spectra—Application to Pseudoisocyanin (Pic). *Chem. Phys. Lett.* **1984**, *111*, 481–486.
- (167) Eisfeld, A.; Briggs, J. S. The J-Band of Organic Dyes: Lineshape and Coherence Length. *Chem. Phys.* **2002**, *281*, 61–70.
- (168) Eisfeld, A.; Briggs, J. S. The J- and H-Bands of Organic Dye Aggregates. *Chem. Phys.* **2006**, *324*, 376–384.
- (169) Eisfeld, A.; Kniprath, R.; Briggs, J. S. Theory of the Absorption and Circular Dichorism Spectra of Helical Molecular Aggregates. *J. Chem. Phys.* **2007**, *126*, 104904.
- (170) Walczak, P. B.; Eisfeld, A.; Briggs, J. S. Exchange Narrowing of the J Band of Molecular Dye Aggregates. *J. Chem. Phys.* **2008**, *128*, 044505.
- (171) Roden, J.; Eisfeld, A.; Briggs, J. S. The J- and H-Bands of Dye Aggregate Spectra: Analysis of the Coherent Exciton Scattering (Ces) Approximation. *Chem. Phys.* **2008**, *352*, 258–266.
- (172) Seibt, J.; Marquetand, P.; Engel, V.; Chen, Z.; Dehm, V.; Wurthner, F. On the Geometry Dependence of Molecular Dimer Spectra with an Application to Aggregates of Perylene Bisimide. *Chem. Phys.* **2006**, *328*, 354–362.
- (173) Seibt, J.; Engel, V. Absorption and Emission Spectroscopy of Molecular Trimers: Cyclic Versus Linear Geometries. *Chem. Phys.* **2008**, *347*, 120–126.
- (174) Seibt, J.; Winkler, T.; Renziehausen, K.; Dehm, V.; Würthner, F.; Meyer, H. D.; Engel, V. Vibronic Transitions and Quantum Dynamics in Molecular Oligomers: A Theoretical Analysis with an Application to Aggregates of Perylene Bisimides. *J. Phys. Chem. A* **2009**, *113*, 13475–13482.
- (175) Bruning, C.; Renziehausen, K.; Engel, V. On the Parameterization of Vibronic Hamiltonians for Molecular Aggregates Using Absorption Line-Shapes as an Input. *J. Chem. Phys.* **2013**, *139*, 054303.
- (176) Spano, F. C.; Yamagata, H. Vibronic Coupling in J-Aggregates and Beyond: A Direct Means of Determining the Exciton Coherence Length from the Photoluminescence Spectrum. *J. Phys. Chem. B* **2011**, *115*, 5133–5143.
- (177) Hestand, N. J.; Spano, F. C. The Effect of Chain Bending on the Photophysical Properties of Conjugated Polymers. *J. Phys. Chem. B* **2014**, *118*, 8352–8363.
- (178) Ambrosek, D.; Kohn, A.; Schulze, J.; Kuhn, O. Quantum Chemical Parametrization and Spectroscopic Characterization of the

- Frenkel Exciton Hamiltonian for a J-Aggregate Forming Perylene Bisimide Dye. *J. Phys. Chem. A* **2012**, *116*, 11451–11458.
- (179) Polyutov, S.; Kuhn, O.; Pullerits, T. Exciton-Vibrational Coupling in Molecular Aggregates: Electronic Versus Vibronic Dimer. *Chem. Phys.* **2012**, *394*, 21–28.
- (180) Bloemsma, E. A.; Silvis, M. H.; Stradomska, A.; Knoester, J. Vibronic Effects and Destruction of Exciton Coherence in Optical Spectra of J-Aggregates: A Variational Polaron Transformation Approach. *Chem. Phys.* **2016**, *481*, 250–261.
- (181) Spano, F. C.; Meskers, S. C. J.; Hennebicq, E.; Beljonne, D. Probing Excitation Delocalization in Supramolecular Chiral Stacks by Means of Circularly Polarized Light: Experiment and Modeling. *J. Am. Chem. Soc.* **2007**, *129*, 7044–7054.
- (182) Spano, F. C.; Meskers, S. C. J.; Hennebicq, E.; Beljonne, D. Using Circularly Polarized Luminescence to Probe Exciton Coherence in Disordered Helical Aggregates. *J. Chem. Phys.* **2008**, *129*, 024704.
- (183) Spano, F. C.; Silvestri, L.; Spearman, P.; Raimondo, L.; Tavazzi, S. Reclassifying Exciton-Phonon Coupling in Molecular Aggregates: Evidence of Strong Nonadiabatic Coupling in Oligothiophene Crystals. *J. Chem. Phys.* **2007**, *127*, 184703.
- (184) Kato, T.; Sasaki, F.; Abe, S.; Kobayashi, S. Theoretical Study on the Absorption Spectra of Pseudoisocyanine Bromide (Pic-Br) Molecular J-Aggregates. *Chem. Phys.* **1998**, *230*, 209–221.
- (185) Ritschel, G.; Suess, D.; Möbius, S.; Strunz, W. T.; Eisfeld, A. Non-Markovian Quantum State Diffusion for Temperature-Dependent Linear Spectra of Light Harvesting Aggregates. *J. Chem. Phys.* **2015**, *142*, 034115.
- (186) Zhang, P.-P.; Li, Z.-Z.; Eisfeld, A. Hierarchy of Equations to Calculate the Linear Spectra of Molecular Aggregates: Time-Dependent and Frequency Domain Formulation. *Int. J. Quantum Chem.* **2017**, *117*, e25386.
- (187) Schulze, J.; Torbjörnsson, M.; Kuhn, O.; Pullerits, T. Exciton Coupling Induces Vibronic Hyperchromism in Light-Harvesting Complexes. *New J. Phys.* **2014**, *16*, 13.
- (188) Bittner, E. R.; Karabuniariev, S.; Herz, L. M. Theory of Non-Condon Emission from the Interchain Exciton in Conjugated Polymer Aggregates. *J. Chem. Phys.* **2007**, *126*, 191102.
- (189) Scholes, G. D.; Fleming, G. R.; Chen, L. X.; Aspuru-Guzik, A.; Buchleitner, A.; Coker, D. F.; Engel, G. S.; van Grondelle, R.; Ishizaki, A.; Jonas, D. M.; et al. Using Coherence to Enhance Function in Chemical and Biophysical Systems. *Nature* **2017**, *543*, 647–656.
- (190) Meier, T.; Zhao, Y.; Chernyak, V.; Mukamel, S. Polarons, Localization, and Excitonic Coherence in Superradiance of Biological Antenna Complexes. *J. Chem. Phys.* **1997**, *107*, 3876–3893.
- (191) Strümpfer, J.; Şener, M.; Schulten, K. How Quantum Coherence Assists Photosynthetic Light-Harvesting. *J. Phys. Chem. Lett.* **2012**, *3*, 536–542.
- (192) Jang, S. J.; Newton, M. D.; Silbey, R. J. Multichromophoric Förster Resonance Energy Transfer. *Phys. Rev. Lett.* **2004**, *92*, 218301.
- (193) Rebentrost, P.; Mohseni, M.; Kassal, I.; Lloyd, S.; Aspuru-Guzik, A. Environment-Assisted Quantum Transport. *New J. Phys.* **2009**, *11*, 12.
- (194) Kassal, I.; Yuen-Zhou, J.; Rahimi-Keshari, S. Does Coherence Enhance Transport in Photosynthesis? *J. Phys. Chem. Lett.* **2013**, *4*, 362–367.
- (195) Tempelaar, R.; Spano, F. C.; Knoester, J.; Jansen, T. L. C. Mapping the Evolution of Spatial Exciton Coherence through Time-Resolved Fluorescence. *J. Phys. Chem. Lett.* **2014**, *5*, 1505–1510.
- (196) Merrifield, R. E. Ionized States in a One-Dimensional Molecular Crystal. *J. Chem. Phys.* **1961**, *34*, 1835–1839.
- (197) Hernandez, J. P.; Choi, S. i. Optical Absorption by Charge-Transfer Excitons in Linear Molecular Crystals. *J. Chem. Phys.* **1969**, *50*, 1524–1532.
- (198) Pollans, W. L.; Choi, S. i. Exciton States and Optical Spectra in Linear Molecular Crystals. *J. Chem. Phys.* **1970**, *52*, 3691–3702.
- (199) Petelenz, P. Mixing of Frenkel Excitons and Ionic Excited States of a Linear Molecular Crystal with Two Molecules in the Unit Cell I. General Model. *Phys. Status Solidi B* **1976**, *78*, 489–500.
- (200) Petelenz, P. Mixing of Frenkel Excitons and Ionic Excited States of a Linear Molecular Crystal with Two Molecules in the Unit Cell. II. Physical Consequences. *Phys. Status Solidi B* **1977**, *79*, 61–70.
- (201) Bounds, P. J.; Petelenz, P.; Siebrand, W. Charge-Transfer Excitons in Anthracene-Crystals - a Theoretical Investigation of Their Optical-Absorption and Thermal-Dissociation. *Chem. Phys.* **1981**, *63*, 303–320.
- (202) Petelenz, P.; Smith, V. H. Theoretical Interpretation of the Electroabsorption Spectrum of the Anthracene Crystal. *Chem. Phys.* **1989**, *131*, 409–421.
- (203) Petelenz, P.; Slawik, M.; Yokoi, K.; Zgierski, M. Z. Theoretical Calculation of the Electroabsorption Spectra of Polyacene Crystals. *J. Chem. Phys.* **1996**, *105*, 4427–4440.
- (204) Slawik, M.; Petelenz, P. Theoretical Interpretation of the Electroabsorption Spectra of Polyacene Crystals. II. Charge-Transfer States. *J. Chem. Phys.* **1999**, *111*, 7576–7582.
- (205) Andzejak, M.; Petelenz, P.; Slawik, M.; Munn, R. W. Theoretical Calculation of the Electro-Absorption Spectrum of the Sexithiophene Single Crystal. *J. Chem. Phys.* **2002**, *117*, 1328–1335.
- (206) Stradomska, A.; Kulig, W.; Petelenz, P. Vibronic Coupling in Frenkel and Charge-Transfer States of Oligothiophene Crystals. *Phys. Status Solidi B* **2011**, *248*, 408–411.
- (207) Stradomska, A.; Kulig, W.; Slawik, M.; Petelenz, P. Intermediate Vibronic Coupling in Charge Transfer States: Comprehensive Calculation of Electronic Excitations in Sexithiophene Crystal. *J. Chem. Phys.* **2011**, *134*, 224505.
- (208) Stradomska, A.; Kulig, W.; Slawik, M.; Petelenz, P. Excited-State Polarizability in Crystalline Sexithiophene: Charge-Transfer and Vibronic Effects. *Chem. Phys. Lett.* **2012**, *529*, 27–30.
- (209) Petelenz, B.; Petelenz, P.; Shurvell, H. F.; Smith, V. H. Reconsideration of the Electroabsorption Spectra of the Tetracene and Pentacene Crystals. *Chem. Phys.* **1988**, *119*, 25–39.
- (210) Kazmaier, P. M.; Hoffmann, R. A Theoretical Study of Crystallochromy-Quantum Interference Effects in the Spectra of Perylene Pigments. *J. Am. Chem. Soc.* **1994**, *116*, 9684–9691.
- (211) Hoffmann, M.; Soos, Z. G. Optical Absorption Spectra of the Holstein Molecular Crystal for Weak and Intermediate Electronic Coupling. *Phys. Rev. B: Condens. Matter Mater. Phys.* **2002**, *66*, 024305.
- (212) Hennessy, M. H.; Pascal, R. A.; Soos, Z. G. Vibronic Structure of Frenkel and Charge-Transfer Excitons in Ptcda. *Mol. Cryst. Liq. Cryst. Sci. Technol., Sect. A* **2001**, *355*, 41–63.
- (213) Hennessy, M. H.; Soos, Z. G.; Pascal, R. A.; Girlando, A. Vibronic Structure of Ptcda Stacks: The Exciton-Phonon-Charge-Transfer Dimer. *Chem. Phys.* **1999**, *245*, 199–212.
- (214) Gisslen, L.; Scholz, R. Crystallochromy of Perylene Pigments: Interference between Frenkel Excitons and Charge-Transfer States. *Phys. Rev. B: Condens. Matter Mater. Phys.* **2009**, *80*, 115309.
- (215) Gisslen, L.; Scholz, R. Crystallochromy of Perylene Pigments: Influence of an Enlarged Polyaromatic Core Region. *Phys. Rev. B: Condens. Matter Mater. Phys.* **2011**, *83*, 155311.
- (216) Hoffmann, M.; Schmidt, K.; Fritz, T.; Hasche, T.; Agranovich, V. M.; Leo, K. The Lowest Energy Frenkel and Charge-Transfer Excitons in Quasi-One-Dimensional Structures: Application to Meptcdi and Ptcda Crystals. *Chem. Phys.* **2000**, *258*, 73–96.
- (217) Cornil, J.; Beljonne, D.; Calbert, J. P.; Bredas, J. L. Interchain Interactions in Organic Pi-Conjugated Materials: Impact on Electronic Structure, Optical Response, and Charge Transport. *Adv. Mater.* **2001**, *13*, 1053–1067.
- (218) Beljonne, D.; Cornil, J.; Silbey, R.; Millie, P.; Bredas, J. L. Interchain Interactions in Conjugated Materials: The Exciton Model Versus the Supermolecular Approach. *J. Chem. Phys.* **2000**, *112*, 4749–4758.
- (219) Cornil, J.; dos Santos, D. A.; Crispin, X.; Silbey, R.; Bredas, J. L. Influence of Interchain Interactions on the Absorption and Luminescence of Conjugated Oligomers and Polymers: A Quantum Mechanical Characterization. *J. Am. Chem. Soc.* **1998**, *120*, 1289.
- (220) Mukamel, S.; Tretiak, S.; Wagersreiter, T.; Chernyak, V. Electronic Coherence and Collective Optical Excitations of Conjugated Molecules. *Science* **1997**, *277*, 781–787.

- (221) Tretiak, S.; Zhang, W. M.; Chernyak, V.; Mukamel, S. Excitonic Couplings and Electronic Coherence in Bridged Naphthalene Dimers. *Proc. Natl. Acad. Sci. U. S. A.* **1999**, *96*, 13003–13008.
- (222) Tretiak, S.; Mukamel, S. Density Matrix Analysis and Simulation If Electronic Excitations in Conjugated and Aggregated Molecules. *Chem. Rev.* **2002**, *102*, 3172–3212.
- (223) Yamagata, H.; Pochas, C. M.; Spano, F. C. Designing J- and H-Aggregates through Wave Function Overlap Engineering: Applications to Poly(3-Hexylthiophene). *J. Phys. Chem. B* **2012**, *116*, 14494–14503.
- (224) Yamagata, H.; Norton, J.; Hontz, E.; Olivier, Y.; Beljonne, D.; Bredas, J. L.; Silbey, R. J.; Spano, F. C. The Nature of Singlet Excitons in Oligoacene Molecular Crystals. *J. Chem. Phys.* **2011**, *134*, 204703.
- (225) Yamagata, H.; Maxwell, D. S.; Fan, J.; Kittilstved, K. R.; Briseno, A. L.; Barnes, M. D.; Spano, F. C. Hj-Aggregate Behavior of Crystalline 7,8,15,16-Tetraazaterrylene: Introducing a New Design Paradigm for Organic Materials. *J. Phys. Chem. C* **2014**, *118*, 28842–28854.
- (226) Hestand, N. J.; Yamagata, H.; Xu, B. L.; Sun, D. Z.; Zhong, Y.; Harutyunyan, A. R.; Chen, G. G.; Dai, H. L.; Rao, Y.; Spano, F. C. Polarized Absorption in Crystalline Pentacene: Theory Vs Experiment. *J. Phys. Chem. C* **2015**, *119*, 22137–22147.
- (227) Hestand, N. J.; Spano, F. C. Interference between Coulombic and Ct-Mediated Couplings in Molecular Aggregates: H- to J-Aggregate Transformation in Perylene-Based Pi-Stacks. *J. Chem. Phys.* **2015**, *143*, 244707.
- (228) Hestand, N. J.; Spano, F. C. Molecular Aggregate Photophysics Beyond the Kasha Model: Novel Design Principles for Organic Materials. *Acc. Chem. Res.* **2017**, *50*, 341–350.
- (229) Austin, A.; Hestand, N. J.; McKendry, I. G.; Zhong, C.; Zhu, X.; Zdilla, M. J.; Spano, F. C.; Szarko, J. M. Enhanced Davydov Splitting in Crystals of a Perylene Diimide Derivative. *J. Phys. Chem. Lett.* **2017**, *8*, 1118–1123.
- (230) Hestand, N. J.; Kazantsev, R. V.; Weingarten, A. S.; Palmer, L. C.; Stupp, S. I.; Spano, F. C. Extended-Charge-Transfer Excitons in Crystalline Supramolecular Photocatalytic Scaffolds. *J. Am. Chem. Soc.* **2016**, *138*, 11762–11774.
- (231) Scholes, G. D.; Ghiggino, K. P.; Oliver, A. M.; Paddonrow, M. N. Through-Space and through-Bond Effects on Exciton Interactions in Rigidly Linked Dinaphthyl Molecules. *J. Am. Chem. Soc.* **1993**, *115*, 4345–4349.
- (232) Scholes, G. D.; Ghiggino, K. P.; Oliver, A. M.; Paddonrow, M. N. Intramolecular Electronic Energy Transfer between Rigidly Linked Naphthalene and Anthracene Chromophores. *J. Phys. Chem.* **1993**, *97*, 11871–11876.
- (233) Harcourt, R. D.; Scholes, G. D.; Ghiggino, K. P. Rate Expressions for Excitation Transfer 0.2. Electronic Considerations of Direct and through-Configuration Exciton Resonance Interactions. *J. Chem. Phys.* **1994**, *101*, 10521–10525.
- (234) Scholes, G. D.; Harcourt, R. D.; Ghiggino, K. P. Rate Expressions for Excitation Transfer. Iii. An Ab Initio Study of Electronic Factors in Excitation Transfer and Exciton Resonance Interactions. *J. Chem. Phys.* **1995**, *102*, 9574–9581.
- (235) Harcourt, R. D.; Ghiggino, K. P.; Scholes, G. D.; Speiser, S. On the Origin of Matrix Elements for Electronic Excitation (Energy) Transfer. *J. Chem. Phys.* **1996**, *105*, 1897–1901.
- (236) Ghiggino, K. P.; Yeow, E. K. L.; Haines, D. J.; Scholes, G. D.; Smith, T. A. Mechanisms of Excitation Energy Transport in Macromolecules. *J. Photochem. Photobiol. A* **1996**, *102*, 81–86.
- (237) Clayton, A. H. A.; Scholes, G. D.; Ghiggino, K. P.; PaddonRow, M. N. Through-Bond and through-Space Coupling in Photoinduced Electron and Energy Transfer: An Ab Initio and Semiempirical Study. *J. Phys. Chem.* **1996**, *100*, 10912–10918.
- (238) Hestand, N. J.; Tempelaar, R.; Knoester, J.; Jansen, T. L. C.; Spano, F. C. Exciton Mobility Control through Sub-Angstrom Packing Modifications in Molecular Crystals. *Phys. Rev. B: Condens. Matter Mater. Phys.* **2015**, *91*, 195315.
- (239) Beljonne, D.; Yamagata, H.; Bredas, J. L.; Spano, F. C.; Olivier, Y. Charge-Transfer Excitations Steer the Davydov Splitting and Mediate Singlet Exciton Fission in Pentacene. *Phys. Rev. Lett.* **2013**, *110*, 1.
- (240) Ide, J.; Mereau, R.; Ducasse, L.; Castet, F.; Olivier, Y.; Martinelli, N.; Cornil, J.; Beljonne, D. Supramolecular Organization and Charge Transport Properties of Self-Assembled Pi-Pi Stacks of Perylene Diimide Dyes. *J. Phys. Chem. B* **2011**, *115*, 5593–5603.
- (241) Gregg, B. A.; Kose, M. E. Reversible Switching between Molecular and Charge Transfer Phases in a Liquid Crystalline Organic Semiconductor. *Chem. Mater.* **2008**, *20*, 5235–5239.
- (242) Yamagata, H.; Spano, F. C. Strong Photophysical Similarities between Conjugated Polymers and J-Aggregates. *J. Phys. Chem. Lett.* **2014**, *5*, 622–632.
- (243) Yamagata, H.; Spano, F. C. Vibronic Coupling in Quantum Wires: Applications to Polydiacetylene. *J. Chem. Phys.* **2011**, *135*, 054906.
- (244) Barford, W.; Marcus, M. Perspective: Optical Spectroscopy in Pi-Conjugated Polymers and How It Can Be Used to Determine Multiscale Polymer Structures. *J. Chem. Phys.* **2017**, *146*, 130902.
- (245) Marcus, M.; Coonjobeeharry, J.; Barford, W. Theory of Optical Transitions in Pi-Conjugated Macrocycles. *J. Chem. Phys.* **2016**, *144*, 154102.
- (246) Barford, W.; Marcus, M. Theory of Optical Transitions in Conjugated Polymers. I. Ideal Systems. *J. Chem. Phys.* **2014**, *141*, 164101.
- (247) Marcus, M.; Tozer, O. R.; Barford, W. Theory of Optical Transitions in Conjugated Polymers. II. Real Systems. *J. Chem. Phys.* **2014**, *141*, 164102.
- (248) Barford, W.; Marcus, M. Theory of Optical Transitions in Curved Chromophores. *J. Chem. Phys.* **2016**, *145*, 124111.
- (249) Yamagata, H.; Spano, F. C. Interplay between Intrachain and Interchain Interactions in Semiconducting Polymer Assemblies: The Hj-Aggregate Model. *J. Chem. Phys.* **2012**, *136*, 184901.
- (250) Bassler, A. K. a. H. *Electronic Processes in Organic Semiconductors: An Introduction*; Wiley-VCH, 2015.
- (251) Agranovich, V. M. *Excitations in Organic Solids*; Oxford University Press: New York, NY, 2009.
- (252) Kilina, S.; Kilin, D.; Tretiak, S. Light-Driven and Phonon-Assisted Dynamics in Organic and Semiconductor Nanostructures. *Chem. Rev.* **2015**, *115*, 5929–5978.
- (253) Zhugayevych, A.; Tretiak, S. Theoretical Description of Structural and Electronic Properties of Organic Photovoltaic Materials. *Annu. Rev. Phys. Chem.* **2015**, *66*, 305–330.
- (254) Zhu, T.; Wan, Y.; Huang, L. Direct Imaging of Frenkel Exciton Transport by Ultrafast Microscopy. *Acc. Chem. Res.* **2017**, *50*, 1725–1733.
- (255) Penwell, S. B.; Ginsberg, L. D. S.; Noriega, R.; Ginsberg, N. S. Resolving Ultrafast Exciton Migration in Organic Solids at the Nanoscale. *Nat. Mater.* **2017**, *16*, 1136.
- (256) Mukamel, S.; Abramavicius, D. Many-Body Approaches for Simulating Coherent Nonlinear Spectroscopies of Electronic and Vibrational Excitons. *Chem. Rev.* **2004**, *104*, 2073–2098.
- (257) Mukamel, S.; Abramavicius, D.; Yang, L. J.; Zhuang, W.; Schweigert, I. V.; Voronine, D. V. Coherent Multidimensional Optical Probes for Electron Correlations and Exciton Dynamics: From Nmr to X-Rays. *Acc. Chem. Res.* **2009**, *42*, 553–562.
- (258) Abramavicius, D.; Palmieri, B.; Voronine, D. V.; Sanda, F.; Mukamel, S. Coherent Multidimensional Optical Spectroscopy of Excitons in Molecular Aggregates; Quasiparticle Versus Supermolecule Perspectives. *Chem. Rev.* **2009**, *109*, 2350–2408.
- (259) Frenkel, J. On the Transformation of Light into Heat in Solids. *I. Phys. Rev.* **1931**, *37*, 17–44.
- (260) Spano, F. C. Temperature Dependent Exciton Emission from Herringbone Aggregates of Conjugated Oligomers. *J. Chem. Phys.* **2004**, *120*, 7643–7658.
- (261) Spano, F. C. Temperature Dependent Emission in Disordered Herringbone Aggregates of Conjugated Oligomers. *Phys. Rev. B: Condens. Matter Mater. Phys.* **2005**, *71*, 235208.

- (262) Zhao, Z.; Spano, F. C. Multiple Mode Exciton-Phonon Coupling: Applications to Photoluminescence in Oligothiophene Thin Films. *J. Phys. Chem. C* **2007**, *111*, 6113–6123.
- (263) Czikkely, V.; Forsterling, H. D.; Kuhn, H. Extended Dipole Model for Aggregates of Dye Molecules. *Chem. Phys. Lett.* **1970**, *6*, 207–210.
- (264) Chang, J. C. Monopole Effects on Electronic Excitation Interactions between Large Molecules. I. Application to Energy Transfer in Chlorophylls. *J. Chem. Phys.* **1999**, *67*, 3901–3909.
- (265) Wong, C. Y.; Curutchet, C.; Tretiak, S.; Scholes, G. D. Ideal Dipole Approximation Fails to Predict Electronic Coupling and Energy Transfer between Semiconducting Single-Wall Carbon Nanotubes. *J. Chem. Phys.* **2009**, *130*, 081104.
- (266) Krueger, B. P.; Scholes, G. D.; Fleming, G. R. Calculation of Couplings and Energy-Transfer Pathways between the Pigments of Lh2 by the Ab Initio Transition Density Cube Method. *J. Phys. Chem. B* **1998**, *102*, 5378–5386.
- (267) Beljonne, D.; Pourtois, G.; Silva, C.; Hennebicq, E.; Herz, L. M.; Friend, R. H.; Scholes, G. D.; Setayesh, S.; Mullen, K.; Bredas, J. L. Interchain Vs. Intrachain Energy Transfer in Acceptor-Capped Conjugated Polymers. *Proc. Natl. Acad. Sci. U. S. A.* **2002**, *99*, 10982–10987.
- (268) Madjet, M. E.; Muh, F.; Renger, T. Deciphering the Influence of Short-Range Electronic Couplings on Optical Properties of Molecular Dimers: Application to "Special Pairs" in Photosynthesis. *J. Phys. Chem. B* **2009**, *113*, 12603–12614.
- (269) Beenken, W. J. D.; Pullerits, T. Excitonic Coupling in Polythiophenes: Comparison of Different Calculation Methods. *J. Chem. Phys.* **2004**, *120*, 2490–2495.
- (270) Kistler, K. A.; Spano, F. C.; Matsika, S. A Benchmark of Excitonic Couplings Derived from Atomic Transition Charges. *J. Phys. Chem. B* **2013**, *117*, 2032–2044.
- (271) Siddiqui, S.; Spano, F. C. H- and J-Aggregates of Conjugated Polymers and Oligomers: A Theoretical Investigation. *Chem. Phys. Lett.* **1999**, *308*, 99–105.
- (272) Soos, Z. G.; Hayden, G. W.; McWilliams, P. C. M.; Etemad, S. Excitation Shifts of Parallel Conjugated Polymers Due to P-Electron Dispersion Forces. *J. Chem. Phys.* **1990**, *93*, 7439–7448.
- (273) Manas, E. S.; Spano, F. C. Absorption and Spontaneous Emission in Aggregates of P-Conjugated Molecules. *J. Chem. Phys.* **1998**, *109*, 8087.
- (274) Barford, W. Exciton Transfer Integrals between Polymer Chains. *J. Chem. Phys.* **2007**, *126*, 134905.
- (275) Niles, E. T.; Roehling, J. D.; Yamagata, H.; Wise, A. J.; Spano, F. C.; Moule, A. J.; Grey, J. K. J-Aggregate Behavior in Poly-3-Hexylthiophene Nanofibers. *J. Phys. Chem. Lett.* **2012**, *3*, 259–263.
- (276) Schlosser, D. W.; Philpott, M. R. "Singlet Excitons in Crystalline Naphthalene, Anthracene, Tetracene and Pentacene. *Chem. Phys.* **1980**, *49*, 181–199.
- (277) Devoe, H. Theory of Hypochromism of Biopolymers - Calculated Spectra for DNA. *Ann. N. Y. Acad. Sci.* **1969**, *158*, 298–307.
- (278) Mahler, H. R.; Mehrotra, B. D.; Kline, B. Some Observations on Hypochromism of DNA. *J. Mol. Biol.* **1964**, *9*, 801–811.
- (279) Rhodes, W. Hypochromism and Other Spectral Properties of Helical Polynucleotides. *J. Am. Chem. Soc.* **1961**, *83*, 3609–3617.
- (280) Thiery, J. Verification of Kuhn-Thomas Sum Rule in Framework of Some Recent Polarizability Theories for Molecular Aggregates. *J. Chem. Phys.* **1965**, *43*, 553–560.
- (281) Holstein, T. Studies of Polaron Motion Part 1. The Molecular-Crystal Model. *Ann. Phys.* **1959**, *8*, 325–342.
- (282) Mukamel, S. *Principles of Nonlinear Optical Spectroscopy*; Oxford University Press: New York, NY, 1995.
- (283) Spano, F. C. Absorption and Emission in Oligo-Phenylene Vinylene Nanoaggregates: The Role of Disorder and Structural Defects. *J. Chem. Phys.* **2002**, *116*, 5877–5891.
- (284) Spano, F. C. The Fundamental Photophysics of Conjugated Oligomer Herringbone Aggregates. *J. Chem. Phys.* **2003**, *118*, 981–994.
- (285) Stradomska, A.; Petelenz, P. Intermediate Vibronic Coupling in Sexithiophene Single Crystals. *J. Chem. Phys.* **2009**, *130*, 094705.
- (286) Stradomska, A.; Petelenz, P. Intermediate Vibronic Coupling in Sexithiophene Single Crystals. II. Three-Particle Contributions. *J. Chem. Phys.* **2009**, *131*, 044507.
- (287) Stradomska, A.; Kulig, W.; Slawik, M.; Petelenz, P. Intermediate Vibronic Coupling in Charge Transfer States: Comprehensive Calculation of Electronic Excitations in Sexithiophene Crystal. *J. Chem. Phys.* **2011**, *134*, 224505.
- (288) Meskers, S. C. J.; Janssen, R. A. J.; Haverkort, J. E. M.; Wolter, J. H. Relaxation of Photo-Excitations in Films of Oligo- and Poly-(Para-Phenylene Vinylene) Derivatives. *Chem. Phys.* **2000**, *260*, 415–439.
- (289) Kuhn, O.; Sundstrom, V. Pump-Probe Spectroscopy of Dissipative Energy Transfer Dynamics in Photosynthetic Antenna Complexes: A Density Matrix Approach. *J. Chem. Phys.* **1997**, *107*, 4154–4164.
- (290) Meier, T.; Chernyak, V.; Mukamel, S. Multiple Exciton Coherence Sizes in Photosynthetic Antenna Complexes Viewed by Pump-Probe Spectroscopy. *J. Phys. Chem. B* **1997**, *101*, 7332–7342.
- (291) Dahlbom, M.; Pullerits, T.; Mukamel, S.; Sundstrom, V. Exciton Delocalization in the B850 Light-Harvesting Complex: Comparison of Different Measures. *J. Phys. Chem. B* **2001**, *105*, 5515–5524.
- (292) Tempelaar, R.; Stradomska, A.; Knoester, J.; Spano, F. C. Anatomy of an Exciton: Vibrational Distortion and Exciton Coherence in H- and J-Aggregates. *J. Phys. Chem. B* **2013**, *117*, 457–466.
- (293) Smyth, C.; Fassioli, F.; Scholes, G. D. Measures and Implications of Electronic Coherence in Photosynthetic Light-Harvesting. *Philos. Trans. R. Soc., A* **2012**, *370*, 3728–3749.
- (294) Thouless, D. J. Electrons in Disordered Systems and the Theory of Localization. *Phys. Rep.* **1974**, *13*, 93–142.
- (295) Schreiber, M.; Toyozawa, Y. Numerical Experiments on the Absorption Lineshape of the Exciton under Lattice Vibrations. I. The Overall Lineshape. *J. Phys. Soc. Jpn.* **1982**, *51*, 1528–1536.
- (296) Schreiber, M.; Toyozawa, Y. Numerical Experiments on the Absorption Lineshape of the Exciton under Lattice-Vibrations.2. The Average Oscillator Strength Per State. *J. Phys. Soc. Jpn.* **1982**, *51*, 1537–1543.
- (297) Petelenz, P.; Zgierski, M. Z. Effect of Electric Field on Mixing of Frenkel Excitons and Charge Transfer States of a Linear Molecular Crystal. *Phys. Status Solidi B* **1975**, *69*, 133–143.
- (298) Spano, F. C. Emission from Aggregates of Oligo-Phenylene Vinylenes: A Recipe for Superradiant H-Aggregates. *Chem. Phys. Lett.* **2000**, *331*, 7–13.
- (299) Spano, F. C. Absorption and Emission in Pinwheel Aggregates of Oligo-Phenylene Vinylene Molecules. *J. Chem. Phys.* **2001**, *114*, 5376–5390.
- (300) Pope, M.; Swenberg, C. E. *Electronic Processes in Organic Crystals and Polymers*, 2nd ed.; Oxford University Press: New York, NY, 1999; Vol. S6.
- (301) Simpson, W. T.; Peterson, D. L. *J. Chem. Phys.* **1957**, *26*, 588.
- (302) Langhals, H. Control of the Interactions in Multichromophores: Novel Concepts. Perylene Bis-Imides as Components for Larger Functional Units. *Helv. Chim. Acta* **2005**, *88*, 1309–1343.
- (303) Langhals, H.; Jona, W. Intense Dyes through Chromophore-Chromophore Interactions: Bi- and Trichromophoric Perylene-3,4:9,10-Bis(Dicarboximide)S. *Angew. Chem., Int. Ed.* **1998**, *37*, 952–955.
- (304) Wang, W.; Han, J. J.; Wang, L. Q.; Li, L. S.; Shaw, W. J.; Li, A. D. Q. Dynamic Pi-Pi Stacked Molecular Assemblies Emit from Green to Red Colors. *Nano Lett.* **2003**, *3*, 455–458.
- (305) Wang, W.; Wan, W.; Zhou, H. H.; Niu, S. Q.; Li, A. D. Q. Alternating DNA and Pi-Conjugated Sequences. Thermophilic Foldable Polymers. *J. Am. Chem. Soc.* **2003**, *125*, 5248–5249.
- (306) Wang, W.; Wan, W.; Stachiw, A.; Li, A. D. Q. Foldamers with Hybrid Biological and Synthetic Sequences as Selective DNA Fluorescent Probes. *Biochemistry* **2005**, *44*, 10751–10756.

- (307) Clark, A. E.; Qin, C. Y.; Li, A. D. Q. Beyond Exciton Theory: A Time-Dependent Dft and Franck-Condon Study of Perylene Diimide and Its Chromophoric Dimer. *J. Am. Chem. Soc.* **2007**, *129*, 7586–7595.
- (308) Yamagata, H.; Hestand, N. J.; Spano, F. C.; Köhler, A.; Scharsich, C.; Hoffmann, S. T.; Bässler, H. The Red-Phase of Poly[2-Methoxy-S-(2-Ethylhexyloxy)-1,4-Phenylenevinylene](Meh-Ppv): A Disordered Hj-Aggregate. *J. Chem. Phys.* **2013**, *139*, 114903.
- (309) Kistler, K. A.; Pochas, C. M.; Yamagata, H.; Matsika, S.; Spano, F. C. Absorption, Circular Dichroism, and Photoluminescence in Perylene Diimide Bichromophores: Polarization-Dependent H- and J-Aggregate Behavior. *J. Phys. Chem. B* **2012**, *116*, 77–86.
- (310) Chang, R.; Hsu, J. H.; Fann, W. S.; Liang, K. K.; Chiang, C. H.; Hayashi, M.; Yu, J.; Lin, S. H.; Chang, E. C.; Chuang, K. R.; et al. Experimental and Theoretical Investigations of Absorption and Emission Spectra of the Light-Emitting Polymer Meh-Ppv in Solution. *Chem. Phys. Lett.* **2000**, *317*, 142–152.
- (311) Wykes, M.; Parambil, R.; Beljon, D.; Gierschner, J. Vibronic Coupling in Molecular Crystals: A Franck-Condon Herzberg-Teller Model of H-Aggregate Fluorescence Based on Quantum Chemical Cluster Calculations. *J. Chem. Phys.* **2015**, *143*, 12.
- (312) Robinson, G. W. Intensity Enhancements of Forbidden Electronic Transitions by Weak Intermolecular Interactions. *J. Chem. Phys.* **1967**, *46*, 572–585.
- (313) Small, G. J. Herzberg-Teller Vibronic Coupling and Dushinsky Effect. *J. Chem. Phys.* **1971**, *54*, 3300.
- (314) Petelenz, P.; Andrzejak, M. Vibronic Interpretation of the Low-Energy Absorption Spectrum of the Sexithiophene Single Crystal. *J. Chem. Phys.* **2000**, *113*, 11306–11314.
- (315) Petelenz, P. Davydov Splitting of Herzberg-Teller Induced Vibronic Transitions. *Chem. Phys. Lett.* **1995**, *240*, 605–609.
- (316) Zhao, Z.; Spano, F. C. Vibronic Fine Structure in the Absorption Spectrum of Oligothiophene Thin Films. *J. Chem. Phys.* **2005**, *122*, 114701.
- (317) Wu, C. C.; Korovyanko, O. J.; Delong, M. C.; Vardeny, Z. V.; Ferraris, J. P. Optical Studies of Distyrylbenzene Single Crystals. *Synth. Met.* **2003**, *139*, 735–738.
- (318) Bassler, H. Localized States and Electronic Transport in Single Component Organic Solids with Diagonal Disorder. *Phys. Status Solidi B* **1981**, *107*, 9.
- (319) Knapp, E. W. Lineshapes of Molecular Aggregates. Exchange Narrowing and Intersite Correlation. *Chem. Phys.* **1984**, *85*, 73–82.
- (320) Knoester, J. Nonlinear Optical Line Shapes of Disordered Molecular Aggregates: Motional Narrowing and the Effect of Intersite Correlations. *J. Chem. Phys.* **1993**, *99*, 8466–8479.
- (321) Luer, L.; Rajendran, S. K.; Stoll, T.; Ganzer, L.; Rehault, J.; Coles, D. M.; Lidzey, D.; Virgili, T.; Cerullo, G. Levy Defects in Matrix-Immobilized J Aggregates: Tracing Intra- and Intersegmental Exciton Relaxation. *J. Phys. Chem. Lett.* **2017**, *8*, 547–552.
- (322) Merdasa, A.; Jimenez, A. J.; Camacho, R.; Meyer, M.; Wurthner, F.; Scheblykin, I. G. Single Levy States-Disorder Induced Energy Funnels in Molecular Aggregates. *Nano Lett.* **2014**, *14*, 6774–6781.
- (323) Vlaming, S. M.; Malyshev, V. A.; Eisfeld, A.; Knoester, J. Subdiffusive Exciton Motion in Systems with Heavy-Tailed Disorder. *J. Chem. Phys.* **2013**, *138*, 214316.
- (324) Eisfeld, A.; Vlaming, S. M.; Malyshev, V. A.; Knoester, J. Excitons in Molecular Aggregates with Levy-Type Disorder: Anomalous Localization and Exchange Broadening of Optical Spectra. *Phys. Rev. Lett.* **2010**, *105*, 137402.
- (325) Klugkist, J. A.; Malyshev, V. A.; Knoester, J. Scaling and Universality in the Optics of Disordered Exciton Chains. *Phys. Rev. Lett.* **2008**, *100*, 216403.
- (326) Bakalis, L. D.; Knoester, J. Pump-Probe Spectroscopy and the Exciton Delocalization Length in Molecular Aggregates. *J. Phys. Chem. B* **1999**, *103*, 6620–6628.
- (327) Paquin, F.; Yamagata, H.; Hestand, N. J.; Sakowicz, M.; Bérubé, N.; Côté, M.; Reynolds, L. X.; Haque, S. A.; Stingelin, N.; Spano, F. C.; et al. Two-Dimensional Spatial Coherence of Excitons in Semicrystalline Polymeric Semiconductors: Effect of Molecular Weight. *Phys. Rev. B: Condens. Matter Mater. Phys.* **2013**, *88*, 155202.
- (328) Heijs, D. J.; Malyshev, V. A.; Knoester, J. Decoherence of Excitons in Multichromophore Systems: Thermal Line Broadening and Destruction of Superradiant Emission. *Phys. Rev. Lett.* **2005**, *95*, 177402.
- (329) Heijs, D. J.; Malyshev, V. A.; Knoester, J. Thermal Broadening of the J-Band in Disordered Linear Molecular Aggregates: A Theoretical Study. *J. Chem. Phys.* **2005**, *123*, 144507.
- (330) Arias, D. H.; Stone, K. W.; Vlaming, S. M.; Walker, B. J.; Bawendi, M. G.; Silbey, R. J.; Bulovic, V.; Nelson, K. A. Thermally-Limited Exciton Delocalization in Superradiant Molecular Aggregates. *J. Phys. Chem. B* **2013**, *117*, 4553–4559.
- (331) Bednarz, M.; Malyshev, V. A.; Knoester, J. Temperature Dependent Fluorescence in Disordered Frenkel Chains: Interplay of Equilibration and Local Band-Edge Level Structure. *Phys. Rev. Lett.* **2003**, *91*, 217401.
- (332) Bednarz, M.; Malyshev, V. A.; Knoester, J. Low-Temperature Dynamics of Weakly Localized Frenkel Excitons in Disordered Linear Chains. *J. Chem. Phys.* **2004**, *120*, 3827–3840.
- (333) Spano, F. C. Temperature-Dependent Emission in Disordered Herringbone Aggregates: Stacking Faults and Point Defects. *J. Lumin.* **2005**, *112*, 395–401.
- (334) Lecuiller, R.; Berrehar, J.; Ganiere, J. D.; Lapersonne-Meyer, C.; Lavallard, P.; Schott, M. Fluorescence Yield and Lifetime of Isolated Polydiacetylene Chains: Evidence for a One-Dimensional Exciton Band in a Conjugated Polymer. *Phys. Rev. B: Condens. Matter Mater. Phys.* **2002**, *66*, 125205.
- (335) Dubin, F.; Melet, R.; Barisien, T.; Grousson, R.; Legrand, L.; Schott, M.; Voliotis, V. Macroscopic Coherence of a Single Exciton State in an Organic Quantum Wire. *Nat. Phys.* **2006**, *2*, 32–35.
- (336) Schott, M. Optical Properties of Single Conjugated Polymer Chains (Polydiacetylenes). In *Photophysics of Molecular Materials: From Single Molecules to Single Crystals*; Lanzani, G., Ed.; Wiley-VCH: Weinheim, Germany, 2006; pp 49–145.
- (337) Brown, P. J.; Thomas, S. D.; Kohler, A.; Wilson, J. S.; Kim, J.-S.; Ramsdale, C. M.; Sirringhaus, H.; Friend, R. H. Effect of Interchain Interactions on the Absorption and Emission of Poly(3-Hexylthiophene). *Phys. Rev. B: Condens. Matter Mater. Phys.* **2003**, *67*, 064203.
- (338) Eisfeld, A.; Marquardt, C.; Paulheim, A.; Sokolowski, M. Superradiance from Two Dimensional Brick-Wall Aggregates of Dye Molecules: The Role of Size and Shape for the Temperature Dependence. *Phys. Rev. Lett.* **2017**, *119*, 097402.
- (339) Monshouwer, R.; Abrahamsson, M.; van Mourik, F.; van Grondelle, R. Superradiance and Exciton Delocalization in Bacterial Photosynthetic Light-Harvesting Systems. *J. Phys. Chem. B* **1997**, *101*, 7241–7248.
- (340) Spano, F. C.; Mukamel, S. Superradiance in Molecular Aggregates. *J. Chem. Phys.* **1989**, *91*, 683–700.
- (341) Chachisvilis, M.; Kuhn, O.; Pullerits, T.; Sundstrom, V. Excitons in Photosynthetic Purple Bacteria: Wavelike Motion or Incoherent Hopping? *J. Phys. Chem. B* **1997**, *101*, 7275–7283.
- (342) Hestand, N. J.; Spano, F. C. Determining the Spatial Coherence of Excitons from the Photoluminescence Spectrum in Charge-Transfer J-Aggregates. *Chem. Phys.* **2016**, *481*, 262–271.
- (343) Muller, M.; Paulheim, A.; Eisfeld, A.; Sokolowski, M. Finite Size Line Broadening and Superradiance of Optical Transitions in Two Dimensional Long-Range Ordered Molecular Aggregates. *J. Chem. Phys.* **2013**, *139*, 044302.
- (344) Lim, S.-H.; Bjorklund, T. G.; Spano, F. C.; Bardeen, C. J. Exciton Delocalization and Superradiance in Tetracene Thin Films and Nanoaggregates. *Phys. Rev. Lett.* **2004**, *92*, 107402.
- (345) Ahn, T. S.; Muller, A. M.; Al-Kaysi, R. O.; Spano, F. C.; Norton, J. E.; Beljon, D.; Bredas, J. L.; Bardeen, C. J. Experimental and Theoretical Study of Temperature Dependent Exciton Delocalization and Relaxation in Anthracene Thin Films. *J. Chem. Phys.* **2008**, *128*, 054505.
- (346) Tanaka, S.; Miyata, K.; Sugimoto, T.; Watanabe, K.; Uemura, T.; Takeya, J.; Matsumoto, Y. Enhancement of the Exciton Coherence

- Size in Organic Semiconductor by Alkyl Chain Substitution. *J. Phys. Chem. C* **2016**, *120*, 7941–7948.
- (347) Khachatryan, B.; Nguyen, T. D.; Vardeny, Z. V.; Ehrenfreund, E. Phosphorescence Superradiance in a Pt-Containing P-Conjugated Polymer. *Phys. Rev. B: Condens. Matter Mater. Phys.* **2012**, *86*, 195203.
- (348) Higgins, D. A.; Reid, P. J.; Barbara, P. F. Structure and Exciton Dynamics in J-Aggregates Studied by Polarization-Dependent near-Field Scanning Optical Microscopy. *J. Phys. Chem.* **1996**, *100*, 1174–1180.
- (349) Misawa, K.; Ono, H.; Minoshima, K.; Kobayashi, T. New Model of Excitonic Bands and Molecular Arrangement of Highly Oriented J-Aggregates in Polymer Films Prepared by a Novel Method. *J. Lumin.* **1994**, *60*–*61*, 812–815.
- (350) Misawa, K.; Ono, H.; Minoshima, K.; Kobayashi, T. New Fabrication Method for Highly Oriented J-Aggregates Dispersed in Polymer Films. *Appl. Phys. Lett.* **1993**, *63*, 577–579.
- (351) von Berlepsch, H.; Moller, S.; Dahne, L. Optical Properties of Crystalline Pseudoisocyanine (Pic). *J. Phys. Chem. B* **2001**, *105*, 5689–5699.
- (352) Balzer, F.; Kollmann, H.; Schulz, M.; Schnakenburg, G.; Lutzen, A.; Schmidtmann, M.; Lienau, C.; Silies, M.; Schiek, M. Spotlight on Excitonic Coupling in Polymorphic and Textured Anilino Squaraine Thin Films. *Cryst. Growth Des.* **2017**, *17*, 6455–6466.
- (353) van Hutten, P. F.; Wildeman, J.; Meetsma, A.; Hadzioannou, G. Molecular Packing in Unsubstituted Semiconducting Phenylenevinylene Oligomer and Polymer. *J. Am. Chem. Soc.* **1999**, *121*, 5910–5918.
- (354) Hoekstra, A.; Meertens, P.; Vos, A. Refinement of the Crystal Structure of Trans-Stilbene. The Molecular Structure in the Crystalline and Gaseous Phases. *Acta Crystallogr., Sect. B: Struct. Crystallogr. Cryst. Chem.* **1975**, *31*, 2813–2817.
- (355) Fichou, D. Structural Order in Conjugated Oligothiophenes and Its Implications on Opto-Electronic Devices. *J. Mater. Chem.* **2000**, *10*, 571–588.
- (356) Porzio, W.; Destri, S.; Mascherpa, M.; Bruckner, S. Structural Aspects of Oligothienyl Series from X-Ray Powder Diffraction Data. *Acta Polym.* **1993**, *44*, 266–272.
- (357) Siegrist, T.; Kloc, C.; Laudise, R. A.; Katz, H. E.; Haddon, R. C. Crystal Growth, Structure, and Electronic Band Structure of Alpha-4t Polymorphs. *Adv. Mater.* **1998**, *10*, 379–382.
- (358) Antolini, L.; Horowitz, G.; Kouki, F.; Garnier, F. Polymorphism in Oligothiophenes with an Even Number of Thiophene Subunits. *Adv. Mater.* **1998**, *10*, 382–385.
- (359) Campbell, R. B.; Robertson, J. M.; Trotter, J. Crystal Structure of Hexacene and a Revision of Crystallographic Data for Tetracene and Pentacene. *Acta Crystallogr.* **1962**, *15*, 289.
- (360) Kang, M. J.; Doi, I.; Mori, H.; Miyazaki, E.; Takimiya, K.; Ikeda, M.; Kuwabara, H. Alkylated Dinaphtho[2,3-B:2',3'-F]Thieno[3,2-B]Thiophenes (C-N-Dnts): Organic Semiconductors for High-Performance Thin-Film Transistors. *Adv. Mater.* **2011**, *23*, 1222.
- (361) Fujita, T.; Atahan-Evrenk, S.; Sawaya, N. P. D.; Aspuru-Guzik, A. Coherent Dynamics of Mixed Frenkel and Charge-Transfer Excitons in Dinaphtho[2,3-B:2',3'-F]Thieno[3,2-B]-Thiophene Thin Films: The Importance of Hole Delocalization. *J. Phys. Chem. Lett.* **2016**, *7*, 1374–1380.
- (362) Sanchez-Carrera, R. S.; Atahan, S.; Schrier, J.; Aspuru-Guzik, A. Theoretical Characterization of the Air-Stable, High-Mobility Dinaphtho[2,3-B:2',3'-F]Thieno[3,2-B]-Thiophene Organic Semiconductor. *J. Phys. Chem. C* **2010**, *114*, 2334–2340.
- (363) Spano, F. C.; Siddiqui, S. Exciton-Vibrational Coupling in Pinwheel Aggregates of P-Conjugated Molecules. *Chem. Phys. Lett.* **1999**, *314*, 481.
- (364) Sun, X. H.; Zhao, Z.; Spano, F. C.; Beljonne, D.; Cornil, J.; Shuai, Z.; Bredas, J.-L. Absorption and Emission in Quaterthiényl Thin Films. *Adv. Mater.* **2003**, *15*, 818–821.
- (365) Petelenz, P.; Andrzejak, M. Davydov Splitting in the Sexithiophene Crystal. *Chem. Phys. Lett.* **2001**, *343*, 139–142.
- (366) Kulig, W.; Petelenz, P. Spectral Shape of Intense Exciton Absorption in Oligothiophene Crystals. *Phys. Rev. B: Condens. Matter Mater. Phys.* **2009**, *79*, 094305.
- (367) Stradomska, A.; Kulig, W.; Petelenz, P. Vibronic Coupling in Frenkel and Charge-Transfer States of Oligothiophene Crystals. *Phys. Status Solidi B* **2011**, *248*, 408–411.
- (368) Meinardi, F.; Cerminara, M.; Sassella, A.; Bonifacio, R.; Tubino, R. Superradiance in Molecular H Aggregates. *Phys. Rev. Lett.* **2003**, *91*, 247401–247404.
- (369) Bree, A.; Lyons, L. E. The Intensity of Ultraviolet-Light Absorption by Monocrystals 0.4. Absorption by Naphthacene of Plane-Polarized Light. *J. Chem. Soc.* **1960**, *5206*–5212.
- (370) Voigt, M.; Langner, A.; Schouwink, P.; Lupton, J. M.; Mahrt, R. F.; Sokolowski, M. Picosecond Time Resolved Photoluminescence Spectroscopy of a Tetracene Film on Highly Oriented Pyrolytic Graphite: Dynamical Relaxation, Trap Emission, and Superradiance. *J. Chem. Phys.* **2007**, *127*, 114705.
- (371) Camposeo, A.; Polo, M.; Tavazzi, S.; Silvestri, L.; Spearman, P.; Cingolani, R.; Pisignano, D. Polarized Superradiance from Delocalized Exciton Transitions in Tetracene Single Crystals. *Phys. Rev. B: Condens. Matter Mater. Phys.* **2010**, *81*, 033306.
- (372) Binder, R.; Polkehn, M.; Ma, T. J.; Burghardt, I. Ultrafast Exciton Migration in an Hj-Aggregate: Potential Surfaces and Quantum Dynamics. *Chem. Phys.* **2017**, *482*, 16–26.
- (373) Eder, T.; Stangl, T.; Gmelch, M.; Remmersen, K.; Laux, D.; Hoger, S.; Lupton, J. M.; Vogelsang, J. Switching between H- and J-Type Electronic Coupling in Single Conjugated Polymer Aggregates. *Nat. Commun.* **2017**, *8*, 1641.
- (374) Brinkmann, M. Structure and Morphology Control in Thin Films of Regioregular Poly(3-Hexylthiophene). *J. Polym. Sci., Part B: Polym. Phys.* **2011**, *49*, 1218–1233.
- (375) Peteau, L. A.; Sherwood, G. A.; Werner, J. H.; Shreve, A. P.; Smith, T. M.; Wildeman, J. Visualizing Core-Shell Structure in Substituted Ppv Oligomer Aggregates Using Fluorescence Lifetime Imaging Microscopy (Flim). *J. Phys. Chem. C* **2011**, *115*, 15607–15616.
- (376) So, W. Y.; Hong, J. Y.; Kim, J. J.; Sherwood, G. A.; Chacon-Madrid, K.; Werner, J. H.; Shreve, A. P.; Peteau, L. A.; Wildeman, J. Effects of Solvent Properties on the Spectroscopy and Dynamics of Alkoxy-Substituted Ppv Oligomer Aggregates. *J. Phys. Chem. B* **2012**, *116*, 10504–10513.
- (377) Peteau, L. A.; Chowdhury, S.; Wildeman, J.; Sfeir, M. Y. Exciton-Exciton Annihilation as a Probe of Interchain Interactions in Ppv-Oligomer Aggregates. *J. Phys. Chem. B* **2017**, *121*, 1707–1714.
- (378) Spano, F. C.; Silvestri, L. Multiple Mode Exciton-Vibrational Coupling in H-Aggregates: Synergistic Enhancement of the Quantum Yield. *J. Chem. Phys.* **2010**, *132*, 094704.
- (379) Schiek, M.; Lutzen, A.; Koch, R.; Al-Shamery, K.; Balzer, F.; Frese, R.; Rubahn, H. G. Nanofibers from Functionalized Para-Phenylene Molecules. *Appl. Phys. Lett.* **2005**, *86*, 153107.
- (380) Guha, S.; Graupner, W.; Resel, R.; Chandrasekhar, M.; Chandrasekhar, H. R.; Glaser, R.; Leising, G. Planarity of Para Hexaphenyl. *Phys. Rev. Lett.* **1999**, *82*, 3625–3628.
- (381) Guha, S.; Graupner, W.; Resel, R.; Chandrasekhar, M.; Chandrasekhar, H. R.; Glaser, R.; Leising, G. Tuning Intermolecular Interactions: A Study of the Structural and Vibrational Properties of P-Hexaphenyl under Pressure. *J. Phys. Chem. A* **2001**, *105*, 6203–6211.
- (382) Adachi, T.; Vogelsang, J.; Lupton, J. M. Chromophore Bending Controls Fluorescence Lifetime in Single Conjugated Polymer Chains. *J. Phys. Chem. Lett.* **2014**, *5*, 2165–2170.
- (383) Alfonso-Hernandez, L.; Nelson, T.; Gelin, M. F.; Lupton, J. M.; Tretiak, S.; Fernandez-Alberti, S. Interference of Interchromophoric Energy-Transfer Pathways in  $\Pi$ -Conjugated Macrocycles. *J. Phys. Chem. Lett.* **2016**, *7*, 4936–4944.
- (384) Thiessen, A.; Würsch, D.; Jester, S.-S.; Aggarwal, A. V.; Idelson, A.; Bange, S.; Vogelsang, J.; Höger, S.; Lupton, J. M. Exciton Localization in Extended  $\Pi$ -Electron Systems: Comparison of Linear and Cyclic Structures. *J. Phys. Chem. B* **2015**, *119*, 9949–9958.

- (385) Gong, J. Q.; Favereau, L.; Anderson, H. L.; Herz, L. M. Breaking the Symmetry in Molecular Nanorings. *J. Phys. Chem. Lett.* **2016**, *7*, 332–338.
- (386) Gong, J. Q.; Parkinson, P.; Kondratuk, D. V.; Gil-Ramírez, G.; Anderson, H. L.; Herz, L. M. Structure-Directed Exciton Dynamics in Templatized Molecular Nanorings. *J. Phys. Chem. C* **2015**, *119*, 6414–6420.
- (387) Parkinson, P.; Kondratuk, D. V.; Menelaou, C.; Gong, J. Q.; Anderson, H. L.; Herz, L. M. Chromophores in Molecular Nanorings: When Is a Ring a Ring? *J. Phys. Chem. Lett.* **2014**, *5*, 4356–4361.
- (388) Kim, T.-W.; Kim, W.; Park, K. H.; Kim, P.; Cho, J.-W.; Shimizu, H.; Iyoda, M.; Kim, D. Chain-Length-Dependent Exciton Dynamics in Linear Oligothiophenes Probed Using Ensemble and Single-Molecule Spectroscopy. *J. Phys. Chem. Lett.* **2016**, *7*, 452–458.
- (389) Park, K. H.; Cho, J.-W.; Kim, T.-W.; Shimizu, H.; Nakao, K.; Iyoda, M.; Kim, D. Defining Cyclic–Acyclic Exciton Transition at the Single-Molecule Level: Size-Dependent Conformational Heterogeneity and Exciton Delocalization in Ethynylene-Bridged Cyclic Oligothiophenes. *J. Phys. Chem. Lett.* **2016**, *7*, 1260–1266.
- (390) Kim, P.; Park, K. H.; Kim, W.; Tamachi, T.; Iyoda, M.; Kim, D. Relationship between Dynamic Planarization Processes and Exciton Delocalization in Cyclic Oligothiophenes. *J. Phys. Chem. Lett.* **2015**, *6*, 451–456.
- (391) Iyoda, M. Syntheses, Structures, and Supramolecular Properties of Giant  $\Pi$ -Expanded Macrocyclic Oligothiophenes. *Heteroat. Chem.* **2007**, *18*, 460–466.
- (392) Rossi, G.; Chance, R. R.; Silbey, R. Conformational Disorder in Conjugated Polymers. *J. Chem. Phys.* **1989**, *90*, 7594–7601.
- (393) Soos, Z. G.; Schweizer, K. S. Absorption Spectrum of Flexible Conjugated Polymers - the Weak Disorder Limit. *Chem. Phys. Lett.* **1987**, *139*, 196–200.
- (394) Hoeben, F. J. M.; Jonkheijm, P.; Meijer, E. W.; Schenning, A. P. H. J. About Supramolecular Assemblies of Pi-Conjugated Systems. *Chem. Rev.* **2005**, *105*, 1491–1546.
- (395) Jeukens, C.; Jonkheijm, P.; Wijnen, F. J. P.; Gielen, J. C.; Christianen, P. C. M.; Schenning, A.; Meijer, E. W.; Maan, J. C. Polarized Emission of Individual Self-Assembled Oligo(P-Phenylenevinylen)-Based Nanofibers on a Solid Support. *J. Am. Chem. Soc.* **2005**, *127*, 8280–8281.
- (396) Chang, M. H.; Hoeben, F. J. M.; Jonkheijm, P.; Schenning, A.; Meijer, E. W.; Silva, C.; Herz, L. M. Influence of Mesoscopic Ordering on the Photoexcitation Transfer Dynamics in Supramolecular Assemblies of Oligo-P-Phenylenevinylylene. *Chem. Phys. Lett.* **2006**, *418*, 196–201.
- (397) Iwaura, R.; Hoeben, F. J. M.; Masuda, M.; Schenning, A.; Meijer, E. W.; Shimizu, T. Molecular-Level Helical Stack of a Nucleotide-Appended Oligo(P-Phenylenevinylylene) Directed by Supramolecular Self-Assembly with a Complementary Oligonucleotide as a Template. *J. Am. Chem. Soc.* **2006**, *128*, 13298–13304.
- (398) Gonzalez-Rodriguez, D.; Schenning, A. Hydrogen-Bonded Supramolecular Pi-Functional Materials. *Chem. Mater.* **2011**, *23*, 310–325.
- (399) Herz, L. M.; Daniel, C.; Silva, C.; Hoeben, F. J. M.; Schenning, A. P. H. J.; Meijer, E. W.; Friend, R. H.; Phillips, R. T. Fast Exciton Diffusion in Chiral Stacks of Conjugated P-Phenylen Vinylene Oligomers. *Phys. Rev. B: Condens. Matter Mater. Phys.* **2003**, *68*, 045203.
- (400) Daniel, C.; Herz, L. M.; Silva, C.; Hoeben, F. J. M.; Jonkheijm, P.; Schenning, A. P. H. J.; Meijer, E. W. Exciton Bimolecular Annihilation Dynamics in Supramolecular Nanostructures of Conjugated Oligomers. *Phys. Rev. B: Condens. Matter Mater. Phys.* **2003**, *68*, 235212.
- (401) Westenhoff, S.; Daniel, C.; Friend, R. H.; Silva, C.; Sundstrom, V.; Yartsev, A. Exciton Migration in a Polythiophene: Probing the Spatial and Energy Domain by Line-Dipole Förster-Type Energy Transfer. *J. Chem. Phys.* **2005**, *122*, 094903.
- (402) Billsten, H. H.; Sundstrom, V.; Polivka, T. Self-Assembled Aggregates of the Carotenoid Zeaxanthin: Time-Resolved Study of Excited States. *J. Phys. Chem. A* **2005**, *109*, 1521–1529.
- (403) Polivka, T.; Sundstrom, V. Ultrafast Dynamics of Carotenoid Excited States - from Solution to Natural and Artificial Systems. *Chem. Rev.* **2004**, *104*, 2021–2071.
- (404) Simonyi, M.; Bikadi, Z.; Zsila, F.; Deli, J. Supramolecular Exciton Chirality of Carotenoid Aggregates. *Chirality* **2003**, *15*, 680–698.
- (405) Spano, F. C.; Zhao, Z.; Meskers, S. C. J. Analysis of the Vibronic Fine Structure in Circularly Polarized Emission Spectra from Chiral Molecular Aggregates. *J. Chem. Phys.* **2004**, *120*, 10594–10604.
- (406) van Dijk, L.; Bobbert, P. A.; Spano, F. C. Optical Spectra and Stokes Shift in Double-Stranded Helical Supramolecular Assemblies. *J. Phys. Chem. B* **2009**, *113*, 9708–9717.
- (407) van Dijk, L.; Bobbert, P. A.; Spano, F. C. Extreme Sensitivity of Circular Dichroism to Long-Range Excitonic Couplings in Helical Supramolecular Assemblies. *J. Phys. Chem. B* **2010**, *114*, 817–825.
- (408) Tempelaar, R.; Stradomska, A.; Knoester, J.; Spano, F. C. Circularly Polarized Luminescence as a Probe for Long-Range Interactions in Molecular Aggregates. *J. Phys. Chem. B* **2011**, *115*, 10592–10603.
- (409) Eisfeld, A.; Seibt, J.; Engel, V. On the Inversion of Geometric Parameters from Absorption and Circular Dichroism Spectroscopy of Molecular Dimers. *Chem. Phys. Lett.* **2008**, *467*, 186–190.
- (410) Seibt, J.; Dehm, V.; Wurthner, F.; Engel, V. Circular Dichroism Spectroscopy of Small Molecular Aggregates: Dynamical Features and Size Effects. *J. Chem. Phys.* **2008**, *128*, 204303.
- (411) Seibt, J.; Engel, V. On the Calculation of Circular Dichroism Spectra Using Quantum Wave-Packet Dynamics with an Application to Molecular Dimers. *J. Chem. Phys.* **2007**, *126*, 074110.
- (412) Padula, D.; Santoro, F.; Pescitelli, G. A Simple Dimeric Model Accounts for the Vibronic Ecd Spectra of Chiral Polythiophenes in Their Aggregated States. *RSC Adv.* **2016**, *6*, 37938–37943.
- (413) Padula, D.; Picconi, D.; Lami, A.; Pescitelli, G.; Santoro, F. Electronic Circular Dichroism in Exciton-Coupled Dimers: Vibronic Spectra from a General All-Coordinates Quantum-Dynamical Approach. *J. Phys. Chem. A* **2013**, *117*, 3355–3368.
- (414) Pescitelli, G.; Padula, D.; Santoro, F. Intermolecular Exciton Coupling and Vibronic Effects in Solid-State Circular Dichroism: A Case Study. *Phys. Chem. Chem. Phys.* **2013**, *15*, 795–802.
- (415) Fujimoto, K. J.; Balashov, S. P. Vibronic Coupling Effect on Circular Dichroism Spectrum: Carotenoid-Retinal Interaction in Xanthorhodopsin. *J. Chem. Phys.* **2017**, *146*, 095101.
- (416) Lewis, F. D.; Liu, X. Y.; Wu, Y. S.; Zuo, X. B. Stepwise Evolution of the Structure and Electronic Properties of DNA. *J. Am. Chem. Soc.* **2003**, *125*, 12729–12731.
- (417) Matile, S.; Berova, N.; Nakanishi, K.; Fleischhauer, J.; Woody, R. W. Structural Studies by Exciton Coupled Circular Dichroism over a Large Distance: Porphyrin Derivatives of Steroids, Dimeric Steroids, and Brevetoxin B. *J. Am. Chem. Soc.* **1996**, *118*, 5198–5206.
- (418) Harada, N.; Chen, S. L.; Nakanishi, K. Quantitative Definition of Exciton Chirality and Distant Effect in Exciton Chirality Method. *J. Am. Chem. Soc.* **1975**, *97*, 5345–5352.
- (419) Tsubaki, K.; Takaishi, K.; Tanaka, H.; Miura, M.; Kawabata, T. Long-Range Exciton-Coupled Circular Dichroism: Application for Determination of the Absolute Configuration in Oligonaphthalenes. *Org. Lett.* **2006**, *8*, 2587–2590.
- (420) Langhals, H.; Hofer, A.; Bernhard, S.; Siegel, J. S.; Mayer, P. Axially Chiral Bichromophoric Fluorescent Dyes. *J. Org. Chem.* **2011**, *76*, 990–992.
- (421) Rodger, A.; Norden, B. *Circular Dichroism and Linear Dichroism*; Oxford University Press: Oxford, U.K., 1997.
- (422) Spano, F. C.; Meskers, S. C. J.; Hennebicq, E.; Beljonne, D. Probing Excitation Delocalization in Supramolecular Chiral Stacks by Means of Circularly Polarized Light: Experiment and Modeling (Vol 129, Pg 7044, 2007). *J. Am. Chem. Soc.* **2007**, *129*, 16278–16278.
- (423) The factor of 1/4 in the rotational line strength was inadvertently omitted from the expression in ref 91 and ref 182.
- (424) Didraga, C.; Klugkist, J. A.; Knoester, J. Optical Properties of Helical Cylindrical Molecular Aggregates: The Homogeneous Limit. *J. Phys. Chem. B* **2002**, *106*, 11474–11486.

- (425) Burin, A. L.; Armbruster, M. E.; Hariharan, M.; Lewis, F. D. Sum Rules and Determination of Exciton Coupling Using Absorption and Circular Dichroism Spectra of Biological Polymers. *Proc. Natl. Acad. Sci. U. S. A.* **2009**, *106*, 989–994.
- (426) Didraga, C.; Knoester, J. Optical Spectra and Localization of Excitons in Inhomogeneous Helical Cylindrical Aggregates. *J. Chem. Phys.* **2004**, *121*, 10687–10698.
- (427) Somsen, O. J. G.; vanGrondelle, R.; vanAmerongen, H. Spectral Broadening of Interacting Pigments: Polarized Absorption by Photosynthetic Proteins. *Biophys. J.* **1996**, *71*, 1934–1951.
- (428) Riehl, J. P.; Richardson, F. S. Circularly Polarized Luminescence Spectroscopy. *Chem. Rev.* **1986**, *86*, 1–16.
- (429) In some early works such as refs 91 and 182, the factor of 4 appearing in the expression for  $g_{\text{lum}}$  (and also  $g_{\text{abs}}$ ) was rolled into the rotational line strength.
- (430) Law, K. Y. Organic Photoconductive Materials: Recent Trends and Developments. *Chem. Rev.* **1993**, *93*, 449–486.
- (431) Borsenberger, P. M.; Weiss, D. S. *Handbook of Imaging Materials*; CRC Press, 2001; pp 369.
- (432) Borsenberger, P. M. *Organic Photoreceptors for Xerography*; CRC Press, 1998; Vol. 59.
- (433) Saito, T.; Sisk, W.; Kobayashi, T.; Suzuki, S.; Iwayanagi, T. Photocarrier Generation Processes of Phthalocyanines Studied by Photocurrent and Electroabsorption Measurements. *J. Phys. Chem.* **1993**, *97*, 8026–8031.
- (434) Tokura, Y.; Koda, T.; Iyechika, Y.; Kuroda, H. Electro-Reflectance Spectra of Charge-Transfer Excitations in Copper Phthalocyanine Single Crystals. *Chem. Phys. Lett.* **1983**, *102*, 174–178.
- (435) Klebe, G.; Graser, F.; Hädicke, E.; Berndt, J. Crystallochromy as a Solid-State Effect: Correlation of Molecular Conformation, Crystal Packing and Colour in Perylene-3,4:9,10-Bis(Dicarboximide) Pigments. *Acta Crystallogr., Sect. B: Struct. Sci.* **1989**, *45*, 69–77.
- (436) Graser, F.; Hädicke, E. Kristallstruktur Und Farbe Bei Perylen-3, 4:9, 10-Bis (Dicarboximid)-Pigmenten. *Liebigs Ann. Chem.* **1980**, *1980*, 1994–2011.
- (437) Graser, F.; Hädicke, E. Kristallstruktur Und Farbe Bei Perylen-3, 4:9, 10-Bis (Dicarboximid)-Pigmenten, 2. *Liebigs Ann. Chem.* **1984**, *1984*, 483–494.
- (438) Hädicke, E.; Graser, F. Structures of Eleven Perylene-3, 4:9, 10-Bis (Dicarboximide) Pigments. *Acta Crystallogr., Sect. C: Cryst. Struct. Commun.* **1986**, *42*, 189–195.
- (439) Hädicke, E.; Graser, F. Structures of Three Perylene-3, 4, 9, 10-Bis (Dicarboximide) Pigments. *Acta Crystallogr., Sect. C: Cryst. Struct. Commun.* **1986**, *42*, 195–198.
- (440) Buncel, E.; Mckerrow, A. J.; Kazmaier, P. M. Solvent-Controlled Aggregation of a Photoconductive Dye. *J. Chem. Soc., Chem. Commun.* **1992**, 1242–1243.
- (441) Kitamura, C.; Abe, Y.; Ohara, T.; Yoneda, A.; Kawase, T.; Kobayashi, T.; Naito, H.; Komatsu, T. Synthesis and Crystallochromy of 1,4,7,10-Tetraalkyltetracenes: Tuning of Solid-State Optical Properties of Tetracenes by Alkyl Side-Chain Length. *Chem. - Eur. J.* **2010**, *16*, 890–898.
- (442) Kitamura, C.; Takenaka, A.; Kawase, T.; Kobayashi, T.; Naito, H. Octaalkyl Tetracene-1,2,3,4,7,8,9,10-Octacarboxylates: Synthesis by Twofold [2 + 2+2] Cycylation and Crystallochromy. *Chem. Commun.* **2011**, *47*, 6653–6655.
- (443) Shockley, W.; Queisser, H. J. Detailed Balance Limit of Efficiency of P-N Junction Solar Cells. *J. Appl. Phys.* **1961**, *32*, 510–519.
- (444) Hanna, M. C.; Nozik, A. J. Solar Conversion Efficiency of Photovoltaic and Photoelectrolysis Cells with Carrier Multiplication Absorbers. *J. Appl. Phys.* **2006**, *100*, 074510.
- (445) Feng, X. T.; Luzanov, A. V.; Krylov, A. I. Fission of Entangled Spins: An Electronic Structure Perspective. *J. Phys. Chem. Lett.* **2013**, *4*, 3845–3852.
- (446) Smith, M. B.; Michl, J. Singlet Fission. *Chem. Rev.* **2010**, *110*, 6891–6936.
- (447) Smith, M. B.; Michl, J. Recent Advances in Singlet Fission. *Annu. Rev. Phys. Chem.* **2013**, *64*, 361–386.
- (448) Král, K. A Note on Triplet-Triplet Fission of Singlet Excitons in Molecular Crystals. *Czech. J. Phys.* **1972**, *22*, 566–571.
- (449) Le, A. K.; Bender, J. A.; Arias, D. H.; Cotton, D. E.; Johnson, J. C.; Roberts, S. T. Singlet Fission Involves an Interplay between Energetic Driving Force and Electronic Coupling in Perylenediimide Films. *J. Am. Chem. Soc.* **2018**, *140*, 814–826.
- (450) Berkelbach, T. C.; Hybertsen, M. S.; Reichman, D. R. Microscopic Theory of Singlet Exciton Fission. III. Crystalline Pentacene. *J. Chem. Phys.* **2014**, *141*, 074705.
- (451) Berkelbach, T. C.; Hybertsen, M. S.; Reichman, D. R. Microscopic Theory of Singlet Exciton Fission. I. General Formulation. *J. Chem. Phys.* **2013**, *138*, 114102.
- (452) Berkelbach, T. C.; Hybertsen, M. S.; Reichman, D. R. Microscopic Theory of Singlet Exciton Fission. II. Application to Pentacene Dimers and the Role of Superexchange. *J. Chem. Phys.* **2013**, *138*, 114103.
- (453) Margulies, E. A.; Miller, C. E.; Wu, Y.; Ma, L.; Schatz, G. C.; Young, R. M.; Wasielewski, M. R. Enabling Singlet Fission by Controlling Intramolecular Charge Transfer in  $\pi$ -Stacked Covalent Terrylenediimide Dimers. *Nat. Chem.* **2016**, *8*, 1120–1125.
- (454) Margulies, E. A.; Logsdon, J. L.; Miller, C. E.; Ma, L.; Simonoff, E.; Young, R. M.; Schatz, G. C.; Wasielewski, M. R. Direct Observation of a Charge-Transfer State Preceding High-Yield Singlet Fission in Terrylenediimide Thin Films. *J. Am. Chem. Soc.* **2017**, *139*, 663–671.
- (455) Gao, F.; Zhao, Y.; Liang, W. Vibronic Spectra of Perylene Bisimide Oligomers: Effects of Intermolecular Charge-Transfer Excitation and Conformational Flexibility. *J. Phys. Chem. B* **2011**, *115*, 2699–2708.
- (456) Lalov, I. J.; Supritz, C.; Reineker, P. Vibronic Spectra of Charge Transfer Excitons and of Mixed Charge Transfer and Frenkel Excitons. *Chem. Phys.* **2007**, *332*, 108–114.
- (457) Lalov, I. J.; Warns, C.; Reineker, P. Model of Mixed Frenkel and Charge-Transfer Excitons in Donor-Acceptor Molecular Crystals: Investigation of Vibronic Spectra. *New J. Phys.* **2008**, *10*, 25.
- (458) Fink, R. F.; Seibt, J.; Engel, V.; Renz, M.; Kaupp, M.; Lochbrunner, S.; Zhao, H. M.; Pfister, J.; Würthner, F.; Engels, B. Exciton Trapping in Pi-Conjugated Materials: A Quantum-Chemistry-Based Protocol Applied to Perylene Bisimide Dye Aggregates. *J. Am. Chem. Soc.* **2008**, *130*, 12858–12859.
- (459) Schubert, A.; Settels, V.; Liu, W.; Würthner, F.; Meier, C.; Fink, R. F.; Schindlbeck, S.; Lochbrunner, S.; Engels, B.; Engel, V. Ultrafast Exciton Self-Trapping Upon Geometry Deformation in Perylene-Based Molecular Aggregates. *J. Phys. Chem. Lett.* **2013**, *4*, 792–796.
- (460) Selig, U.; Nuernberger, P.; Dehm, V.; Settels, V.; Gsanger, M.; Engels, B.; Würthner, F.; Brixner, T. Similarities and Differences in the Optical Response of Perylene-Based Hetero-Bichromophores and Their Monomeric Units. *ChemPhysChem* **2013**, *14*, 1413–1422.
- (461) Settels, V.; Schubert, A.; Tafipolski, M.; Liu, W.; Stehr, V.; Topczak, A. K.; Pflaum, J.; Deibel, C.; Fink, R. F.; Engel, V.; et al. Identification of Ultrafast Relaxation Processes as a Major Reason for Inefficient Exciton Diffusion in Perylene-Based Organic Semiconductors. *J. Am. Chem. Soc.* **2014**, *136*, 9327–9337.
- (462) Engels, B.; Engel, V. The Dimer-Approach to Characterize Opto-Electronic Properties of and Exciton Trapping and Diffusion in Organic Semiconductor Aggregates and Crystals. *Phys. Chem. Chem. Phys.* **2017**, *19*, 12604–12619.
- (463) Wise, A. J.; Zhang, Y.; Fan, J.; Wudl, F.; Briseno, A. L.; Barnes, M. D. Spectroscopy of Discrete Vertically Oriented Single-Crystals of N-Type Tetraazaterrylene: Understanding the Role of Defects in Molecular Semiconductor Photovoltaics. *Phys. Chem. Chem. Phys.* **2014**, *16*, 15825–15830.
- (464) Deibel, C.; Mack, D.; Gorenflo, J.; Scholl, A.; Krause, S.; Reinert, F.; Rauh, D.; Dyakonov, V. Energetics of Excited States in the Conjugated Polymer Poly(3-Hexylthiophene). *Phys. Rev. B: Condens. Matter Mater. Phys.* **2010**, *81*, 085202.
- (465) Sirringhaus, H.; Sakanoue, T.; Chang, J.-F. Charge-Transport Physics of High-Mobility Molecular Semiconductors. *Phys. Status Solidi B* **2012**, *249*, 1655–1676.

- (466) Zhao, Y.; Liang, W. Charge Transfer in Organic Molecules for Solar Cells: Theoretical Perspective. *Chem. Soc. Rev.* **2012**, *41*, 1075–1087.
- (467) Ortmann, F.; Bechstedt, F.; Hannewald, K. Charge Transport in Organic Crystals: Theory and Modelling. *Phys. Status Solidi B* **2011**, *248*, 511–525.
- (468) Luzanov, A. V.; Casanova, D.; Feng, X. T.; Krylov, A. I. Quantifying Charge Resonance and Multiexciton Character in Coupled Chromophores by Charge and Spin Cumulant Analysis. *J. Chem. Phys.* **2015**, *142*, 224104.
- (469) Pieniazek, P. A.; Krylov, A. I.; Bradforth, S. E. Electronic Structure of the Benzene Dimer Cation. *J. Chem. Phys.* **2007**, *127*, 044317.
- (470) Senthilkumar, K.; Grozema, F. C.; Bickelhaupt, F. M.; Siebbeles, L. D. A. Charge Transport in Columnar Stacked Triphenylenes: Effects of Conformational Fluctuations on Charge Transfer Integrals and Site Energies. *J. Chem. Phys.* **2003**, *119*, 9809–9817.
- (471) Valeev, E. F.; Coropceanu, V.; da Silva, D. A.; Salman, S.; Bredas, J. L. Effect of Electronic Polarization on Charge-Transport Parameters in Molecular Organic Semiconductors. *J. Am. Chem. Soc.* **2006**, *128*, 9882–9886.
- (472) Mikolajczyk, M. M.; Zaleśny, R.; Czyżnikowska, Ż.; Toman, P.; Leszczynski, J.; Bartkowiak, W. Long-Range Corrected Dft Calculations of Charge-Transfer Integrals in Model Metal-Free Phthalocyanine Complexes. *J. Mol. Model.* **2011**, *17*, 2143–2149.
- (473) Tibergien, A.; Delacote, G. Evaluation of Crystalline Tetracene Triplet Davydov Splitting. *Chem. Phys. Lett.* **1971**, *8*, 88–90.
- (474) Petelenz, P.; Smith, V. H. Theoretical Interpretation of the Electroabsorption Spectrum of the Anthracene Crystal. *Chem. Phys.* **1989**, *131*, 409–421.
- (475) Heinemeyer, U.; Scholz, R.; Gisslen, L.; Alonso, M. I.; Osso, J. O.; Garriga, M.; Hinderhofer, A.; Kytka, M.; Kowarik, S.; Gerlach, A.; Schreiber, F. Exciton-Phonon Coupling in Diindenoperylene Thin Films. *Phys. Rev. B: Condens. Matter Mater. Phys.* **2008**, *78*, 085210.
- (476) Loutfy, R. O.; Hsiao, C. K.; Kazmaier, P. M. Photoconductivity of Organic Particle Dispersions - Squaraine Dyes. *Photogr. Sci. Eng.* **1983**, *27*, 5–9.
- (477) Dulmage, W.; Light, W.; Marino, S.; Salzberg, C.; Smith, D.; Staudenmayer, W. An Aggregate Organic Photoconductor. I. Chemical Composition, Preparation, Physical Structure, and Optical Properties. *J. Appl. Phys.* **1978**, *49*, 5543–5554.
- (478) Mizuguchi, J.; Rochat, A. C. A New near-Infrared Photoreceptor Based on 1,4-Dithioketo-3,6-Diphenyl-Pyrrolo-3,4-C-Pyrrole. *J. Imaging Sci.* **1988**, *32*, 135–140.
- (479) Bredas, J.-L.; Norton, J. E.; Cornil, J.; Coropceanu, V. Molecular Understanding of Organic Solar Cells: The Challenges. *Acc. Chem. Res.* **2009**, *42*, 1691–1699.
- (480) Tempelaar, R.; Koster, L. J. A.; Havenith, R. W. A.; Knoester, J.; Jansen, T. L. C. Charge Recombination Suppressed by Destructive Quantum Interference in Heterojunction Materials. *J. Phys. Chem. Lett.* **2016**, *7*, 198–203.
- (481) Aragó, J.; Troisi, A. Dynamics of the Excitonic Coupling in Organic Crystals. *Phys. Rev. Lett.* **2015**, *114*, 026402.
- (482) Aragó, J.; Troisi, A. Regimes of Exciton Transport in Molecular Crystals in the Presence of Dynamic Disorder. *Adv. Funct. Mater.* **2016**, *26*, 2316–2325.
- (483) Fornari, R. P.; Aragó, J.; Troisi, A. Exciton Dynamics in Phthalocyanine Molecular Crystals. *J. Phys. Chem. C* **2016**, *120*, 7987–7996.
- (484) Womick, J. M.; Moran, A. M. Vibronic Enhancement of Exciton Sizes and Energy Transport in Photosynthetic Complexes. *J. Phys. Chem. B* **2011**, *115*, 1347–1356.
- (485) Dean, J. C.; Mirkovic, T.; Toa, Z. S. D.; Oblinsky, D. G.; Scholes, G. D. Vibronic Enhancement of Algae Light Harvesting. *Chem.* **2016**, *1*, 858–872.
- (486) Lee, M. H.; Troisi, A. Vibronic Enhancement of Excitation Energy Transport: Interplay between Local and Non-Local Exciton-Phonon Interactions. *J. Chem. Phys.* **2017**, *146*, 075101.
- (487) Abramavicius, D.; Valkunas, L. Role of Coherent Vibrations in Energy Transfer and Conversion in Photosynthetic Pigment-Protein Complexes. *Photosynth. Res.* **2016**, *127*, 33–47.
- (488) O'Reilly, E. J.; Olaya-Castro, A. Non-Classicality of the Molecular Vibrations Assisting Exciton Energy Transfer at Room Temperature. *Nat. Commun.* **2014**, *5*, 3012.
- (489) Fuller, F. D.; Pan, J.; Gelzinis, A.; Butkus, V.; Senlik, S. S.; Wilcox, D. E.; Yocom, C. F.; Valkunas, L.; Abramavicius, D.; Ogilvie, J. P. Vibronic Coherence in Oxygenic Photosynthesis. *Nat. Chem.* **2014**, *6*, 706–711.
- (490) Novoderezhkin, V. I.; Romero, E.; van Grondelle, R. How Exciton-Vibrational Coherences Control Charge Separation in the Photosystem II Reaction Center. *Phys. Chem. Chem. Phys.* **2015**, *17*, 30828–30841.
- (491) Lemaur, V.; da Silva Filho, D. A.; Coropceanu, V.; Lehmann, M.; Geerts, Y.; Piris, J.; Debije, M. G.; van de Craats, A. M.; Senthilkumar, K.; Siebbeles, L. D. A.; et al. Charge Transport Properties in Discotic Liquid Crystals: A Quantum-Chemical Insight into Structure–Property Relationships. *J. Am. Chem. Soc.* **2004**, *126*, 3271–3279.
- (492) Kwon, O.; Coropceanu, V.; Gruhn, N. E.; Durivage, J. C.; Laquindanum, J. G.; Katz, H. E.; Cornil, J.; Brédas, J. L. Characterization of the Molecular Parameters Determining Charge Transport in Anthradithiophene. *J. Chem. Phys.* **2004**, *120*, 8186–8194.
- (493) Calzado, C. J.; Malrieu, J.-P. Comparison between Explicitly Correlated and Density Functional Theory Calculations in Mixed-Valence Model Systems. *Chem. Phys. Lett.* **2000**, *317*, 404–413.
- (494) Newton, M. D. Quantum Chemical Probes of Electron-Transfer Kinetics: The Nature of Donor-Acceptor Interactions. *Chem. Rev.* **1991**, *91*, 767–792.
- (495) Huang, J.; Kertesz, M. Intermolecular Transfer Integrals for Organic Molecular Materials: Can Basis Set Convergence Be Achieved? *Chem. Phys. Lett.* **2004**, *390*, 110–115.
- (496) Huang, J.; Kertesz, M. Validation of Intermolecular Transfer Integral and Bandwidth Calculations for Organic Molecular Materials. *J. Chem. Phys.* **2005**, *122*, 234707.
- (497) Jordan, K. D.; Paddon-Row, M. N. Long-Range Interactions in a Series of Rigid Nonconjugated Dienes. 1. Distance Dependence of The.Pi.+,Pi.- And.Pi.+\*,Pi.-\* Splittings Determined from Ab Initio Calculations. *J. Phys. Chem.* **1992**, *96*, 1188–1196.
- (498) Barford, W. Excitons in Conjugated Polymers: A Tale of Two Particles. *J. Phys. Chem. A* **2013**, *117*, 2665–2671.
- (499) Barford, W.: *Electronic and Optical Properties of Conjugated Polymers*; Clarendon Press: Oxford, 2005; Vol. 129.
- (500) Würthner, F. Perylene Bisimide Dyes as Versatile Building Blocks for Functional Supramolecular Architectures. *Chem. Commun.* **2004**, 1564–1579.
- (501) Balakrishnan, K.; Datar, A.; Naddo, T.; Huang, J.; Oitker, R.; Yen, M.; Zhao, J.; Zang, L. Effect of Side-Chain Substituents on Self-Assembly of Perylene Diimide Molecules: Morphology Control. *J. Am. Chem. Soc.* **2006**, *128*, 7390–7398.
- (502) Jones, B. A.; Facchetti, A.; Wasielewski, M. R.; Marks, T. J. Tuning Orbital Energetics in Arylene Diimide Semiconductors. Materials Design for Ambient Stability of N-Type Charge Transport. *J. Am. Chem. Soc.* **2007**, *129*, 15259–15278.
- (503) Giri, G.; Verploegen, E.; Mannsfeld, S. C. B.; Atahan-Evrenk, S.; Kim, D. H.; Lee, S. Y.; Becerril, H. A.; Aspuru-Guzik, A.; Toney, M. F.; Bao, Z. A. Tuning Charge Transport in Solution-Sheared Organic Semiconductors Using Lattice Strain. *Nature* **2011**, *480*, 504–U124.
- (504) Molina-Lopez, F.; Yan, H.; Gu, X.; Kim, Y.; Toney, M. F.; Bao, Z. Electric Field Tuning Molecular Packing and Electrical Properties of Solution-Shearing Coated Organic Semiconducting Thin Films. *Adv. Funct. Mater.* **2017**, *27*, 1605503.
- (505) Krieg, E.; Bastings, M. M. C.; Besenius, P.; Rybtchinski, B. Supramolecular Polymers in Aqueous Media. *Chem. Rev.* **2016**, *116*, 2414–2477.

- (506) Mizuguchi, J.; Tojo, K. Electronic Structure of Perylene Pigments as Viewed from the Crystal Structure and Excitonic Interactions. *J. Phys. Chem. B* **2002**, *106*, 767–772.
- (507) Lambrecht, J.; Isenberg, C.; Bruhn, C.; Saragi, T. P. I. Self-Assembled  $\pi$ -Conjugated Organic Wires with Unique Properties. *ChemistrySelect* **2017**, *2*, 3572–3576.
- (508) Fan, J.; Zhang, L.; Briseno, A. L.; Wudl, F. Synthesis and Characterization of 7,8,15,16-Tetraazaterrylene. *Org. Lett.* **2012**, *14*, 1024–1026.
- (509) Labastide, J. A.; Thompson, H. B.; Marques, S. R.; Colella, N. S.; Briseno, A. L.; Barnes, M. D. Directional Charge Separation in Isolated Organic Semiconductor Crystalline Nanowires. *Nat. Commun.* **2016**, *7*, 10629.
- (510) Maniukiewicz, W.; Bojarska, J.; Olczak, A.; Dobruchowska, E.; Wiatrowski, M. 2,9-Di-3-Pentylanthra[1,9-Def:6,5,10-D'e'f']-Diisoquinoline-1,3,8,10-Tetrone. *Acta Crystallogr., Sect. E: Struct. Rep. Online* **2010**, *66*, o2570–o2571.
- (511) Zaumseil, J.; Sirringhaus, H. Electron and Ambipolar Transport in Organic Field-Effect Transistors. *Chem. Rev.* **2007**, *107*, 1296–1323.
- (512) Jurchescu, O. D.; Baas, J.; Palstra, T. T. M. Effect of Impurities on the Mobility of Single Crystal Pentacene. *Appl. Phys. Lett.* **2004**, *84*, 3061–3063.
- (513) Dimitrakopoulos, C. D.; Malenfant, P. R. L. Organic Thin Film Transistors for Large Area Electronics. *Adv. Mater.* **2002**, *14*, 99–117.
- (514) Lin, Y. Y.; Gundlach, D. J.; Nelson, S. F.; Jackson, T. N. Stacked Pentacene Layer Organic Thin-Film Transistors with Improved Characteristics. *IEEE Electron Device Lett.* **1997**, *18*, 606–608.
- (515) Klauk, H.; Halik, M.; Zschieschang, U.; Schmid, G.; Radlik, W.; Weber, W. High-Mobility Polymer Gate Dielectric Pentacene Thin Film Transistors. *J. Appl. Phys.* **2002**, *92*, 5259–5263.
- (516) Anthony, J. E. Functionalized Acenes and Heteroacenes for Organic Electronics. *Chem. Rev.* **2006**, *106*, 5028–5048.
- (517) Bendikov, M.; Wudl, F.; Perepichka, D. F. Tetraphiafulvalenes, Oligoacenes, and Their Buckminsterfullerene Derivatives: The Brick and Mortar of Organic Electronics. *Chem. Rev.* **2004**, *104*, 4891–4946.
- (518) Jadhav, P. J.; Brown, P. R.; Thompson, N.; Wunsch, B.; Mohanty, A.; Yost, S. R.; Hontz, E.; Van Voorhis, T.; Bawendi, M. G.; Bulovic, V.; et al. Triplet Exciton Dissociation in Singlet Exciton Fission Photovoltaics. *Adv. Mater.* **2012**, *24*, 6169–6174.
- (519) Burdett, J. J.; Bardeen, C. J. The Dynamics of Singlet Fission in Crystalline Tetracene and Covalent Analogs. *Acc. Chem. Res.* **2013**, *46*, 1312–1320.
- (520) Burdett, J. J.; Bardeen, C. J. Quantum Beats in Crystalline Tetracene Delayed Fluorescence Due to Triplet Pair Coherences Produced by Direct Singlet Fission. *J. Am. Chem. Soc.* **2012**, *134*, 8597–8607.
- (521) Rao, A.; Wilson, M. W. B.; Hodgkiss, J. M.; Albert-Seifried, S.; Bassler, H.; Friend, R. H. Exciton Fission and Charge Generation Via Triplet Excitons in Pentacene/C-60 Bilayers. *J. Am. Chem. Soc.* **2010**, *132*, 12698–12703.
- (522) Chan, W. L.; Ligges, M.; Zhu, X. Y. The Energy Barrier in Singlet Fission Can Be Overcome through Coherent Coupling and Entropic Gain. *Nat. Chem.* **2012**, *4*, 840–845.
- (523) Chan, W. L.; Berkelbach, T. C.; Provorse, M. R.; Monahan, N. R.; Tritsch, J. R.; Hybertsen, M. S.; Reichman, D. R.; Gao, J. L.; Zhu, X. Y. The Quantum Coherent Mechanism for Singlet Fission: Experiment and Theory. *Acc. Chem. Res.* **2013**, *46*, 1321–1329.
- (524) Congreve, D. N.; Lee, J. Y.; Thompson, N. J.; Hontz, E.; Yost, S. R.; Reusswig, P. D.; Bahlke, M. E.; Reineke, S.; Van Voorhis, T.; Baldo, M. A. External Quantum Efficiency above 100% in a Singlet-Exciton-Fission-Based Organic Photovoltaic Cell. *Science* **2013**, *340*, 334–337.
- (525) Thorsmolle, V. K.; Averitt, R. D.; Demsar, J.; Smith, D. L.; Tretiak, S.; Martin, R. L.; Chi, X.; Crone, B. K.; Ramirez, A. P.; Taylor, A. J. Morphology Effectively Controls Singlet-Triplet Exciton Relaxation and Charge Transport in Organic Semiconductors. *Phys. Rev. Lett.* **2009**, *102*, 017401.
- (526) Yost, S. R.; Lee, J.; Wilson, M. W. B.; Wu, T.; McMahon, D. P.; Parkhurst, R. R.; Thompson, N. J.; Congreve, D. N.; Rao, A.; Johnson, K.; et al. A Transferable Model for Singlet-Fission Kinetics. *Nat. Chem.* **2014**, *6*, 492–497.
- (527) Pac, B.; Petelenz, P. Lowest Singlet Exciton in Pentacene: Modern Calculations Versus Classic Experiments. *ChemPhysChem* **2014**, *15*, 2801–2809.
- (528) Roberts, S. T.; McAnally, R. E.; Mastron, J. N.; Webber, D. H.; Whited, M. T.; Brutchey, R. L.; Thompson, M. E.; Bradforth, S. E. Efficient Singlet Fission Discovered in a Disordered Acene Film. *J. Am. Chem. Soc.* **2012**, *134*, 6388–6400.
- (529) Monahan, N. R.; Sun, D.; Tamura, H.; Williams, K. W.; Xu, B.; Zhong, Y.; Kumar, B.; Nuckolls, C.; Harutyunyan, A. R.; Chen, G.; et al. Dynamics of the Triplet-Pair State Reveals the Likely Coexistence of Coherent and Incoherent Singlet Fission in Crystalline Hexacene. *Nat. Chem.* **2017**, *9*, 341–346.
- (530) Zirzlmeier, J.; Lehnher, D.; Coto, P. B.; Chernick, E. T.; Casillas, R.; Basel, B. S.; Thoss, M.; Tykwienski, R. R.; Guldi, D. M. Singlet Fission in Pentacene Dimers. *Proc. Natl. Acad. Sci. U. S. A.* **2015**, *112*, 5325–5330.
- (531) Pensack, R. D.; Tilley, A. J.; Parkin, S. R.; Lee, T. S.; Payne, M. M.; Gao, D.; Jahnke, A. A.; Oblinsky, D. G.; Li, P.-F.; Anthony, J. E.; et al. Exciton Delocalization Drives Rapid Singlet Fission in Nanoparticles of Acene Derivatives. *J. Am. Chem. Soc.* **2015**, *137*, 6790–6803.
- (532) Busby, E.; Berkelbach, T. C.; Kumar, B.; Chernikov, A.; Zhong, Y.; Hlaing, H.; Zhu, X. Y.; Heinz, T. F.; Hybertsen, M. S.; Sfeir, M. Y.; et al. Multiphonon Relaxation Slows Singlet Fission in Crystalline Hexacene. *J. Am. Chem. Soc.* **2014**, *136*, 10654–10660.
- (533) Zimmerman, P. M.; Bell, F.; Casanova, D.; Head-Gordon, M. Mechanism for Singlet Fission in Pentacene and Tetracene: From Single Exciton to Two Triplets. *J. Am. Chem. Soc.* **2011**, *133*, 19944–19952.
- (534) Zimmerman, P. M.; Musgrave, C. B.; Head-Gordon, M. A Correlated Electron View of Singlet Fission. *Acc. Chem. Res.* **2013**, *46*, 1339–1347.
- (535) Tempelaar, R.; Reichman, D. R. Vibronic Exciton Theory of Singlet Fission. II. Two-Dimensional Spectroscopic Detection of the Correlated Triplet Pair State. *J. Chem. Phys.* **2017**, *146*, 174704.
- (536) Tempelaar, R.; Reichman, D. R. Vibronic Exciton Theory of Singlet Fission. I. Linear Absorption and the Anatomy of the Correlated Triplet Pair State. *J. Chem. Phys.* **2017**, *146*, 174703.
- (537) Cook, J. D.; Carey, T. J.; Arias, D. H.; Johnson, J. C.; Damrauer, N. H. Solvent-Controlled Branching of Localized Versus Delocalized Singlet Exciton States and Equilibration with Charge Transfer in a Structurally Well-Defined Tetracene Dimer. *J. Phys. Chem. A* **2017**, *121*, 9229–9242.
- (538) Cook, J. D.; Carey, T. J.; Damrauer, N. H. Solution-Phase Singlet Fission in a Structurally Well-Defined Norbornyl-Bridged Tetracene Dimer. *J. Phys. Chem. A* **2016**, *120*, 4473–4481.
- (539) Kumarasamy, E.; Sanders, S. N.; Tayebjee, M. J. Y.; Asadpoordarvish, A.; Hele, T. J. H.; Fuemmeler, E. G.; Pun, A. B.; Yablon, L. M.; Low, J. Z.; Paley, D. W.; et al. Tuning Singlet Fission in Pi-Bridge-Pi Chromophores. *J. Am. Chem. Soc.* **2017**, *139*, 12488–12494.
- (540) Yong, C. K.; Musser, A. J.; Bayliss, S. L.; Lukman, S.; Tamura, H.; Bubnova, O.; Hallani, R. K.; Meneau, A.; Resel, R.; Maruyama, M.; et al. The Entangled Triplet Pair State in Acene and Heteroacene Materials. *Nat. Commun.* **2017**, *8*, 12.
- (541) Burdett, J. J.; Muller, A. M.; Gosztola, D.; Bardeen, C. J. Excited State Dynamics in Solid and Monomeric Tetracene: The Roles of Superradiance and Exciton Fission. *J. Chem. Phys.* **2010**, *133*, 144506.
- (542) Clark, L. B.; Philpott, M. R. Anisotropy of the Singlet Transitions of Crystalline Anthracene. *J. Chem. Phys.* **1970**, *53*, 3790–3801.
- (543) Morris, G. C.; Sceats, M. G. The 4000  $\text{cm}^{-1}$  Transition of Crystal Anthracene. *Chem. Phys.* **1974**, *3*, 164–179.

- (544) Tavazzi, S.; Raimondo, L.; Silvestri, L.; Spearman, P.; Camposeo, A.; Polo, M.; Pisignano, D. Dielectric Tensor of Tetracene Single Crystals: The Effect of Anisotropy on Polarized Absorption and Emission Spectra. *J. Chem. Phys.* **2008**, *128*, 154709.
- (545) Prikhotko, A. F.; Tsikora, L. I. Spectral Investigations of Pentacene. *Optics and Spectroscopy-Ussr* **1968**, *25*, 242.
- (546) Zanker, V.; Preuss, J. Microspectrometrical Measurements on Single Crystals of Tetracene and Pentacene in Dependence of Thickness and Temperature. *Zeitschrift Fur Angewandte Physik* **1969**, *27*, 363–365.
- (547) Chernikov, A.; Yaffe, O.; Kumar, B.; Zhong, Y.; Nuckolls, C.; Heinz, T. F. Spectroscopic Study of Anisotropic Excitons in Single Crystal Hexacene. *J. Phys. Chem. Lett.* **2014**, *5*, 3632–3635.
- (548) Cudazzo, P.; Gatti, M.; Rubio, A.; Sottile, F. Frenkel Versus Charge-Transfer Exciton Dispersion in Molecular Crystals. *Phys. Rev. B: Condens. Matter Mater. Phys.* **2013**, *88*, 195152.
- (549) Tiago, M. L.; Northrup, J. E.; Louie, S. G. Ab Initio Calculation of the Electronic and Optical Properties of Solid Pentacene. *Phys. Rev. B: Condens. Matter Mater. Phys.* **2003**, *67*, 115212.
- (550) Sharifzadeh, S.; Darancet, P.; Kronik, L.; Neaton, J. B. Low-Energy Charge-Transfer Excitons in Organic Solids from First-Principles: The Case of Pentacene. *J. Phys. Chem. Lett.* **2013**, *4*, 2197–2201.
- (551) Schuster, R.; Knupfer, M.; Berger, H. Exciton Band Structure of Pentacene Molecular Solids: Breakdown of the Frenkel Exciton Model. *Phys. Rev. Lett.* **2007**, *98*, 037402.
- (552) Roth, F.; Schuster, R.; Konig, A.; Knupfer, M.; Berger, H. Momentum Dependence of the Excitons in Pentacene. *J. Chem. Phys.* **2012**, *136*, 204708.
- (553) Sebastian, L.; Weiser, G.; Peter, G.; Bässler, H. Charge-Transfer Transitions in Crystalline Anthracene and Their Role in Photoconductivity. *Chem. Phys.* **1983**, *75*, 103–114.
- (554) Sebastian, L.; Weiser, G.; Bässler, H. Charge-Transfer Transitions in Solid Tetracene and Pentacene Studied by Electro-Absorption. *Chem. Phys.* **1981**, *61*, 125–135.
- (555) Anger, F.; Osso, J. O.; Heinemeyer, U.; Broch, K.; Scholz, R.; Gerlach, A.; Schreiber, F. Photoluminescence Spectroscopy of Pure Pentacene, Perfluoropentacene, and Mixed Thin Films. *J. Chem. Phys.* **2012**, *136*, 054701.
- (556) Aoki-Matsumoto, T.; Furuta, K.; Yamada, T.; Moriya, H.; Mizuno, K.; Matsui, A. H.: *Excitonic Photoluminescence in Pentacene Single Crystal*; World Scientific Publ Co Pte Ltd: Singapore, 2001.
- (557) He, R.; Chi, X.; Pinczuk, A.; Lang, D. V.; Ramirez, A. P. Extrinsic Optical Recombination in Pentacene Single Crystals: Evidence of Gap States. *Appl. Phys. Lett.* **2005**, *87*, 211117.
- (558) Zhang, Y. W.; Kim, B.; Yao, S.; Bondar, M. V.; Belfield, K. D. Controlled Aggregation and Enhanced Two-Photon Absorption of a Water-Soluble Squaraine Dye with a Poly(Acrylic Acid) Template. *Langmuir* **2013**, *29*, 11005–11012.
- (559) Sanyal, S.; Painelli, A.; Pati, S. K.; Terenziani, F.; Sissa, C. Aggregates of Quadrupolar Dyes for Two-Photon Absorption: The Role of Intermolecular Interactions. *Phys. Chem. Chem. Phys.* **2016**, *18*, 28198–28208.
- (560) Tempelaar, R.; Jansen, T. L. C.; Knoester, J. Exciton–Exciton Annihilation Is Coherently Suppressed in H-Aggregates, but Not in J-Aggregates. *J. Phys. Chem. Lett.* **2017**, *8*, 6113–6117.
- (561) Zang, H.; Zhao, Y.; Liang, W. Quantum Interference in Singlet Fission: J- and H-Aggregate Behavior. *J. Phys. Chem. Lett.* **2017**, *8*, 5105–5112.
- (562) Spano, F. C.; Mukamel, S. Nonlinear Susceptibilities of Molecular Aggregates—Enhancement of Chi(3) by Size. *Phys. Rev. A: At., Mol., Opt. Phys.* **1989**, *40*, 5783–5801.
- (563) Knoester, J.; Spano, F. C. Unusual Behavior of 2-Photon Absorption from 3-Level Molecules in a One-Dimensional Lattice. *Phys. Rev. Lett.* **1995**, *74*, 2780–2783.
- (564) Shafeekh, K. M.; Das, S.; Sissa, C.; Painelli, A. Asymmetric Squaraine Dyes: Spectroscopic and Theoretical Investigation. *J. Phys. Chem. B* **2013**, *117*, 8536–8546.
- (565) Terenziani, F.; Painelli, A.; Katan, C.; Charlote, M.; Blanchard-Desce, M. Charge Instability in Quadrupolar Chromophores: Symmetry Breaking and Solvatochromism. *J. Am. Chem. Soc.* **2006**, *128*, 15742–15755.
- (566) Terenziani, F.; D'Avino, G.; Painelli, A. Multichromophores for Nonlinear Optics: Designing the Material Properties by Electrostatic Interactions. *ChemPhysChem* **2007**, *8*, 2433–2444.
- (567) Sissa, C.; Terenziani, F.; Painelli, A.; Manna, A. K.; Pati, S. K. Resonance Energy Transfer between Polar Charge-Transfer Dyes: A Focus on the Limits of the Dipolar Approximation. *Chem. Phys.* **2012**, *404*, 9–15.
- (568) Guasch, J.; Grisanti, L.; Souto, M.; Lloveras, V.; Vidal-Gancedo, J.; Ratera, I.; Painelli, A.; Rovira, C.; Veciana, J. Intra- and Intermolecular Charge Transfer in Aggregates of Tetrathiafulvalene-Triphenylmethyl Radical Derivatives in Solution. *J. Am. Chem. Soc.* **2013**, *135*, 6958–6967.
- (569) Hu, H. H.; Przhonska, O. V.; Terenziani, F.; Painelli, A.; Fishman, D.; Ensley, T. R.; Reichert, M.; Webster, S.; Bricks, J. L.; Kachkovski, A. D.; et al. Two-Photon Absorption Spectra of a near-Infrared 2-Azaazulene Polymethine Dye: Solvation and Ground-State Symmetry Breaking. *Phys. Chem. Chem. Phys.* **2013**, *15*, 7666–7678.
- (570) Egorov, V. V.; Alfimov, M. V. Theory of the J-Band: From the Frenkel Exciton to Charge Transfer. *Phys.-Usp.* **2007**, *50*, 985–1029.
- (571) Hestand, N. J.; Zheng, C. Y.; Penmetcha, A. R.; Cona, B.; Cody, J. A.; Spano, F. C.; Collison, C. J. Confirmation of the Origins of Panchromatic Spectra in Squaraine Thin Films Targeted for Organic Photovoltaic Devices. *J. Phys. Chem. C* **2015**, *119*, 18964–18974.
- (572) Lidzey, D. G.; Bradley, D. D. C.; Skolnick, M. S.; Virgili, T.; Walker, S.; Whittaker, D. M. Strong Exciton-Photon Coupling in an Organic Semiconductor Microcavity. *Nature* **1998**, *395*, 53–55.
- (573) Lidzey, D. G.; Bradley, D. D. C.; Armitage, A.; Walker, S.; Skolnick, M. S. Photon-Mediated Hybridization of Frenkel Excitons in Organic Semiconductor Microcavities. *Science* **2000**, *288*, 1620–1623.
- (574) Coles, D. M.; Somaschi, N.; Michetti, P.; Clark, C.; Lagoudakis, P. G.; Savvidis, P. G.; Lidzey, D. G. Polariton-Mediated Energy Transfer between Organic Dyes in a Strongly Coupled Optical Microcavity. *Nat. Mater.* **2014**, *13*, 712–719.
- (575) Spano, F. C. Optical Microcavities Enhance the Exciton Coherence Length and Eliminate Vibronic Coupling in J-Aggregates. *J. Chem. Phys.* **2015**, *142*, 184707.
- (576) Orgiu, E.; George, J.; Hutchison, J. A.; Devaux, E.; Dayen, J. F.; Doudin, B.; Stellacci, F.; Genet, C.; Schachenmayer, J.; Genes, C.; et al. Conductivity in Organic Semiconductors Hybridized with the Vacuum Field. *Nat. Mater.* **2015**, *14*, 1123–1129.
- (577) Bellessa, J.; Bonnand, C.; Plenet, J. C.; Mugnier, J. Strong Coupling between Surface Plasmons and Excitons in an Organic Semiconductor. *Phys. Rev. Lett.* **2004**, *93*, 036404.
- (578) Fofang, N. T.; Park, T. H.; Neumann, O.; Mirin, N. A.; Nordlander, P.; Halas, N. J. Plexcitonic Nanoparticles: Plasmon-Exciton Coupling in Nanoshell-J-Aggregate Complexes. *Nano Lett.* **2008**, *8*, 3481–3487.
- (579) Vasa, P.; Wang, W.; Pomraenke, R.; Lammers, M.; Maiuri, M.; Manzoni, C.; Cerullo, G.; Lienau, C. Real-Time Observation of Ultrafast Rabi Oscillations between Excitons and Plasmons in Metal Nanostructures with J-Aggregates. *Nat. Photonics* **2013**, *7*, 128–132.
- (580) Zeb, M. A.; Kirton, P. G.; Keeling, J. Exact States and Spectra of vibrationally Dressed Polaritons. *ACS Photonics* **2018**, *5*, 249–257.
- (581) Wu, N.; Feist, J.; Garcia-Vidal, F. J. When Polarons Meet Polaritons: Exciton-Vibration Interactions in Organic Molecules Strongly Coupled to Confined Light Fields. *Phys. Rev. B: Condens. Matter Mater. Phys.* **2016**, *94*, 195409.
- (582) Herrera, F.; Spano, F. C. Theory of Nanoscale Organic Cavities: The Essential Role of Vibration-Photon Dressed States. *ACS Photonics* **2018**, *5*, 65–79.